ORNL/NRC/LTR-04/15

Contract Program or Project Title:	Heavy-Section Steel Technology (HSST) Program
Subject of this Document:	Probabilistic Structural Mechanics Analysis of the Degraded Davis-Besse RPV Head
Type of Document:	Letter Report
Authors:	P. T. Williams S. Yin B. R. Bass
Date of Document:	September 2004
Responsible NRC Individual and NRC Office or Division	M. T. Kirk Division of Engineering Technology Office of Nuclear Regulatory Research

Prepared for the
U. S. Nuclear Regulatory Commission
Washington, D.C. 20555-0001
Under Interagency Agreement DOE 1886-N653-3Y
NRC JCN NoY6533

OAK RIDGE NATIONAL LABORATORY
Oak Ridge, Tennessee 37831-6085
managed and operated by
UT-Battelle, LLC for the
U. S. DEPARTMENT OF ENERGY
under Contract No. DE-AC05-00OR22725

ORNL/NRC/LTR-04/15

Probabilistic Structural Mechanics Analysis of the Degraded Davis-Besse RPV Head

P. T. Williams
S. Yin
B. R. Bass

Oak Ridge National Laboratory
Oak Ridge, Tennessee

Manuscript Completed – May 2004
Date Published – September 2004

Prepared for the
U.S. Nuclear Regulatory Commission
Office of Nuclear Regulatory Research
Under Interagency Agreement DOE 1886-N653-3Y

NRC JCN No. Y6533

OAK RIDGE NATIONAL LABORATORY
Oak Ridge, Tennessee 37831-6085
managed and operated by
UT-Battelle, LLC for the
U. S. DEPARTMENT OF ENERGY
under Contract No. DE-AC05-00OR22725

Probabilistic Structural Mechanics Analysis of the Degraded Davis-Besse RPV Head

P. T. Williams, S. Yin, and B. R. Bass
Oak Ridge National Laboratory
P. O. Box 2008
Oak Ridge, TN, 37831-6085

Abstract

The Heavy-Section Steel Technology (HSST) Program at Oak Ridge National Laboratory (ORNL) has performed a probabilistic structural mechanics (PSM) analysis of the damaged Davis-Besse reactor pressure vessel head in support of the United States Nuclear Regulatory Commission's ongoing forensic investigations. This report documents the results of that PSM analysis, including a description of the Davis-Besse wastage-area damage model, the technical basis for the model, and the results of sensitivity studies based on a cladding capacity analysis (CCA) and an Accident Sequence Precursor (ASP) investigation of the wastage cavity. A companion report describes the HSST experimental program carried out at ORNL in parallel with the PSM analysis.

The CCA and ASP studies provide approximate answers to three questions regarding the Davis Besse event:

(1) What applied pressure would have failed the wastage-cavity cladding at the time of discovery (TOD) on 16 February 2002? (CCA)

(2) How much longer could the Davis-Besse RPV have continued in service without failure of the pressure boundary if the wastage cavity had not been discovered on 16 February 2002? (CCA)

(3) Including uncertainties in the "As-Found" damage state of the wastage cavity, what was the probability of failure one year before the TOD, and how do these uncertainties affect the estimated probability of failure at TOD? (ASP)

The answer to question No. #1 required the construction of a detailed finite-element model (FEM) of the Davis Besse wastage cavity which incorporated the results of extensive laboratory measurements and metallographic examinations of the damaged site after it had been removed from the RPV head. The Davis-Besse cladding material was carefully characterized in terms of both strength (plastic-flow properties) and fracture toughness (ductile-tearing initiation and flaw growth). The fracture-toughness characterization (at a service temperature of 600 °F) was carried out by the HSST Program using pre-cracked Charpy V-Notch specimens taken from the Davis-Besse wastage cavity. All of the characterization studies included investigations of the uncertainties in the property measurements.

The results of the deterministic FEM analysis indicate that, for the most conservative assumptions made in the study regarding flaw size and depth, the estimated failure pressures all exceeded the relief-valve set-point pressure of 2500 psi. This result is in agreement with the forensic finding that exposure of the wastage cavity to the nominal operating pressure of 2165 psi did not produce any evidence of ductile crack initiation at the TOD. Median pressures needed to fail the wastage cavity (by ductile-tearing initiation of the Model Flaw) were estimated to range between 3000 and 5200 psi, representing a 1.4 to 2.4 margin against the operating pressure. A 90 percent confidence interval covering the median estimates was 2710 psi to 6500 psi (or 1.25 to 3.0 margin against the operating pressure).

Question No. #2 was addressed with a PSM analysis that reflected the very limited *state-of-knowledge* of how the wastage cavity might be expected to evolve over time beyond the known damage state at the TOD. An *Expert Elicitation* was carried out by the NRC staff to provide estimates for the wastage-cavity growth rate and the rate of stress-corrosion crack development due to exposure of the unbacked cladding

to the concentrated boric acid solution inside the wastage cavity. The resulting best-estimate predicts that the cumulative probability of survival decreases to 50% after approximately 230 days of additional operation. When applying the most conservative flaw model, this median time decreased to approximately 150 days of additional operation. In these studies, the consequences of failure were expressed in terms of a range of break sizes leading to a loss-of-coolant accident (LOCA). Additionally, the results from the CCA sensitivity study can be used to provide an approximate 90 % confidence interval covering the best estimate for the median failure of the cladding. These results predict that, at a confidence level of 90%, Davis-Besse could have continued operating from 2 to 22 months before cladding failure would be expected.

Question No. #3 was addressed by a modification to the PSM analysis that incorporated additional uncertainty in damage state of the wastage cavity at the TOD. At the TOD, the best-estimate probability of cladding failure was estimated to be approximately 20%. At 1 year before the TOD, the ASP analysis estimated a low probability of failure of approximately 1%.

CONTENTS

Section **Page**

1 Introduction 1
1.1 Method of Analysis 1
1.2 Background of the Davis-Besse Degraded RPV Head Problem 2
1.3 Accident Sequence Precursor Program 3
1.4 Previous ORNL Studies of the Davis-Besse RPV Head Degradation Problem 6
1.4.1 Detailed Finite-Element Global and Submodels of Wastage Area and Cavity 6
1.4.2 Results of Wastage-Cavity Growth-Pattern Study [13] 7
1.5 Scope of this Report 12
2 Davis-Besse Wastage-Area Damage Model 13
2.1 Detailed 3D FEM Model for Deterministic Analyses 13
2.1.1 Modeled Wastage Cavity Footprint 13
2.1.2 Wastage Cavity 13
2.1.3 Modeled Surface Flaws 18
2.2 Simplified Wastage-Area Damage Model for Monte Carlo Simulations 19
2.2.1 Damage Model Geometry, Loading, and Constraint Conditions 21
2.2.2 Damage-State Parameters 21
2.2.3 Failure Mechanisms – Development of a Plastic-Collapse Fragility Curve 23
2.2.4 Failure Mechanisms – Development of a Ductile-Tearing Model 42
2.2.5 Assumed Wastage-Area Damage Model Accident Sequence 67
2.2.6 Results of an Expert Elicitation for Input Distributions 79
2.2.7 Best-Estimate, More Conservative, and Less Conservative Sampling Distributions 93
2.2.8 Variance Reduction – The Method of Antithetic Variates 93
2.2.9 LOCA Screening Rules 96
2.2.10 LOCA Break Size Definitions 100
2.2.11 Cavity Growth-Shape Scaling Rules 100
3 Results and Discussion 101
3.1 Results of Deterministic FEM Analysis 101
3.2 Cladding Capacity Analysis (CCA) – Sensitivity Study Results 104
3.2.1 Convergence of Monte Carlo Simulations 104
3.2.2 Best-Estimate CCA Results 107
3.2.3 Results of the CCA Sensitivity Study 107
3.3 Accident Sequence Precursor Analysis – Best Estimate and Sensitivity Study Results 111
3.3.1 Case Matrix for ASP Study 118
3.3.2 Best-Estimate ASP Results 118
3.3.3 Results of the ASP Sensitivity Study 118
4 Summary and Conclusions 124

References 126
Appendix A 130
Appendix B 135
Appendix C 270

LIST OF TABLES

Table **Page**

1. Plastic-Flow Properties for SS Cladding 26
2. "Goodness of Fit" Statistics for Yield and Ultimate Stress Statistical Distributions 26
3. Results of Bivariate Sampling Protocols for a Range of Correlation Coefficients, ... 40
4. Ductile-Tearing Data Extracted from Table 13 of NUREG/CR-5511 [35]. 45
5a. Ductile-Tearing Data Used in Development of J_{Ic} Statistical Distributions 46
5b. Statistical Distributions Fitted to J_{Ic} Data from Three Sources 46
6. Summary of Candidate Input Sampling Distributions 81
7. LOCA Sizes Defined by Effective Break Sizes 100
8a. DB Submodel Pressures to Initiate Ductile Tearing for the 5th, 50th , and 95th Percentiles with Margins Against Ductile Initiation at the Operating Pressure of 2165 psi 102
8b. DB Submodel Pressures to Initiate Ductile Tearing for the 5th, 50th , and 95th Percentiles with Margins Against Ductile Initiation at the Relief-Valve Setpoint Pressure of 2500 psi 102
9. Case Matrix for Cladding Capacity Analysis (CCA) 105
10. Monte Carlo Results – Summary of LOCA Probabilities (N = 50,000) 105
11. Times to Failure after TOD 108
12. Case Matrix for ASP Sensitivity Study 119
13. Case Matrix Layout Key 119
14. Summary of LOCA Probabilities for ASP Sensitivity Study 119

LIST OF FIGURES

Figure **Page**

1. Depictions of Davis-Besse RPV and wastage cavity: (a) Davis-Besse Nuclear Power Station RPV [7]; (b) schematic of a typical nuclear power reactor showing the relationship of the CRDM nozzles to the RPV head and the location of the damaged area [7]; 4
1. (continued) (c) sketch of RPV head degradation; and (d) photograph presenting a plan view of the wastage-area footprint showing remaining J-groove weld, irregular topography of exposed unbacked cladding, and irregular sidewalls of the wastage cavity [7]. 5
2. Finite-element global model and submodels applied in previous analyses [11,13] of the Davis-Besse head and wastage area..... 8
3. Geometry of the hemispherical RPV head and closure flange used in the global model [11,13]. 8
4. Geometry of submodel relative to nozzles #3, #11, #15, and #16 in the RPV head. 9
5. Wastage-cavity submodel [11,13] developed from a ProEngineer® solid model and then meshed with MSC Patran®..... 9
6. A computational study was carried out in [13] to determine the sensitivity of burst pressures, predicted by finite-element analyses, to the geometry of estimated growth patterns of the wastage cavity "footprint": (a) self-similar and ellipsoidal growth patterns and (b) circular burst disk. 10
7. The FEM-predicted burst pressures of irregularly-shaped "footprint" growth patterns are compared in [13] to burst pressure predictions for circular diaphragms under lateral pressure loading based on an instability theory proposed by Chakrabarty and Alexander [15]. 11
8. Davis-Besse global model of RPV closure head for the current study includes a simplified wastage-cavity definition and inner cladding layer..... 14
9. Davis-Besse submodel includes: (a) nozzles #3, #11, #15, #16 (Alloy 600); (b) a refined definition of the wastage-cavity morphology in the base material (A 533B pressure vessel steel), ... 15
9. (continued) (c) wastage cavity footprint; (d) irregular geometry of wastage cavity walls based on geometric measurements from the dental mold taken by BWXT [16]. 16
9. (continued) (e) irregular exposed cladding topography based on a sinusoidal waveform, and (f) J-groove weld near a modeled surface flaw. 17
10. Geometry, loading, and constraint conditions for the Davis-Besse RPV head *damage model* – a ¼ symmetry burst disk with a centered surface flaw, where h_0 = 0.25 in. and L = 2.0 in..... 20
11. Spherical geometry of deformation assumed in Chakrabarty and Alexander's plastic instability theory. 22
12. Plots of true stress vs. true strain from the data in Table 1. 27
13. Probability density functions for fitted statistical marginal distributions based on data in Table 1: (a) yield true stress and (b) ultimate true stress..... 28
14. Statistical distributions approximating the material variability in the yield and ultimate stresses of cladding at 550 °F to 600 °F: (a) yield true stress CDFs with adjustments to match Davis-Besse best-estimate value of 30.9 ksi and (b) ultimate true stress CDFs with adjustments to match Davis-Besse best-estimate value of 72 ksi. 33
15. Frequency histograms of sampled fragility curve slopes based on (a) perfect correlation between yield and ultimate stresses, (b) bivariate lognormal joint distribution with correlation coefficient of 0.06931, (c) bivariate gamma joint distribution with correlation coefficient of 0.06931, and (d) uncorrelated yield and ultimate stresses and, therefore, statistically independent. The correlation coefficient of 0.06931 was statistically inferred from the data in Table 1..... 40

LIST OF FIGURES (continued)

Figure **Page**

16. The intersection of the fragility curve with the *y*-axis is equal to the initial undeformed cladding thickness, h_0, which is assumed known in the current analysis: (a) a sampling of fragility curves based on their cumulative probability resulting from the *bivariate lognormal* joint distribution for yield and ultimate stress and (b) damage state partitioning based on an uncertain fragility curve slope with cumulative probability of 97.5%. 41
17. Net-section plastic collapse pressures estimated by modified C&A (1970) theory compared to P_{NI} values determined from 3D finite-element ABAQUS solutions: (a) $a/t = 0.05$, (b) $a/t = 0.125$, (c) $a/t = 0.25$, (Ductile tearing not simulated for these cases.) 43
17 (continued) Net-section plastic collapse pressures estimated by modified C&A (1970) theory compared to P_{NI} values determined from 3D finite-element ABAQUS solutions: (d) $a/t = 0.5$, and (e) combined plot. (Ductile tearing not simulated for these cases.) 44
18. Ductile-tearing data for cladding from several sources: (a) J_{Ic} data and (b) average tearing modulus data. 47
19. Statistical distributions for J_{Ic}: (a) probability density of lognormal distribution fitted to the 12 Davis-Besse PCCVN data points and (b) lognormal cumulative distribution function compared to cumulative probabilities of Davis-Besse PCCVN J_{Ic} data estimated by the median rank order statistic $p = (i-0.3)/(n+0.4)$. 50
19. (continued) fitted distributions for separate samples of J_{Ic} data from 0.5T C(T) clad overlay (NUREG/CR-5511 and 6363) and PCCVN specimens from PVRUF and Davis-Besse cladding materials: (c) probability densities and (d) cumulative distribution functions. 51
20. J_R curves (a) fitted from data available in ref. [1] for unirradiated 0.5TCS fracture specimens at 550 °F and (b) comparing NUREG/CR C(T) J_R curves with PCCVN J_R curves. 53
21. Finite-element models used in calculating applied *J*-integrals produced by pressure loading of burst disk: (a) ($a/t = 0.5$, $2L/a = 16$) (b) ($a/t = 0.25$, $2L/a = 32$), and (c) ($a/t = 0.125$, $2L/a = 64$) 54
21. (continued) Finite-element models used in calculating applied *J*-integrals produced by pressure loading of burst disk: (d) ($a/t = 0.05$, $2L/a = 160$) (e) ($a/t = 0.8$, $2L/a = 10$) 55
22. *J-integral* driving forces – applied pressure as a function of J_I and a/t for a 2-inch long flaw. 56
23. A-tip tearing instability plots with J_R vs T_R curves from ref. [35] and $J_{applied}$ vs $T_{applied}$ curves from finite-element simulations of burst disks with 2-inch long surface flaws centered in the burst disk. 57
24. A-tip tearing instability plots with J_R vs T_R curves from ref. [35] and $J_{applied}$ vs $T_{applied}$ curves from finite-element simulations of burst disks with 2-inch long surface flaws centered in the burst disk. Applied *J-T* curves are for a range of flaw depths ($0.0125 \text{ in.} \le a \le 0.125 \text{ in.}$) and varying applied pressures. 58
25. C-tip tearing instability plots with J_R vs T_R curves from ref. [35] and $J_{applied}$ vs $T_{applied}$ curves from finite-element simulations of burst disks for "As-Found" flaw with initial 2-inch long with A-tip collapse. 58
26. Driving-force curves used in C-Tip ductile-tearing instability analyses: (a) models were developed for varying R_{cavity} and constant $2L = 2a = 2.0$ in, $t_{clad} = 0.25$ in., (b) applied driving force $J_{applied}$ at C-tip at 2.165 ksi for varying R_{cavity}, and (c) applied dJ/da at C-tip at 2.165 ksi for varying R_{cavity}. 60
27. Given a J_R curve in power-law model form and estimated flow stress, σ_f, the initiation toughness, J_{Ic}, and local tearing modulus, T_R, are uniquely defined (see ASTM E-1820). 61
28. Lognormal distribution characterizing the uncertainty in the J_R curve power-law exponent, *m*. 63

LIST OF FIGURES (continued)

Figure **Page**

29. Plot of $J_{applied}$ as a function of R_{cavity} and $a_{A\text{-}tip}$ for a burst disk with a 2 inch centered flaw under 2.165 ksi applied pressure. $J_{applied}$ solutions from FEM models (using best-estimate stress vs strain data) were fitted to a surface function by TableCurve® 3D. 66
30. Time line for cladding capacity analysis – accident sequence of wastage-area damage model. 68
31. For the "cladding-capacity" analysis, the "As-Found" damage state is assumed known and fixed. For constant cavity and flaw growth rates, the accumulation of damage follows, in the absence of ductile tearing, a linear path towards the fragility curve. 68
32. An example flaw growth history (with ductile tearing) calculated using MathCad®. The case conditions are based on the median values from the more conservative (MC) sampling distribution for $dR/d\tau$, best-estimate distribution for $da/d\tau$, J_{Ic}, and m. 72
33. Evolution of the (a) driving force, $J_{applied}$, and (b) tearing modulus, $T_{applied}$ for the example problem. 75
34. Failure-assessment diagram using the damage-state growth path calculated for the example problem. 76
35. Schematic descriptions of the model flaw's (a) A-tip and C-tip before A-tip ligament collapse and (b) C-tip location after A-tip ligament collapse. 77
36. Candidate sampling distributions for cavity size at one year before discovery, τ_0: (a) probability densities and (b) cumulative probabilities. (ASP analysis only). 83
37. Candidate sampling distributions for cavity wastage rate, $dR/d\tau$: (a) probability densities for two beta distributions, (b) probability densities for two triangular distributions, ... 84
37. (continued) Candidate sampling distributions for cavity wastage rate, $dR/d\tau$: (c) probability densities for two Weibull distributions, and (d) cumulative probabilities. 85
38. Candidate sampling distributions for the Case 1 flaw initiation time , $\Delta\tau_{\text{flaw-ini (1)}}$: (a) probability densities and (b) cumulative probabilities. (ASP analysis only). 86
39. Candidate sampling distributions for the Case 2 flaw initiation time , $\Delta\tau_{\text{flaw-ini (1)}}$: (a) probability densities and (b) cumulative probabilities. (ASP analysis only). 87
40. Candidate sampling distributions for flaw growth rate , $da/d\tau$: (a) probability densities and (b) cumulative probabilities. 88
41. Event trees based on LOCA screening rules representing (a) best-estimate (BE), ... 97
41. (continued) Event trees based on LOCA screening rules representing: (b) more conservative (MC), ... 98
41. (continued) and (c) less conservative (LC) rules. 99
42. Load paths ($J_{applied}$ vs Applied Pressure) for three model surface flaws placed in the Davis-Besse finite-element submodel compared to the cladding material's ductile-tearing initiation fracture toughness with cumulative probabilities from the lognormal model shown in Fig. 19. 102
43. A scaling rule is applied to the Driving-Force Model (Eq. (44) to bring the Monte Carlo model driving forces into agreement with the results of the detailed FEM wastage cavity submodel (a) scaling required for Model Flaw 1, (b) scaling required for Model Flaw 3, and (c) linear fit developed between Model Flaws 1 and 3. 103
44. Convergence of Case 001 as a function of the number of antithetic paired realizations at 1 year after time of discovery. 106
45. LOCA probability history for: (a) the best-estimate Cladding Capacity Analysis (CCA) case (Case CCA-001) with a further categorization into small-break LOCA (SBLOCA), medium-break LOCA (MBLOCA), and large-break LOCAs (LBLOCA) and (b) varying model flaw depth at TOD, 0.035 in., 0.065 in., and 0.0995 in. 108

LIST OF FIGURES (continued)

Figure **Page**

46. Sensitivity of CCA LOCA probabilities to: (a) model flaw depth at TOD (b) cavity growth/shape rules. 109
47. Sensitivity of CCA LOCA probabilities to LOCA binning rules (a) total LOCA probability, (b) SBLOCA probability, (c) MBLOCA probability and (d) LBLOCA probability..... 109
48. Sensitivity of CCA LOCA probabilities to modeling of A-tip ductile tearing (a) total LOCA probability, (b) SBLOCA probability, (c) MBLOCA probability and (d) LBLOCA probability..... 110
49. Comparison of beta distributions for effective cavity radius at TOD-1 year, τ_0, where the original distribution (based on the results of an *Expert Elicitation*) has been revised to produce a sampled $R_{1(\text{median})}$ closer to the observed valued used in the CCA: (a) probability densities and (b) cumulative probabilities. 112
50. Comparison of Weibull distributions for the time of flaw initiation (relative to TOD), $\Delta\tau_{\text{flaw-ini}(2)}$ (see the time line in Fig. 1), where the original distribution (based on the results of an *Expert Elicitation*) has been revised to produce a sampled $R_{1(\text{median})}$ closer to the observed valued used in the CCA: (a) probability densities and (b) cumulative probabilities. 113
51. Best-estimate sampling distribution for cavity wastage rate compared to sampled values: (a) probability density and (b) cumulative probabilities. 114
52. Best-estimate sampling distribution for flaw growth rate compared to sampled values: (a) probability density and (b) cumulative probabilities. 115
53. Distribution of uncertain effective cavity radius calculated for the time of discovery (TOD): (a) frequency distribution and (b) cumulative probabilities. 116
54. Distribution of uncertain effective flaw depth calculated for the time of discovery (TOD): (a) probability density and (b) cumulative probabilities 117
55. Comparison of LOCA probability histories between the CCA study and the ASP study conditions where the deviation is due to uncertainties in cavity wastage rate, cavity size at TOD-1, flaw growth rate, and flaw initiation time. For the CCA study, the damage state at TOD was treated as known with no uncertainty..... 120
56. LOCA probability history for the best-estimate ASP case (Case ASP-001) with a further categorization into small-break LOCA (SBLOCA), medium-break LOCA (MBLOCA), and large-break LOCAs (LBLOCA). 121
57. LOCA probability histories for full case matrix: (a) total LOCA probabilities, (b) SBLOCA probabilities,..... 122
57. (continued) LOCA probability histories for full case matrix: (c) MBLOCA probabilities, and (d) LBLOCA probabilities. 123

1 Introduction

1.1 Method of Analysis

In support of both the United States Nuclear Regulatory Commission's (NRC's) investigation into the structural integrity of the damaged Davis-Besse reactor pressure vessel (RPV) head and the NRC's Accident Sequence Precursor (ASP) Program,[1] the Heavy-Section Steel Technology (HSST) Program at Oak Ridge National Laboratory (ORNL) has carried out a *probabilistic structural mechanics* (PSM) analysis of the degraded RPV head [1]. The objective of this report is to present a description of the Davis-Besse wastage-area damage model, the technical basis for the model, and the results of two PSM studies: (1) a *cladding capacity analysis* (CCA) of the wastage cavity as it existed at the time of discovery (TOD) and (2) an ASP study for a time period ranging from 1 year before the TOD up to the TOD. A companion report [2] describes a parallel experimental program performed by HSST at ORNL.

PSM is an analysis methodology that combines deterministic damage models with probabilistic representations of unknown or uncertain input parameters [3]. Random variations in the plastic-flow and ductile-tearing properties of the cladding, damage accumulation rates (in terms of cavity-wastage and flaw-growth rates), and flaw-initiation times for the damage model are combined to make an assessment of the reliability of the structure. The method of *Monte Carlo Simulation* [4] was selected to combine these uncertainties by randomly sampling from their prospective distributions to obtain the required inputs for multiple deterministic *realizations* of the *damage state* of the degraded RPV head. By repeating the damage-state realizations a large number of times, the resulting *failure states* (defined as the *consequences* of the damage states) constitute a random sample from the probability distribution over the output induced by the combined probability distributions sampled over the several input variables [4].

In both the CCA and ASP studies, a *probability of failure* is estimated from the fraction of the total number of simulations whose results predict some degree of damage that is judged to be equivalent to structural failure. In the CCA study, the "As-Found" damage state at TOD is assumed known; however, in the ASP study, estimated uncertainties in the "As-Found" condition of the wastage cavity are incorporated into the analysis.

[1] The statutory ASP Program is under the functional responsibility of the NRC's Office of Nuclear Regulatory Research.

The *consequences* or *degrees of failure* of the damage state can be ranked by differentiating between *small-break* (SBLOCA), *medium-break* (MBLOCA), and *large-break* (LBLOCA) *loss-of-coolant accidents*. In this report, the damage states are investigated over a time interval that begins one year before the day of discovery (i.e., 16 February 2001) and extends beyond the day of discovery until failure of the cladding is predicted for all postulated conditions. These results address questions raised as part of the statutory requirements of the ASP analysis as well as the question concerning how long the Davis-Besse RPV could have continued in service (i.e., if the wastage cavity had not been discovered on 16 February 2002) before the failure of the vessel.

1.2 Background of the Davis-Besse Degraded RPV Head Problem

Pursuant to the licensee's commitments to NRC Bulletin 2001-01 [5], the Davis-Besse Nuclear Power Station[2] began a refueling outage [6] on February 16, 2002 that included a 100% volumetric inspection of the sixty-nine RPV head penetrations. With emphasis placed on control-rod drive-mechanism (CRDM) nozzles, these inspections identified five nozzles with cracks that needed repair before restarting [7], including axial indications in three CRDM nozzles (nozzles # 1, 2, and 3, located near the center of the RPV head) that were experiencing pressure-boundary leakage.

The repair procedure included roll-expanding the CRDM nozzle into the surrounding RPV head and then machining along the axis of the nozzle to a point above the indications. On March 6, 2002, the licensee prematurely terminated the machining process on nozzle # 3. During the removal of the machining apparatus, the nozzle was mechanically agitated and subsequently displaced (or tipped) in the downhill direction (away from the top of the RPV head) until its flange contacted the flange of the adjacent CRDM nozzle. To identify the cause of the displacement, the licensee investigated the condition of the RPV head surrounding nozzle # 3. This investigation included removing the CRDM nozzle from the RPV head, removing boric acid deposits from the top of the RPV head, and ultrasonically measuring the thickness of the RPV head in the vicinity of CRDM nozzles # 1, 2, and 3.

Upon completion of the removal of boric-acid crystal deposits on March 7, 2002, the licensee conducted a visual examination of the area and identified a large cavity in the RPV head on the downhill side of CRDM nozzle # 3 [1]. Follow-up characterization by ultrasonic testing (UT) indicated wastage of the low-alloy steel RPV head adjacent to the nozzle. The wastage region was found to extend approximately

[2] The Davis-Besse Nuclear Power Station is located in Oak Harbor, Ohio. Operated by First Energy Nuclear Operating Company (FENOC), Davis-Besse achieved initial criticality on 12 August 1977, and it came online on 31 July 1978. Manufactured by Babcock and Wilcox (B&W), the raised-loop pressurized water reactor (PWR) has a licensed thermal-power output of 2772 MW(t) and a *capacity* of 873 net MW(e), where *capacity* is defined by the Energy Information Administration (EIA) as the net summer capability as reported in EIA survey form 860.

5 inches downhill on the RPV head from the penetration for CRDM nozzle # 3, with a width of approximately 4 to 5 inches at its widest part. In addition to damage described above, follow-up metallographic studies, carried out by BWXT [16] and discussed in Sect. 2.1.3, discovered a group of surface cracks located in the cladding on the side exposed to the corrosive environment.

The investigation of the causative conditions surrounding the degradation of the RPV head at Davis-Besse is continuing [7]. Boric acid or other contaminants could be contributing factors. Other factors contributing to the degradation might include the environment of the RPV head during both operating and shutdown conditions (e.g., wet/dry), the duration for which the RPV head was exposed to boric acid, and the source of the boric acid (e.g., leakage from the CRDM nozzle or from sources above the RPV head such as CRDM flanges).

See Fig. 1a for a photograph of the Davis-Besse RPV, Fig. 1b for a schematic of a typical nuclear power reactor showing the relative location of the head degradation, Fig. 1c for a cutaway sketch of the wastage cavity, and Fig. 1d for a photograph of the wastage area footprint.

1.3 Accident Sequence Precursor Program

The NRC established the Accident Sequence Precursor (ASP) Program [8] in 1979 in response to the findings of the *Risk Assessment Review Group* as reported in NUREG/CR-0400 [9]. The ASP Program has the primary objective of systematically evaluating the operating experience of the U.S. nuclear power plant fleet to identify, document, and rank those operating events that were most significant in terms of the potential for inadequate core cooling and core damage (precursors). From SECY-99-289 [8], the ASP Program also has the following secondary objectives: (1) to categorize the precursors for plant-specific and generic implications, (2) to provide a measure that can be used to trend nuclear plant core damage risk, and (3) to provide a check on the dominant core damage scenarios predicted by probabilistic risk assessment (PRA) analyses.

(a)

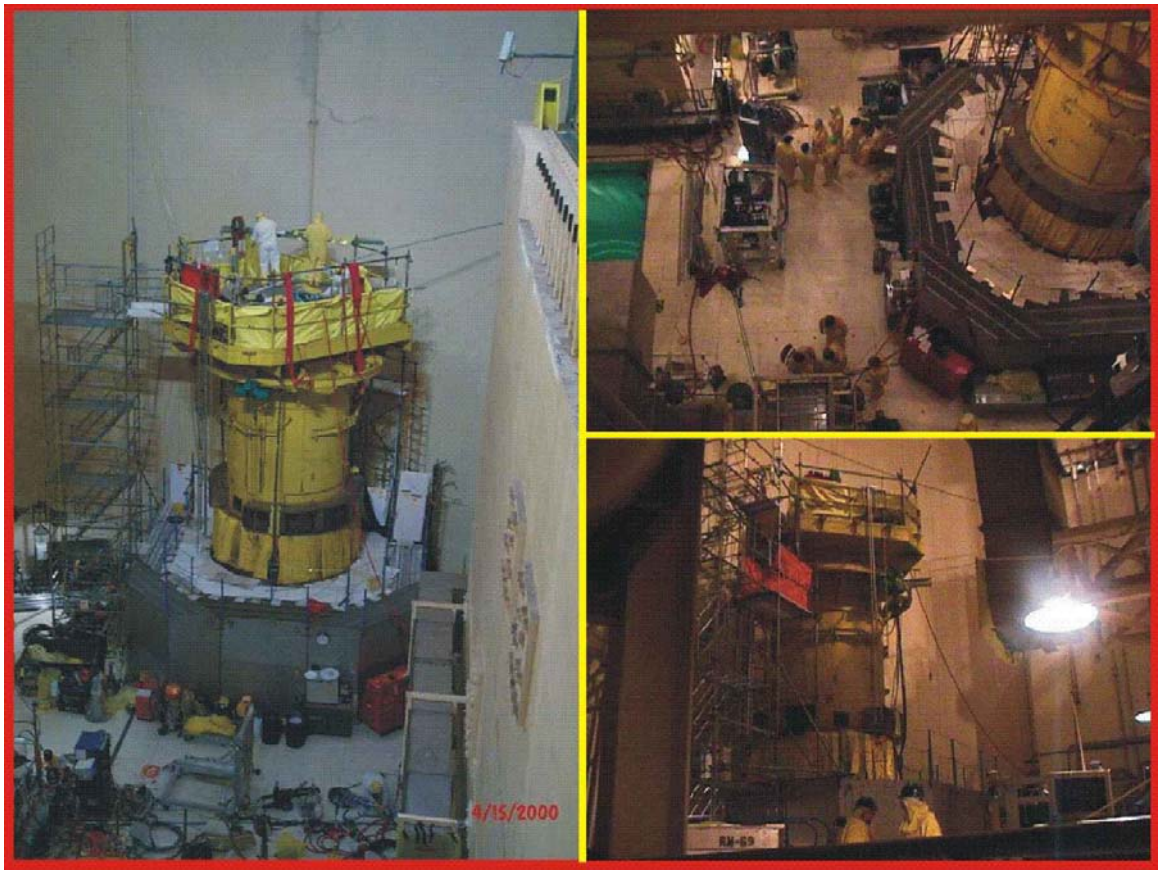

(b)

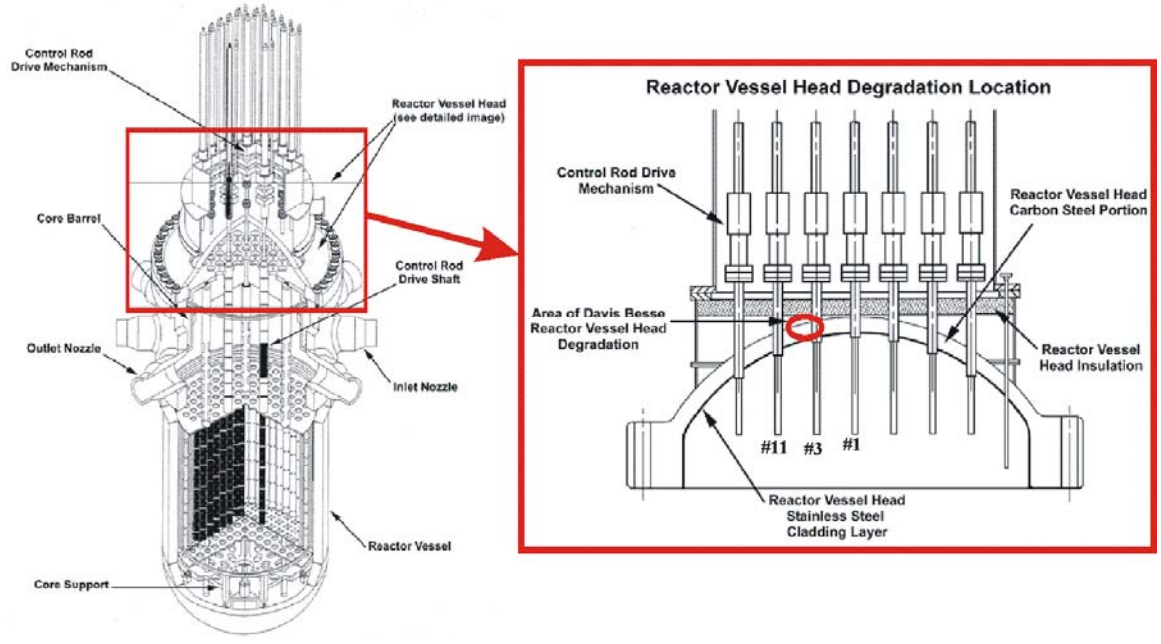

Fig. 1. Depictions of Davis-Besse RPV and wastage cavity: (a) Davis-Besse Nuclear Power Station RPV [7]; (b) schematic of a typical nuclear power reactor showing the relationship of the CRDM nozzles to the RPV head and the location of the damaged area [7];

(c)

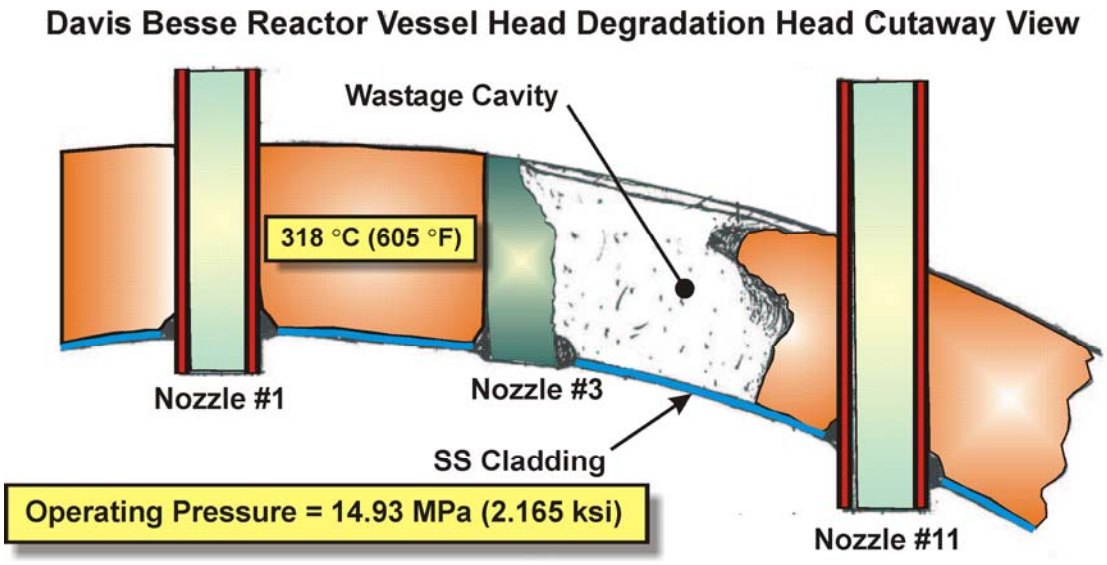

(d)

Fig. 1. (continued) (c) sketch of RPV head degradation; and (d) photograph presenting a plan view of the wastage-area footprint showing remaining J-groove weld, irregular topography of exposed unbacked cladding, and irregular sidewalls of the wastage cavity [7].

An ASP is an operational event or a plant condition that is an important element of a postulated accident sequence[3] associated with inadequate core cooling, a sequence that would be expected to result in core damage [10]. The ASP Program identifies nuclear power plant events that are considered precursors to accidents with the potential for severe core damage and uses risk assessment methodologies to estimate the significance of the events. The figure of merit for ASP analyses is the conditional core damage probability (CCDP), where the CCDP is the conditional probability of core damage given the failures observed in the event. Events with CCDPs greater than 1.0×10^{-6} are judged to be accident sequence precursors.

1.4 Previous ORNL Studies of the Davis-Besse RPV Head Degradation Problem

Previous ORNL reports have described (1) the development of a stochastic model for the estimation of the probability of failure of the wastage cavity by plastic collapse under internal pressure loading [11,12] and (2) the technical basis for applying a surrogate damage model (specifically, a circular burst disk) [13] to simulate the initial damage state, damage accumulation, and failure consequences for the irregularly shaped wastage region in the Davis-Besse RPV head.

1.4.1 Detailed Finite-Element Global and Submodels of Wastage Area and Cavity

Detailed finite-element models were constructed and applied in the studies discussed in [11-13]. The results of these analyses were used in the development of a more detailed 3D finite-element wastage-area damage model to be described in Sect. 2. The results of the detailed 3D FEM model in turn provided guidance in the construction of a simplified model for use in Monte Carlo simulations. The following discussion provides a summary description of those prior FEM analyses.

The submodeling capabilities of the ABAQUS finite-element code [14] were employed in the plastic-collapse stochastic model development described in [11, 12] and in the cavity growth studies described in [13] to focus the available computational resources on the region around the wastage area cavity at CRDM nozzle # 3. Submodeling can be used to investigate a portion of a model with a refined mesh, where the boundary conditions of the *submodel* are driven by an interpolation of the displacement solution obtained from a relatively coarse *global model*. The technique is appropriate and accurate when it is necessary to obtain a refined, detailed solution in a local region, and the detailed modeling of that local region has a negligible effect on the global solution. Communication between models proceeds in one direction only, from the global model to the submodel. As shown in Figs. 2a and 3, the initial global

[3] An *accident sequence* is a combination of events leading from an *initiating event* that challenges safety systems to an undesired *consequence*. The sequence is ordered, starting with the initiating event, and proceeds through sequential failures leading to the final consequence [3].

model consisted of the full RPV head (with all 69 penetrations) and closure flange. No cladding or CRDM nozzles were included in the global model used in the studies described in refs. [11-13].

The initial submodel (see Fig. 2b) consisted of the cladding (SS308), base (A533B), and CRDM nozzles (A600) #3, #11, #15, and #16. The plan views of the RPV head in Fig. 4a and 4b indicate the position and geometry of the submodel with respect to the global model. Figure 5 shows the ProEngineer® solid model of the wastage cavity submodel. This solid model was imported into MSC Patran® where the finite-element mesh was constructed.

1.4.2 Results of Wastage-Cavity Growth-Pattern Study [13]

The results of a study of the sensitivity of burst-pressure predictions to the modeled shape of the wastage-cavity footprint were reported in [13]. As shown in Fig. 6, three growth patterns were examined: (1) *self-similar* (relative to the "as-found" cavity geometry), (2) *ellipsoidal*, and (3) circular (i.e., a circular burst disk). Detailed finite-element analyses were carried out, using the global/submodel approach described in Sect. 1.4.1, for the postulated self-similar and ellipsoidal growth patterns, and a plastic-instability theory for circular diaphragms under lateral-pressure loading developed by Chakrabarty and Alexander [15] was applied for the circular growth pattern. The results of that growth-pattern study are summarized in Fig. 7, where the 5^{th} , 50^{th}, and 95^{th} % percentile curves for the circular growth pattern model are based on a scaling of the stochastic model for uncertainties in plastic-collapse burst pressure predictions developed in [11,12]. Drawn from the results summarized in Fig. 7, a fundamental conclusion is that the unbacked area of the cladding is the dominant geometric parameter for burst-pressure predictions of a model of the Davis-Besse wastage cavity when the unbacked stainless steel cladding does not contain any crack-like flaws; the specific shape of the footprint represents a second-order effect. This conclusion allowed the development of the wastage-area damage-state failure model to be based on failure predictions for a *circular diaphragm under lateral-pressure loading*. Subsequent discovery of surface flaws in the wastage-cavity cladding added another failure mechanism, namely the potential for cladding failure by ductile tearing.

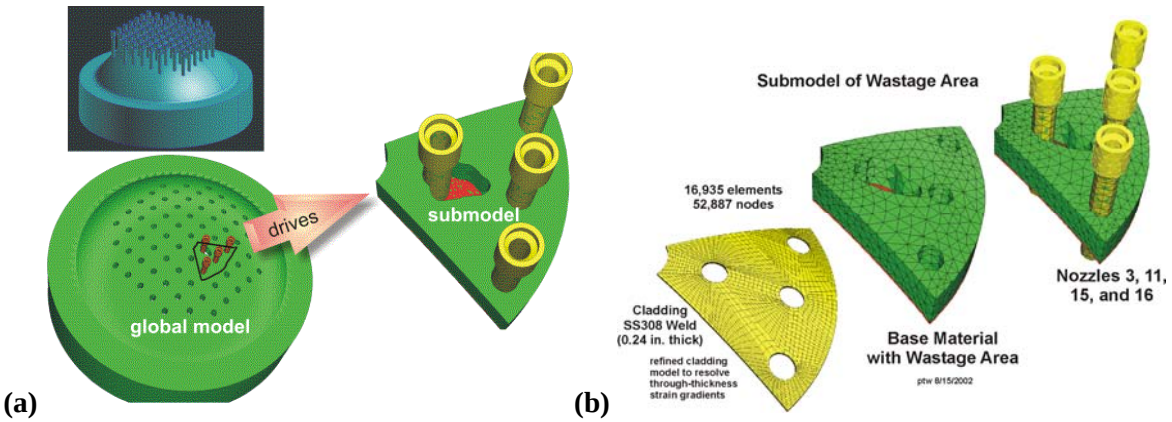

Fig. 2. Finite-element global model and submodels applied in previous analyses [11,13] of the Davis-Besse head and wastage area. The displacements at the vertical side boundaries of the submodel are driven by the global model. Both models were exposed to the same internal pressure loading.

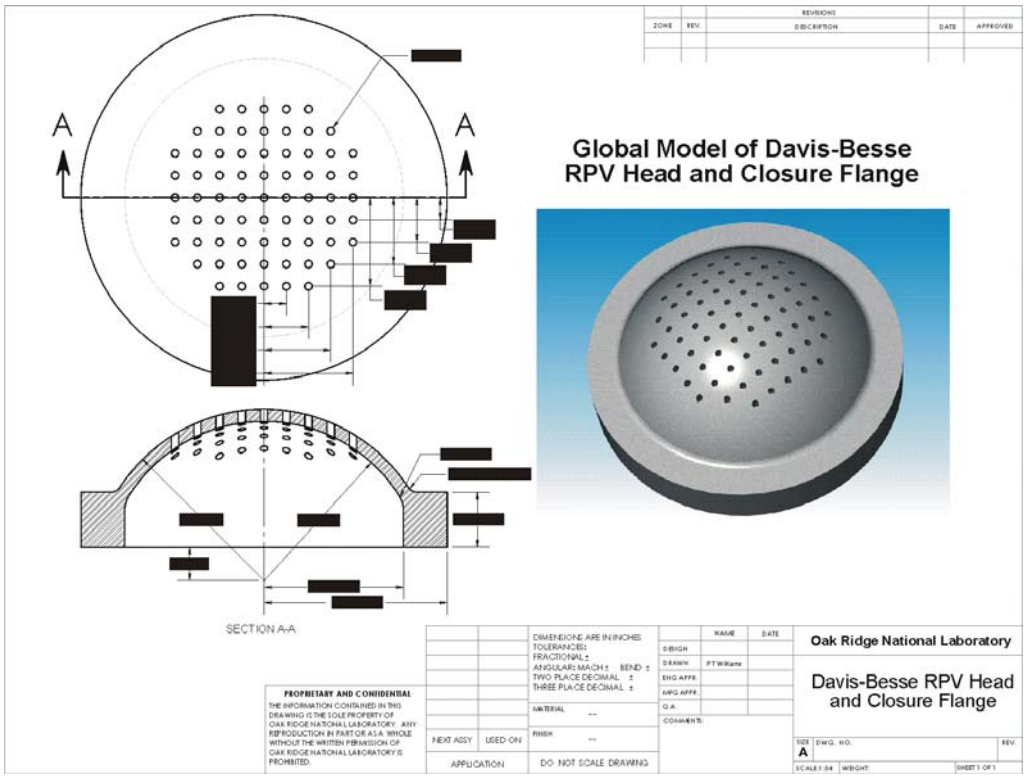

Fig. 3. Geometry of the hemispherical RPV head and closure flange used in the global model [11,13] (B&W proprietary dimensions have been blacked out).

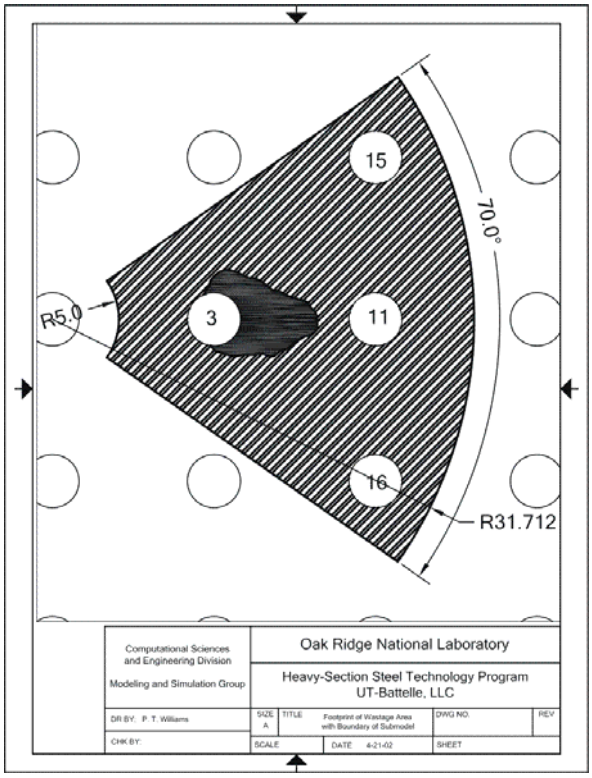

Fig. 4. Geometry of submodel relative to nozzles #3, #11, #15, and #16 in the RPV head.

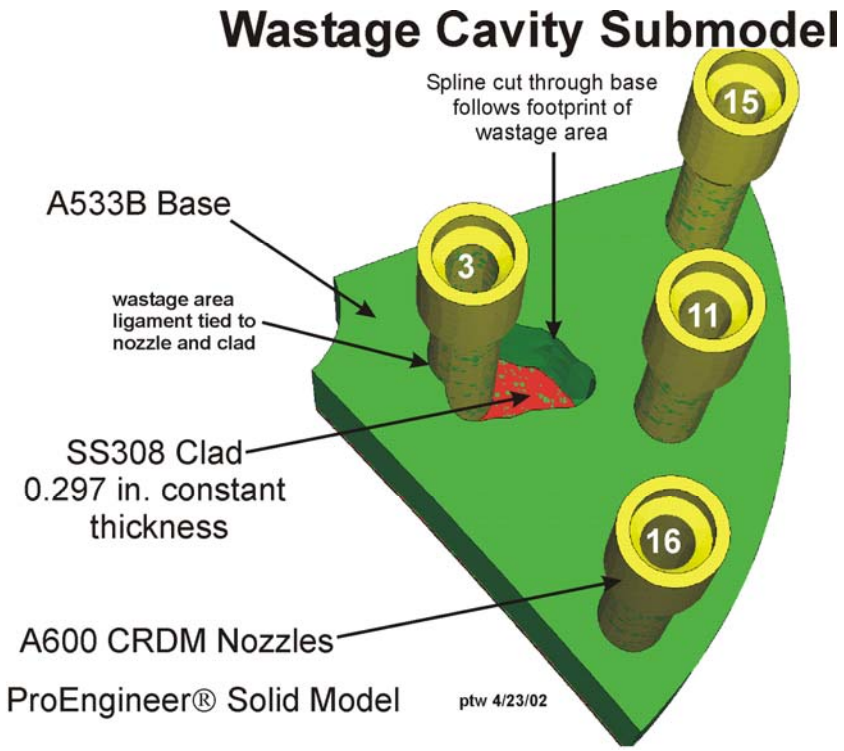

Fig. 5. Wastage-cavity submodel [11,13] developed from a ProEngineer® solid model and then meshed with MSC Patran®.

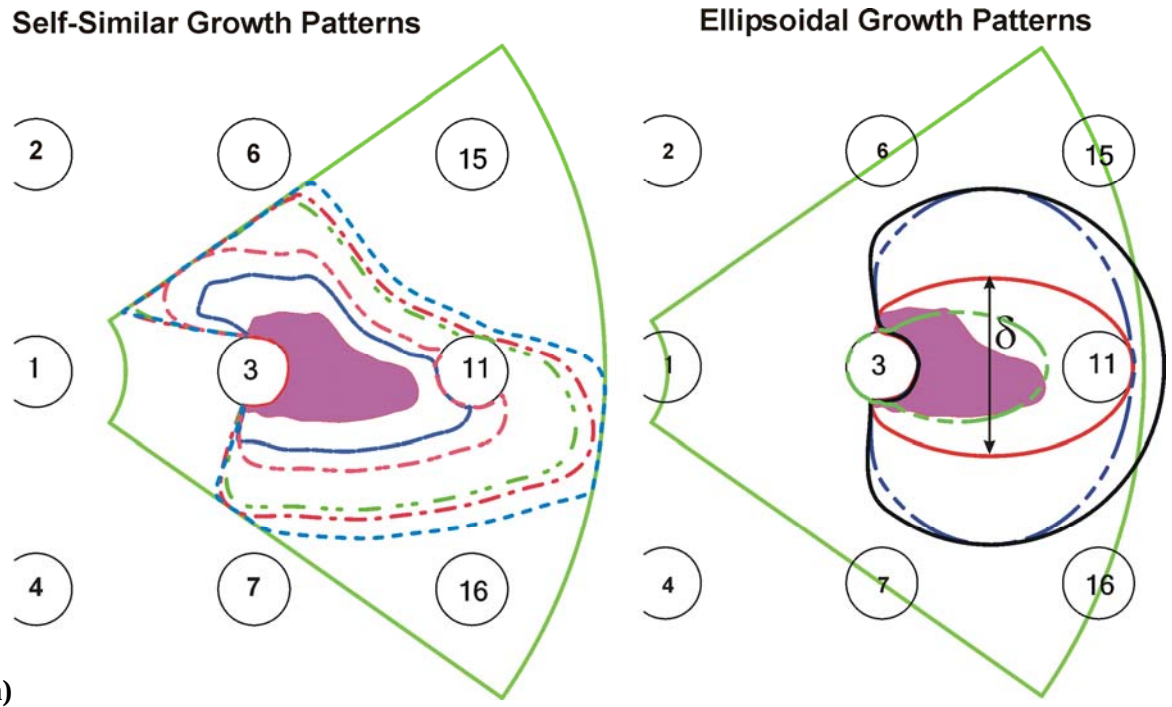

(a)

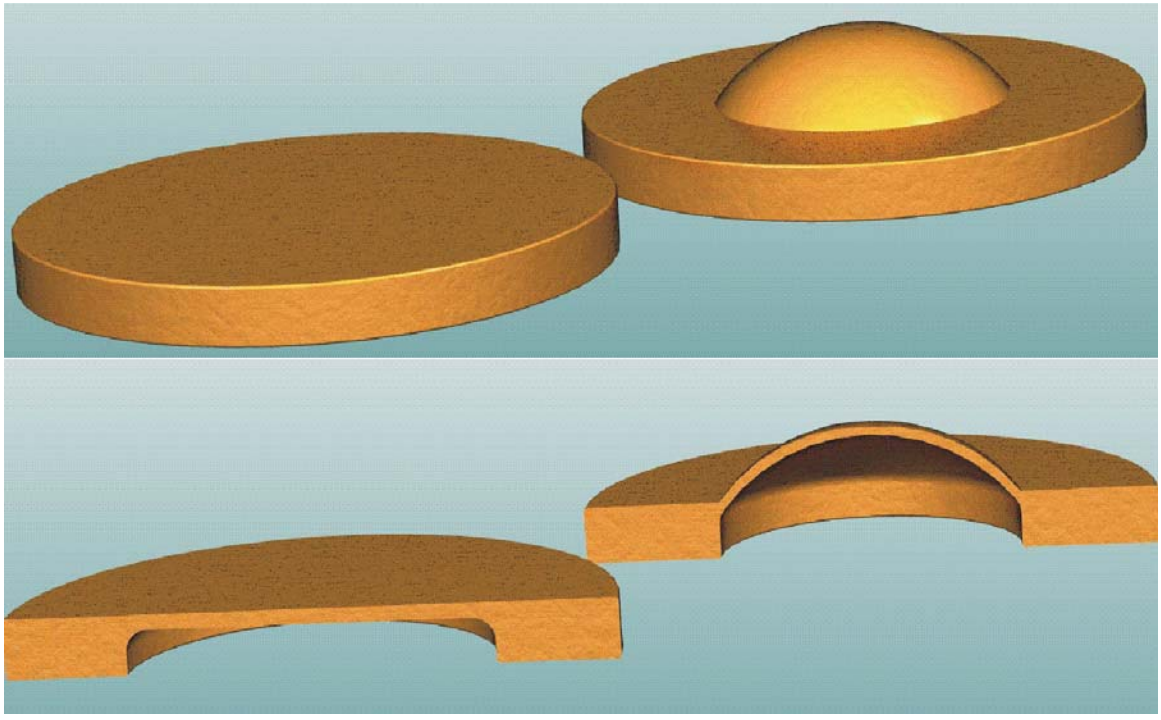

(b)

Fig. 6. A computational study was carried out in [13] to determine the sensitivity of burst pressures, predicted by finite-element analyses, to the geometry of estimated growth patterns of the wastage cavity "footprint": (a) self-similar and ellipsoidal growth patterns and (b) circular burst disk.

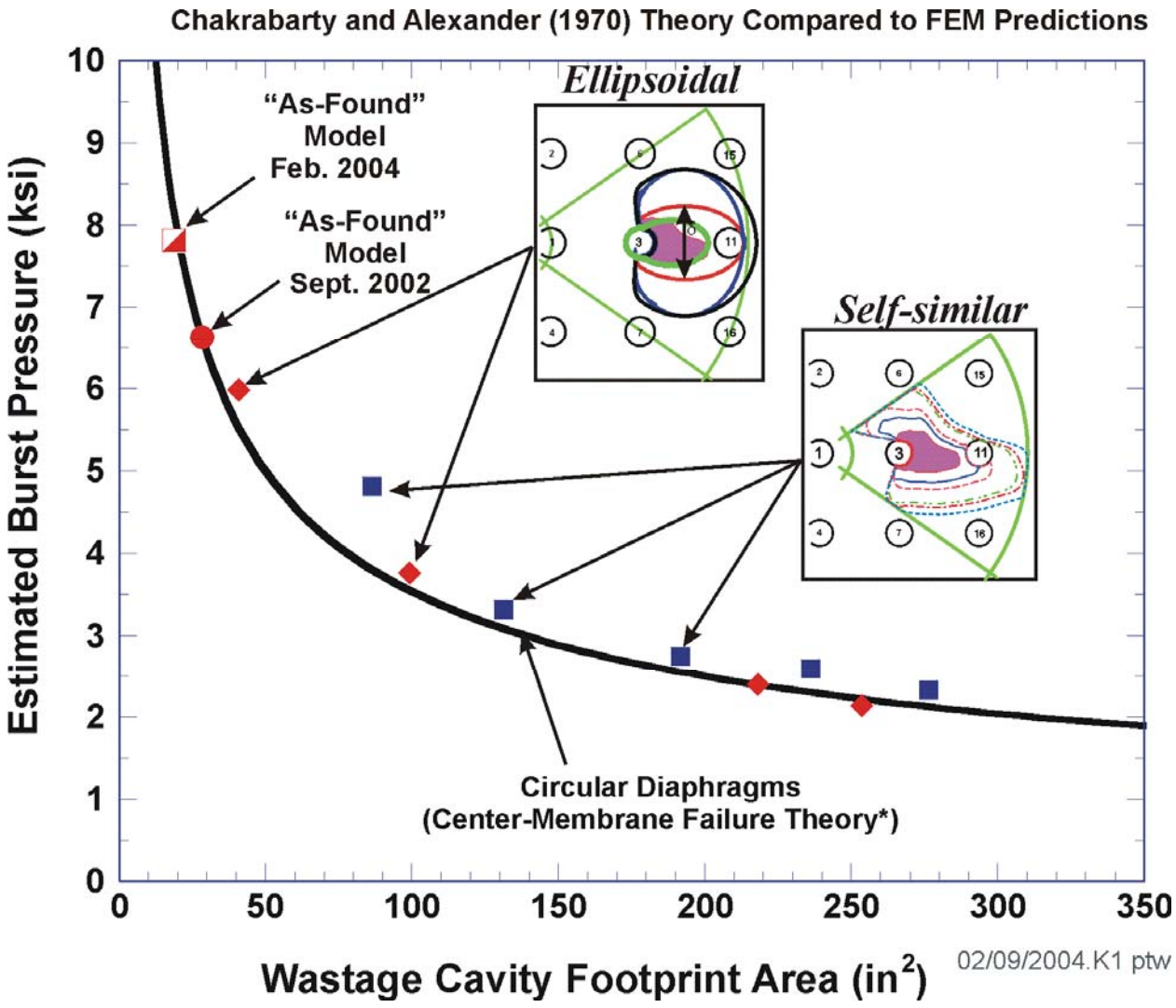

Fig. 7. The FEM-predicted burst pressures of irregularly-shaped "footprint" growth patterns are compared in [13] to burst pressure predictions for circular diaphragms under lateral pressure loading based on an instability theory proposed by Chakrabarty and Alexander [15].

1.5 Scope of this Report

Section 2 presents the development of the Davis-Besse *wastage-area damage model*, including both a detailed 3-dimensional FEM model and a simplified model for Monte Carlo simulations. Section 3 presents the results of the deterministic simulations using the FEM model as well as best-estimate and sensitivity Monte Carlo simulations in support of both the CCA and the ASP studies. Section 4 provides a summary and conclusions. Appendix A provides a description of the of the Davis-Besse Monte Carlo damage state code along with a flowchart and guidance for its use. Appendix B presents a detailed listing of the CCA and ASP Monte Carlo results in terms of tables of LOCA probabilities as a function of time starting at 1 year before TOD up to TOD. Appendix C presents the final report on the examination of the reactor pressure vessel head degradation at Davis-Besse carried out by BWXT Technologies, Inc. at Lynchburg, VA.

2 Davis-Besse Wastage-Area Damage Model

2.1 Detailed 3D FEM Model for Deterministic Analyses

A detailed 3-dimensional FEM submodel of the Davis-Besse wastage cavity was developed from the results [16] of visual inspections, dye-penetrant testing, scanning electron microscopy, energy dispersive spectroscopy, metallography, Knoop microhardness testing, and wastage cavity geometric measurements carried out by the Lynchburg Technology Center for Metallurgical Examinations, BWXT Technologies, Inc., and reported in [16]. The submodeling approach described in [11-13] was used for the current study, where a detailed submodel is driven both by direct pressure loading and by the displacement solution obtained from a coarser global model (see Fig. 8).

The wastage cavity submodel shown in Fig. 9 consisted of four CRDM nozzles (specifically #3, #11, #15, and #16)[4], the base material with wastage cavity, the J-groove weld for nozzle #3, the backed cladding, the exposed unbacked cladding, and a modeled cladding surface flaw on the wastage cavity side of the unbacked cladding.

2.1.1 Modeled Wastage Cavity Footprint

Details of the wastage cavity footprint were obtained from photographs available in [16] (Fig. 9c) (see Appendix C) and then digitized to a locus of 66 points which were used to construct a spline curve that established the basis for the footprint. The irregular topography of the unbacked cladding region exposed to the corrosive effects of the boric acid was also simulated by a sinusoidal waveform applied to the exposed upper surface.

2.1.2 Wastage Cavity

During examinations at BWXT Lynchburg, a “dental mold” [16] of the wastage cavity was prepared to establish a permanent record of the wastage-cavity shape. The photographs available in [16] were applied in the construction of a solid model (see Fig. 9d) using the Solidworks® [17] modeling software.

[4] For CRDM nozzles #3, #11, #15, and #16, the corresponding *core grid locations* are G9, F10, E9, and G11, respectively. Nozzles #15 and #16 are unused spare nozzles [1].

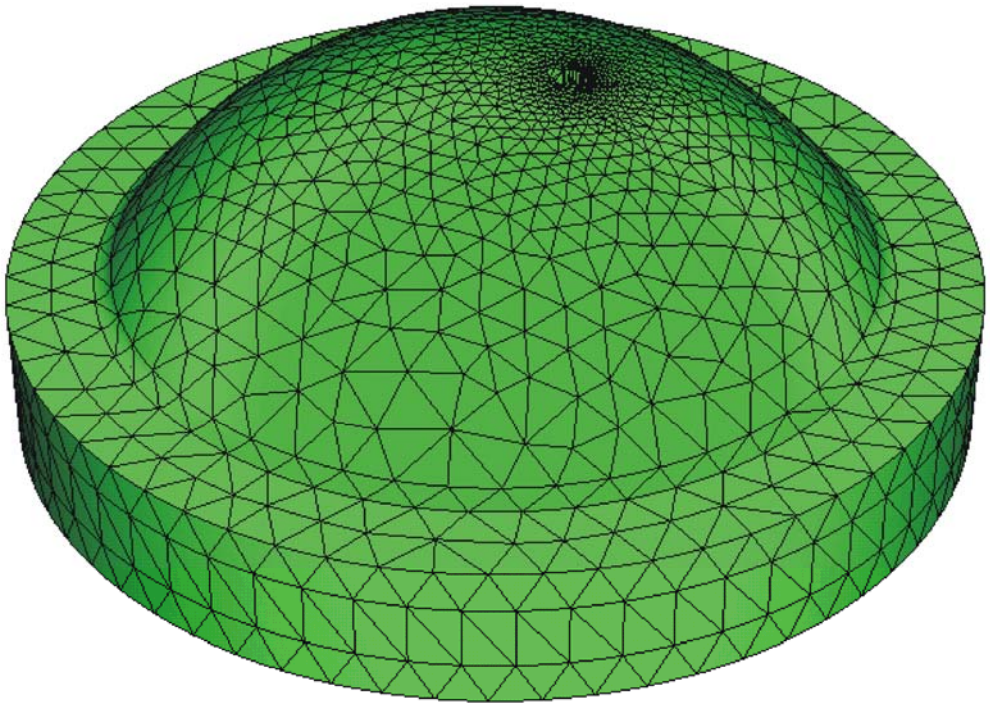

(a)

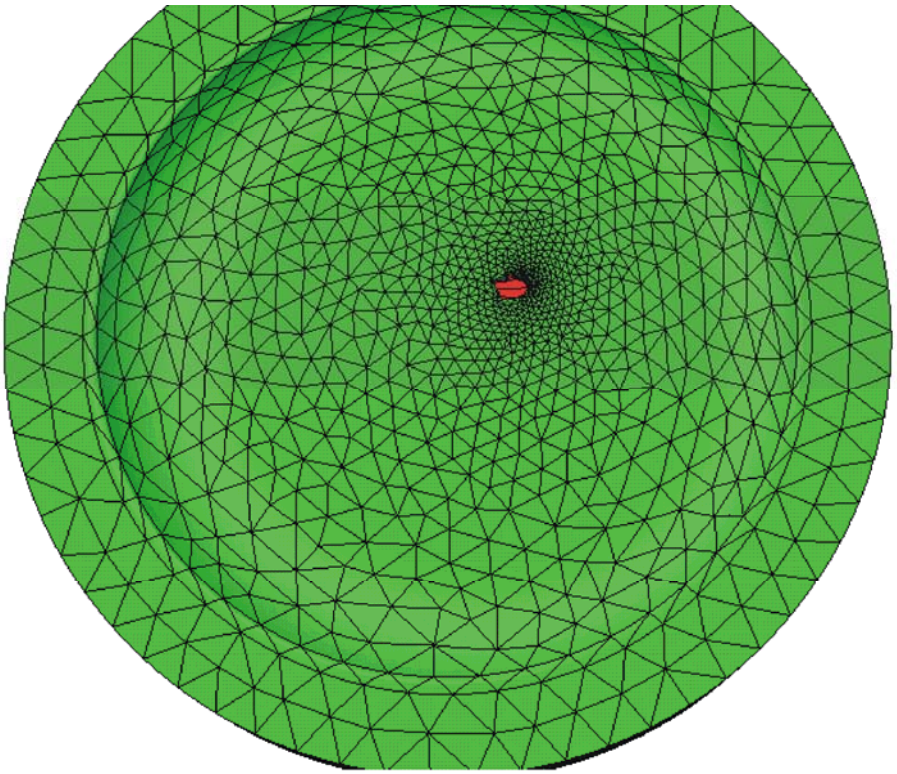

(b)

Fig. 8. Davis-Besse global model of RPV closure head for the current study includes a simplified wastage-cavity definition and inner cladding layer.

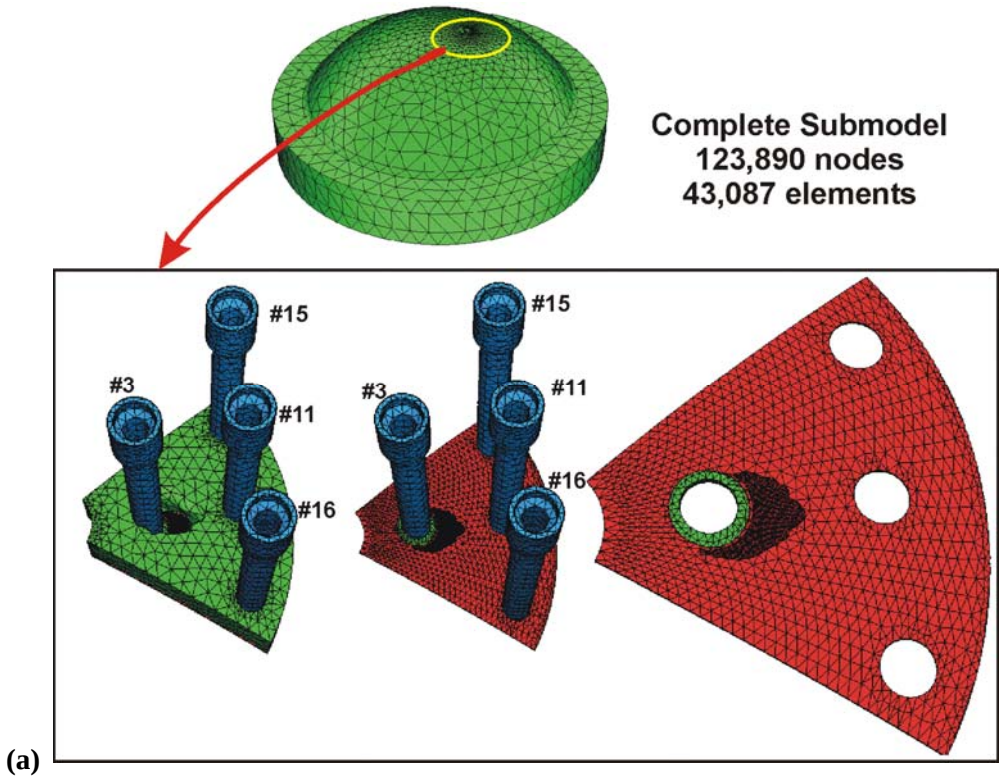

(a)

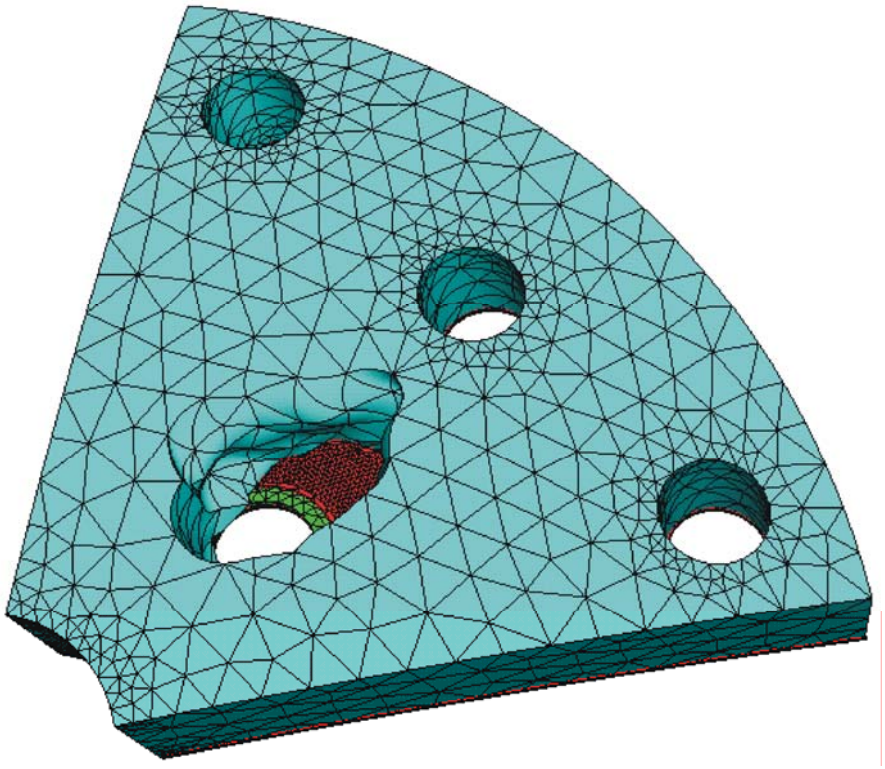

(b)

Fig. 9. Davis-Besse submodel includes: (a) nozzles #3, #11, #15, #16 (Alloy 600); (b) a refined definition of the wastage-cavity morphology in the base material (A 533B pressure vessel steel),

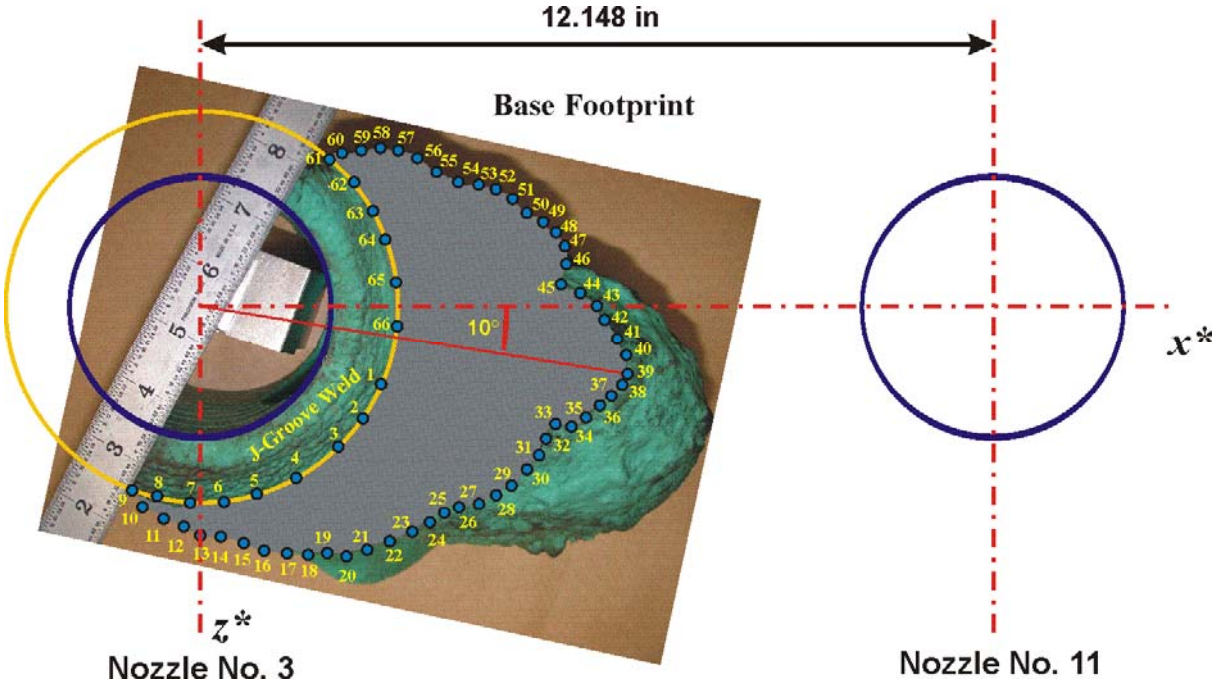

(c) Wastage Cavity Submodel Includes Definition of Variable Cavity Walls Estimated from Dental Mold

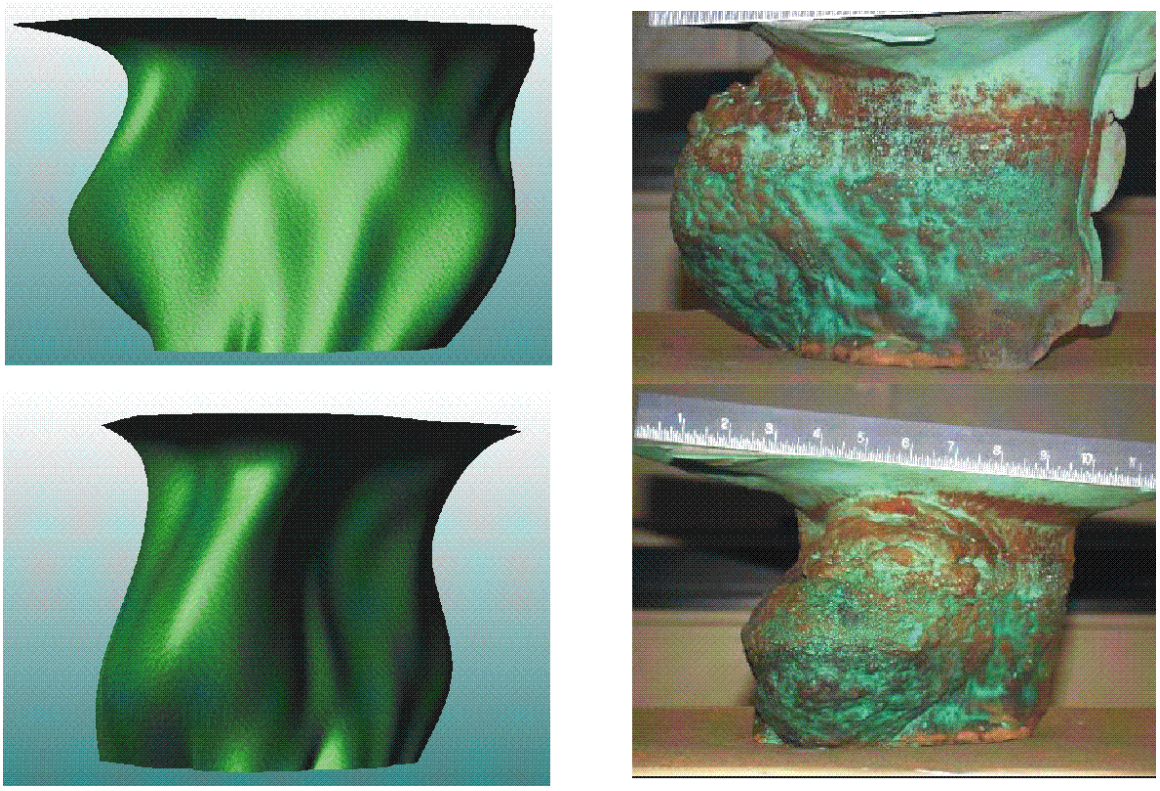

(d)

Fig. 9. (continued) (c) wastage cavity footprint; (d) irregular geometry of wastage cavity walls based on geometric measurements from the dental mold taken by BWXT [16].

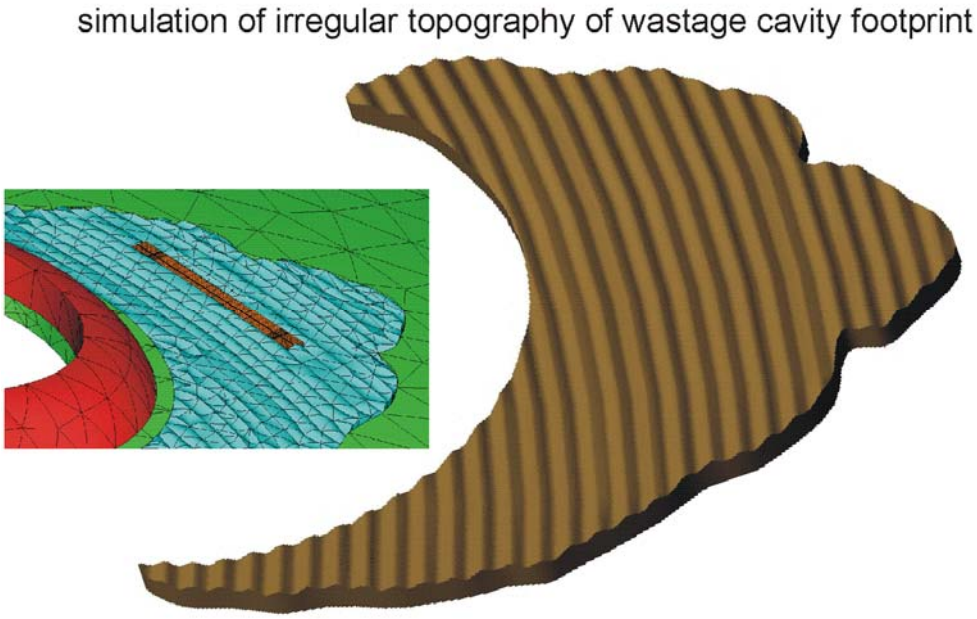

(e)

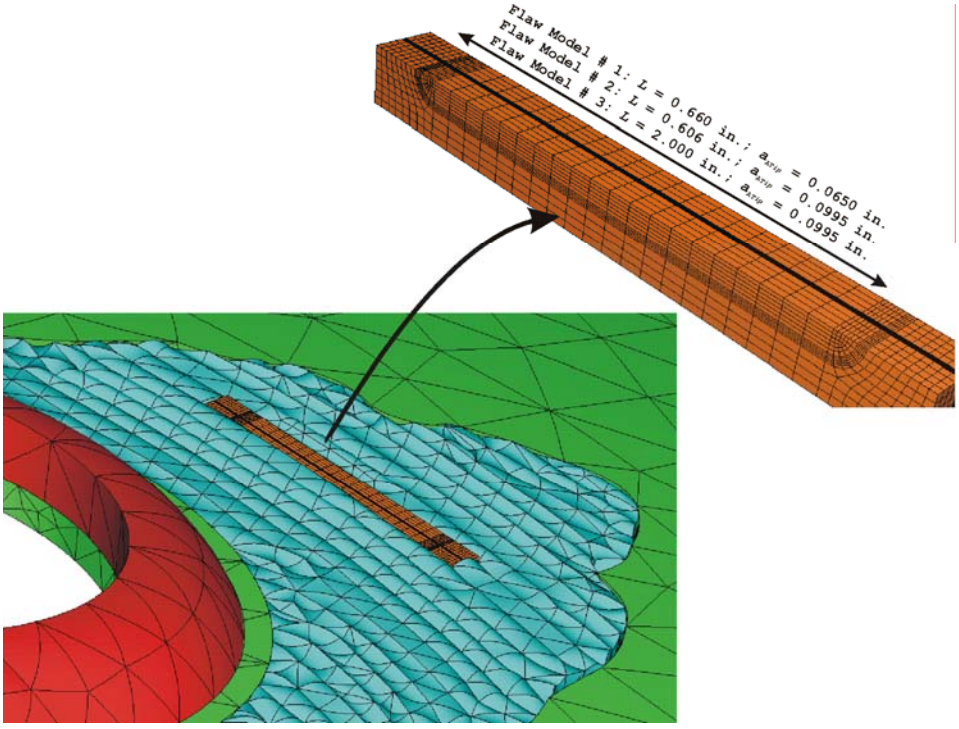

(f)

Fig. 9. (continued) (e) irregular exposed cladding topography based on a sinusoidal waveform, and (f) J-groove weld near a modeled surface flaw.

This solid model of the dental mold was then applied in a *loft cut* operation to remove material from the base section, thus forming the degraded wastage cavity within a Solidworks® solid model of the damaged RPV head. The solid model of the RPV head's base material with wastage cavity was then imported into MSC Patran® to create the finite-element mesh of the wastage cavity submodel.

2.1.3 Modeled Surface Flaws

Extensive metallographic analyses were carried out by BWXT [16] to better define the nature and depth of the cladding flaws. These analyses identified two key features of the cracks observed in the cladding [18].

(1) The cracking was more prevalent and the cracks were much deeper than was originally thought, based on the initial preliminary investigation reported in the Summer of 2003 [16]. Cracking existed on the cladding interface, as evident in the initial findings. Each cross section examined near the center of the exposed cavity region revealed several distinct cracks.

(2) The crack morphology was intergranular and/or interdendritic in nature. This morphology is characteristic of intergranular stress corrosion cracking (IGSCC) prevalent in relatively high-carbon stainless steels used in boiling-water-reactor (BWR) service environments.

The following summary of the BWXT findings is quoted from [16]:

> **The exposed Type 308 stainless steel cladding surface area was approximately 16.5 square inches. The average cladding thickness measured by dial calipers was 0.256", with a minimum thickness of 0.202" and maximum thickness of 0.314". Thickness measurements taken on a transverse metallographic mount prepared through the thinnest portion of exposed cladding indicated a minimum cladding thickness of 0.179". This area, which was located in an uncracked region of the cladding adjacent to the J-groove weld, was not accessible during the dial caliper measurements. The cladding mechanical properties and chemical composition appeared uniform across the cladding thickness. The underside (reactor coolant system or RCS side) of the cladding and the unexposed portions of cladding did not contain any cracks or other signs of deterioration.**
>
> **Shallow intergranular attack (IGA) was observed on all exposed cladding surfaces examined. Deeper cracks, which extended a maximum 0.057" below the exposed cladding surface, followed a mixed interdendritic/intergranular path. These cracks initiated in the IGA and propagated under a stress-corrosion cracking mechanism along the ferrite stringers under the influence of an applied tensile stress (i.e., system pressure). The minimum observed distance from an exposed cladding crack tip to the RCS side of the cladding was 0.188".**

Based on the results of these examinations, three modeled surface flaws (see Fig. 9f) were developed as representative of a best-estimate flaw and two bounding flaws (see Fig. 10 for a generic description of the model flaw geometry).

Flaw Model #1 – $a_{A\text{-}tip}$ = 0.065 in., L = 0.66 in.; (best-estimate) characteristic of deep flaws observed in the Davis-Besse wastage cavity cladding

Flaw Model #2 – $a_{A\text{-}tip}$ = 0.0995 in., L = 0.606 in.; characteristic of the deepest flaw observed in the Davis-Besse wastage cavity cladding

Flaw Model #3 – $a_{A\text{-}tip}$ = 0.0995 in., L = 2.0 in.; characteristic of the ASME Boiler and Pressure Vessel

Code representation of cracks,[5] using the proximity rules and conservative flaw characterization procedures established in Sect. XI, Division 1, Subsection IWA-3300 [19], Division 2, Subsection IWB-3600 [20], and Appendix A [21].

2.2 Simplified Wastage-Area Damage Model for Monte Carlo Simulations

The damage states of the Davis-Besse degraded RPV head at different times (on the time-line history of the head) are estimated from the results of PSM analyses of a simplified *damage model* consisting of a circular diaphragm (or burst disk) under lateral-pressure loading (see Fig. 10). The multiple defects, observed in the Davis-Besse wastage cavity after extraction from the RPV head, are simulated in the model by a single long surface flaw (L = 2 in.) centered in the unloaded side of the diaphragm with an uncertain (i.e., sampled) flaw growth rate. The assumed transferability of the results of the PSM analysis from the circular-diaphragm damage model back to the actual wastage area in the Davis-Besse RPV head is inferred from the results of the study described in [13] and summarized in Sect. 1.4.2.

For failure by plastic collapse of the cavity and/or the remaining ligament below the modeled flaw, similitude between the calculated structural reliability of the damage model and the Davis-Besse wastage cavity is established by matching the effective unbacked area under load and the depth of the model flaw. Additional scaling (to be discussed) is required to establish similitude of the elastic-plastic crack driving forces (i.e., J-integrals) between the flaw in the burst-disk damage model and the modeled flaw in the detailed Davis-Besse wastage cavity submodel.

[5] It is recognized that the ASME Code does not explicitly treat cracks in the cladding in terms of a structural challenge to the RPV; however, the spirit and intent of the Code is applied herein for this special case of unbacked cladding being required to maintain the integrity of the pressure boundary.

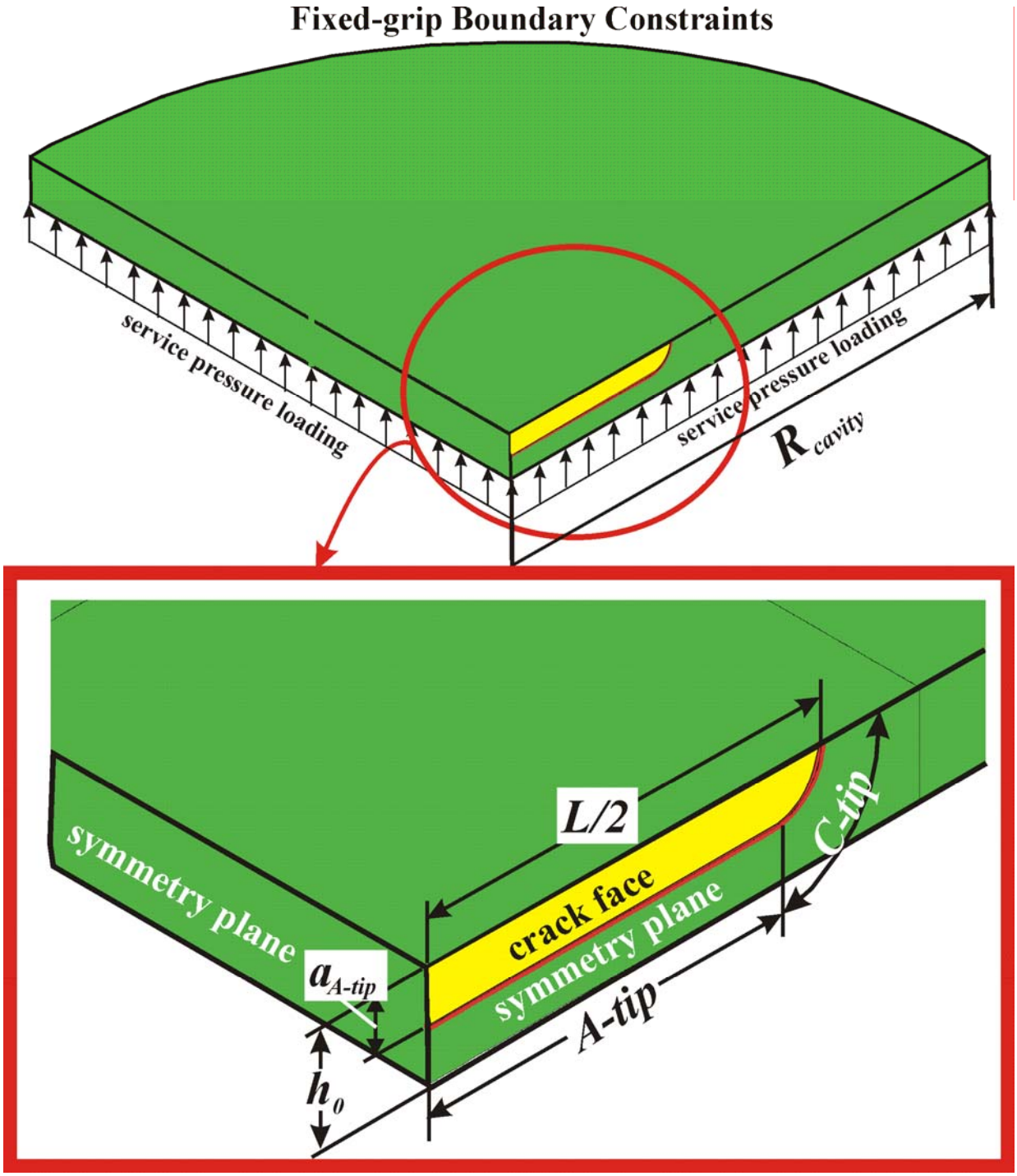

Fig. 10. Geometry, loading, and constraint conditions for the Davis-Besse RPV head *damage model* – a ¼ symmetry burst disk with a centered surface flaw, where h_0 = 0.25 in. and L = 2.0 in.

2.2.1 Damage Model Geometry, Loading, and Constraint Conditions

Figure 10 presents a ¼-symmetry representation of the damage model used in this study in which a circular diaphragm with radius, R_{cavity}, and undeformed thickness, h_0, is loaded on one side by a uniform applied pressure, $P_{applied}$. A flat-bottomed surface flaw of length, L, is centered in the diaphragm on its outer, unloaded surface. The depth of the crack tip, $a_{A\text{-}tip}$, is constant along the length (L-2 $a_{A\text{-}tip}$) of the flat bottom of the flaw. This bottom section of the crack tip is designated as the *A-tip*. The two *C-tips* of the flaw are circular arcs tracing the path of the crack tip from the *A-tip* up to the unloaded free surface of the diaphragm. The radius, R_{cavity}, is scaled so that the diaphragm's loaded area matches the "as-found" or postulated unbacked surface area, $A_{wastage}$, of the irregularly shaped wastage-cavity footprint, and the "as-found" model flaw depth, $a_{A\text{-}tip}$, is equal to either a flaw depth representative of the observed range of flaws (0.036 to 0.099 inches) in the wastage cavity ("as-found" condition) or an uncertain flaw depth sampled from statistical distributions (to be described):

$$R_{cavity} = +\sqrt{\frac{A_{wastage}}{\pi}}\ ;\ a_{A-tip} = \begin{array}{c}\text{fixed at time of discovery for CCA studies}\\ \text{or sampled for ASP analyses}\end{array} \qquad (1)$$

The outer edge of the diaphragm is constrained by an *encastre* boundary condition.

2.2.2 Damage-State Parameters

The two uncertain geometric parameters in Eq. (1) (see Figs. 10 and 11) are the effective cavity radius, R_{cavity}, and the initial flaw depth of the *A-tip* of the centered modeled flaw, $a_{A\text{-}tip}$. Together, (R_{cavity}, $a_{A\text{-}tip}$) define a *damage state point* for the wastage-cavity damage model. Given this damage state point and a prescribed applied pressure, $P_{applied}$, the *failure state* of the model can then be determined based on the position of the state point in damage space relative to the model's *fragility curve*, developed from the instability theory due to Chakrabarty and Alexander [15] (see Sect. 2.2.3). This *fragility curve* is based on an assumed failure mechanism of plastic collapse of the remaining ligament (termed an *A-tip* collapse) below the centered flaw in the damage model. Additional potential *A-tip* failure modes consisting of either ductile-tearing initiation or tearing initiation followed by unstable ductile tearing of the *A-tip* are also included in the analysis. Upon the failure of the *A-tip*, failure mechanisms for the *C-tips* and remaining wastage cavity material are then investigated to determine the final failure state (expressed in terms of LOCA size) of the cavity at the time of discovery. Along the locus of damage-state points defined in damage space by the fragility curve, *A-tip* failure is predicted for the given applied pressure; therefore, the fragility curve partitions the damage space of the wastage cavity into stable and unstable (failed) regions.

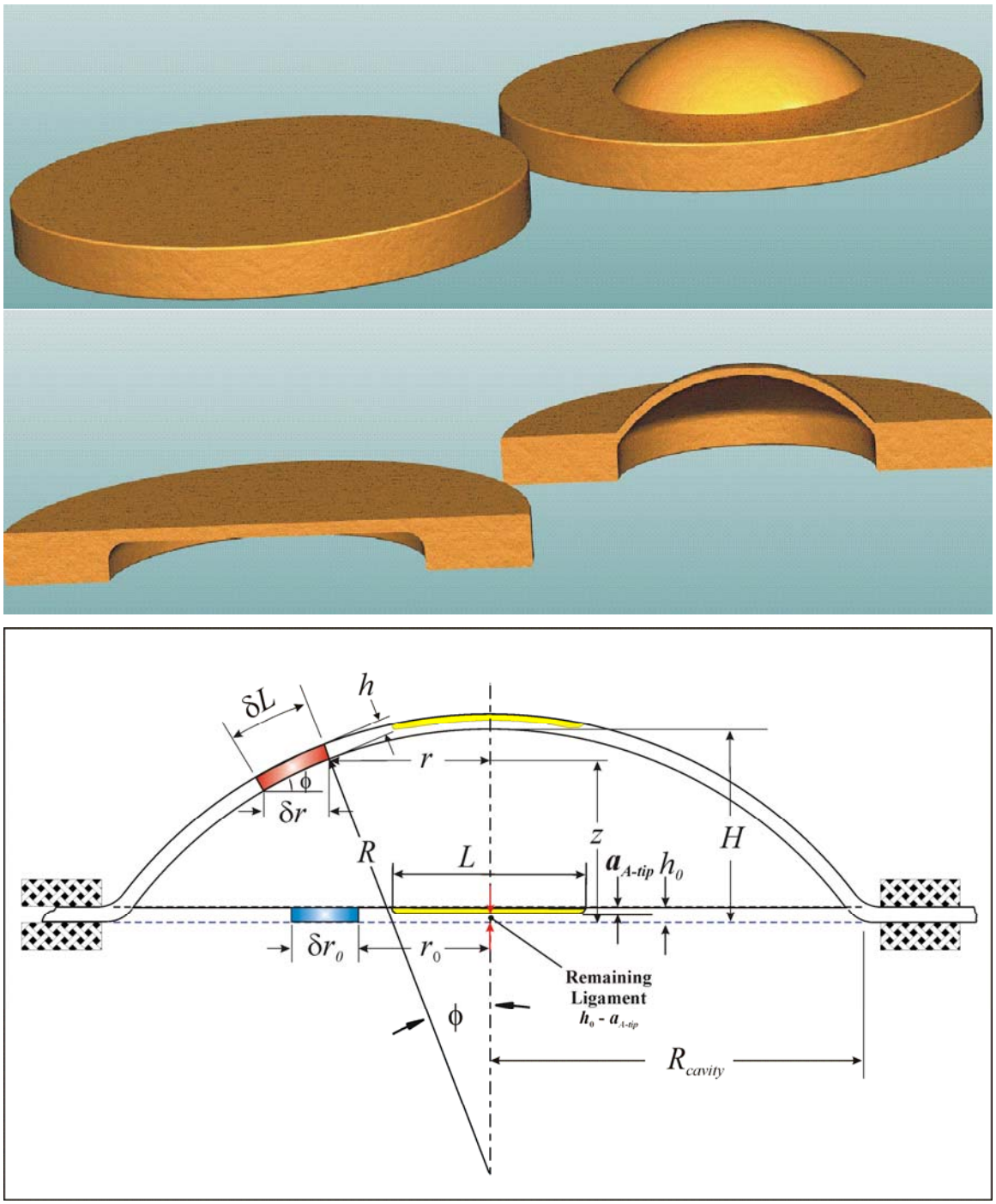

Fig. 11. Spherical geometry of deformation assumed in Chakrabarty and Alexander's [15] plastic instability theory. Chakrabarty and Alexander assumed that the burst disk was unflawed, i.e., $a_{A\text{-}tip} = 0$.

2.2.3 Failure Mechanisms – Development of a Plastic-Collapse Fragility Curve

The *fragility curve* applied in the PSM analysis for the Davis-Besse problem for an unbacked cladding model with a centered flaw has the following functional form:

$$a_{A-tip(crit)} = h_0 + \left(S \times R_{cavity}\right);\ 0 \le R_{cavity} \le R_{intercept}$$

where

$a_{A-tip(crit)}$ = the critical flaw depth at which plastic collapse occurs
h_0 = initial undeformed thickness of the cladding
S = fragility curve slope
R_{cavity} = effective radius of the wastage cavity
$R_{intercept} = \left|\frac{h_0}{S}\right|$; for a specified applied pressure, $P_{applied}$

(2)

The slope, S (a function of the specified applied pressure, $P_{applied}$, and cladding plastic flow properties), of the fragility curve can be developed from an instability criterion due to Chakrabarty and Alexander [15] with a modification for this analysis to treat the remaining ligament below the flaw.

When the damage state of the wastage-area intersects the fragility curve, the remaining ligament of the A-tip is predicted to fail by plastic collapse. The value of $R_{intercept}$ places an upper bound on the size of the wastage cavity (irrespective of the presence of the model flaw) for the specified applied pressure. The flaw's A-tip may approach the fragility curve by flaw growth due to exposure to the corrosive environment of the wastage cavity, by flaw growth due to stable ductile tearing, or by flaw growth due to unstable ductile tearing. When the damage state of the wastage-area model intersects the fragility curve due to combined growth of the flaw and cavity, the remaining ligament below the flaw is predicted to fail by plastic collapse, and the bottom of the model flaw blows out of the cavity, leaving a 2-inch long rip in the cladding. Additional failure sequences may then follow toward complete failure of the wastage cavity.

The burst pressure for a circular diaphragm under lateral pressure loading can be estimated using the Chakrabarty and Alexander (1970) [15] instability criterion as discussed in [11]. In the PSM damage model, the failure of an *unflawed* wastage cavity is simulated by failure due to plastic instability of a pressure-loaded circular diaphragm (i.e., burst disk) with a fixed-grip constraint (encastre boundary condition) along the edges. The radius of the diaphragm matches the effective radius, R_{cavity}, of the wastage cavity based on a specified unbacked wastage area (see Eq. (1)).

For a given material defined by its plastic-flow properties (K, n)[6] and unflawed geometry (R_{cavity}, $a_{A\text{-}tip}$= 0), the failure pressure (i.e., the burst pressure) can be estimated by the following procedure (see Fig. 11 for a description of the undeformed and deformed geometries):[7]

- Calculate the effective critical radial true strain at $\phi = 0°$. $\tilde{\varepsilon}_{crit} = \dfrac{2(2-n)(1+2n)}{11-4n}$
- Calculate the corresponding effective critical true stress. $\tilde{\sigma}_{crit}(K,n) = K\,\tilde{\varepsilon}_{crit}^{\,n}$
- Calculate the critical radial deformed thickness at $\phi = 0°$. $h_{crit} = h_0 \exp\left(-\tilde{\varepsilon}_{crit}\right)$
- Calculate the polar height at the critical condition. $H_{crit} = R_{cavity}\sqrt{\exp\left(\dfrac{\tilde{\varepsilon}_{crit}}{2}\right)-1}$
- Calculate the corresponding bulge curvature radius. $R_{crit} = \dfrac{H_{crit}^2 + R_{cavity}^2}{2H_{crit}}$
- Finally, calculate the predicted burst pressure. $p_{burst} = \dfrac{2h_{crit}\tilde{\sigma}_{crit}}{R_{crit}}$

For a surface flaw centered in a circular diaphragm, this procedure can be modified by replacing the initial undeformed diaphragm thickness, h_0, with the undeformed remaining ligament thickness below the flaw (see Fig. 11) such that

$$h_{crit} = \left(h_0 - a_{A-tip(crit)}\right)\exp\left(-\tilde{\varepsilon}_{crit}\right) \tag{3}$$

where $a_{\text{A-tip}(crit)}$ is the critical flaw depth at the deepest point of the flaw.

The above procedure can be inverted to solve for the critical flaw depth at failure, $a_{A\text{-tip}(crit)}$, as a function of the cladding's plastic flow properties, (K, n), the initial cladding thickness, h_0, applied pressure, $P_{applied}$, and cavity radius, R_{cavity}, to obtain

$$a_{A-tip(crit)}\left(K,n,h_0,P_{applied},R_{cavity}\right) = \left[\left(\frac{-P_{applied}\exp\left[\dfrac{\tilde{\varepsilon}_{crit}(n)}{2}\right]}{4\tilde{\sigma}_{crit}\left(K,n\right)\exp\left[-\tilde{\varepsilon}_{crit}(n)\right]\sqrt{\exp\left[\dfrac{\tilde{\varepsilon}_{crit}(n)}{2}-1\right]}}\right)\times R_{cavity}\right] + h_0 \tag{4}$$

where

[6] A power-law constitutive model is assumed for plastic deformation, where $\tilde{\sigma}(K,n) = K\,\tilde{\varepsilon}^{\,n}$.

[7] Following the notational conventions of Dowling [34], $\tilde{\sigma}$ and $\tilde{\varepsilon}$ are true stress and true strain, respectively, and σ and ε are engineering stress and engineering strain, respectively.

$$\tilde{\varepsilon}_{crit}(n) = \frac{2(2-n)(1+2n)}{11-4n}$$

$$\tilde{\sigma}_{crit}(K,n) = K\left[\tilde{\varepsilon}_{crit}(n)\right]^n$$

The parameter, *S*, in Eq. (2) is, therefore, from Eq. (4) for a given applied pressure, $P_{applied}$:

$$S\left(K,n \mid P_{applied}\right) = \frac{-P_{applied}\exp\left[\dfrac{\tilde{\varepsilon}_{crit}(n)}{2}\right]}{4\tilde{\sigma}_{crit}(K,n)\exp[-\tilde{\varepsilon}_{crit}(n)]\sqrt{\exp\left[\dfrac{\tilde{\varepsilon}_{crit}(n)}{2}\right]-1}} \tag{5}$$

If we assume that the initial cladding thickness, h_0, is known, then for a specified applied pressure the dominant sources of uncertainty in the construction of the fragility curve are the plastic flow properties of the cladding, (*K*, *n*). Note that uncertainties in the initial cladding thickness can be treated independently from the uncertainties in the slope of the fragility curve.

2.2.3.1 Stochastic Model for Plastic-Flow Properties – Sampling for $\hat{\sigma}_{yield}$ and $\hat{\sigma}_{ult}$

In Eq. (5), the dominant sources of uncertainty in the slope of the fragility curve are the plastic flow properties of the cladding as characterized by the coefficient, *K*, and exponent, *n*, of the power-law representation of the true effective stress vs. true strain curve for a given temperature. Table 1 presents a database of plastic-flow properties for 550 °F ≤ *temperature* ≤ 600 °F used in this study, and Fig. 12 compares the stress vs. strain curves developed from power-law fits of the data in Table 1 to the best-estimate constitutive properties for the Davis-Besse cladding material. It was decided to focus the stochastic modeling task on characterizing the uncertainties of the yield and ultimate stresses which, for a fixed temperature, are presumably due either to *material variability* between heats or *spatial variability* within a single heat. It will be shown in Sect. 2.2.3.2 how the parameters *K* and *n* can be calculated from sampled values of $\hat{\sigma}_{yield}$ and $\hat{\sigma}_{ult}$.

As discussed in refs. [22, 23], independent samples of yield and ultimate stress indicate that a statistical correlation exists between the two properties. In refs. [22, 23], a bivariate lognormal distribution was selected as the joint distribution since the fitted marginal distributions for their dataset (TP304 stainless steel pipe material) followed lognormal distributions *reasonably well.* For this study, several marginal distributions were fitted to the set of yield and ultimate true stress data in Table 1 (see Table 2 for the *Goodness of Fit* statistics of Anderson-Darling [24], Kolmogorov-Smirnov [25], and equi-probable Chi-square [26]; and also see Figs. 13a and 13b) using the *ExpertFit*© [27] statistical software. Three marginal distributions were selected for further study, and they have the following forms:

Table 1. Plastic-Flow Properties for SS Cladding

Source	Material	Specimen ID	Test Temp. (°F)	True Stresses Yield (ksi)	True Stresses Ultimate (ksi)	*K** (ksi)	*n** (-)
NUREG/CR-3927		CPC-79	550.0	29.79	73.24	102.09	0.218
NUREG/CR-3927		CPC-80	550.0	29.79	74.40	103.86	0.221
NUREG/CR-5511	3-wire Cladding	A20A	550.0	31.70	72.96	100.94	0.206
NUREG/CR-5511	3-wire Cladding	A20B	550.0	36.60	69.97	93.18	0.168
NUREG/CR-6363	3-wire Cladding	A18C	550.0	28.60	75.37	103.56	0.227
NUREG/CR-6363	3-wire Cladding	A24A	550.0	31.00	71.54	99.00	0.206
HSST Clad Burst Tests	PVRUF Cladding	1-1	600.0	29.81	68.94	95.45	0.206
HSST Clad Burst Tests	PVRUF Cladding	1-2	600.0	28.85	68.05	94.41	0.209
HSST Clad Burst Tests	PVRUF Cladding	1-3	600.0	28.14	66.44	92.16	0.209
HSST Clad Burst Tests	PVRUF Cladding	1-4	600.0	29.30	66.44	92.16	0.199
HSST Clad Burst Tests	PVRUF Cladding	2-1	600.0	29.82	70.03	97.14	0.209
HSST Clad Burst Tests	PVRUF Cladding	2-2	600.0	29.93	69.56	96.37	0.207
HSST Clad Burst Tests	PVRUF Cladding	2-3	600.0	30.97	68.24	93.98	0.197
HSST Clad Burst Tests	PVRUF Cladding	2-4	600.0	31.22	67.59	92.88	0.194
BWXT	DB Cladding	B2C2A1	600.0	30.53	70.53	97.66	0.206
BWXT	DB Cladding	B2C2A2	600.0	31.36	73.49	101.96	0.209
NSE Handbook	SS 308/308L	Table II	600.0	31.00	69.65	114.91	0.228

* $\tilde{\sigma}_{eff} = K\left(\tilde{\varepsilon}\right)^{n}$ where $\tilde{\sigma}_{eff}$ = true effective stress and $\tilde{\varepsilon}$ = true total strain
See Appendix C for a discussion of the BWXT [16] investigations.

Table 2. "Goodness of Fit" Statistics for Yield and Ultimate Stress Statistical Distributions

Sampled Variate	Marginal Distribution	Point Estimates for Parameters location	scale	shape	Goodness of Fit Test	Test Statistic	Critical Values for Level of Significance (α) 0.25	0.15	0.1	0.05	0.025	0.01	0.005
Yield Stress	inverted Weibull	0	29.7279	24.7640	Anderson-Darling	0.406	0.452	NA	0.608	0.722	0.836	0.99	NA
					Kolmogorov-Smirnov	0.625	NA	NA	0.779	0.843	0.907	0.973	NA
					equi-probable chi^2	2.706	5.385	6.745	7.779	9.488	NA	13.277	NA
Yield Stress	lognormal	0	3.4159	0.0567	Anderson-Darling	0.862	0.447	NA	0.600	0.715	0.830	0.984	1.102
					Kolmogorov-Smirnov	0.754	NA	0.740	0.782	0.854	0.950	0.988	NA
					equi-probable chi^2	7.412	5.385	6.745	7.779	9.488	NA	13.277	NA
Yield Stress	gamma	28.1119	1.6878	1.4118	Anderson-Darling	0.768	1.248	NA	1.933	2.492	3.070	3.857	4.500
					Kolmogorov-Smirnov	0.922	NA	1.099	1.182	1.311	1.429	1.572	NA
					equi-probable chi^2	8.000	5.385	6.745	7.779	9.488	NA	13.277	NA
Ultimate Stress	inverted Weibull	0	69.0596	30.7746	Anderson-Darling	0.255	0.452	NA	0.608	0.722	0.836	0.99	NA
					Kolmogorov-Smirnov	0.518	NA	NA	0.779	0.843	0.907	0.973	NA
					equi-probable chi^2	3.294	5.385	6.745	7.779	9.488	NA	13.277	NA
Ultimate Stress	lognormal	0	4.2532	0.0375	Anderson-Darling	0.311	0.447	NA	0.600	0.715	0.830	0.984	1.102
					Kolmogorov-Smirnov	0.551	NA	0.740	0.782	0.854	0.950	0.988	NA
					equi-probable chi^2	2.706	5.385	6.745	7.779	9.488	NA	13.277	NA
Ultimate Stress	gamma	66.241	2.830	1.462	Anderson-Darling	0.560	1.248	NA	1.933	2.492	3.070	3.857	4.500
					Kolmogorov-Smirnov	0.649	NA	1.099	1.182	1.311	1.429	1.572	NA
					equi-probable chi^2	2.706	5.385	6.745	7.779	9.488	NA	13.277	NA

*NA = critical point not available

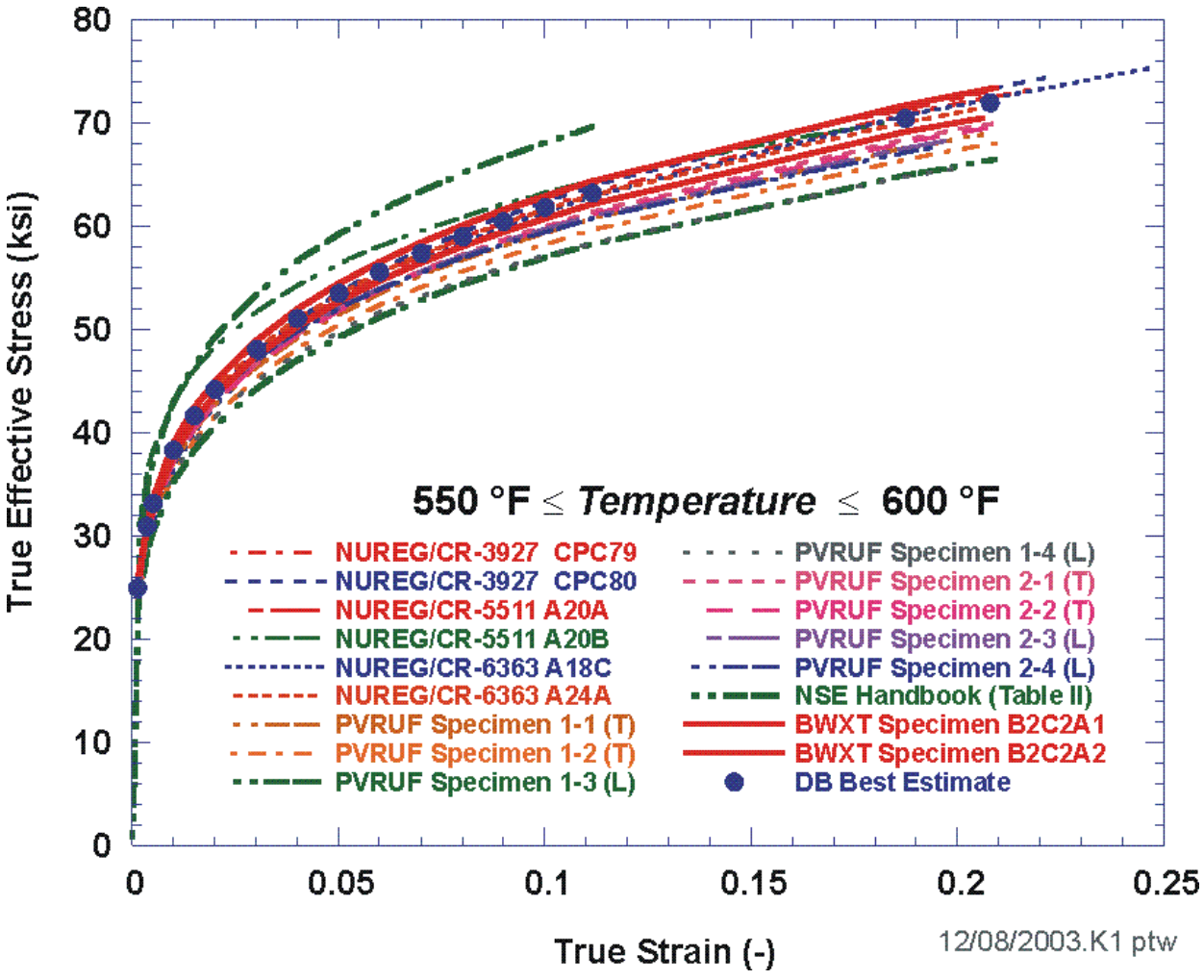

Fig. 12. Plots of true stress vs. true strain from the data in Table 1.

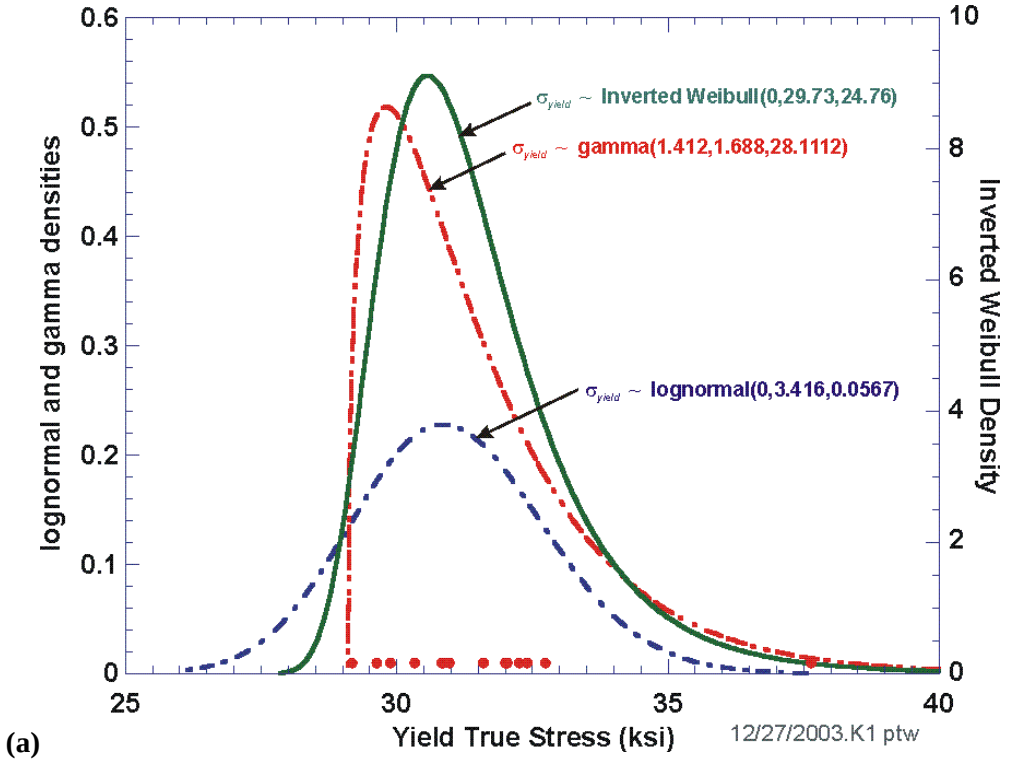

(a)

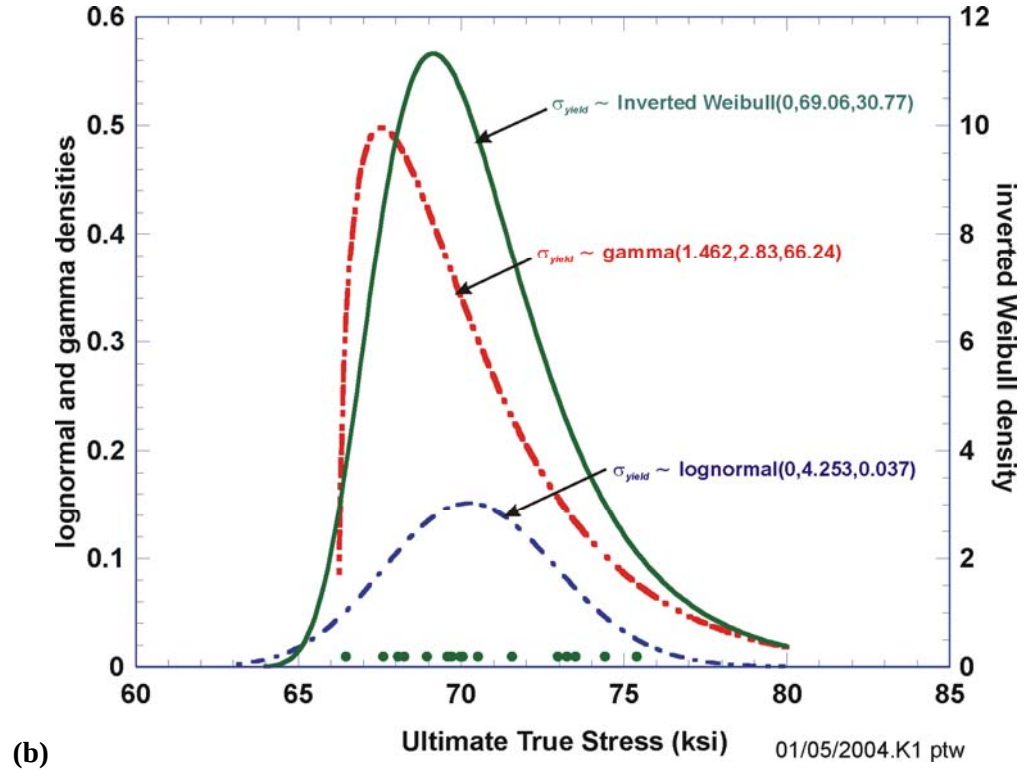

(b)

Fig. 13. Probability density functions for fitted statistical marginal distributions based on data in Table 1: (a) yield true stress and (b) ultimate true stress.

INVERTED WEIBULL MARGINAL DISTRIBUTIONS

Inverted Weibull Distribution for Yield True Stress – $W^{-1}(a,b,c)$ with

$a_{yield} = 0$, $b_{yield} = 29.7279$, and $c_{yield} = 24.764$

Inverted Weibull Distribution for Ultimate True Stress – $W^{-1}(a,b,c)$ with
$a_{ult} = 0$, $b_{ult} = 69.056$, and $c_{ult} = 30.7746$

where a = location parameter, b = scale parameter, c = shape parameter, and the inverted Weibull probability density and cumulative distribution functions are defined below.

density:
$$f(x) = \begin{cases} c\,b^{c}\left(x-a\right)^{-(c+1)} \exp\left[-\left(\frac{x-a}{b}\right)^{-c}\right] & \text{if } x > a \\ 0 & \text{otherwise} \end{cases}$$

CDF:
$$\Pr(X \le x) = F\left(x \mid a,b,c\right) = \begin{cases} \exp\left[-\left(\frac{x-a}{b}\right)^{-c}\right] & \text{if } x > a \\ 0 & \text{otherwise} \end{cases}$$

Sampling from a 3-parameter Inverted Weibull Distribution: $X_i \leftarrow W^{-1}(a,b,c)$

A random number is drawn from a uniform distribution on the open interval (0,1) and then transformed to an inverted Weibull variate with the inverted Weibull percentile function.

$$U_i \leftarrow U(0,1)$$
$$X_{(i)} = a + \frac{b}{\left[-\ln(U_i)\right]^{1/c}}$$

LOGNORMAL MARGINAL DISTRIBUTIONS

Lognormal Distribution for Yield True Stress – $LN(\gamma, \mu_{\log}, \sigma_{\log})$ with

$\gamma = 0,\ \mu_{\log(yield)} = 3.4159, \sigma_{\log(yield)} = 0.0567$

Lognormal Distribution for Ultimate True Stress – $LN(\gamma, \mu_{\log}, \sigma_{\log})$ with

$\gamma = 0,\ \ \mu_{\log(ult)} = 4.2532,\ \ \sigma_{\log(ult)} = 0.0375$

where $\mu_{\log}$ = lognormal mean (scale parameter), $\sigma_{\log}$ = lognormal standard deviation (shape parameter), and γ is the location parameter . The lognormal probability density and cumulative distribution functions are defined below.

density:
$$f(x) = \begin{cases} \dfrac{1}{(x-\gamma)\sqrt{2\pi\sigma_{\log}^2}} \exp\left\{ \dfrac{-\left[\ln(x-\gamma) - \mu_{\log}\right]^2}{2\sigma_{\log}^2} \right\} & \text{if } x > \gamma \\ 0 & \text{otherwise} \end{cases}$$

CDF:
$$F(x) = \begin{cases} \Phi\left[\dfrac{\ln(x-\gamma) - \mu_{\log}}{\sigma_{\log}} \right] & \text{if } x > \gamma \\ 0 & \text{otherwise} \end{cases} \quad \text{where } \Phi(z) = \int_{-\infty}^{z} \frac{1}{\sqrt{2\pi}} \exp\left(\frac{-\xi^2}{2} \right) d\xi$$

Sampling from a 3-parameter Lognormal Distribution: $X_i \leftarrow LN(\gamma, \mu_{\log}, \sigma_{\log})$

The log-transformed deviate is sampled from a normal distribution with mean equal to the lognormal mean, $\mu_{\log}$, and standard deviation equal to the lognormal standard deviation, $\sigma_{\log}$. A standard normal unit variate is first sampled. The following rational function [28] represents an accurate approximation of the standard normal percentile function:

$$\begin{aligned} x &= \begin{cases} p & \text{for } p < \dfrac{1}{2} \\ 1-p & \text{for } p \geq \dfrac{1}{2} \end{cases} \\ y &= \sqrt{-2\ln(x)} \\ Z_p &= \operatorname{sgn}\left(p - \frac{1}{2} \right)\left(y + \frac{a_0 + a_1 y + a_2 y^2 + a_3 y^3 + a_4 y^4}{b_0 + b_1 y + b_2 y^2 + b_3 y^3 + b_4 y^4} \right) \end{aligned} \qquad (6)$$

where

$$\text{sgn}(x) = \begin{cases} -1 & \text{if } x < 0 \\ +1 & \text{if } x \geq 0 \end{cases}$$

and the coefficients of the rational function are:

$$\begin{aligned} a_0 &= \text{-}0.3222324310880000 & b_0 &= 0.0993484626060 \\ a_1 &= \text{-}1.0000000000000000 & b_1 &= 0.5885815704950 \\ a_2 &= \text{-}0.3422420885470000 & b_2 &= 0.5311034623660 \\ a_3 &= \text{-}0.0204231210245000 & b_3 &= 0.1035377528500 \\ a_4 &= \text{-}0.0000453642210148 & b_4 &= 0.0038560700634 \end{aligned}$$

The standard normal deviate is scaled to obtain the required quantile, and the log-transformed deviate is then converted into the required random deviate by the exponential function.

$$U_i \leftarrow U(0,1)$$

$$y = \begin{cases} \sqrt{-2\ln(U_i)} & \text{for } U_i < \dfrac{1}{2} \\ \sqrt{-2\ln(1-U_i)} & \text{for } U_i \geq \dfrac{1}{2} \end{cases}$$

$$Z_i = \text{sgn}\left(U_i - \frac{1}{2}\right)\left(y + \frac{a_0 + a_1 y + a_2 y^2 + a_3 y^3 + a_4 y^4}{b_0 + b_1 y + b_2 y^2 + b_3 y^3 + b_4 y^4}\right)$$

$$Y_i = \mu_{\log} + Z_i \sigma_{\log}$$

$$X_i = \gamma + \exp(Y_i)$$

GAMMA MARGINAL DISTRIBUTIONS

Gamma Distribution for Yield True Stress – gamma(α, β, γ) with

$\alpha = 1.411176, \beta = 1.6878, \gamma = 28.112$

Gamma Distribution for Ultimate True Stress – gamma(α, β, γ) with
$\alpha = 1.4623, \beta = 2.83, \gamma = 66.24053$

where α is the shape parameter, β is the scale parameter, and γ is the location parameter . The gamma probability density and cumulative distribution functions are defined below.

density: $$f(x)=\begin{cases}\dfrac{(x-\gamma)^{\alpha-1}}{\beta^{a}\Gamma(\alpha)}\exp\left\{\dfrac{-(x-\gamma)}{\beta}\right\} & \text{if } x>\gamma \\ 0 & \text{otherwise}\end{cases} \quad \text{where } \Gamma(z)=\int_0^{\infty} t^{z-1}\exp(-t)\,dt$$

CDF: $$F(x)=\begin{cases}1-\exp\left[\dfrac{-(x-\gamma)}{\beta}\right]\displaystyle\sum_{j=0}^{\alpha-1}\frac{\left[(x-\gamma)/\beta\right]^{j}}{j!} & \text{if } x>\gamma \\ 0 & \text{otherwise}\end{cases} \quad \text{if } \alpha \text{ is an integer}$$

If α is not an integer, there is no closed form for $F(x)$.

Sampling from a 3-parameter Gamma Distribution: $X_i \leftarrow \text{gamma}(\alpha,\beta,\gamma)$

The gamma distributed deviate is sampled from a standard gamma distribution, $gamma(\alpha,1,0)$, and then converted into the required random deviate by the following scaling:

$$Y_i \leftarrow \text{gamma}(\alpha,1,0)$$
$$X_i = \gamma + \beta Y_i$$

The inverse sampling $Y_i \leftarrow \text{gamma}(\alpha,1,0)$ is accomplished with the FORTRAN subroutine **CDFGAM** available in the numerical library *dcdflib* obtained from the public-domain software repository *netlib* maintained at ORNL (see http://www.netlib.org). This subroutine uses the numerical procedures and coding specified in ref. [29].

As shown in Fig. 14, the above marginal distributions were then shifted to force their medians to pass through the current best-estimate values for the Davis-Besse cladding material, specifically $\sigma_{yield(med)} = 30.9$ ksi and $\sigma_{ult(med)} = 72$ ksi, derived from the average of the two sample points obtained from BWXT in Table 1.

For the sampled vector $X_k = \left\{\tilde{\sigma}_{yield}, \tilde{\sigma}_{ult}\right\}^T$ with $k = 1,2,\ldots,n$ (where n = sample size), the 2×2 symmetric covariance matrix can be estimated by

$$\hat{\Sigma}_{(2\times 2)} = \begin{bmatrix}\hat{\Sigma}_{11} & \hat{\Sigma}_{12} \\ \hat{\Sigma}_{21} & \hat{\Sigma}_{22}\end{bmatrix} \text{ where } \hat{\Sigma}_{ij} = \frac{\displaystyle\sum_{k=1}^{n}\left(X_{ik}-\overline{X_i}\right)\left(X_{jk}-\overline{X_j}\right)}{n} \tag{7}$$

and the correlation coefficient, ρ_{12}, is then estimated by the maximum-likelihood estimator

$$\rho_{12} = \frac{\hat{\Sigma}_{12}}{\sqrt{\hat{\Sigma}_{11}\hat{\Sigma}_{22}}} = \rho_{21} \tag{8}$$

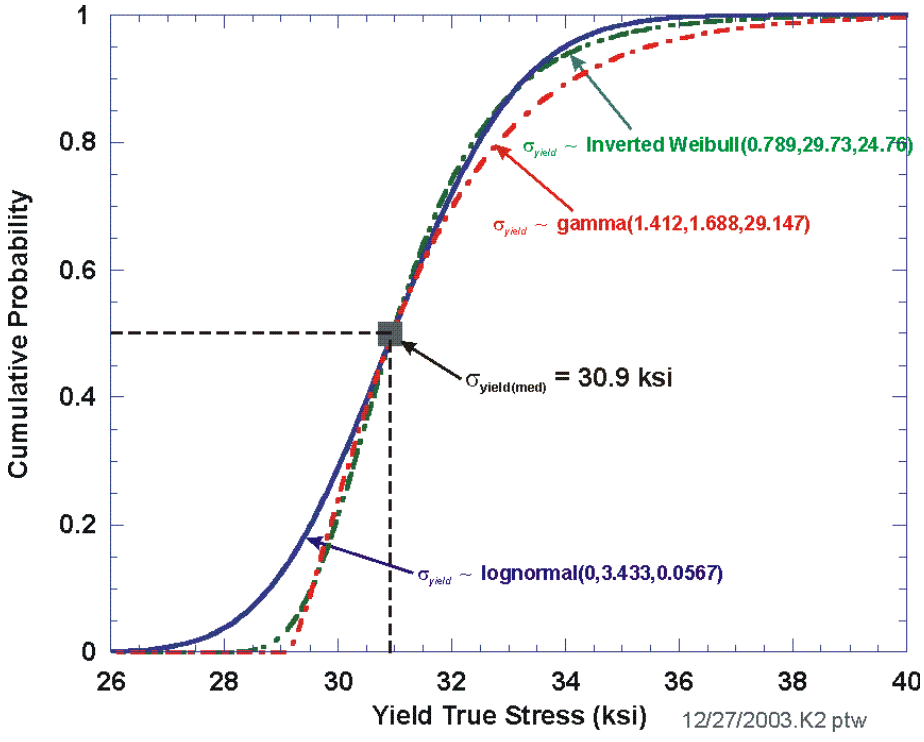

(a)

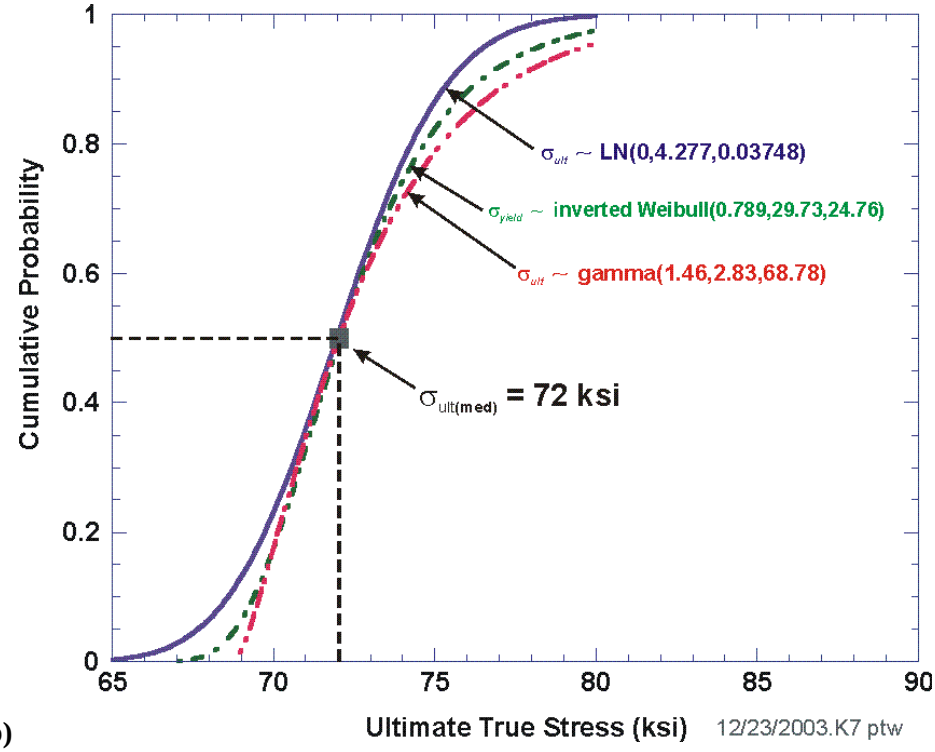

(b)

Fig. 14. Statistical distributions approximating the material variability in the yield and ultimate stresses of cladding at 550 °F to 600 °F: (a) yield true stress CDFs with adjustments to match Davis-Besse best-estimate value of 30.9 ksi and (b) ultimate true stress CDFs with adjustments to match Davis-Besse best-estimate value of 72 ksi.

From the data in Table 1, a maximum likelihood estimate of the covariance matrix is

$$\hat{\Sigma}_{(2\times2)} = \begin{bmatrix} 3.51519 & 0.35491 \\ 0.35491 & 7.45912 \end{bmatrix} \text{ and } \rho_{12} = 0.06931$$

and an estimate of the covariance matrix for the log-transformed data is

$$\hat{\Sigma}_{(2\times2)(\log)} = \begin{bmatrix} 0.0034112 & 0.0001978 \\ 0.0001978 & 0.0014929 \end{bmatrix} \text{ and } \rho_{12(\log)} = 0.08765$$

The statistically-inferred level of correlation between the true yield and true ultimate stresses for cladding is consistent with the data (after conversion to true stresses) presented in [22,23], where

TP304 Stainless Steel Piping

$$\hat{\Sigma}_{(2\times2)} = \begin{bmatrix} 4.4013 & 1.5280 \\ 1.5280 & 84.4235 \end{bmatrix} \text{ and } \rho_{12} = 0.07927$$

$$\hat{\Sigma}_{(2\times2)(\log)} = \begin{bmatrix} 0.0085228 & 0.0008016 \\ 0.0008016 & 0.0109623 \end{bmatrix} \text{ and } \rho_{12(\log)} = 0.08293$$

Three bivariate distributions along with the uncorrelated case were chosen to test the sensitivity of the Monte Carlo LOCA probability estimates to the degree and method of correlation when sampling the yield and ultimate stresses. (Compare the results of Case CCA-001 with Cases CCA-019, CCA-020, and CCA-021 in Table 10 of Sec. 3.2.)

(1) Bivariate Inverted Weibull Distribution – $\rho_{12} = 1$ **(perfect correlation)**

A single random number is drawn from a uniform distribution on the open interval (0,1) and then transformed to inverted Weibull variates for both yield and ultimate true stresses:

$$\begin{aligned} U_i &\leftarrow U(0,1) \\ \tilde{\sigma}_{yield(i)} &= a_{yield} + \frac{b_{yield}}{\left[-\ln(U_i)\right]^{1/c_{yield}}} \\ \tilde{\sigma}_{ult(i)} &= a_{ult} + \frac{b_{ult}}{\left[-\ln(U_i)\right]^{1/c_{ult}}} \end{aligned} \tag{9}$$

(2) Bivariate Lognormal Distribution – $\rho_{12} = 0.06931;\ \rho_{12(\log)} = 0.08765$ **(inferred from data)**

The sampling of a multivariate lognormal random vector follows from the procedures discussed in [30, 31]. The first step is to carry out a Cholesky decomposition (factorization) of the log-transformed correlation matrix. For the log-transformed data in Table 1:

$$\Sigma_{2\times 2(\log)} = CC^T$$

where C is the 2×2 lower triangular Cholesky factor

$$C = \begin{bmatrix} c_{11} & c_{12} \\ c_{21} & c_{22} \end{bmatrix} = \begin{bmatrix} 0.05666 & 0 \\ 0.013151 & 0.035097 \end{bmatrix}$$

For a bivariate lognormal joint distribution, the sampling protocol for the vector $X_i = \left\{\widetilde{\sigma}_{yield(i)}, \widetilde{\sigma}_{ult(i)}\right\}^T$ is as follows:

$$\begin{aligned} &Z_1 \leftarrow N(0,1); Z_2 \leftarrow N(0,1) \text{ where } Z_1 \text{ and } Z_2 \text{ are IID} \\ &Y_1 = \mu_{yield(\log)} + \left(c_{11} \times Z_1\right) \\ &Y_2 = \mu_{ult(\log)} + \left(c_{21} \times Z_1\right) + \left(c_{22} \times Z_2\right) \\ &X_i = \begin{Bmatrix} \exp(Y_1) \\ \exp(Y_2) \end{Bmatrix}_{(i)} = \begin{Bmatrix} \widetilde{\sigma}_{yield} \\ \widetilde{\sigma}_{ult} \end{Bmatrix}_{(i)} \end{aligned} \tag{10}$$

where IID refers to *independent and identically distributed* random variates, and Z_1 and Z_2 are standard-unit-normal variates.

(3) Bivariate Gamma Distribution – $\rho_{12} = 0.06931$ **(inferred from data)**

The sampling protocol of the bivariate gamma random vector $X_i = \left\{\widetilde{\sigma}_{yield(i)}, \widetilde{\sigma}_{ult(i)}\right\}^T$ follows from the procedures discussed in ref. [32] with the requirement that the two variates must be positively correlated and $\rho \le \min\left\{\alpha_1, \alpha_2\right\} / \sqrt{\alpha_1 \alpha_2}$. These requirements are met by the yield and ultimate stress sample dataset in Table 1. The protocol relies on a special property of gamma distributions.

$$\begin{aligned} &Y_1 \leftarrow \text{gamma}\left(\alpha_1 - \rho_{12}\sqrt{\alpha_1\alpha_2}, 1, 0\right) \\ &Y_2 \leftarrow \text{gamma}\left(\alpha_2 - \rho_{12}\sqrt{\alpha_1\alpha_2}, 1, 0\right) \text{ independent of } Y_1 \\ &Y_3 \leftarrow \text{gamma}\left(\rho_{12}\sqrt{\alpha_1\alpha_2}, 1, 0\right) \text{ independent of } Y_1 \text{ and } Y_2 \\ &X_i = \begin{Bmatrix} \gamma_1 + \beta_1\left(Y_1 + Y_3\right) \\ \gamma_2 + \beta_2\left(Y_2 + Y_3\right) \end{Bmatrix}_{(i)} = \begin{Bmatrix} \widetilde{\sigma}_{yield} \\ \widetilde{\sigma}_{ult} \end{Bmatrix}_{(i)} \end{aligned} \tag{11}$$

The above technique is known as *trivariate reduction*, since the three random variates Y_1, Y_2, and Y_3 are "reduced" to the two final random variates $\left\{\widetilde{\sigma}_{yield(i)}, \widetilde{\sigma}_{ult(i)}\right\}^T$, see [33].

(4) Univariate Inverted Weibull Distribution – $\rho_{12} = 0$ **(uncorrelated)**

Two IID random numbers are drawn from a uniform distribution on the open interval (0,1) and then transformed to inverted Weibull variates for both yield and ultimate true stresses:

$$U_{1(i)} \leftarrow U(0,1); U_{2(i)} \leftarrow U(0,1) \text{ where } U_{1(i)} \text{ and } U_{2(i)} \text{ are IID}$$

$$\sigma_{yield(i)} = a_{yield} + \frac{b_{yield}}{\left[-\ln(U_{1(i)})\right]^{1/c_{yield}}} \tag{12}$$

$$\sigma_{ult(i)} = a_{ult} + \frac{b_{ult}}{\left[-\ln(U_{2(i)})\right]^{1/c_{ult}}}$$

2.2.3.2 Stochastic Model for Plastic-Flow Properties – Calculating (*K*, *n*) from estimates for $\tilde{\sigma}_{yield}$ and $\tilde{\sigma}_{ult}$

Dowling [34] provides a derivation of a method for estimating the true strain at the ultimate true stress based on a power-law representation of the plastic flow properties of the material. The following relationships between engineering stress and strain (σ, ε) and true stress and true strain ($\tilde{\sigma}, \tilde{\varepsilon}$) for deformation well beyond yielding hold:

$$\begin{aligned} \tilde{\varepsilon} &= \ln(1+\varepsilon) \\ \tilde{\sigma} &= \sigma(1+\varepsilon) \end{aligned} \tag{13}$$

where the overhead curl denotes a true stress or strain. The true strain is also related to the initial, A_i, and deformed, A, cross-sectional areas (for example in a tensile roundbar specimen) by

$$\begin{aligned} \tilde{\varepsilon} &= \ln\left(\frac{A_i}{A}\right) \\ \exp(\tilde{\varepsilon}) &= \left(\frac{A_i}{A}\right) \end{aligned} \tag{14}$$

From the definition of the true effective stress, $\tilde{\sigma}$, we have

$$\begin{aligned} &\tilde{\sigma} = \left(\frac{P}{A}\right) = \left(\frac{P}{A_i}\right)\left(\frac{A_i}{A}\right) = \sigma\left(\frac{A_i}{A}\right) \\ &\therefore \\ &\sigma = \tilde{\sigma}\left(\frac{A}{A_i}\right) = \tilde{\sigma}\exp(-\tilde{\varepsilon}) \end{aligned} \tag{15}$$

Differentiating the final expression in Eq. (15) with respect to the true strain, $\tilde{\varepsilon}$, gives

$$\frac{d\sigma}{d\tilde{\varepsilon}} = \left(\frac{1}{\exp(\tilde{\varepsilon})}\right)\left(\frac{d\tilde{\sigma}}{d\tilde{\varepsilon}} - \tilde{\sigma}\right) \tag{16}$$

At the ultimate stress, we apply the following constraint condition

$$\left.\frac{d\sigma}{d\tilde{\varepsilon}}\right|_{\sigma=\sigma_{ult}} = \left(\frac{1}{\exp(\tilde{\varepsilon}_{ult})}\right)\left(\frac{d\tilde{\sigma}_{ult}}{d\tilde{\varepsilon}_{ult}} - \tilde{\sigma}_{ult}\right) = 0 \tag{17}$$

where the condition in Eq. (17) holds only when

$$\frac{d\tilde{\sigma}_{ult}}{d\tilde{\varepsilon}_{ult}} = \tilde{\sigma}_{ult} \tag{18}$$

Applying a power-law constitutive model, the constraint condition produces the following result

$$\begin{aligned} \tilde{\sigma} &= K\tilde{\varepsilon}^{n} \\ \frac{d\tilde{\sigma}}{d\tilde{\varepsilon}} &= Kn\tilde{\varepsilon}^{n-1} \\ &\therefore \\ Kn\tilde{\varepsilon}_{ult}^{n-1} &= K\tilde{\varepsilon}_{ult}^{n} \\ n &= \left(\tilde{\varepsilon}_{ult}^{n}\right)\left(\tilde{\varepsilon}_{ult}^{1-n}\right) \\ n &= \tilde{\varepsilon}_{ult} \end{aligned} \tag{19}$$

Therefore, the exponent of the power-law constitutive model can be viewed as an estimate of the true strain at ultimate.

From Eq. (13), the 0.2% offset engineering yield strain and engineering yield stress are related to the true strain and true stress by

$$\begin{aligned} \tilde{\varepsilon}_{yield} &= \ln\left(1+\varepsilon_{yield}\right) \\ \tilde{\sigma}_{yield} &= \sigma_{yield}\left(1+\varepsilon_{yield}\right) \end{aligned} \tag{20}$$

From the definition of the 0.2% offset engineering yield strain, we have

$$\varepsilon_{yield} = 0.002 + \left(\frac{\sigma_{yield}}{E}\right) \tag{21}$$

where E is the modulus of elasticity. From Eq. (20)

$$\exp\left(\tilde{\varepsilon}_{yield}\right) = \varepsilon_{yield} + 1 \tag{22}$$

Combining Eqs. (21) and (22), we obtain

$$\exp\left(\tilde{\varepsilon}_{yield}\right) = 1.002 + \left(\frac{\sigma_{yield}}{E}\right) \tag{23}$$

From Eq. (20), the engineering yield stress is related to the true yield stress and engineering yield strain by

$$\sigma_{yield} = \frac{\tilde{\sigma}_{yield}}{\left(1+\varepsilon_{yield}\right)} \tag{24}$$

Combining Eqs. (22) and (24) in Eq. (23) results in

$$\exp\left(\tilde{\varepsilon}_{yield}\right) = 1.002 + \left[\frac{\tilde{\sigma}_{yield}}{E\exp\left(\tilde{\varepsilon}_{yield}\right)}\right] \tag{25}$$

Multiplying Eq. (25) by $\xi \equiv \exp\left(\tilde{\varepsilon}_{yield}\right)$ produces the following quadratic equation

$$\xi^2 - 1.002\xi - \left(\frac{\tilde{\sigma}_{yield}}{E}\right) = 0 \tag{26}$$

Solving Eq. (26) for its positive root gives

$$\xi = \exp\left(\tilde{\varepsilon}_{yield}\right) = \frac{1.002 + \sqrt{(1.002)^2 + \left(\frac{4\tilde{\sigma}_{yield}}{E}\right)}}{2}$$

or (27)

$$\tilde{\varepsilon}_{yield} = \ln\left(\frac{1.002 + \sqrt{(1.002)^2 + \left(\frac{4\tilde{\sigma}_{yield}}{E}\right)}}{2}\right)$$

Given the estimate for $\tilde{\varepsilon}_{ult}$ by Eq. (19), the relation for $\tilde{\varepsilon}_{yield}$ from Eq. (27), and sampled values of $\tilde{\sigma}_{yield(i)}$ and $\tilde{\sigma}_{ult(i)}$ (from the sampling protocols of Eqs. (9), (10), (11) or (12)), the values for the power-law coefficient, $K_{(i)}$, and exponent, $n_{(i)}$, can now be calculated by solving the following nonlinear system of equations for the two unknowns ($K_{(i)}, n_{(i)}$) :

$$\tilde{\sigma}_{yield(i)} - K_{(i)}\left[\ln\left(\frac{1.002+\sqrt{1.002^2+\left(4\tilde{\sigma}_{yield(i)}/E\right)}}{2}\right)\right]^{n(i)} = 0$$
$$\tilde{\sigma}_{ult(i)} - K_{(i)}\left(n_{(i)}\right)^{n(i)} = 0 \qquad (28)$$

With the sampled values for $\left(K_{(i)}, n_{(i)}\right)$, the slope of the fragility curve can then be calculated from Eq. (5) or

$$S_{(i)} = \frac{-P_{applied}\exp\left[\frac{\tilde{\varepsilon}_{crit}(n_{(i)})}{2}\right]}{4\tilde{\sigma}_{crit}(K_{(i)}, n_{(i)})\exp[-\tilde{\varepsilon}_{crit}(n_{(i)})]\sqrt{\exp\left[\frac{\tilde{\varepsilon}_{crit}(n_{(i)})}{2}\right]-1}} \qquad (29)$$

and the sampled fragility curve is then, from Eq. (2):

$$a_{A-tip(crit)(i)} = h_0 + \left(S_{(i)} \times R_{cavity}\right) \qquad (30)$$

Table 3 shows the results of one uncorrelated and three correlated bivariate samplings from the yield and ultimate stress stochastic models described by Eqs. (9)-(12). Figure 15 presents histograms (N=10,000) of the resulting sampled fragility curve slopes obtained with the three bivariate joint distributions and the one uncorrelated sampling protocol for yield and ultimate true stresses.

The objectives of multivariate sampling are: (1) to retain the characteristics of the individual marginal distributions for each component of the vector and (2) to reproduce the input correlation coefficient in the generated samples. If these two objectives are met, then the multivariate sampling protocol is said to *maintain control* over the intended multivariate joint probability distribution. The simulated data in Table 3 indicate that the bivariate lognormal protocol maintains better control over the resulting sampled bivariate distribution than the bivariate gamma protocol. The bivariate lognormal joint distribution was, therefore, chosen for the best-estimate case, and the other three options were included as special cases (cf. Cases CCA-001, CCA-019, CCA-020, and CCA-021 in Table 10 of Sec. 3.2) in the sensitivity-study case matrix.

Figure 16a provides an example of the varying partitioning of the damage-state space produced by sampling from the bivariate lognormal joint distribution for yield and ultimate stress. The cumulative probabilities for the slope of the fragility curve have been estimated from order statistics with a sample size of 10,000. In Fig. 16b, random bivariate sampling produced a fragility curve associated with a specific cumulative probability of 97.5%.

Table 3. Results of Bivariate Sampling Protocols for a Range of Correlation Coefficients, $\widetilde{X}_i = \left\{\widetilde{\sigma}_{yield(i)}, \widetilde{\sigma}_{ult(i)}\right\}^T$

Case No.	Sampling Protocol	Sampled Variate	Marginal Distributions	Joint Distribution	Input Distribution Statistics						Simulation Statistics (N = 10,000)					Sampled Quantiles		
					Mean	Variance	2.50%	Median	97.50%	Correlation	Mean	Variance	Correlation	Covariance Matrix		2.50%	Median	97.50%
1	Fully Correlated	Yield Stress	inverted Weibull	bivariate inverted Weibull	31.259	2.651	28.99	30.96	35.27	1	31.272	2.611	0.99996	2.611	4.825	yield	30.97	30.97
		Ultimate Stress	inverted Weibull		72.602	9.055	68.36	72.06	80.00		72.626	8.918		4.825	8.918	68.45	72.09	79.88
2	Jones and Miller (1966)	Yield Stress	lognormal	bivariate lognormal	31.010	3.515	27.71	30.96	34.60	0.06931	30.993	2.986	0.06994	2.986	0.324	27.71	30.97	34.49
		Ultimate Stress	lognormal		72.110	7.459	66.96	72.06	77.55		72.080	7.188		0.324	7.188	66.99	72.04	77.56
3	Arnold (1967)	Yield Stress	gamma	bivariate gamma	31.493	4.022	29.26	30.96	36.72	0.06931	31.512	4.043	0.05514	4.043	0.373	29.29	30.96	36.81
	trivariate reduction	Ultimate Stress	gamma		72.906	11.711	69.10	72.06	81.85		72.932	11.301		0.373	11.301	69.08	72.06	81.48
4	Uncorrelated	Yield Stress	inverted Weibull	NA	31.259	2.651	28.99	30.96	35.27	0	31.267	2.670	-0.01427	2.670	-0.070	28.98	30.96	35.31
		Ultimate Stress	inverted Weibull		72.602	9.055	68.36	72.06	80.00		72.600	9.000		-0.070	9.000	68.38	72.05	79.90

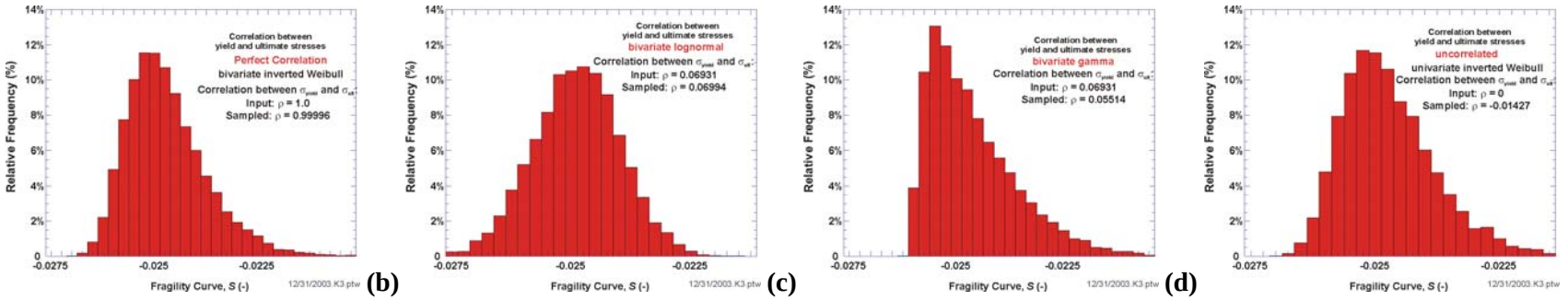

Fig. 15. Frequency histograms of sampled fragility curve slopes based on (a) perfect correlation between yield and ultimate stresses, (b) bivariate lognormal joint distribution with correlation coefficient of 0.06931, (c) bivariate gamma joint distribution with correlation coefficient of 0.06931, and (d) uncorrelated yield and ultimate stresses and, therefore, statistically independent. The correlation coefficient of 0.06931 was statistically inferred from the data in Table 1.

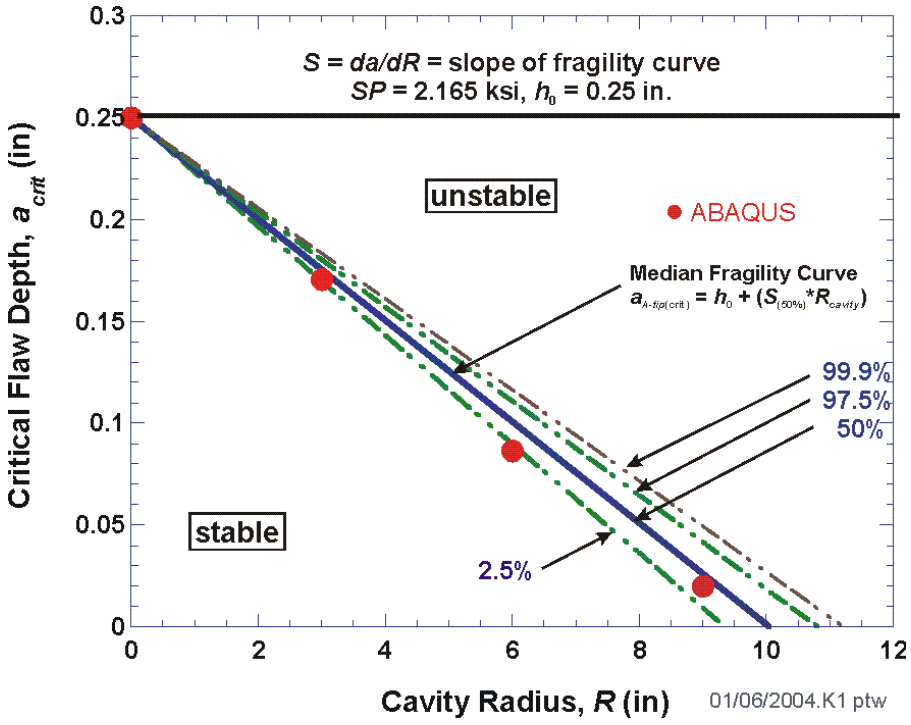

(a)

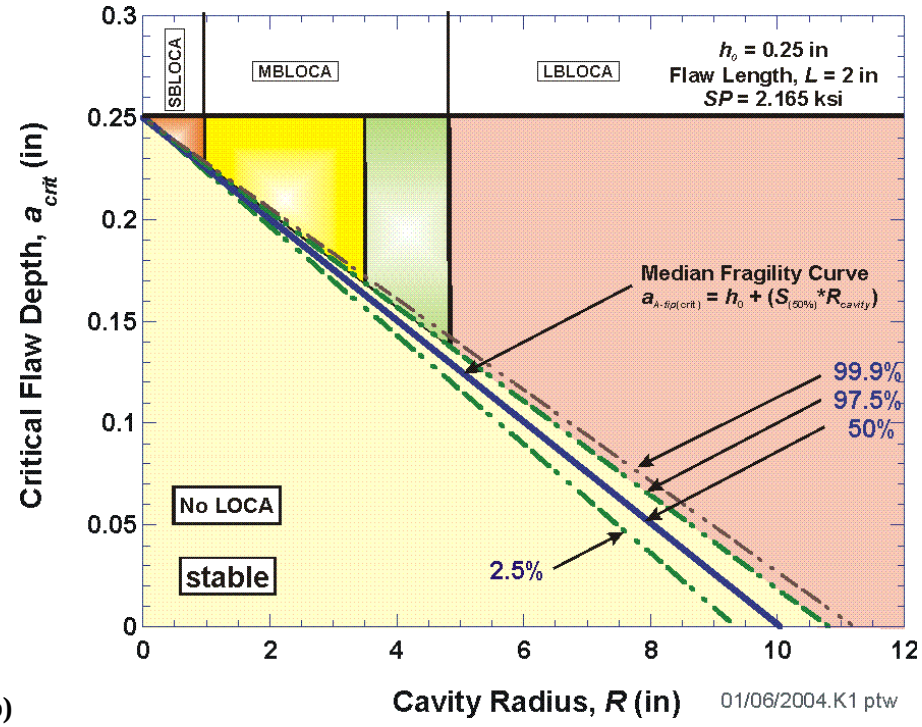

(b)

Fig. 16. The fragility curve stochastic model for $P_{applied}$ = 2.165 ksi produces a slope with its uncertainty described by the distributions shown in Fig. 15. The intersection of the fragility curve with the *y*-axis is equal to the initial undeformed cladding thickness, h_0, which is assumed known in the current analysis: (a) a sampling of fragility curves based on their cumulative probability resulting from the *bivariate lognormal* joint distribution for yield and ultimate stress and (b) damage state partitioning based on an uncertain fragility curve slope with cumulative probability of 97.5%.

In Fig. 17, the predictions of the modified Chakrabarty and Alexander's instability theory [**15**] are compared to the pressures at numerical instability, PNI, predicted by 3-dimensional finite-element models of the 2-inch long model flaw centered in 0.25 inch thick burst disks with varying radius. These results indicated good agreement between the modified instability theory and the detailed finite-element models up to a relative flaw depth of $a/t = 0.5$.

For flaws with $a/t \geq 0.5$, the modified instability theory becomes slightly nonconservative, i.e., the theory produces burst pressures greater than those estimated by the finite-element models. With reference to the BWXT forensic investigation [16], however, the deepest crack observed in the Davis-Besse wastage had an $a/t < 0.5$, and most of the cracks are significantly shallower; therefore, the above model is appropriate for this study.

2.2.4 Failure Mechanisms – Development of a Ductile-Tearing Model

A stochastic model for ductile-tearing initiation was developed from data in [35, 36]. Table 4 presents ductile tearing data for three-wire series-arc stainless steel weld overlay cladding published in NUREG/CR-5511 [35]. Table 5a presents additional ductile tearing data for stainless steel cladding published in NUREG/CR-6363 [36] and data from pre-cracked Charpy V-notch (PCCVN) specimens made from PVRUF and Davis-Besse cladding materials [2]. The ductile-tearing data in Tables 4 and 5 are plotted as a function of temperature in Fig. 18. The J_{Ic} data at 288 °C (550 °F) from NUREG/CR-5511 have been extrapolated to 318.33 °C (605 °F) using a curve fit developed from the data in Table 4. The extrapolated J_{Ic} data are also presented in Table 5a.

The ExpertFit© statistical software [**27**] was used to fit several statistical distributions (see Table 5b) to different groupings of the J_{Ic} data in Table 5a. The resulting fit for the J_{Ic} data from NUREG/CR-5511 [35] and NUREG/CR-6363 [36] produced a log-logistic distribution with the following form:

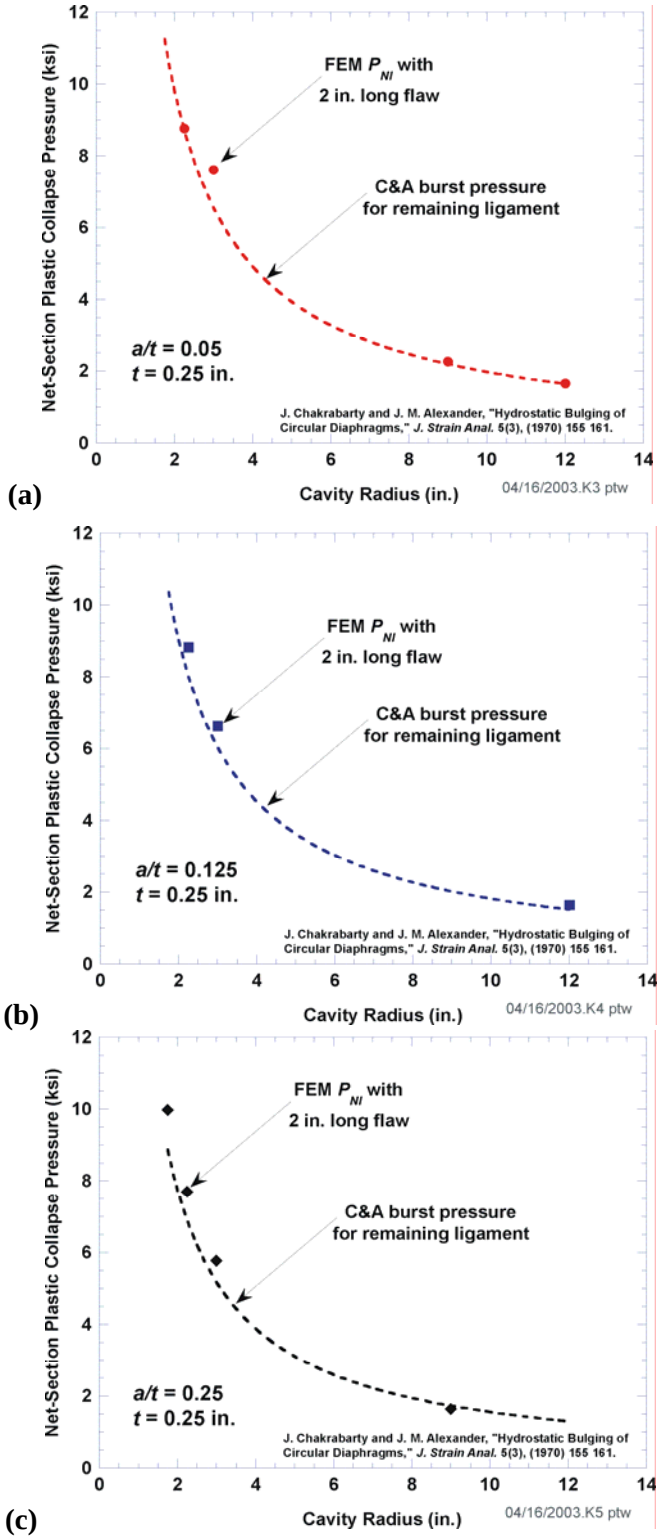

Fig. 17. Net-section plastic collapse pressures estimated by modified C&A (1970) theory compared to P_{NI} values determined from 3D finite-element ABAQUS solutions: (a) a/t = 0.05, (b) a/t = 0.125, (c) a/t = 0.25, (Ductile tearing not simulated for these cases.)

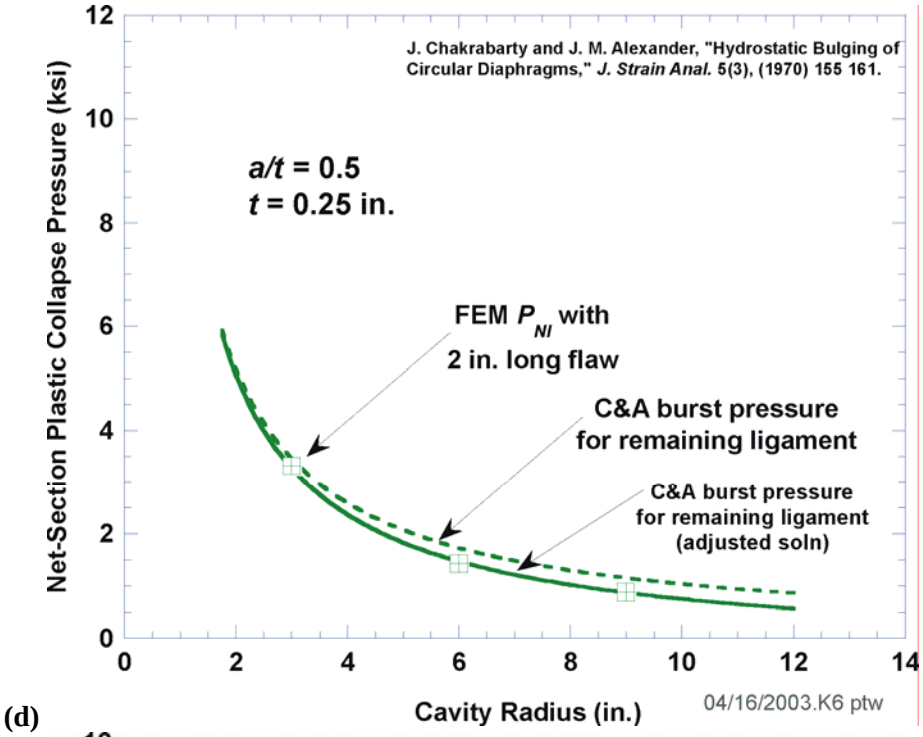

(d)

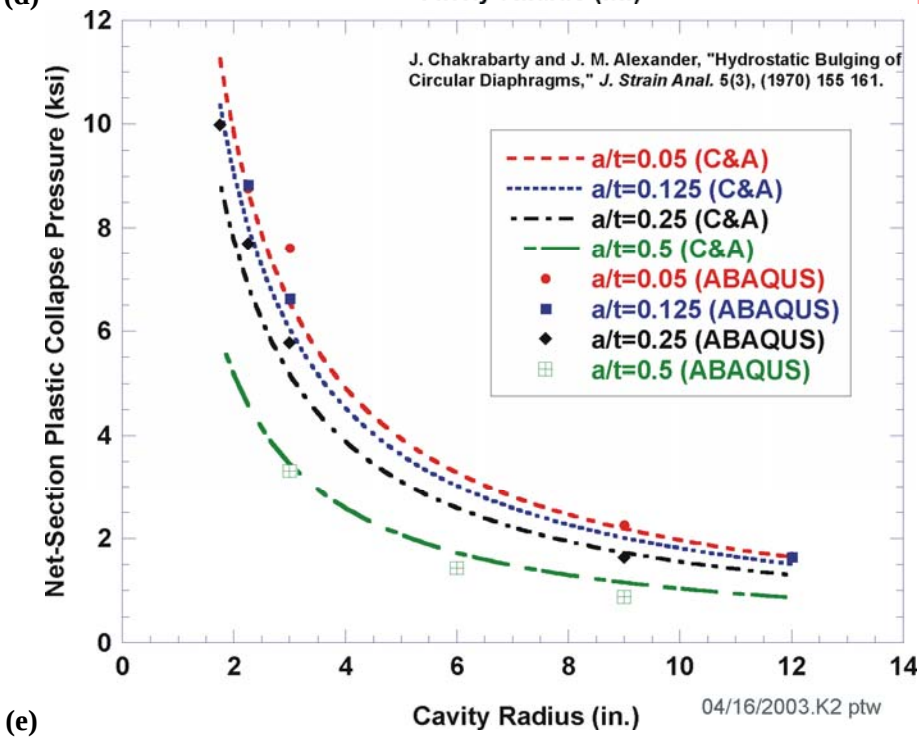

(e)

Fig. 17 (continued) Net-section plastic collapse pressures estimated by modified C&A (1970) theory compared to P_{NI} values determined from 3D finite-element ABAQUS solutions: (d) a/t = 0.5, and (e) combined plot. (Ductile tearing not simulated for these cases.)

Table 4. Ductile-Tearing Data Extracted from Table 13 of NUREG/CR-5511 [35].

Specimen	Test Temperature (°C)	J_{Ic} (kJ/m^2)	Tearing Modulus
Unirradiated Specimens			
A13G	-75	117	64
H2	-75	137	49
A15B[a]	20	165	270
A13D	20	134	209
A10G	20	171	176
A10E	120	128	246
H5	120	119	229
H3	120	120	232
A13F[a]	120	159	359
H6	200	90	240
H4	200	111	231
A15D	288	77	267
A13C	288	66	170
H1	288	82	192
Irradiated Specimens			
A15F	-75	78	40
A15G	-75	56	36
A13A	30	144	177
A15C	50	124	146
A10F	120	94	175
A15A	288	25	191

[a] Specimen was not side-grooved, while all other specimens in table were side-grooved 20%.

Table 5a. Ductile-Tearing Data Used in Development of J_{Ic} Statistical Distributions

J_{Ic} Distribution Values								
Specimen ID	Test Temp. (°C)	J_{IC} or J_Q (kJ/m^2)	Reference	Remarks	Oper. Temp. (°C)	J_{IC} (kJ/m^2)	Average Tearing Modulus
A15D	288	76	NUREG/CR-5511	Three-wire cladding study	318	72.17	267
A13C	288	70	NUREG/CR-5511	Three-wire cladding study	318	66.47	170
H1	288	83	NUREG/CR-5511	Three-wire cladding study	318	78.82	192
H10	288	85	NUREG/CR-6363	Aged 3-wire cladding at 288 °C for 1605 hrs.	318	80.71	
AA04	288	93	NUREG/CR-6363	Aged 3-wire cladding at 288 °C for 1605 hrs.	318	88.31	
AA02	288	59	NUREG/CR-6363	Aged 3-wire cladding at 288 °C for 1605 hrs.	318	56.02	
AA13	288	91	NUREG/CR-6363	Aged 3-wire cladding at 288 °C for 20,000 hrs.	318	86.41	
AA15	288	77	NUREG/CR-6363	Aged 3-wire cladding at 288 °C for 20,000 hrs.	318	73.12	
H15	288	111	NUREG/CR-6363	Aged 3-wire cladding at 343 °C for 20,000 hrs.	318	105.4	
H16	288	110	NUREG/CR-6363	Aged 3-wire cladding at 343 °C for 20,000 hrs.	318	104.45	
R3P1	315.6	166.2	ORNL/NRC/LTR-04/13	Pre-cracked Charpy Test Results PVRUF	316	166.2	N/E
R3T1	315.6	197.2	ORNL/NRC/LTR-04/13	Pre-cracked Charpy Test Results PVRUF	316	197.2	214.71
R3T6	315.6	161.7	ORNL/NRC/LTR-04/13	Pre-cracked Charpy Test Results PVRUF	316	161.7	172.69
R4P2	315.6	121.6	ORNL/NRC/LTR-04/13	Pre-cracked Charpy Test Results PVRUF	316	121.6	242.13
R4T2	315.6	185.7	ORNL/NRC/LTR-04/13	Pre-cracked Charpy Test Results PVRUF	316	185.7	160.19
R4T5	315.6	184.2	ORNL/NRC/LTR-04/13	Pre-cracked Charpy Test Results PVRUF	316	184.2	N/E
R5P2	315.6	143.7	ORNL/NRC/LTR-04/13	Pre-cracked Charpy Test Results PVRUF	316	143.7	130.56
R5T1	315.6	182.2	ORNL/NRC/LTR-04/13	Pre-cracked Charpy Test Results PVRUF	316	182.2	154.6
R5T5	315.6	216.5	ORNL/NRC/LTR-04/13	Pre-cracked Charpy Test Results PVRUF	316	216.5	181.15
R0T1	315.6	139.5	ORNL/NRC/LTR-04/13	Pre-cracked Charpy Test Results PVRUF	316	139.5	92.15
R0T2	315.6	123.7	ORNL/NRC/LTR-04/13	Pre-cracked Charpy Test Results PVRUF	316	123.7	76.79
R0T3	315.6	112.7	ORNL/NRC/LTR-04/13	Pre-cracked Charpy Test Results PVRUF	316	112.7	113.54
R0T5	315.6	158.3	ORNL/NRC/LTR-04/13	Pre-cracked Charpy Test Results PVRUF	316	158.3	104.26
R0T6	315.6	103.8	ORNL/NRC/LTR-04/13	Pre-cracked Charpy Test Results PVRUF	316	103.8	91.28
TS1	315.6	137.9	ORNL/NRC/LTR-04/13	Pre-cracked Charpy Test Results Davis-Besse	316	137.9	110.9
TS2	315.6	180.85	ORNL/NRC/LTR-04/13	Pre-cracked Charpy Test Results Davis-Besse	316	180.85	180.85
TS4	315.6	121	ORNL/NRC/LTR-04/13	Pre-cracked Charpy Test Results Davis-Besse	316	121	103.52
TS5	315.6	132.41	ORNL/NRC/LTR-04/13	Pre-cracked Charpy Test Results Davis-Besse	316	132.41	132.3
LS1	315.6	96.43	ORNL/NRC/LTR-04/13	Pre-cracked Charpy Test Results Davis-Besse	316	96.43	107.73
LS2	315.6	93.21	ORNL/NRC/LTR-04/13	Pre-cracked Charpy Test Results Davis-Besse	316	93.21	103.03
LS3	315.6	100.92	ORNL/NRC/LTR-04/13	Pre-cracked Charpy Test Results Davis-Besse	316	97.76	117.08
LS4	315.6	101.47	ORNL/NRC/LTR-04/13	Pre-cracked Charpy Test Results Davis-Besse	316	100.92	128.21
LS5	315.6	97.958	ORNL/NRC/LTR-04/13	Pre-cracked Charpy Test Results Davis-Besse	316	101.47	125.11
TL1	315.6	108.15	ORNL/NRC/LTR-04/13	Pre-cracked Charpy Test Results Davis-Besse	316	108.15	74.79
TL3	315.6	128.2	ORNL/NRC/LTR-04/13	Pre-cracked Charpy Test Results Davis-Besse	316	128.2	113.7
TL4	315.6	137.57	ORNL/NRC/LTR-04/13	Pre-cracked Charpy Test Results Davis-Besse	316	137.57	115.08

NUREG data extrapolated to 318.33 °C (605 °F).

Table 5b. Statistical Distributions Fitted to J_{Ic} Data from Three Sources

J_{Ic} Data Source	Marginal Distribution	Sample Size	Point Estimates for Parameters			Goodness of Fit Test	Test Statistic	Critical Values for Level of Significance (α)						
			location	scale	shape			0.25	0.15	0.1	0.05	0.025	0.01	0.005
NUREG/CR-5511						Anderson-Darling	0.177	0.416	NA	0.549	0.644	0.75	0.884	0.985
NUREG/CR-6363	log-logistic	10	0	79.9486	9.3076	Kolmogorov-Smirnov	0.390	NA	NA	0.679	0.73	0.774	0.823	NA
(1/2T C(T))						equi-probable chi^2	NA	NA	NA	NA	NA	NA	NA	NA
						Anderson-Darling	0.470	0.436	NA	0.585	0.698	0.810	0.96	1.075
Davis-Besse	lognormal	12	0	4.7656	0.1909	Kolmogorov-Smirnov	0.673	NA	0.726	0.767	0.838	0.932	0.969	NA
(PCCVN)						equi-probable chi^2	2.667	4.108	5.317	6.251	7.815	NA	11.345	NA
						Anderson-Darling	0.212	0.450	NA	0.605	0.719	0.833	0.985	NA
PVRUF	Weibull	14	0	170.30	5.41	Kolmogorov-Smirnov	0.461	NA	NA	0.760	0.819	0.880	0.944	NA
(PCCVN)						equi-probable chi^2	1.429	4.108	5.317	6.251	7.815	NA	11.345	NA

1/2T C(T) = pre-cracked compact tension specimens

PCCVN = pre-cracked Charpy V-Notch specimen

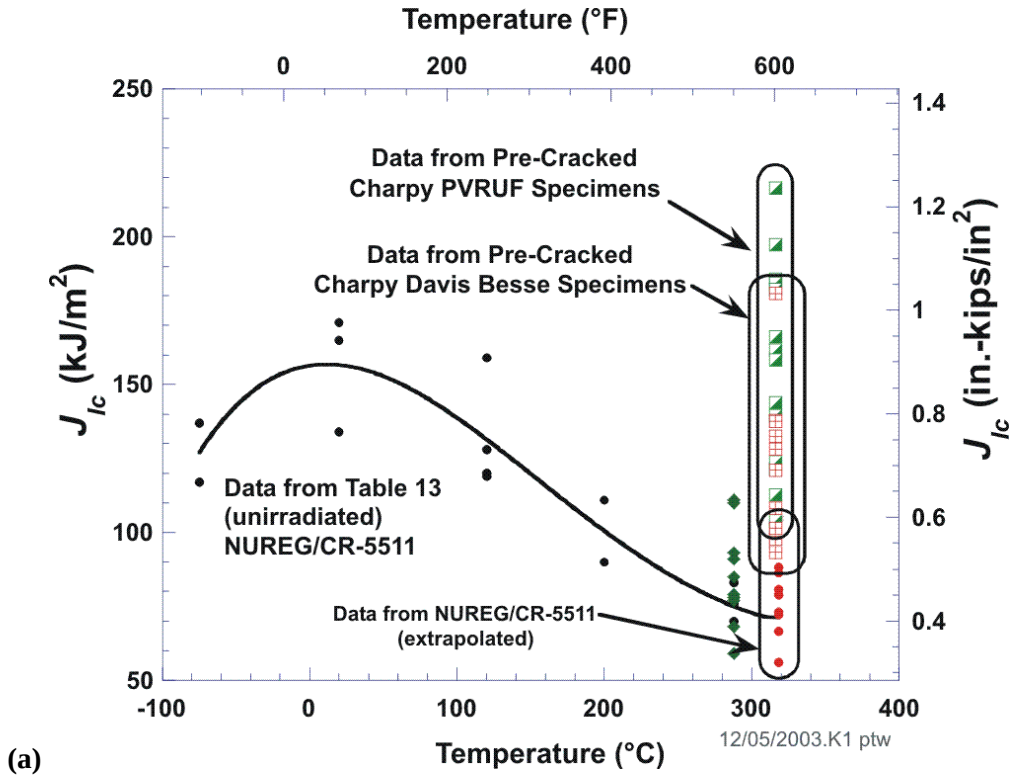

(a)

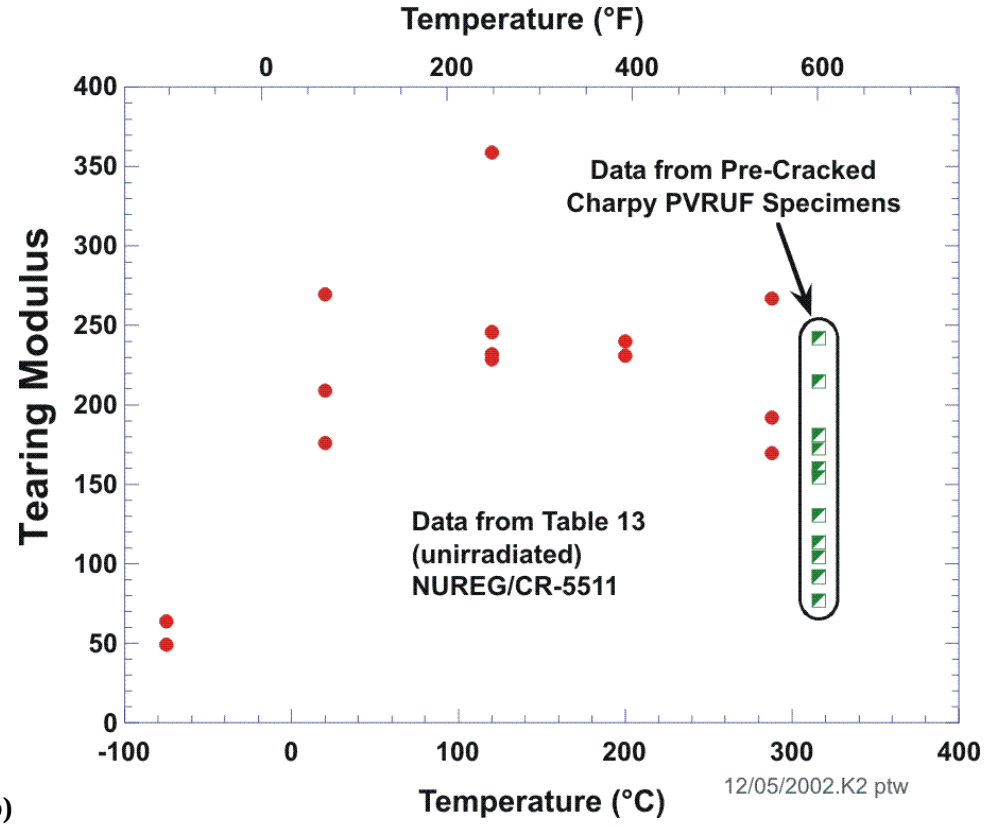

(b)

Fig. 18. Ductile-tearing data for cladding from several sources: (a) J_{Ic} data and (b) average tearing modulus data.

Log-logistic Distribution for NUREG C(T) J_{Ic} Data – $LL(\alpha, \beta, \gamma)$ with

$\alpha = 9.30759$, $\beta = 79.94864$ kJ/m^2, and $\gamma = 0$.

The log-logistic probability density and cumulative distribution functions are defined below.

density:
$$f(x) = \begin{cases} \dfrac{\alpha\left(\dfrac{x-\gamma}{\beta}\right)^{\alpha-1}}{\beta\left[1+\left(\dfrac{x-\gamma}{\beta}\right)^{\alpha}\right]^2} & \text{if } x > \gamma \\ 0 & \text{otherwise} \end{cases}$$

CDF:
$$F(x) = \begin{cases} \dfrac{1}{1+\left(\dfrac{x-\gamma}{\beta}\right)^{-\alpha}} & \text{if } x > \gamma \\ 0 & \text{otherwise} \end{cases}$$

The corresponding percentile function is

$$J_{Ic}(p \mid \alpha, \beta, \gamma) = \gamma + \beta \exp\left[\frac{-\ln\left(\dfrac{1-p}{p}\right)}{\alpha}\right]; \text{ for } 0 < p < 1 \qquad (31)$$

A lognormal distribution was fitted to the Davis-Besse PCCVN data (N = 12) where:

Lognormal Distribution for Davis-Besse PCCVN J_{Ic} Data – $LN(\gamma, \mu_{\log}, \sigma_{\log})$ with
$\gamma = 0$, $\mu_{\log(ult)} = 4.76562$, $\sigma_{\log(ult)} = 0.19088$

where $\mu_{\log}$ = lognormal mean (scale parameter), $\sigma_{\log}$ = lognormal standard deviation (shape parameter), and γ is the location parameter . The lognormal probability density and cumulative distribution functions are defined below.

density:
$$f(x) = \begin{cases} \dfrac{1}{(x-\gamma)\sqrt{2\pi\sigma_{\log}^2}} \exp\left\{\dfrac{-\left[\ln(x-\gamma)-\mu_{\log}\right]^2}{2\sigma_{\log}^2}\right\} & \text{if } x > \gamma \\ 0 & \text{otherwise} \end{cases}$$

CDF: $$F(x) = \begin{cases} \Phi\left[\dfrac{\ln(x-\gamma)-\mu_{\log}}{\sigma_{\log}}\right] & \text{if } x > \gamma \\ 0 & \text{otherwise} \end{cases} \quad \text{where } \Phi(z) = \int_{-\infty}^{z} \frac{1}{\sqrt{2\pi}} \exp\left(\frac{-\xi^2}{2}\right) d\xi$$

A Weibull distribution was fitted to the PVRUF PCCVN data (N = 14) where:

Weibull Distribution for PVRUF PCCVN J_{Ic} Data - $W(a,b,c))$ with
location parameter, a = 0, scale parameter, b = 170.4 kJ/m^2, and shape parameter, c = 5.41

where

density: $$f(x) = \begin{cases} c\, b^{-c} (x-a)^{c-1} \exp\left\{-\left[\dfrac{x-a}{b}\right]^c\right\} & \text{if } x > a \\ 0 & \text{otherwise} \end{cases}$$

CDF: $$F(x) = \begin{cases} 1-\exp\left\{-\left[\dfrac{x-a}{b}\right]^c\right\} & \text{if } x > a \\ 0 & \text{otherwise} \end{cases}$$

Figures 19a and 19b present plots of the probability density and *CDF* of the lognormal distribution for the Davis-Besse PCCVN data. Figures 19c and 19d compare the fitted distributions for the three J_{Ic} samples, 0.5T C(T) data reported in NUREG/CR-5511 [35] and NUREG/CR-6363 [36] (log-logistic), PCCVN data from the PVRUF cladding (Weibull), and PCCVN data from the Davis-Besse cladding (lognormal).

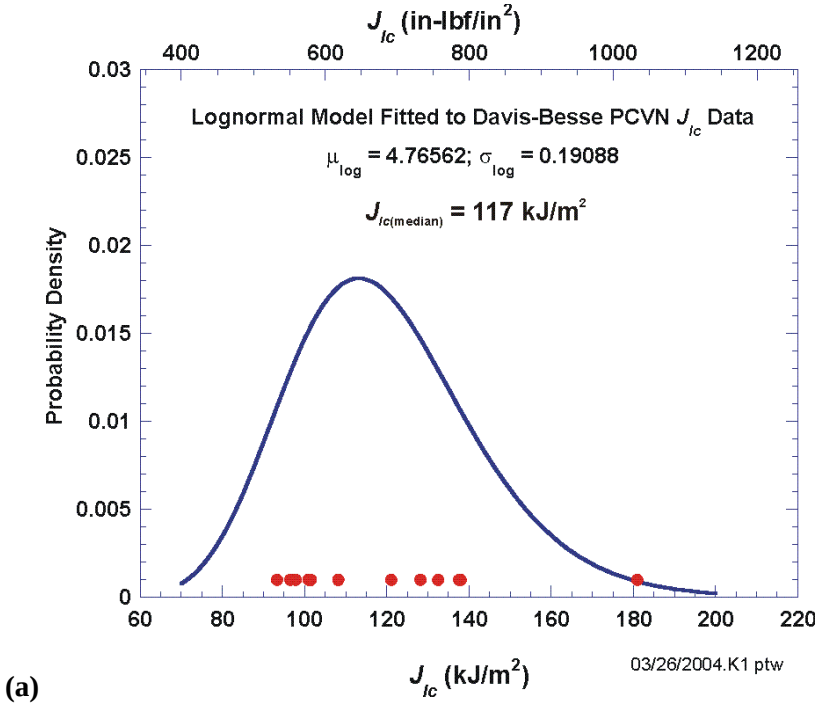

(a)

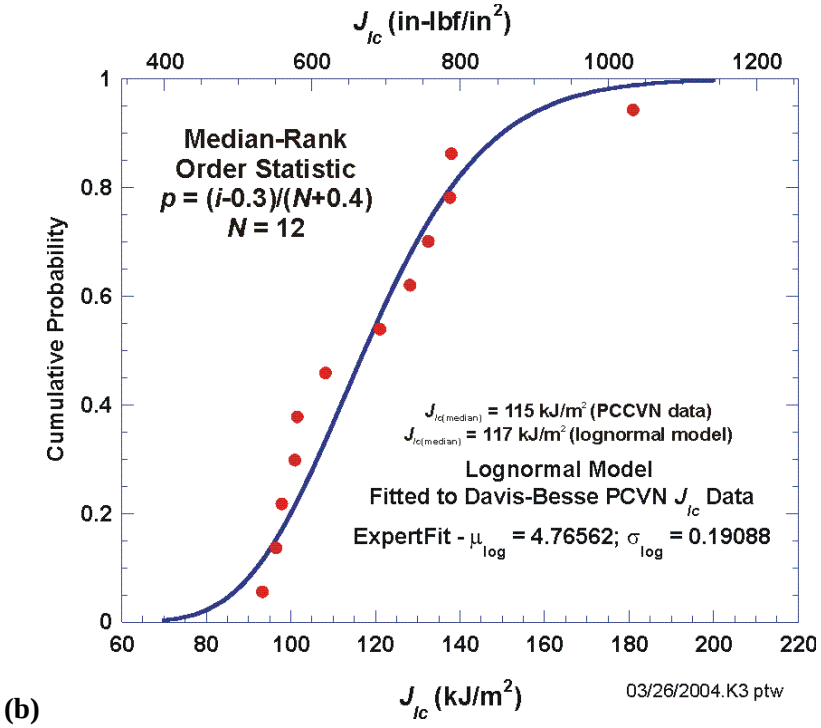

(b)

Fig. 19. Statistical distributions for J_{Ic}: (a) probability density of lognormal distribution fitted to the 12 Davis-Besse PCCVN data points and (b) lognormal cumulative distribution function compared to cumulative probabilities of Davis-Besse PCCVN J_{Ic} data estimated by the median rank order statistic $p = (i-0.3)/(n+0.4)$.

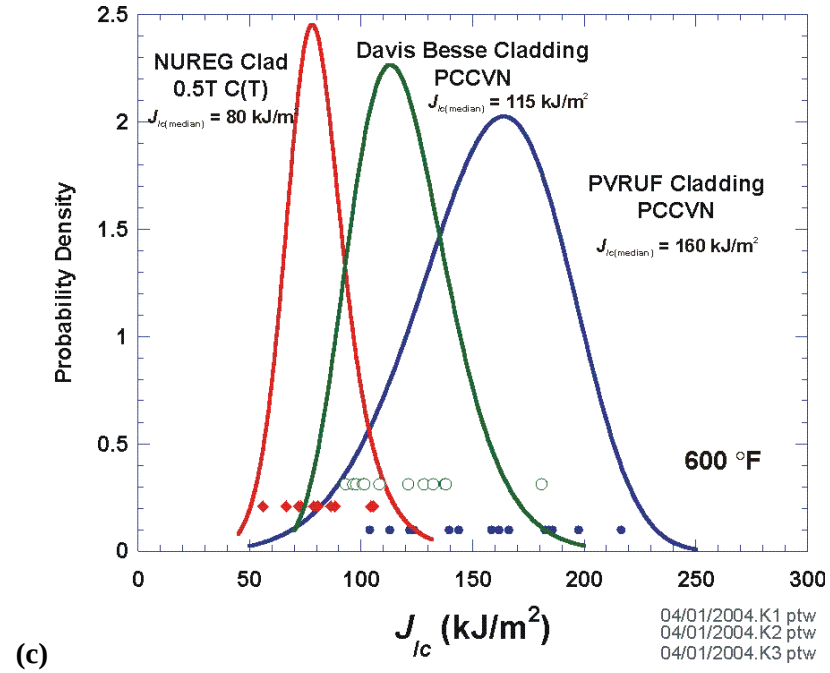

(c)

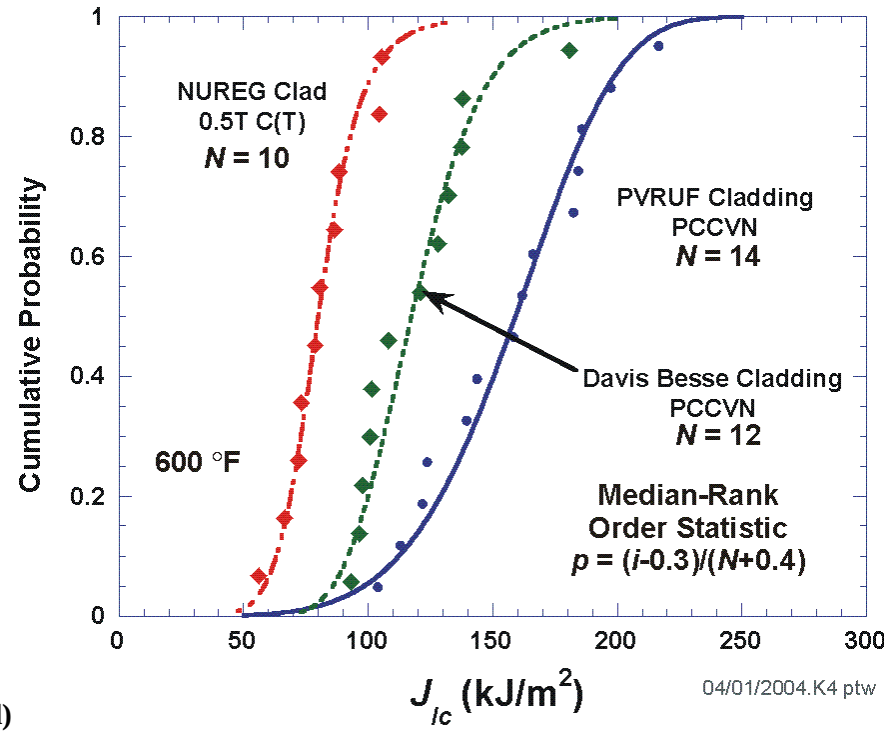

(d)

Fig. 19. (continued) fitted distributions for separate samples of J_{Ic} data from 0.5T C(T) clad overlay (NUREG/CR-5511 and 6363) and PCCVN specimens from PVRUF and Davis-Besse cladding materials: (c) probability densities and (d) cumulative distribution functions.

2.2.4.1 Ductile-Tearing Instability Analyses

At a test temperature of 288 °C (550 °F), J_R curves are available in [35] for three ½ C(T) (20% side grooved) unirradiated fracture specimens. One irradiated test is available at this test temperature but was not used in the analysis, since in the Davis-Besse problem the location of the wastage cavity is far away from the beltline of the RPV and, therefore, is only marginally affected by irradiation. The data-fitted J_R curves from [35] and from the PCCVN Davis-Besse specimens are presented in Fig. 20. The applied driving-force curves calculated from finite-element models (see Fig. 21) for a range of flaw depths (all with 2.0 inch long surface flaws centered in the "As-Found" burst disk model) are shown in Fig. 22. The results from Fig. 20 and 22 can be used to carry out a tearing-instability analysis based on the theory described in [37].

2.2.4.1.1 A-Tip Ductile-Tearing Instability

Two *J-T* A-tip instability analyses are shown in Figs. 23 and 24. Tearing-instability theory [37] employs *J-T* curves to define regions of stable and unstable ductile tearing. The J_R-T_R material curves are constructed from *JR* data for a given material at a specified test temperature where the tearing modulus is defined in [37] by

$$T_R = \frac{E}{\sigma_0^2}\left(\frac{dJ_R}{da}\right)\Bigg|_{J=J_R} \tag{32}$$

The applied tearing moduli are calculated numerically from finite-element results in Fig. 22 such that

$$T_{applied} = \frac{E}{\sigma_0^2}\left(\frac{\partial J}{\partial a}\right)\Bigg|_{J=J_{applied}} \tag{33}$$

The differentiation required in Eq. (33) was carried out using central, forward, and backward 2nd-order finite-difference ratios derived for unequal partitions. From the theory discussed in [37], ductile tearing of a given flaw is predicted to become unstable when two conditions are met:

$$J_{applied} \geq J_R \quad \text{and} \quad T_{applied} \geq T_R \tag{34}$$

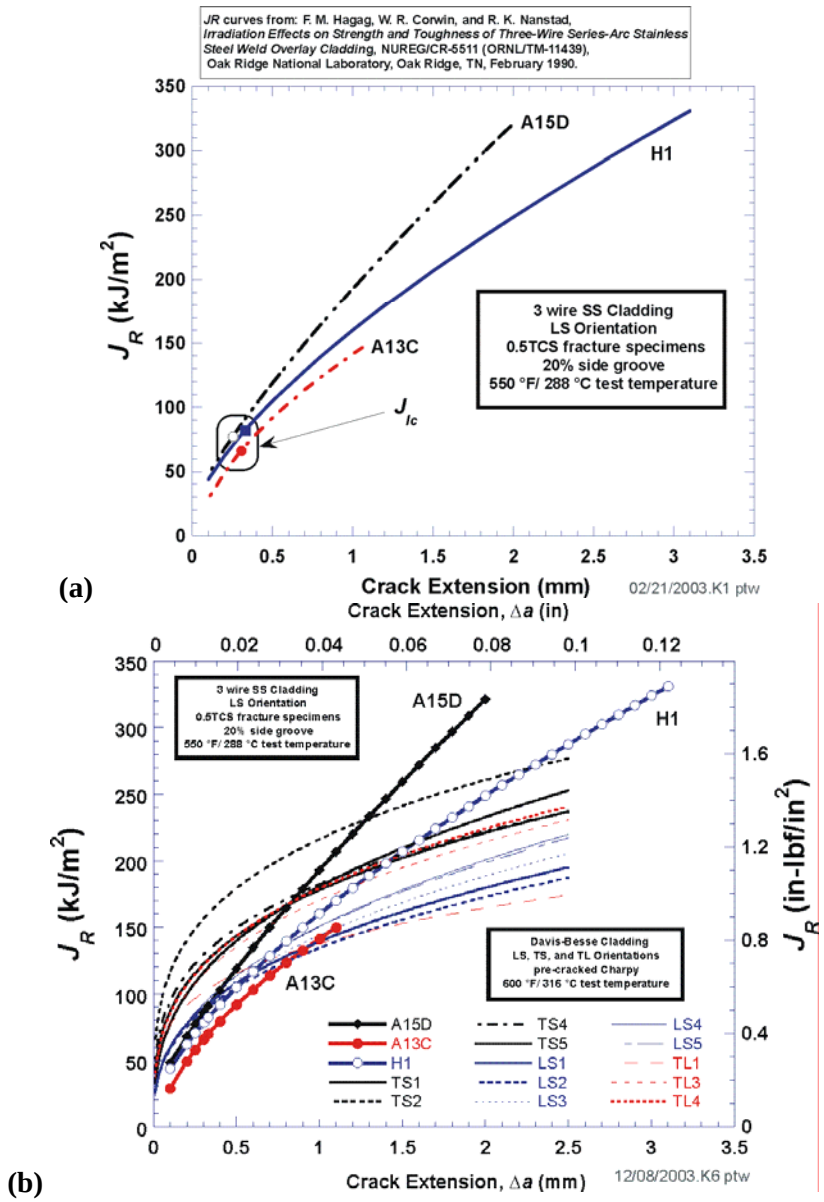

Fig. 20. J_R curves (a) fitted from data available in ref. [1] for unirradiated 0.5TCS fracture specimens at 550 °F and (b) comparing NUREG/CR C(T) J_R curves with PCCVN J_R curves.

A region of instability is therefore defined in (J,T) space to the right of an experimentally-derived (J_R,T_R) curve. A flaw becomes unstable when its ($J_{applied}$,$T_{applied}$) locus intersects a material's (J_R,T_R) curve.

In Fig. 23 two applied pressures are examined, the nominal operating pressure of 2.165 ksi and the relief-valve setpoint pressure of 2.5 ksi. A range of flaw depths were also investigated. At the operating pressure, flaws with depths up to at least 0.0625 in. are predicted to be stable from the data from all three test specimens. At the set-point pressure, the flaw at a depth of 0.0625 in. is predicted to be unstable from the most conservative of the three test specimens, A13C.

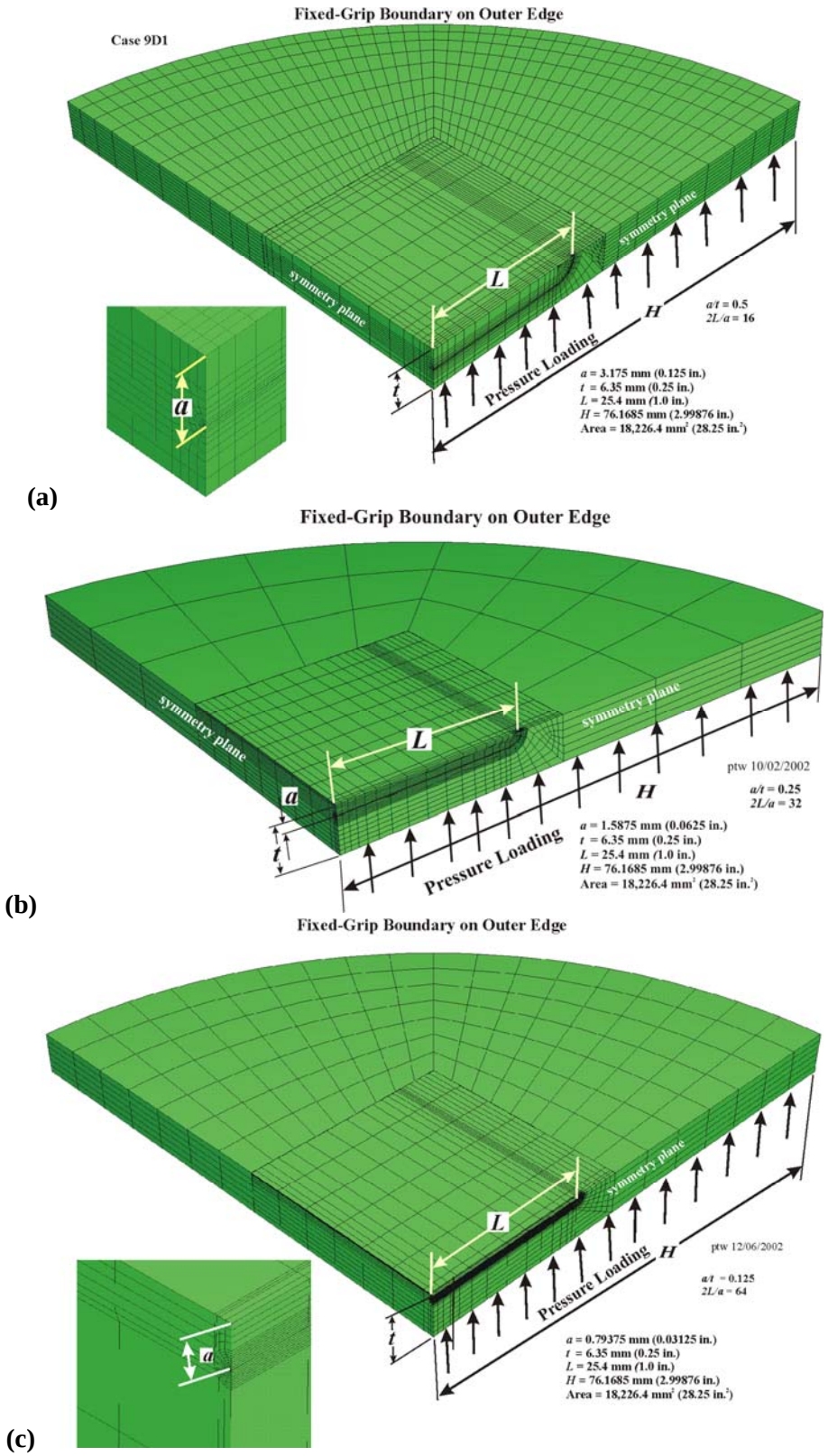

Fig. 21. Finite-element models used in calculating applied *J*-integrals produced by pressure loading of burst disk: (a) (a/t = 0.5, $2L/a$ = 16) (b) (a/t = 0.25, $2L/a$ = 32), and (c) (a/t = 0.125, $2L/a$ = 64)

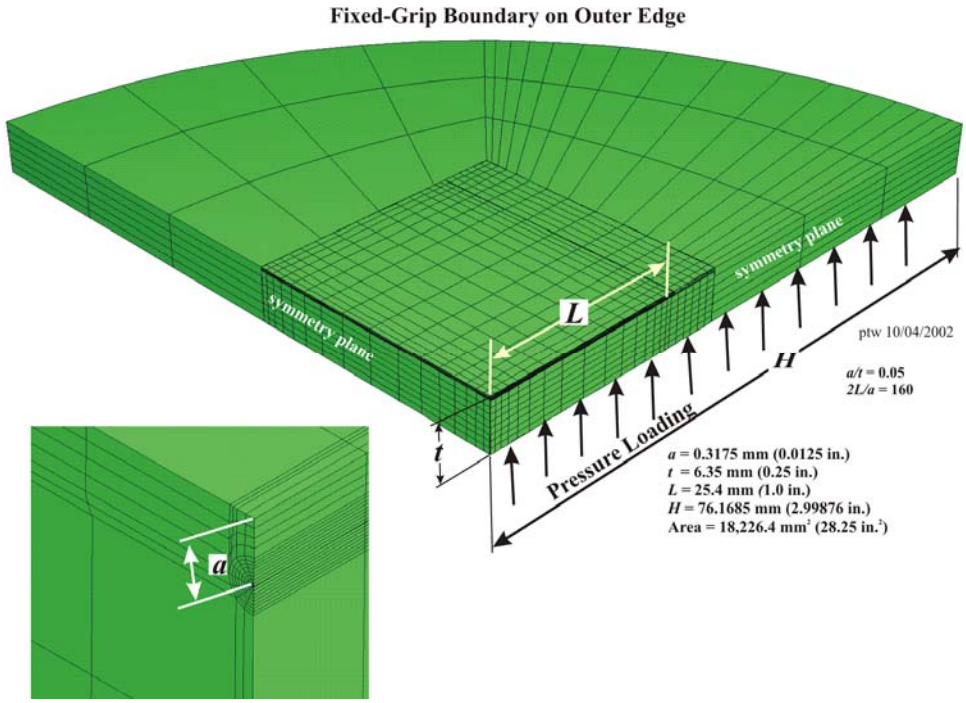

(d)

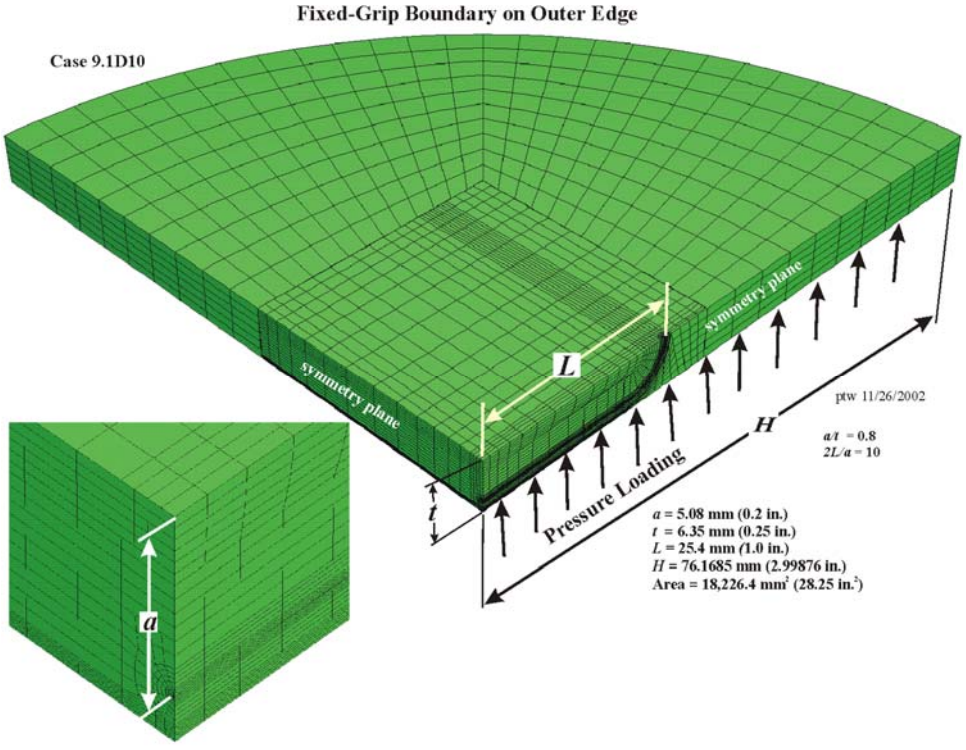

(e)

Fig. 21. (continued) Finite-element models used in calculating applied *J*-integrals produced by pressure loading of burst disk: (d) (*a*/*t* = 0.05, 2*L*/*a* = 160) (e) (*a*/*t* = 0.8, 2*L*/*a* = 10)

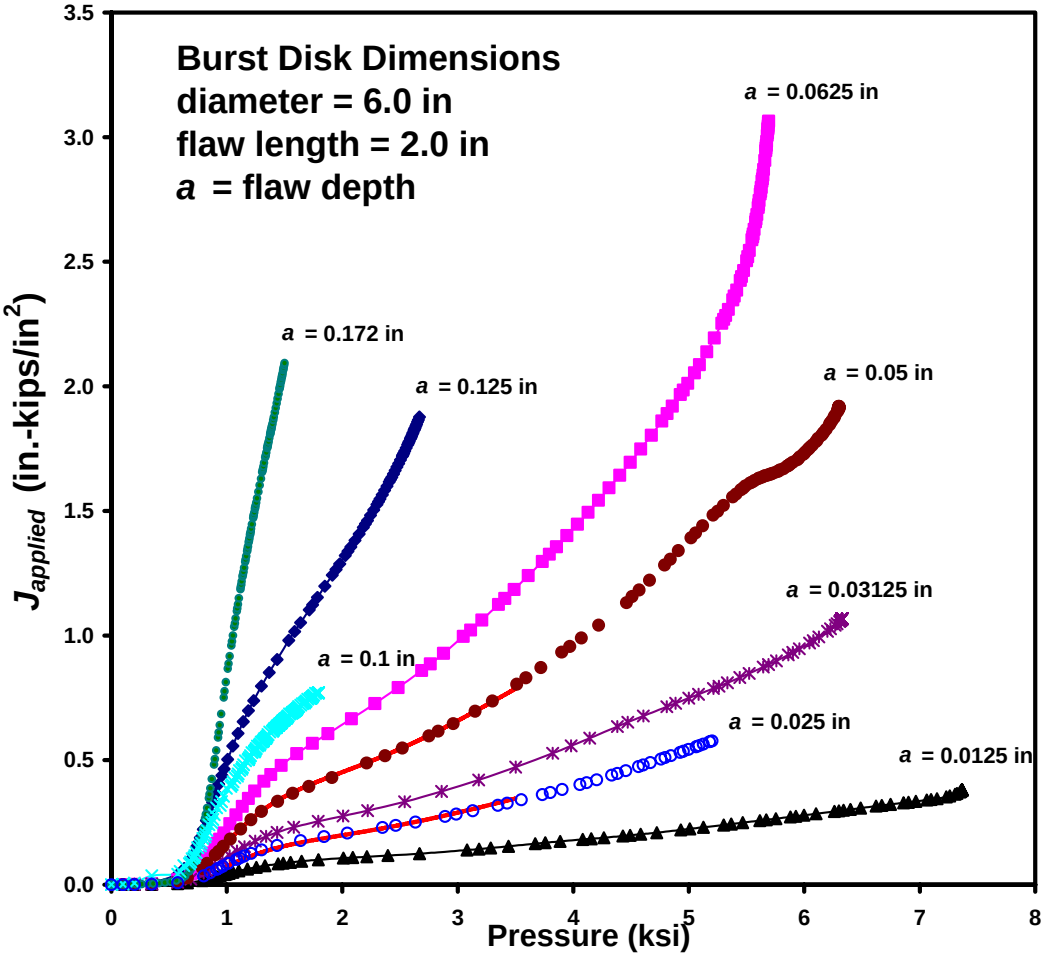

Fig. 22. *J-integral* driving forces – applied pressure as a function of J_I and *a/t* for a 2-inch long flaw.

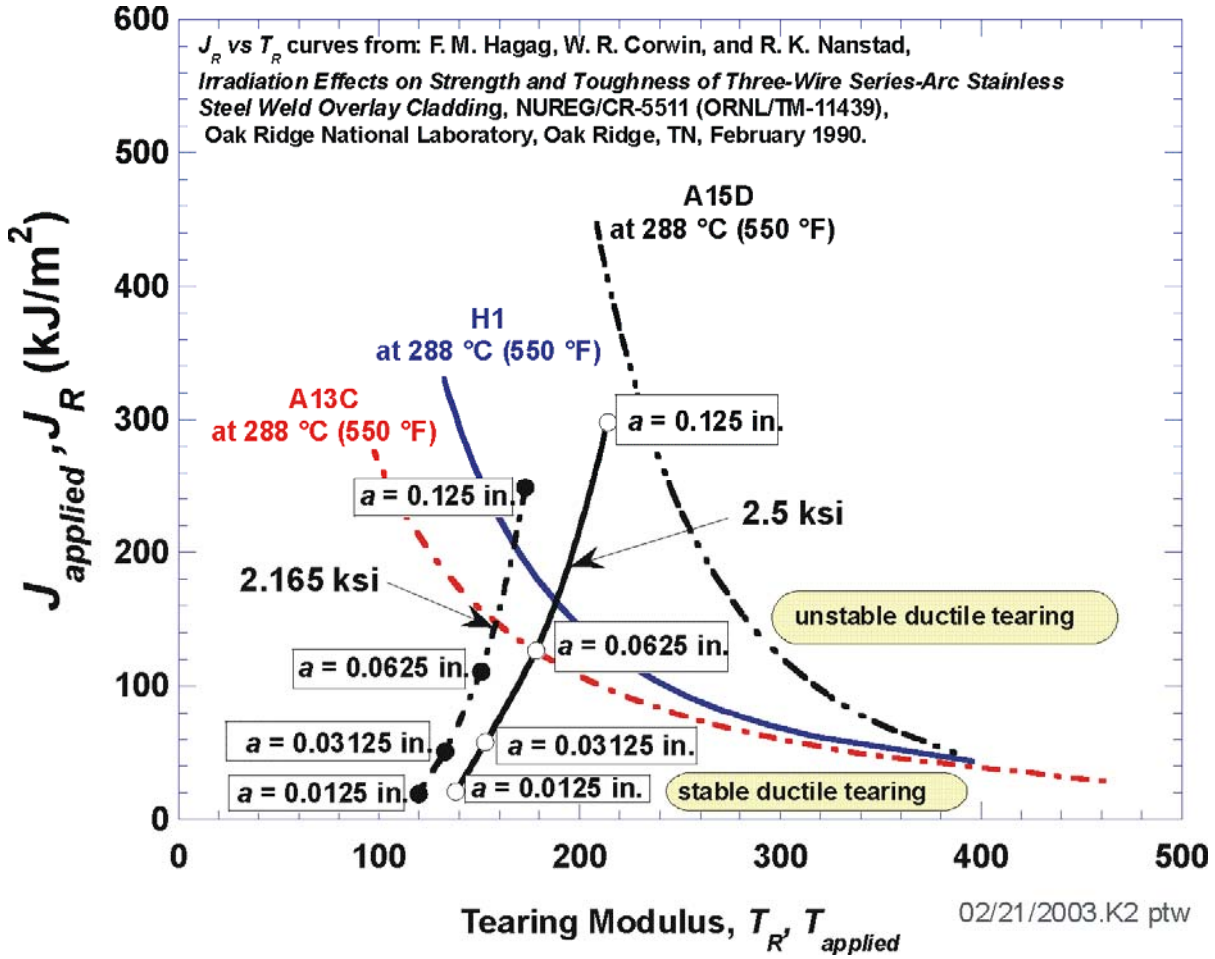

Fig. 23. A-tip tearing instability plots with J_R vs T_R curves from ref. [35] and $J_{applied}$ vs $T_{applied}$ curves from finite-element simulations of burst disks with 2-inch long surface flaws centered in the burst disk. Applied *J-T* curves are for two applied pressures (the nominal operating pressure of 2.165 ksi and the relief-valve setpoint pressure of 2.5 ksi) with varying flaw depths 0.0125 in. $\leq a_{A\text{-}tip} \leq$ 0.125 in.

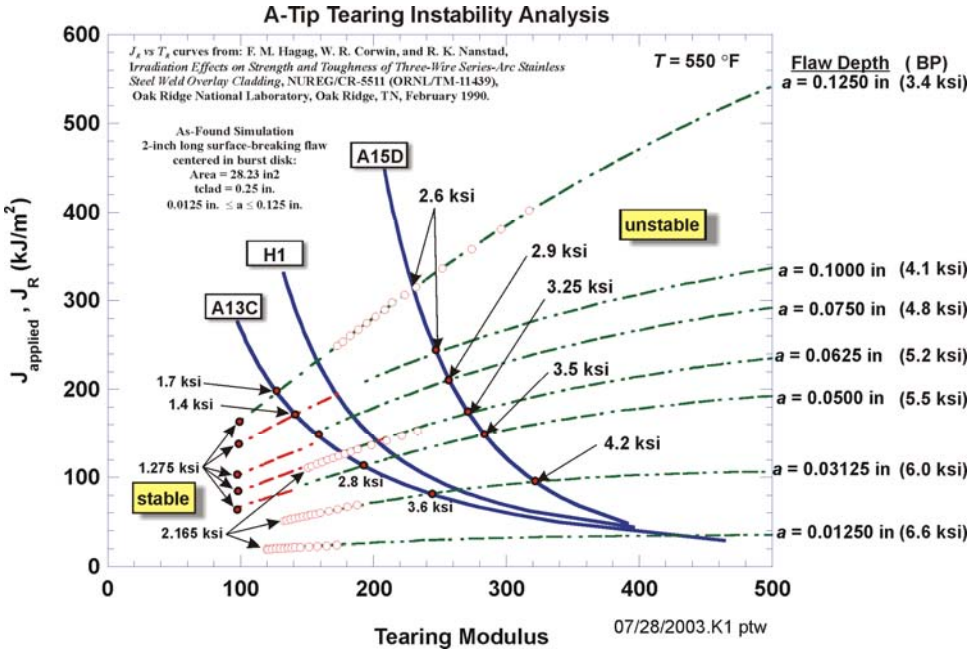

Fig. 24. A-tip tearing instability plots with J_R vs T_R curves from ref. [35] and $J_{applied}$ vs $T_{applied}$ curves from finite-element simulations of burst disks with 2-inch long surface flaws centered in the burst disk. Applied J-T curves are for a range of flaw depths ($0.0125 \text{ in.} \le a \le 0.125 \text{ in.}$ **) and varying applied pressures.**

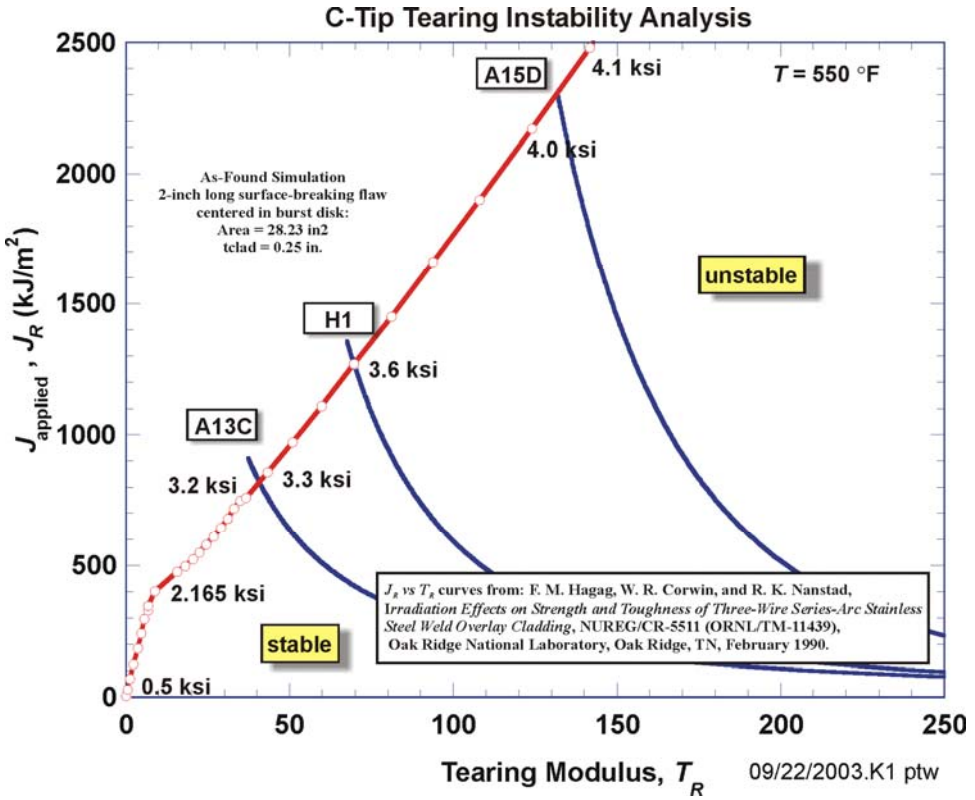

Fig. 25. C-tip tearing instability plots with J_R vs T_R curves from ref. [35] and $J_{applied}$ vs $T_{applied}$ curves from finite-element simulations of burst disks for "As-Found" flaw with initial 2-inch long with A-tip collapse.

In Fig. 24, seven flaws (at depths of $0.0125\text{ in.} \le a \le 0.125\text{ in.}$) are exposed to a range of applied pressures. Above approximately 2.6 ksi, the deepest flaw is predicted to fail by plastic collapse at a burst pressure of 3.4 ksi. The other six flaws all fail by plastic collapse at pressures higher than 3.4 ksi. The smaller flaw (a = 0.0125 in.) is seen to remain stable in Fig. 24 over the full range of applied pressures based on all three test specimens.

2.2.4.2 C-Tip Ductile-Tearing Instability

Figure 25 presents the results of a tearing-instability analysis of the C-tip of the model flaw after the assumed collapse of the A-tip's remaining ligament for the "As-Found" condition. This analysis indicates that for pressures below approximately 3.25 ksi, the C-tip will not experience unstable ductile tearing.

The wastage-area damage model analysis carries out a C-tip ductile-tearing instability analysis after failure of the A-tip remaining ligament by plastic collapse. A series of finite-element models (see Fig. 26a for an example) were constructed for varying values of R_{cavity} with a failed A-tip flaw with constant $2L$ = 2.0 in. Each model was loaded up to an applied pressure of 2.165 ksi, corresponding to the nominal operating pressure of the Davis-Besse RPV. The resulting applied driving forces, $J_{applied}$, and driving force gradients, dJ/da, are shown in Figs. 26b and 26c, respectively, for a range of cavity radii.

To apply the tearing-instability test of Eq. (34), estimates of the cladding's tearing modulus, T_R, must be developed as a function of J_R. If the J_R curves of Fig. 20 can be characterized by the power-law form

$$J_R = C(\Delta a^m) \tag{35}$$

then the local material tearing modulus, T_R, is from Eq. (32)

$$T_R = \left(\frac{E}{\sigma_f^2}\right)\left(\frac{dJ_R}{da}\right) = \left(\frac{E}{\sigma_f^2}\right) \times m \times C \times \Delta a^{(m-1)} \tag{36}$$

Given the elastic modulus, E, and estimated flow stress, σ_f, the remaining three variables required by the ductile-tearing model are J_{Ic}, C, and m. Applying the definition of J_{Ic} in ASTM E-1820 [38], sampled estimates of two of these parameters (J_{Ic} and m) allows the calculation of the third parameter, C. In Fig. 27, the ductile-tearing initiation toughness, J_{Ic}, is defined in ASTM E-1820 as the intersection of the J_R curve with a 0.2 mm offset blunting line given by

$$J_{(0.2\text{ mm offset})} = 2\sigma_f(\Delta a - \Delta a_0) \tag{37}$$

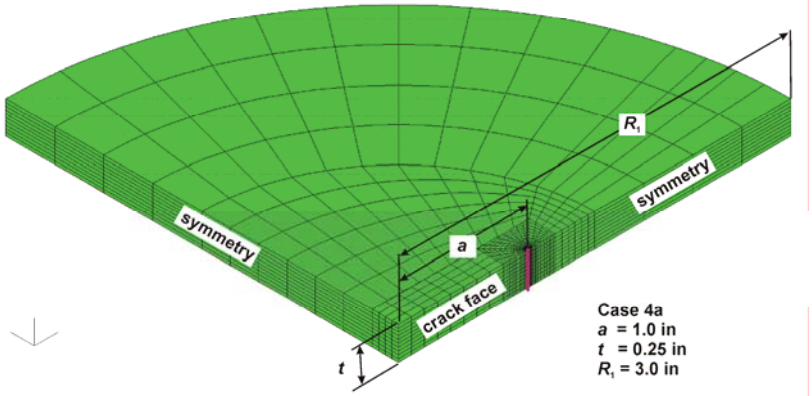

(a)

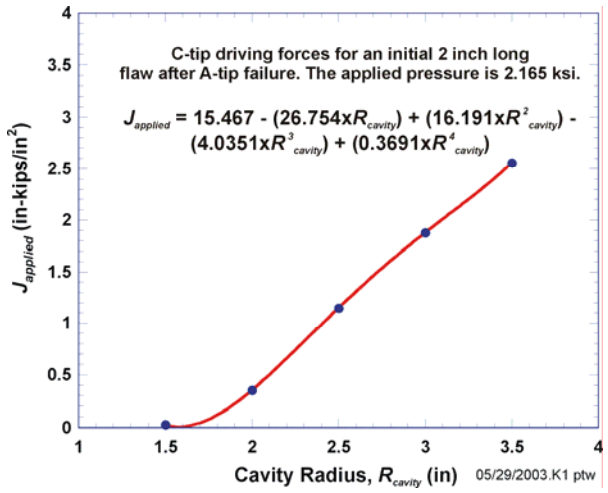

(b)

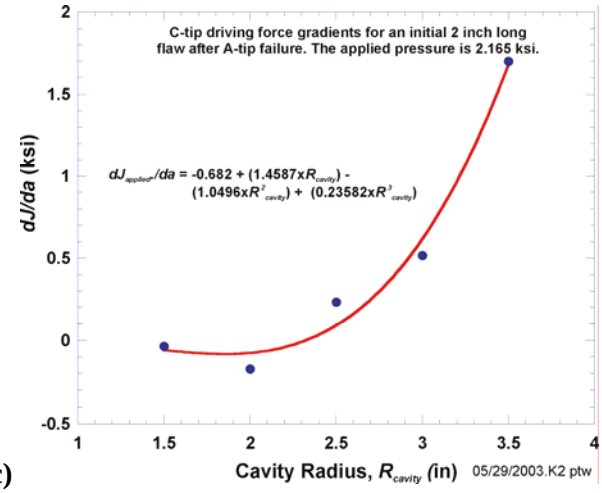

(c)

Fig. 26. Driving-force curves used in C-Tip ductile-tearing instability analyses: (a) models were developed for varying R_{cavity} and constant $2L = 2a = 2.0$ in, $t_{clad} = 0.25$ in., (b) applied driving force $J_{applied}$ at C-tip at 2.165 ksi for varying R_{cavity}, and (c) applied dJ/da at C-tip at 2.165 ksi for varying R_{cavity}.

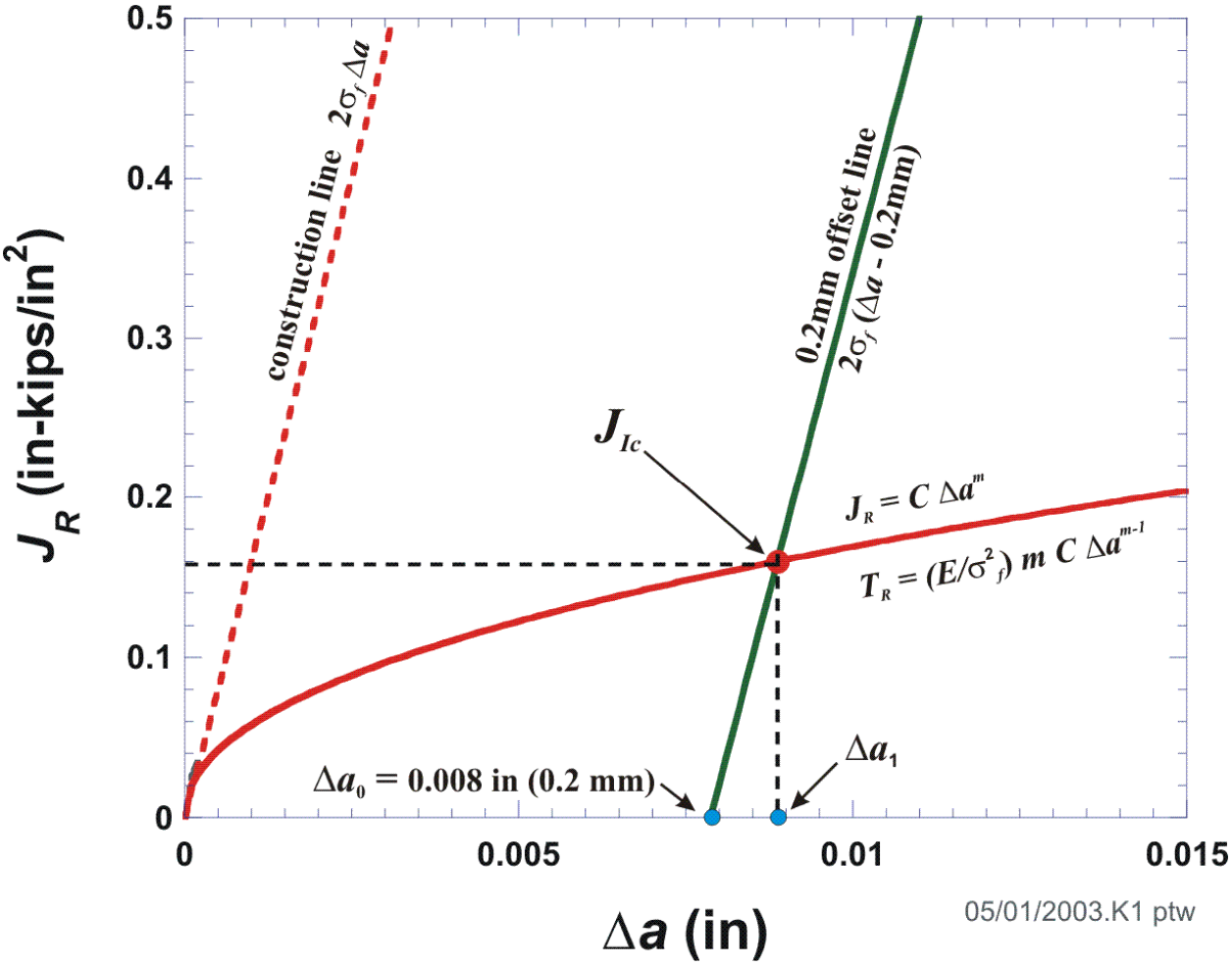

Fig. 27. Given a J_R curve in power-law model form and estimated flow stress, σ_f, the initiation toughness, J_{Ic}, and local tearing modulus, T_R, are uniquely defined (see ASTM E-1820).

where the prescribed offset is $\Delta a_0 = 0.2$ mm (0.008 in). Therefore, with an estimate of J_{Ic} and the power-law exponent, *m*, the power-law coefficient, *C*, is

$$J_{Ic} = C\Delta a^m \Rightarrow C = \frac{J_{Ic}}{\Delta a^m}$$

$$J_{Ic} = 2\sigma_f(\Delta a - \Delta a_0) \Rightarrow \Delta a = \frac{J_{Ic}}{2\sigma_f} + \Delta a_0 \tag{38}$$

$$\therefore \quad C = \frac{J_{Ic}}{\left(\frac{J_{Ic}}{2\sigma_f} + \Delta a_0\right)^m}$$

The local tearing modulus then follows from Eq. (36). In the wastage-area damage model, the values of J_{Ic} and *m* are sampled from a bivariate lognormal distribution to be described in Sect. 2.2.4.4.

2.2.4.3 Model for J_R Curve Power-Law Exponent, *m*

A lognormal distribution was developed to characterize the uncertainty in the power-law exponent, *m*, (see Eq. (35)) used in constructing a J_R vs Δa curve (see Fig. 28). A mean value for *m* of 0.68141 was estimated from specimen H1 in the data presented in NUREG/CR-5511 [35]. In Table B15(a) of NUREG/CR-6004 [22], a variance of 0.0159 is given for *m* for a stainless steel flux weld. Covariance data for correlated sampling of J_{Ic} and *m* are also presented in the Table B15(a):

Table B15(a): Stainless steel flux weld

$$\left[\hat{\Sigma}\right] = \begin{bmatrix} 2.756\times10^4 & -8.141 \\ -8.141 & 0.0159 \end{bmatrix};\ \mu_{J_{Ic}} = 194.65;\ \mu_m = 0.733;\ \text{and}$$

$$\rho_{12} = \frac{-8.141}{\sqrt{\left(2.756\times10^4\right)\left(0.0159\right)}} = -0.3889$$

log-transform of covariance matrix (39)

$$\hat{\Sigma}_{ij(\log)} = \ln\left(1 + \frac{\hat{\Sigma}_{ij}}{\left|\mu_i \mu_j\right|}\right)$$

$$\left[\hat{\Sigma}_{(\log)}\right] = \begin{bmatrix} 0.5466189 & -0.05875121 \\ -0.05875121 & 0.02916359 \end{bmatrix} \text{ and}$$

$$\rho_{12(\log)} = \frac{-0.05875121}{\sqrt{\left(0.5466189\right)\left(0.02916359\right)}} = -0.46532243$$

A lognormal correlation coefficient of -0.4653224 was calculated from the data in NUREG/CR-6004 and then applied in the construction of a lognormal bivariate distribution for sampling correlated (J_{Ic}, *m*) data pairs as described in the following section.

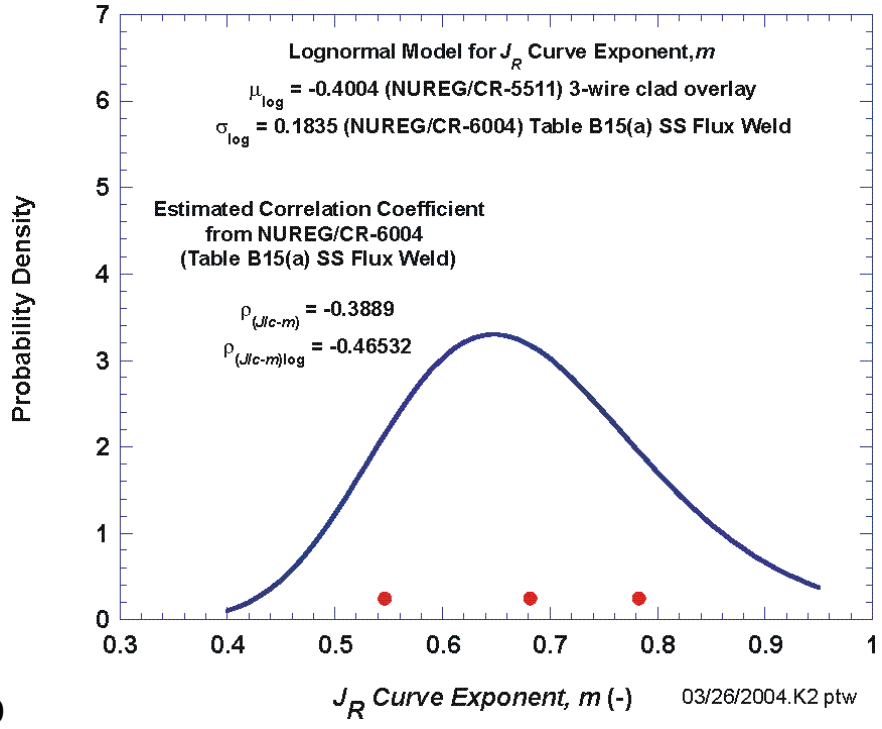

(a)

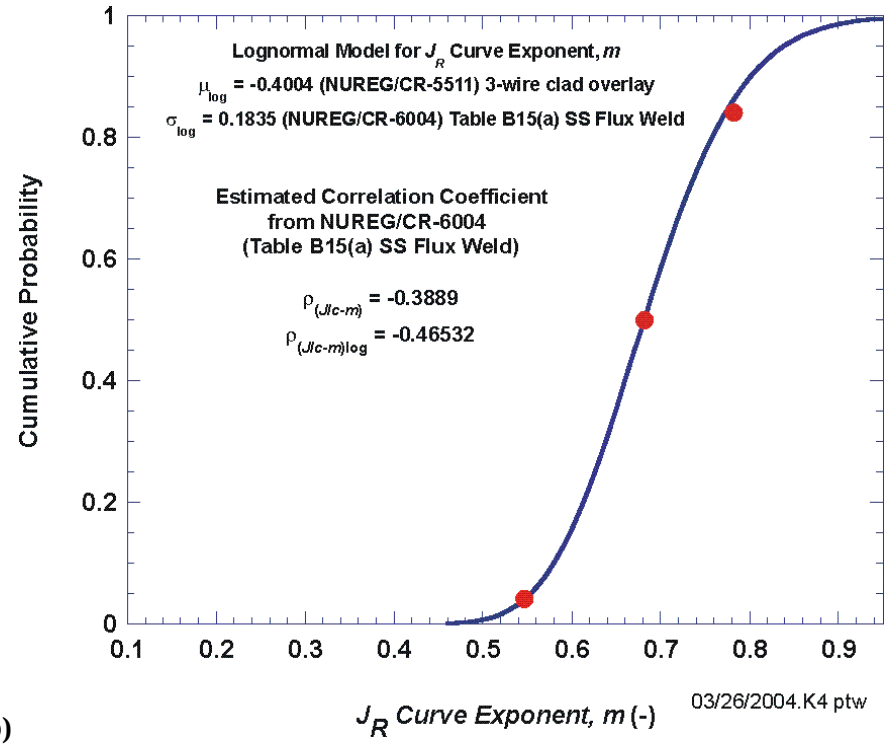

(b)

Fig. 28. Lognormal distribution characterizing the uncertainty in the J_R curve power-law exponent, *m*. The lognormal distribution with (a) probability density and (b) CDF has been fitted using a mean value from the data reported in NUREG/CR-5511 for overlay cladding and a variance from data in NUREG/CR-6004 for stainless steel flux weld.

2.2.4.4 Bivariate Lognormal Distribution – $\rho_{12} = -0.388901$; $\rho_{12(\log)} = -0.465322$ (correlation between J_{Ic} and m inferred from data in NUREG/CR-6004, Table B.15(a) for stainless steel flux weld)

The sampling of a multivariate lognormal random vector follows from the procedures discussed in [30, 31].

Estimate Log-Transformed Covariance Between J_{Ic} and m

The first step requires the estimation of the log-transformed covariance between J_{Ic} and m. From Fig. 19, $\sigma_{JIc(\log)} = 0.19088; \quad \therefore \ \sigma^2_{JIc(\log)} = 0.036435$ and from Fig. 28, $\sigma_{m(\log)} = 0.1835; \quad \therefore \ \sigma^2_{m(\log)} = 0.033672$

Applying the log-transformed correlation coefficient calculated in Sect. 2.2.4.3:

$$\text{cov}(J_{Ic}, m)_{(\log)} = \rho_{12(\log)} \sqrt{\sigma^2_{J_{Ic}(\log)} \sigma^2_{m(\log)}} = -0.0162981$$

where (40)

$\rho_{12(\log)} = -0.46532243$

Perform Cholesky Factorization

The second step is to carry out a Cholesky decomposition (factorization) of the log-transformed correlation matrix.

$$\hat{\Sigma}_{(2\times2)(\log)} = \begin{bmatrix} \sigma^2_{J_{Ic}(\log)} & \text{cov}(J_{Ic}, m)_{(\log)} \\ \text{cov}(J_{Ic}, m)_{(\log)} & \sigma^2_{m(\log)} \end{bmatrix} = \begin{bmatrix} 0.036435 & -0.0162981 \\ -0.0162981 & 0.033672 \end{bmatrix} \tag{41}$$

and

$$\Sigma_{2\times2(\log)} = CC^T$$

where C is the 2×2 lower triangular Cholesky factor

$$C = \begin{bmatrix} c_{11} & c_{12} \\ c_{21} & c_{22} \end{bmatrix} = \begin{bmatrix} 0.19088 & 0 \\ -0.08538 & 0.16242 \end{bmatrix}$$

Bivariate Sampling Protocol for $\{\tilde{J}_{Ic},\tilde{m}\}^T$

Finally, for a bivariate lognormal joint distribution, the protocol for the correlated sample $X_i=\{\tilde{J}_{Ic(i)},\tilde{m}_{(i)}\}^T$ is as follows:

$$\begin{aligned}
&\text{Given: } \mu_{J_{Ic}(\log)} = 4.76562;\ \mu_{m(\log)} = -0.4334;\\
&c_{11} = 0.19088,\ c_{22} = 0.16242;\ c_{21} = -0.08538\\
&\\
&\tilde{Z}_{1(i)} \leftarrow N(0,1); \tilde{Z}_{2(i)} \leftarrow N(0,1) \text{ where } \tilde{Z}_{1(i)} \text{ and } \tilde{Z}_{2(i)} \text{ are IID}\\
&\tilde{Y}_{1(i)} = \mu_{J_{Ic}(\log)} + \left(c_{11}\times \tilde{Z}_{1(i)}\right)\\
&\tilde{Y}_{2(i)} = \mu_{m(\log)} + \left(c_{21}\times \tilde{Z}_{1(i)}\right) + \left(c_{22}\times \tilde{Z}_{2(i)}\right)\\
&\tilde{X}_i = \begin{Bmatrix} \exp(\tilde{Y}_{1(i)}) \\ \exp(\tilde{Y}_{2(i)}) \end{Bmatrix} = \begin{Bmatrix} \widetilde{J_{Ic(i)}} \\ \widetilde{m_{(i)}} \end{Bmatrix}
\end{aligned} \tag{42}$$

where IID refers to *independent and identically distributed* random variates, and Z_1 and Z_2 are standard-unit-normal variates.

2.2.4.5 Driving Force ($J_{applied}$) Surface Function of ($a_{A\text{-}tip}$, R_{cavity})

Based on the results of a matrix of finite-element solutions for $J_{applied}$ as a function of varying $a_{A\text{-}tip}$ and R_{cavity}, a continuous surface function was fitted using TableCurve® 3D's *Selective Subset Algorithm* [39]. The resulting 7-parameter selective-subset surface function for a constant applied pressure of 2165 psi had the following form (see Fig. 29)

$$\begin{aligned}
\ln\left(J_{applied}\right) = C_0 + \frac{C_1}{\sqrt{a_{A-tip}}} + \frac{C_2}{a_{A-tip}} + C_3 R_{cavity} + C_4 R_{cavity} \ln\left(R_{cavity}\right) + \\
C_5\left[\ln\left(R_{cavity}\right)\sqrt{R_{cavity}}\right] + C_6\left[\ln\left(R_{cavity}\right)\right]^2
\end{aligned} \tag{43}$$

with R_{cavity} [in], $a_{A\text{-}tip}$ [in], and $J_{applied}$ [kJ/m^2] for 2.165 ksi applied lateral pressure.

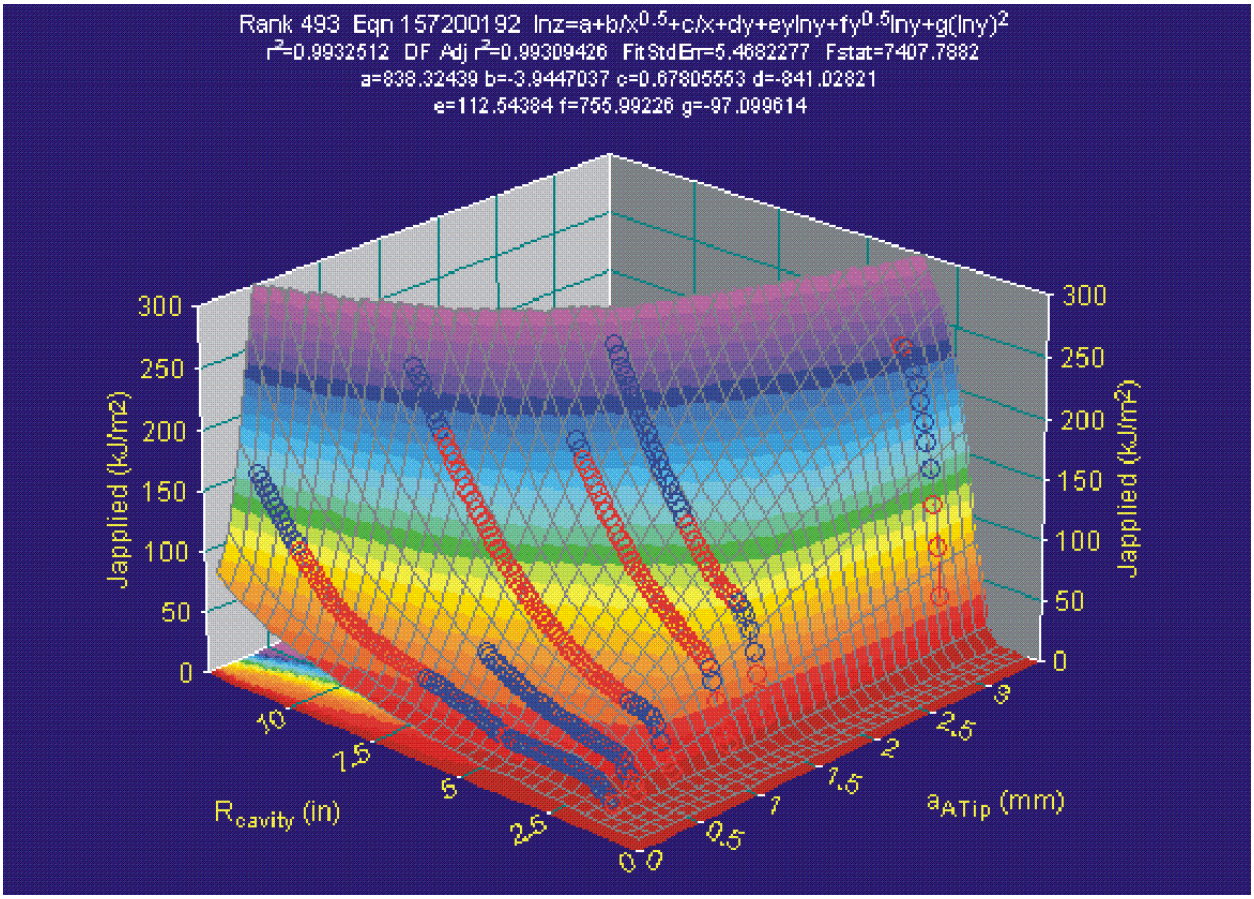

Fig. 29. Plot of $J_{applied}$ as a function of R_{cavity} and $a_{A\text{-}tip}$ for a burst disk with a 2 inch centered flaw under 2.165 ksi applied pressure. $J_{applied}$ solutions from FEM models (using best-estimate stress vs strain data) were fitted to a surface function by TableCurve® 3D.

or

$$J_{applied}\left(a_{A-tip},R_{cavity}\right)=\exp\left\{C_0+\frac{C_1}{\sqrt{a_{A-tip}}}+\frac{C_2}{a_{A-tip}}+C_3R_{cavity}+C_4R_{cavity}\ln\left(R_{cavity}\right)+C_5\left[\ln\left(R_{cavity}\right)\sqrt{R_{cavity}}\right]+C_6\left[\ln\left(R_{cavity}\right)\right]^2\right\}$$

$$\left.\frac{\partial J_{applied}\left(a_{A-tip},R_{cavity}\right)}{\partial a_{A-tip}}\right|_{R_{cavity}}=-\frac{1}{a_{A-tip}}\left(\frac{C_1}{2\sqrt{a_{A-tip}}}+\frac{C_2}{a_{A-tip}}\right)\exp\left\{C_0+\frac{C_1}{\sqrt{a_{A-tip}}}+\frac{C_2}{a_{A-tip}}+C_3R_{cavity}+C_4R_{cavity}\ln\left(R_{cavity}\right)+C_5\left[\ln\left(R_{cavity}\right)\sqrt{R_{cavity}}\right]+C_6\left[\ln\left(R_{cavity}\right)\right]^2\right\} \tag{44}$$

with the fitted parameters

$$\begin{aligned} C_0 &= 838.324387886275 \quad C_3 = \text{-}841.0282062799881 \\ C_1 &= \text{-}3.944703731724143 \quad C_4 = 112.5438397120073 \\ C_2 &= 0.6780555298560729 \quad C_5 = 755.9922572599784 \\ C_6 &= \text{-}97.09961384574772 \end{aligned} \tag{45}$$

and

$$\begin{aligned} & J_{applied} \left[\frac{\text{kJ}}{\text{m}^2}\right] \text{ or } \left[\frac{\text{N}}{\text{mm}}\right] \\ & a_{A-tip} \ [\text{mm}] \\ & R_{cavity} \ [\text{in.}] \end{aligned} \tag{46}$$

2.2.5 Assumed Wastage-Area Damage Model Accident Sequence

As previously discussed, an *accident sequence* is a combination of events leading from an *initiating event* to an undesired *consequence*. The sequence is ordered, starting with the initiating event, and proceeds through sequential failures leading to the *consequence* [3]. The *consequences* in this study are formulated in terms of *loss-of-coolant-accidents* (LOCAs) ranked by break size. The time-line for this analysis is shown in Fig. 30, where seven distinct time stations are identified: (1) $\tau_{cavity\text{-}ini}$, the time when the wastage cavity initiates, (2) $\tau_{flaw\text{-}ini}$, the time when the flaw initiates, (3) τ_0 , one year before the discovery of the wastage cavity, (4) $\tau_{DT\text{-}ini}$, the time of ductile-tearing initiation, (5) τ_1, the time of discovery (February-March, 2002), (6) τ_2, six weeks after the time of discovery, and (7) τ_3, one year after the time of discovery. With the inclusion of the ductile-tearing model into the analysis, an additional time station is introduced into the problem, the time of initiation of ductile tearing, $\tau_{DT\text{-}ini}$.

For the Davis-Besse Wastage-Area Damage Model, the *damage state* {now defined by the five parameters [R_{cavity}, $a_{A\text{-}tip}$, $J_{applied}(a_{A\text{-}tip}, R_{cavity})$, $T_{applied}(a_{A\text{-}tip}, R_{cavity})$, T_R] at different points in time} can be calculated from sampled values for the cavity growth rate, $dR_{cavity}/d\tau$, flaw growth rate, $da_{A-tip}/d\tau$, and ductile-tearing initiation fracture toughness, J_{Ic}.

2.2.5.1 Cladding-Capacity Analysis – Damage State Determination (without A-tip ductile tearing)

In the *cladding-capacity* analysis, the "as-found" damage state is assumed known to a sufficient degree of certainty that the (R_1, a_1) is represented by a fixed point (see Fig. 31) where at τ_1

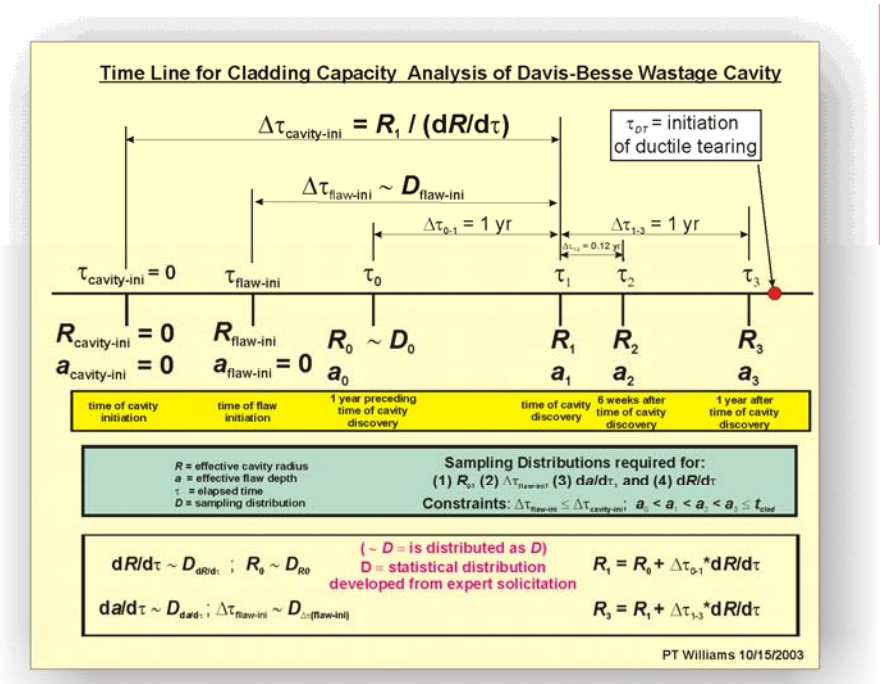

Fig. 30. Time line for cladding capacity analysis – accident sequence of wastage-area damage model.

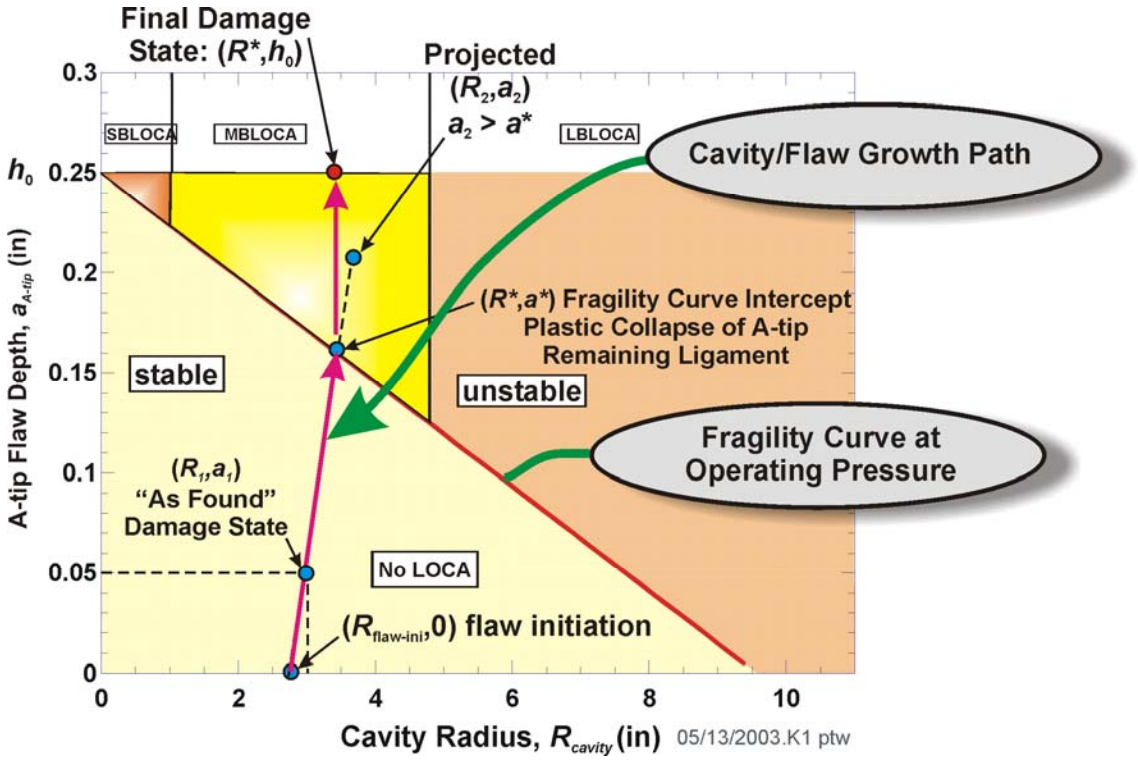

Fig. 31. For the "cladding-capacity" analysis, the "As-Found" damage state is assumed known and fixed. For constant cavity and flaw growth rates, the accumulation of damage follows, in the absence of ductile tearing, a linear path towards the fragility curve.

$$R_1 = 2.443 \text{ inches; corresponding to an unbacked wastage area of } 18.75 \text{ in}^2$$
$$a_1 = 0.065 \text{ inches; corresponding to current best-estimate of prototypic flaw depth} \tag{47}$$

Cavity growth rates, $dR_{cavity}/d\tau$, and flaw *A-tip* growth rates, $da_{A-tip}/d\tau$, are then sampled[8] from statistical distributions derived from an *Expert Elicitation* process to be discussed.

$$\frac{dR_{cavity}}{d\tau} \sim D_{(dR/d\tau)}$$
$$\frac{da_{A-tip}}{d\tau} \sim D_{(da/d\tau)} \tag{48}$$

The elapsed time since cavity initiation, $\Delta\tau_{cavity-ini}$, can then be calculated from the known value for R_1 by

$$\Delta\tau_{cavity-ini} = \frac{R_1}{\left(\frac{dR_{cavity}}{d\tau}\right)} \tag{49}$$

The elapsed time since flaw initiation, $\Delta\tau_{flaw-ini}$, is calculated from the time required to grow the flaw at τ_1 and is constrained to be no greater than the elapsed time since cavity initiation, $\Delta\tau_{cavity-ini}$,

$$\Delta\tau_{flaw-ini} = \min\left[\frac{a_1}{\left(\frac{da_{A-tip}}{d\tau}\right)}, \Delta\tau_{cavity-ini}\right] \tag{50}$$

The damage state at the time of flaw initiation, $\left(R_{flaw-ini}, 0\right)$, is then

$$R_{flaw-ini} = R_1 - \left(\Delta\tau_{flaw-ini} \times \frac{dR_{cavity}}{d\tau}\right)$$
$$a_{flaw-ini} \equiv 0 \tag{51}$$

The damage states at τ_2 and τ_3 are calculated by

$$R_2 = R_1 + \left(\Delta\tau_2 \times \frac{dR_{cavity}}{d\tau}\right)$$
$$a_2 = a_1 + \left(\Delta\tau_2 \times \frac{da_{A-tip}}{d\tau}\right) \tag{52}$$

[8] The notation $\widehat{X} \sim D$ should be read as "the random variate, X, is distributed as the statistical distribution *D*."

$$R_3 = R_1 + \left(\Delta\tau_3 \times \frac{dR_{cavity}}{d\tau} \right)$$
$$a_3 = a_1 + \left(\Delta\tau_3 \times \frac{da_{A-tip}}{d\tau} \right) \tag{53}$$

where $\Delta\tau_2$ and $\Delta\tau_3$ have been previously defined

$$\Delta\tau_2 \equiv \frac{6}{52} = 0.11538 \text{ year}$$
$$\Delta\tau_3 \equiv 1 \text{ year} \tag{54}$$

2.2.5.2 Cladding-Capacity Analysis – Damage State Determination (with A-tip ductile tearing)

As discussed in Sect. 2.2.5.1, the "as-found" damage state in the *cladding-capacity* analysis is assumed known to a sufficient degree of certainty that the (R_1, a_1) is represented by a fixed state point as shown in Fig. 32. For this purely illustrative example, we selected the values $R_1 = 3$ inches; $a_1 = 0.05$ inches.

Cavity growth rates, $dR_{cavity}/d\tau$, and flaw *A-tip* growth rates, $da_{A-tip}/d\tau$, are then sampled from statistical distributions derived from an *Expert Elicitation* process.

$$\widehat{\frac{dR_{cavity}}{d\tau}} \sim D_{(dR/d\tau)}$$
$$\widehat{\frac{da_{A-tip}}{d\tau}} \sim D_{(da_{A-tip}/d\tau)} \tag{55}$$

The position of the model flaw tip is assumed to be a function of the contribution due to the elapsed time of exposure to the corrosive environment after cavity initiation, $a_{A\text{-}tip(\text{env})}$, and possibly due to a contribution from stable ductile tearing

$$a_{A-tip} = \begin{cases} a_{A-tip(env)} + a_{A-tip(DT)} & \text{for } J_{applied}\left(a_{A-tip}, R_{cavity}\right) \geq J_{Ic} \\ a_{A-tip(env)} & \text{for } J_{applied}\left(a_{A-tip}, R_{cavity}\right) < J_{Ic} \end{cases} \tag{56}$$

where

$$a_{A-tip(env)}(\tau) = \left(\tau - \tau_{flaw-ini}\right)\widehat{\frac{da_{A-tip}}{d\tau}} \tag{57}$$

The elapsed time since cavity initiation, $\Delta\tau_{cavity-ini}$, is calculated from the known value for R_1 by

$$\Delta\tau_{cavity-ini} = \left(\tau_1 - \tau_{cavity-ini}\right) = \frac{R_1}{\left(\widehat{\frac{dR_{cavity}}{d\tau}}\right)} \tag{58}$$

All elapsed times are measured relative to the time of cavity initiation, $\tau_{cavity\text{-}ini} = 0$.

Determination of the Time of Flaw Initiation, $\tau_{flaw\text{-}ini}$

If the damage state at $\tau_1 = R_1 / \left(dR_{cavity} / d\tau\right)$ is such that

$$J_{applied}(a_1, R_1) < J_{Ic} \tag{59}$$

then the time of flaw initiation is calculated directly by

$$\tau_{flaw-ini} = \tau_1 - \frac{a_1}{\left(\widehat{\frac{da_{A-tip}}{d\tau}}\right)} \tag{60}$$

However if $J_{applied}(a_1, R_1) \geq J_{Ic}$, then the time of flaw initiation, $\tau_{flaw-ini}$, is calculated as the solution to the following nonlinear equation

$$a_1 - (\tau_1 - \tau_{flaw-ini})\left(\frac{da_{A-tip}}{d\tau}\right) - \Delta a_{DT}(a_1, R_1) = 0$$

where (61)

$$\Delta a_{DT}(a,R) = \begin{cases} \left(\frac{J_{applied}(a,R)}{C}\right)^{\frac{1}{m}} - \left(\frac{J_{Ic}}{C}\right)^{\frac{1}{m}} & \text{for } J_{applied}(a,R) \geq J_{Ic} \\ 0 & J_{applied}(a,R) < J_{Ic} \end{cases}$$

where the sampled J_R curve has been offset such that, at the point of ductile tearing initiation, the apparent initial flaw extension due to blunting is ignored, and at $J_{applied} = J_{Ic}$, $\Delta a_{DT} = 0$.

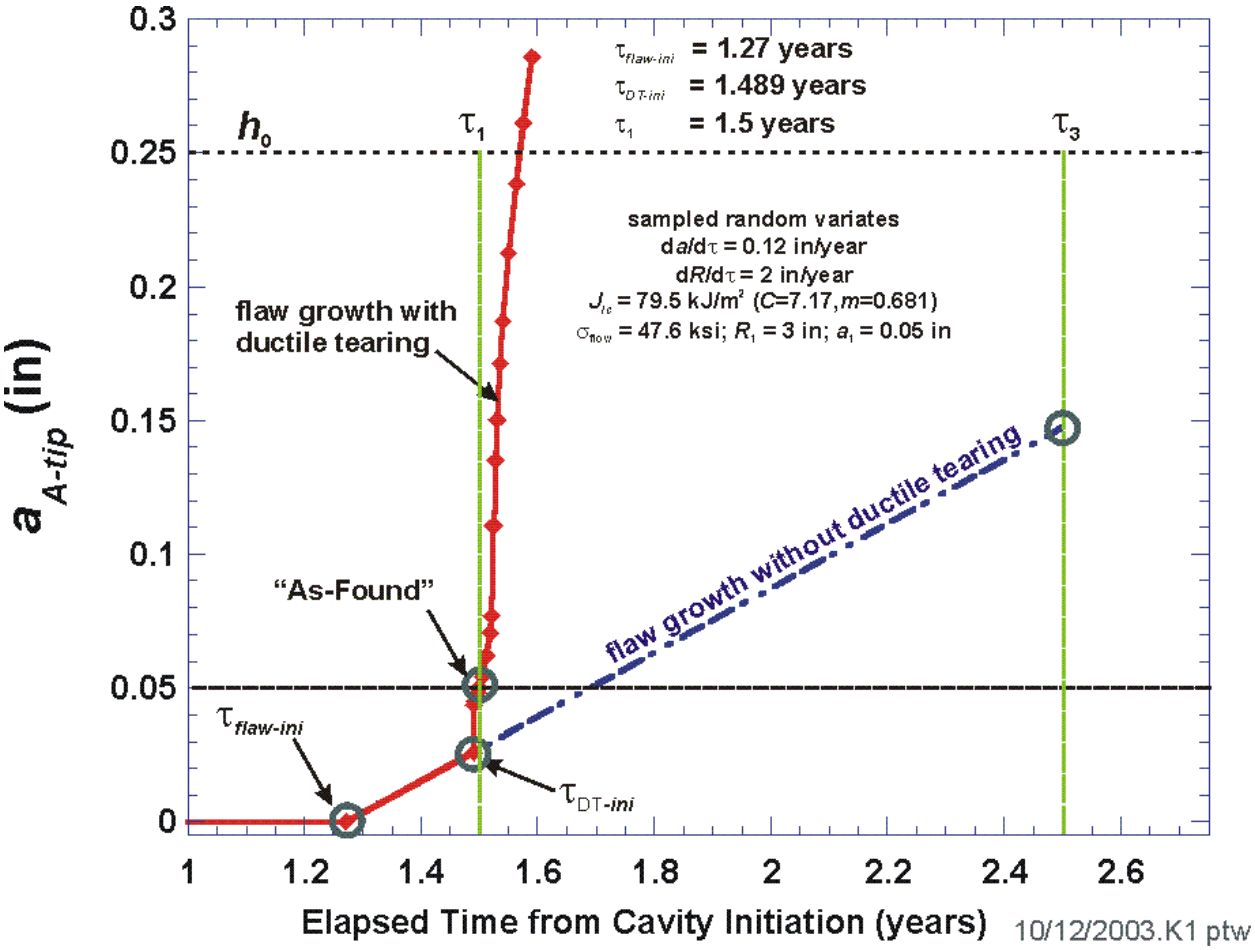

Fig. 32. An example flaw growth history (with ductile tearing) calculated using MathCad®. The case conditions are based on the median values from the more conservative (MC) sampling distribution for $dR/d\tau$, best-estimate distribution for $da/d\tau$, J_{Ic}, and m. The "As-Found" condition is assumed known (R_{cavity}, $a_{A\text{-}tip}$) = (3.0, 0.05) for this example case.

The elapsed time since flaw initiation, $\Delta\tau_{flaw-ini}$, (relative to cavity initiation) is constrained to be no greater than the elapsed time since cavity initiation, $\Delta\tau_{cavity-ini}$,

$$\Delta\tau_{flaw-ini(c)} = \min\left[\Delta\tau_{flaw-ini}, \Delta\tau_{cavity-ini}\right]$$
$$\text{or} \qquad (62)$$
$$\tau_{flaw-ini} \geq 0; \tau_{cavity-ini} \equiv 0$$

Determination of the Time of Ductile-Tearing Initiation, $\tau_{DT\text{-}ini}$

The time of ductile-tearing initiation, $\tau_{DT\text{-}ini}$, is calculated by solving the following system of nonlinear equations

$$J_{Ic} - J_{applied}\left(a_{A-tip(DT-ini)}, R_{cavity}\left(\tau_{DT-ini}\right)\right) = 0$$

$$a_{A-tip(DT-ini)} - \left[\left(\tau_{DT-ini} - \tau_{flaw-ini}\right)\widehat{\frac{da_{A-tip}}{d\tau}}\right] - \left\{\left[\frac{J_{applied}\left(a_{A-tip(DT-ini)}, R_{cavity}\left(\tau_{DT-ini}\right)\right)}{C}\right]^{\frac{1}{m}} - \left[\frac{J_{Ic}}{C}\right]^{\frac{1}{m}}\right\} = 0$$

for the flaw tip position, $a_{A\text{-}tip(DT\text{-}ini0}$, and $\tau_{DT\text{-}ini}$.

Determination of the flaw-tip position, $a_{A\text{-}tip}$, for Times After Ductile-Tearing Initiation, $\tau_{DT\text{-}ini}$

After ductile-tearing has been initiated, flaw tip position, $a_{A\text{-}tip}$, can be calculated by solving the following nonlinear equation

$$a_{A-tip} - \left[\left(\tau - \tau_{flaw-ini}\right)\widehat{\frac{da_{A-tip}}{d\tau}}\right] - \left\{\left[\frac{J_{applied}\left(a_{A-tip}, R_{cavity}(\tau)\right)}{C}\right]^{\frac{1}{m}} - \left[\frac{J_{Ic}}{C}\right]^{\frac{1}{m}}\right\} = 0 \qquad (64)$$

where for a given time, $\tau > \tau_{DT\text{-}ini}$, $R_{cavity}(\tau) = \left(\tau - \tau_{cavity-ini}\right)\left(\widehat{\frac{dR_{cavity}}{d\tau}}\right)$.

Figures 32-34 present the results of an example case using the median values of $\widehat{da_{A-tip}/d\tau}$ and $\widehat{dR_{cavity}/d\tau}$ from their best-estimate (BE) distributions.

Another critical time to be determined is the point at which the flaw-cavity growth path intersects the fragility curve. This time, τ^*, is the solution of the following nonlinear equation set:

$$a^*_{A-tip} - \left[\left(\tau^* - \tau_{flaw-ini}\right)\frac{\widehat{da_{A-tip}}}{d\tau}\right] - \left\{\left[\frac{J_{applied}\left(a^*_{A-tip}, R_{cavity}(\tau^*)\right)}{C}\right]^{\frac{1}{m}} - \left[\frac{J_{Ic}}{C}\right]^{\frac{1}{m}}\right\} = 0$$
$$a^*_{A-tip} - h_0 - \left(S \times R_{cavity}(\tau^*)\right) = 0 \qquad (65)$$

For a cladding initial thickness of $h_0 = 0.25$ in and a fragility curve slope of S = -0.026117, the intersection point on the fragility curve in Fig. 34 is

$$a^*_{A-tip} = 0.1701 \text{ in; } R^* = 3.058 \text{ in; and } \tau^* = 2.162 \text{ years .}$$

The Davis-Besse damage model makes the assumption that the uncertain sampled cavity and flaw growth rates are constant over time. From this assumption and in the absence of ductile tearing of the A-tip, the cavity/flaw growth path, as shown in Fig. 31, follows a straight line approaching the *fragility curve* with increasing time from $\tau_{flaw-ini}$. If ductile tearing of the A-tip occurs, then the cavity/flaw growth path becomes nonlinear. At the point of intersection of the cavity/flaw growth path with the fragility curve, the remaining ligament under the A-tip portion of the flaw is predicted by the modified Chakrabarty and Alexander [15] instability theory to collapse by plastic tensile instability for an applied pressure of 2.165 ksi (i.e., the nominal operating pressure for the Davis-Besse RPV). The damage states below the fragility curve are assumed to be stable conditions with no LOCA. At the intersection of the cavity/flaw growth path with the fragility curve, the flaw configuration in Fig. 35a is assumed to instantaneously convert to the configuration shown in Fig. 35b, and the damage state projects vertically to the *final damage state*, designated as $\left(R^*, h_0\right)$ for example in Fig. 31.

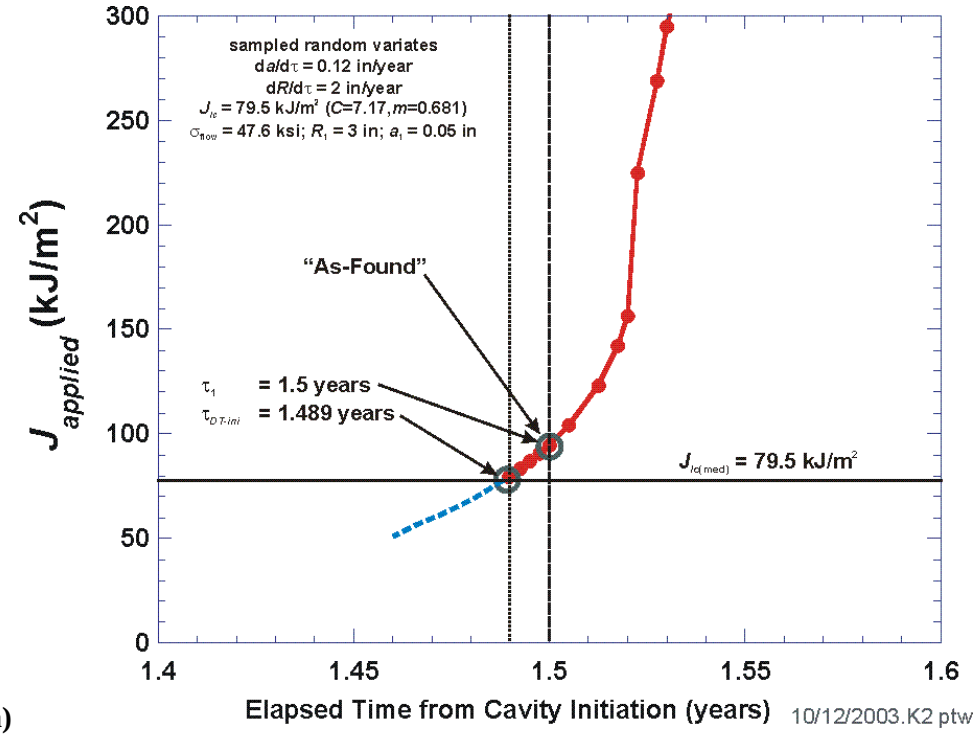

(a)

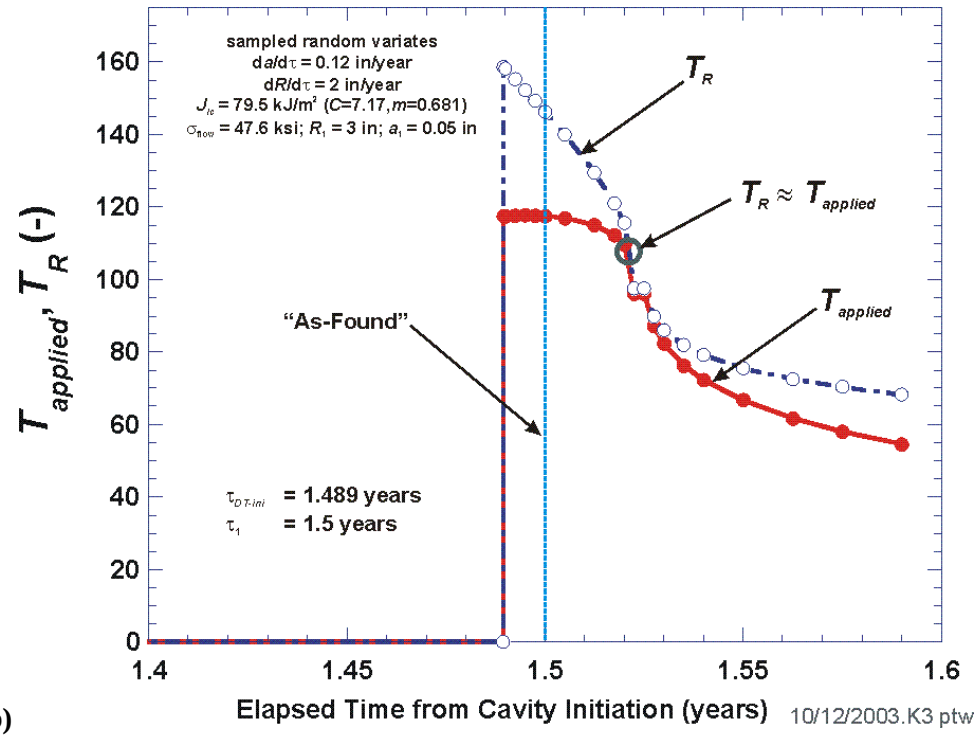

(b)

Fig. 33. Evolution of the (a) driving force, $J_{applied}$, and (b) tearing modulus, $T_{applied}$ for the example problem.

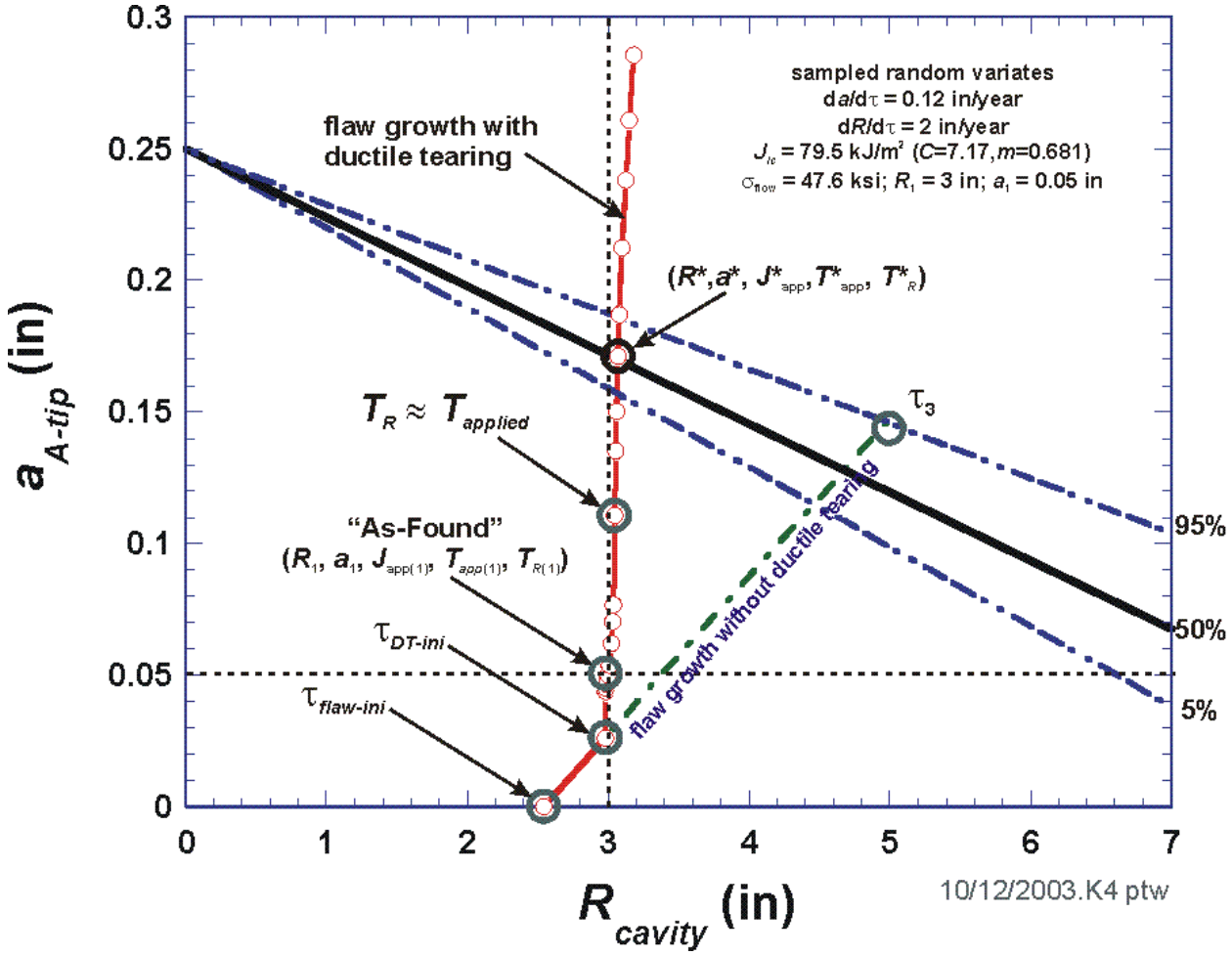

Fig. 34. Failure-assessment diagram using the damage-state growth path calculated for the example problem.

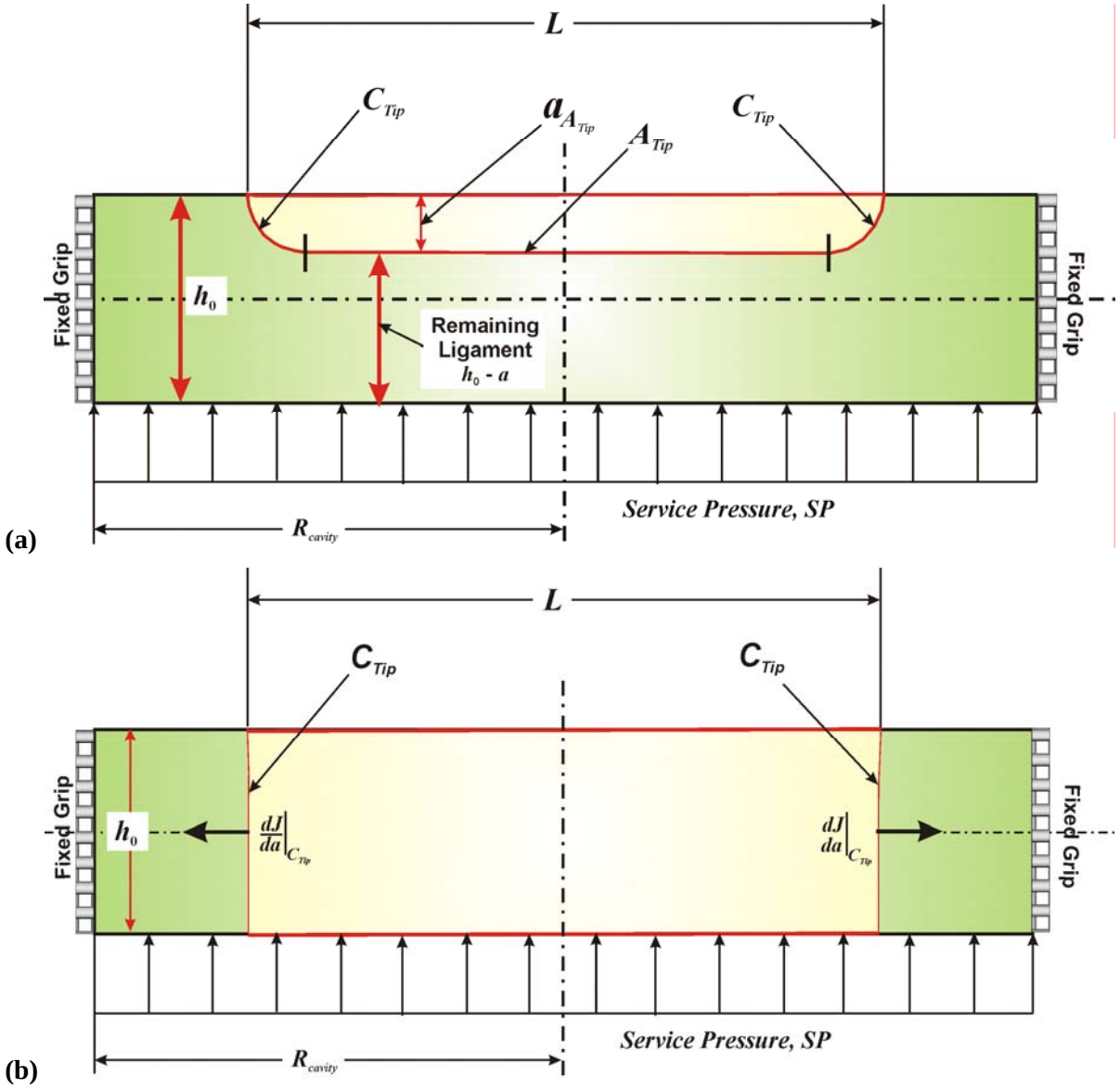

Fig. 35. Schematic descriptions of the model flaw's (a) A-tip and C-tip before A-tip ligament collapse and (b) C-tip location after A-tip ligament collapse.

The damage state at the intersection of the cavity/flaw growth path (defined by the line connecting the damage states $\left(R_{flaw-ini},0\right)$ and $\left(R_2,a_2\right)_{projected}$) is designated (R^*,a^*) in Fig. 31. This intersection point is calculated by

$$R^* = \max\left\langle \left\{ \frac{\left[\left[h_0 + \left(\frac{da_{A-tip}}{dR_{cavity}} \times R_{flaw-ini} \right)\right]\right]}{\left[\left(\frac{da_{A-tip}}{dR_{cavity}} \right) - S\right]} \right\}, 0 \right\rangle$$
$$a^* = \max\left\langle \left[h_0 + \left(S \times R^* \right)\right], 0 \right\rangle \tag{66}$$

where S is the uncertain slope of the fragility curve sampled from Eq. (29) and $\frac{da_{A-tip}}{dR_{cavity}}$ is calculated from the uncertain sampled cavity and flaw growth rates

$$\frac{da_{A-tip}}{dR_{cavity}} = \frac{\left(\frac{da_{A-tip}}{d\tau} \right)}{\left(\frac{dR_{cavity}}{d\tau} \right)} \tag{67}$$

2.2.5.3 ASP Analysis – Damage State Determination

For the ASP analysis, the damage state at the time of discovery, τ_1, is treated as uncertain. This uncertainty is expressed in terms of a statistical distribution for the elapsed time since flaw initiation, $\Delta\tau_{flaw-ini}$, relative to the time of discovery (see the Time Line in Fig. 30) and an uncertainty in the cavity size at time station τ_0.

$$\Delta\tau_{flaw-ini} \sim D_{(\Delta\tau_{flaw-ini})}$$
$$\Delta\tau_{flaw-ini(c)} = \min\left[\Delta\tau_{flaw-ini}, \Delta\tau_{cavity-ini} \right] \tag{68}$$

$$R_0 \sim D_{(R_0)} \tag{69}$$

where the damage state at τ_1 is now calculated by

$$R_1 = R_0 + \left(\Delta\tau_0 \times \frac{dR_{cavity}}{d\tau} \right)$$
$$a_1 = \min\left\{ \max\left[\left(\Delta\tau_{flaw-ini(c)} \times \frac{da_{A-tip}}{d\tau} \right), 0 \right], h_0 \right\} \quad (70)$$

and the values for $\Delta\tau_0$ and h_0 are fixed at

$$\Delta\tau_0 \equiv 1 \text{ year}$$
$$h_0 \equiv 0.25 \text{ inch}$$

The damage states at time stations $\tau_{flaw-ini}, \tau_2,$ and τ_3 then follow from Eqs. (51)-(54) and (56)-(70).

2.2.6 Results of an Informal Expert Elicitation

An informal expert elicitation was carried out within the NRC to provide expert judgments that were then used to develop statistical distributions for the following random variates for both the CCA and ASP studies: (1) the cavity wastage rate in terms of the time rate of change of the effective cavity radius, $dR/d\tau$, and (2) the rate of A-tip flaw growth, $da/d\tau$, due only to the exposure of the flaw to a corrosive environment, i.e., $da/d\tau$ does not include flaw growth due to ductile tearing. For the ASP study only, two additional random variate distributions are required: (3) the effective cavity radius at 1 year before discovery, R_0, and (4) the time of flaw initiation, $\Delta\tau_{flaw-ini}$, relative to the time of discovery. See Sect. 2.2.5.3 for a description of how these two distributions are applied in the ASP study.

For this elicitation, three *subject-matter experts* were asked to provide a best estimate (assigned a probability of 50%), a low estimate (assigned a probability of 5%), and a high estimate (assigned a probability of either 95% or 99.9%) for the four random variates described above. These expert judgments (see below) were then combined using the following aggregation procedure. In the case of the cavity wastage rate, $dR/d\tau$, and flaw initiation time, $\Delta\tau_{flaw-ini}$, two bins were constructed. The $dR/d\tau$ (1) bin contained the extremes of the aggregated sample from the minimum of 0.5 in/yr to 7.0 in/yr. The second bin, $dR/d\tau$ (2), reflected a more optimistic view of the wastage rate and was used only as a sensitivity check case (CCA-010) in the CCA study and not used at all in the ASP study. For the flaw initiation time, $\Delta\tau_{flaw-ini}$, the estimates from Subject-Matter Expert No. # 2 were used exclusively in the ASP study. For R_0 and $da/d\tau$, the highest and lowest values established the selected upper and lower bounds.

These six cases were then fitted to a range of distributions including triangular, normal, lognormal, beta, Weibull, and uniform. The final aggregate estimates and distribution fittings are presented in Table 6 and Figs. 36-40.

.

Judgments Obtained from Informal Expert Elicitation

Parameter Description	Parameter Units	Subject Matter Expert ID No.#	Lower Bound	Median (BE) Value	Upper Bound
			Associated Percentiles		
			5%	50%	95%/99.9%
Effective Cavity		#1	0	1.25	2
Radius at TOD-1	(in.)	#2	0	1.125	2.5
R_0		#3	0	1.5	2.25
Effecive Cavity		#1	1	2	7
Wastage Rate	(in./year)	#2	0.5	2	6
$dR/d\tau$		#3	0.75	1.5	(-)
Flaw Initiation		#1	12	36	48
Time w.r.t. TOD	(months)	#2	1	6	60
$\Delta\tau_{flaw\text{-}ini}$		#3	(-)	(-)	(-)
Effective Flaw		#1	0.001	0.01	0.1
Growth Rate	(in./month)	#2	0.001	0.01	0.1
$da/d\tau$		#3	0.004	0.01	0.04

Table 6. Summary of Candidate Input Sampling Distributions

Davis-Besse CCA/ASP Studies - Aggregation of Expert Judgments						
Random Variates	**Cavity Size**	**Cavity Wastage Rate**		**Flaw Initiation Time**		**Flaw Growth Rate, $da/d\tau$**
	at τ_0, R_0	**$dR/d\tau$ (1)**	**$dR/d\tau$ (2)**	**$\Delta\tau_{flaw\text{-}ini}$ (1)**	**$\Delta\tau_{flaw\text{-}ini}$ (2)**	
Percentiles	**(in)**	**(in/yr)**	**(in/yr)**	**(months)**	**(months)**	**(in/month)**
5%	**0**	**0.5**	**0.1**	**12**	**1**	**0.001**
50% (median)	**1**	**2**	**1**	**36**	**6**	**0.01**
95% or 99.9%	**2.5**	**7**	**3**	**48**	**60**	**0.1**
Distributions	**Distribution Parameters, Percentiles, and Moments**					
Triangular						
lower bound	0.00	-0.6062	-0.4460	2.6509	-5.0994	
upper bound	3.1937	8.7849	3.7679	55.0697	61.9364	
shape parameter	0.1801	2	0.9689766	36	6	
5%	0	0.5	0.1	12	1	
50%	1	3.4105	1.3440	32.22	18.9	
95% or 99.9%	2.5	7	3	48	60	
mean	1.6368	3.3929	1.4303	31.2402	20.9457	
variance	0.4037	3.9173	0.7665	117.3208	215.1634	
Normal						
mean	1.2501			29.9999		
standard deviation	0.7599			10.94318		
5%	0			12		
50%	1.2501			30.00		
95%	2.5			48		
variance	0.5775			119.7533		
Lognormal						
logmean		0.6264			1.4223	-5.3080
logstandard deviation		0.8022			0.8647	0.9726
5%		0.5			1	0.001
50%		1.87082			4.1465	0.01
95% or 99.9%		7			60	0.1
variance		0.6435			0.7477	0.9459
Beta						
shape parameter 1	1.0614	0.6478	0.8605	2.0712	0.4451	0.4621
shape parameter 2	1.9386	2.3522	2.1395	0.9288	2.5549	2.5379
lower bound	0.0000	0.4611	0.0429	-0.1129	0.9738	0.0009
upper bound	3.1435	10.6305	4.0986	48.9374	67.1177	0.1115
5%	0.0989	0.5	0.1	12	1	0.001
50%	1	2	1	36	6	0.01
95% or 99.9%	2.5	7	3	48	60	0.1
mean	1.1121	2.6571	1.2062	33.7516	10.7866	0.0180
variance	0.0572	4.3773	0.0511	128.5645	138.1917	0.0004
Weibull						
location parameter	0.0000	0.3646	-0.0612		0.6492	0.0003
scale parameter	1.2579	2.3224	1.3836		7.8524	0.0141
shape parameter	1.5974	1.0451	1.3816		0.9555	0.9864
5%	0.196	0.5	0.1		1	0.001
50%	1	2	1		6	0.01
95% or 99.9%	2.5	7	3		60	0.1
mean	1.0920	2.6463	1.2025		8.663342	0.0144
variance	0.5933	4.7693	0.8574		70.390404	0.0002
Uniform						
lower bound						-0.00422
upper bound						0.10010
5%						0.001
50%						0.0479
99.9%						0.1
mean						0.0479
variance						0.0009

Statistical Distributions Used in the Monte Carlo Analysis

A standard uniform distribution on the interval $U(0,1)$ is the starting point for all of the transformation methods that draw random variates from nonuniform continuous distributions. A uniform distribution is defined by the following:

Uniform Distribution – $U(a,b)$

PDF:
$$f_U(x \mid a,b) = \begin{cases} 0 \;\; ; & x < a \\ \dfrac{1}{b-a}; & a \le x \le b \\ 0 \;\; ; & x > b \end{cases}$$

CDF:
$$\Pr(X \le x) = F_U(x \mid a,b) = \begin{cases} 0 \;\; ; & x < a \\ \dfrac{x-a}{b-a}; & a \le x \le b \\ 1 \;\; ; & x > b \end{cases}$$

Moments for a uniform distribution:

Mean
$$\mu = \frac{a+b}{2}$$

Variance
$$\sigma^2 = \frac{(b-a)^2}{12}$$

Sampling from a 2-parameter uniform distribution: $U_i \leftarrow U(a,b)$

Sampling from a standard uniform distribution, $U(0,1)$, is accomplished computationally with a *Random Number Generator*. The random number generator (available from the *ranlib* statistical library (function **RANF()**) used in this analysis is based on a combination of two multiplicative linear congruential generators [40] with a combined period of 2.3×10^{18}. The sampled uniform deviate can then be scaled to the required range by

$$\begin{aligned} P_i &\leftarrow U(0,1) \\ X_i &= a + (b-a) P_i \end{aligned} \tag{71}$$

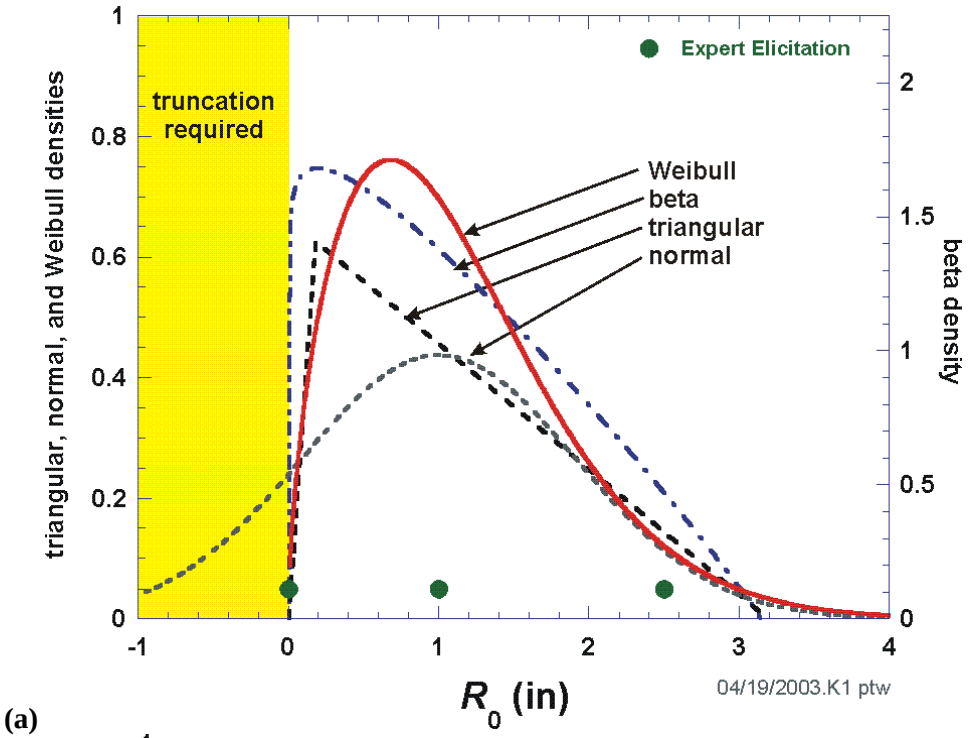

(a)

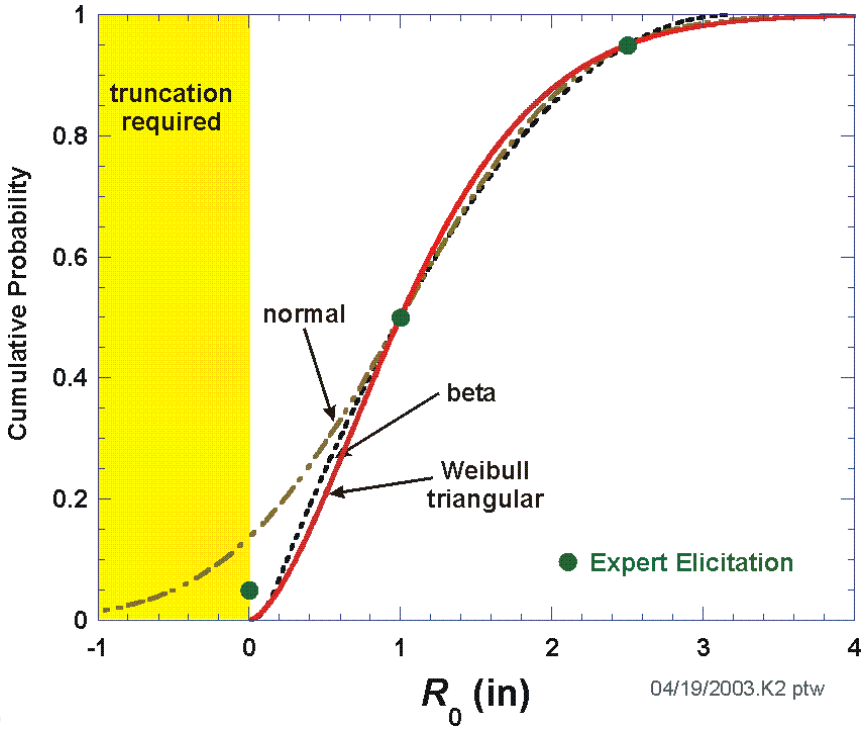

(b)

Fig. 36. Candidate sampling distributions for cavity size at one year before discovery, τ_0: (a) probability densities and (b) cumulative probabilities. (ASP analysis only).

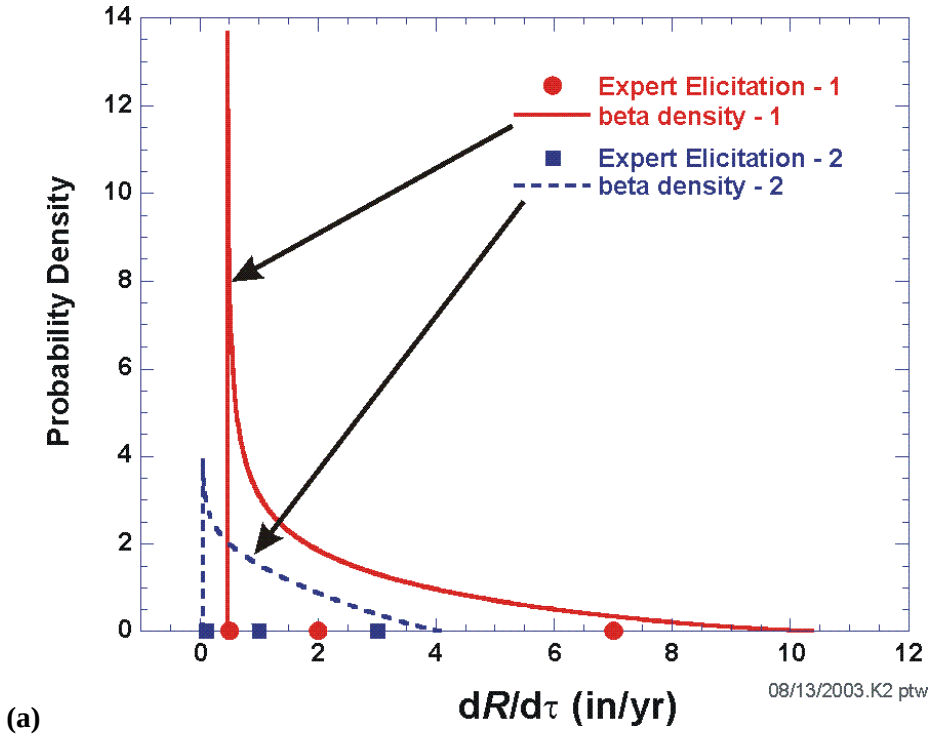

(a)

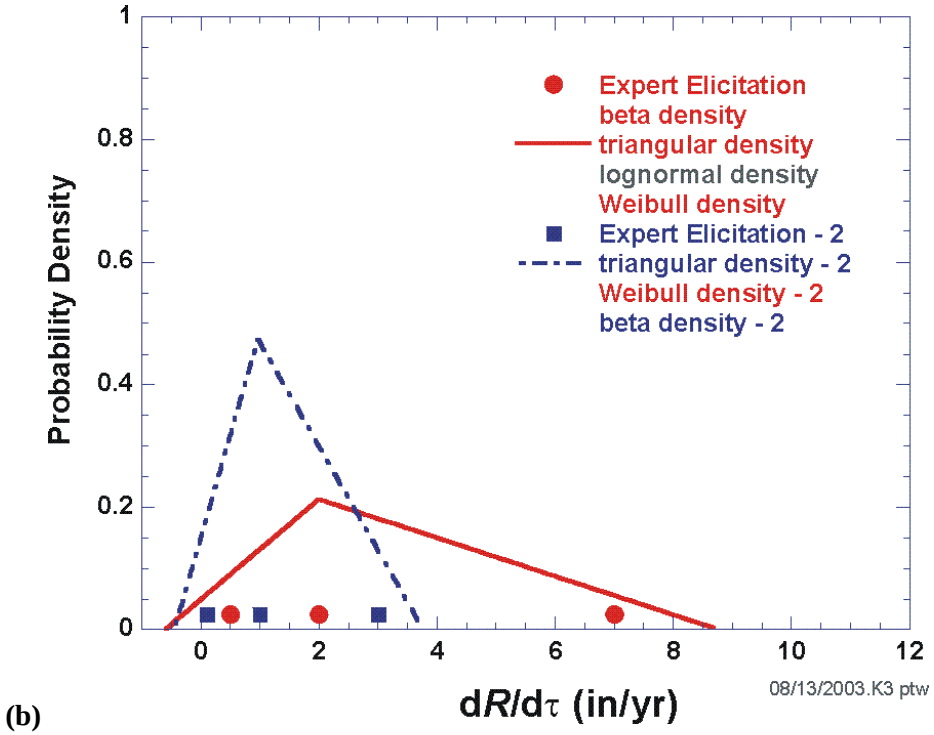

(b)

Fig. 37. Candidate sampling distributions for cavity wastage rate, $dR/d\tau$: (a) probability densities for two beta distributions, (b) probability densities for two triangular distributions,

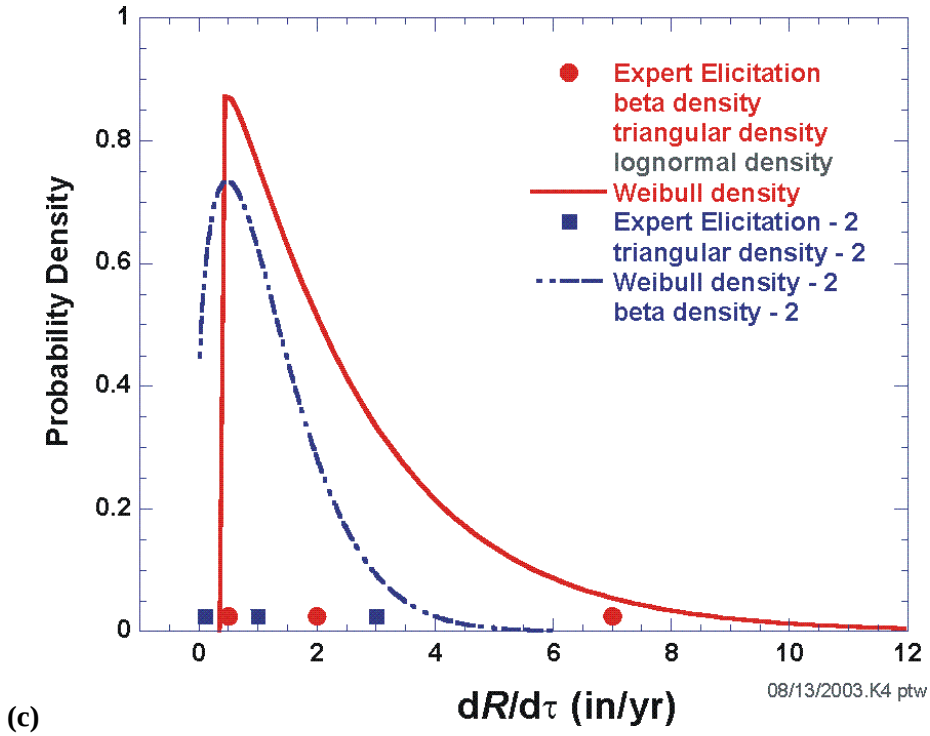

(c)

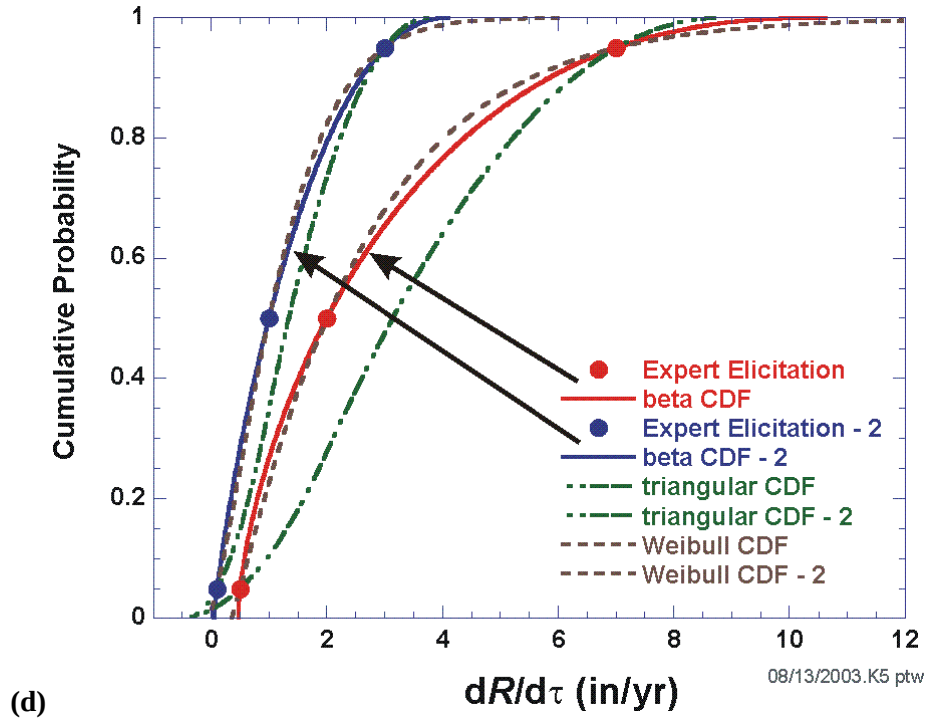

(d)

Fig. 37. (continued) Candidate sampling distributions for cavity wastage rate, $dR/d\tau$: (c) probability densities for two Weibull distributions, and (d) cumulative probabilities.

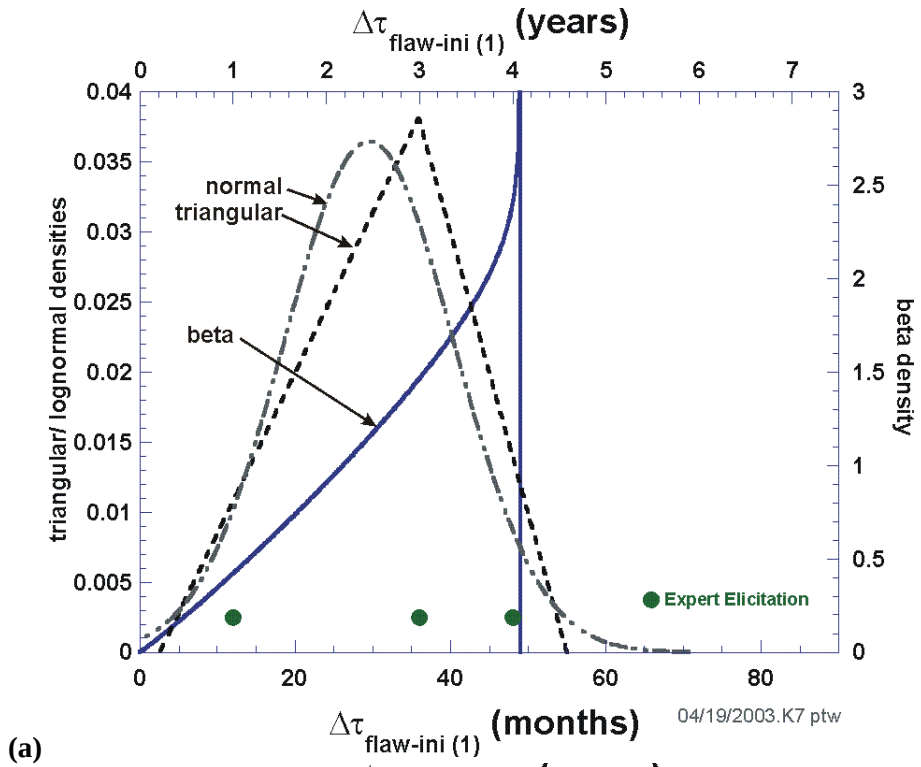

(a)

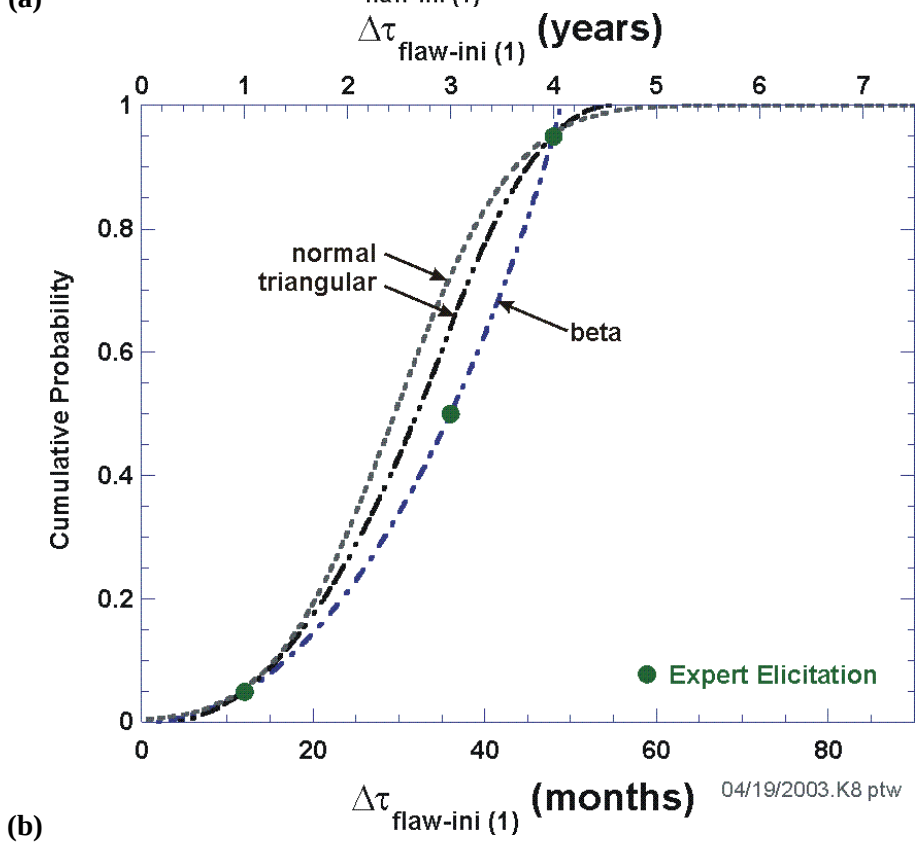

(b)

Fig. 38. Candidate sampling distributions for the Case 1 flaw initiation time, $\Delta\tau_{\text{flaw-ini (1)}}$: (a) probability densities and (b) cumulative probabilities. (ASP analysis only).

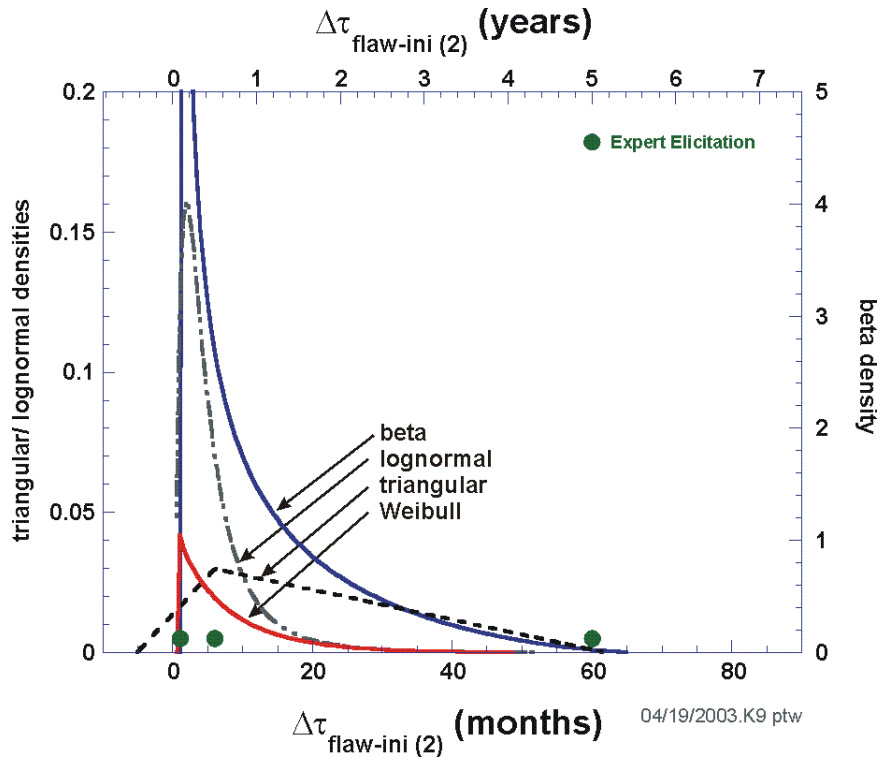

(a)

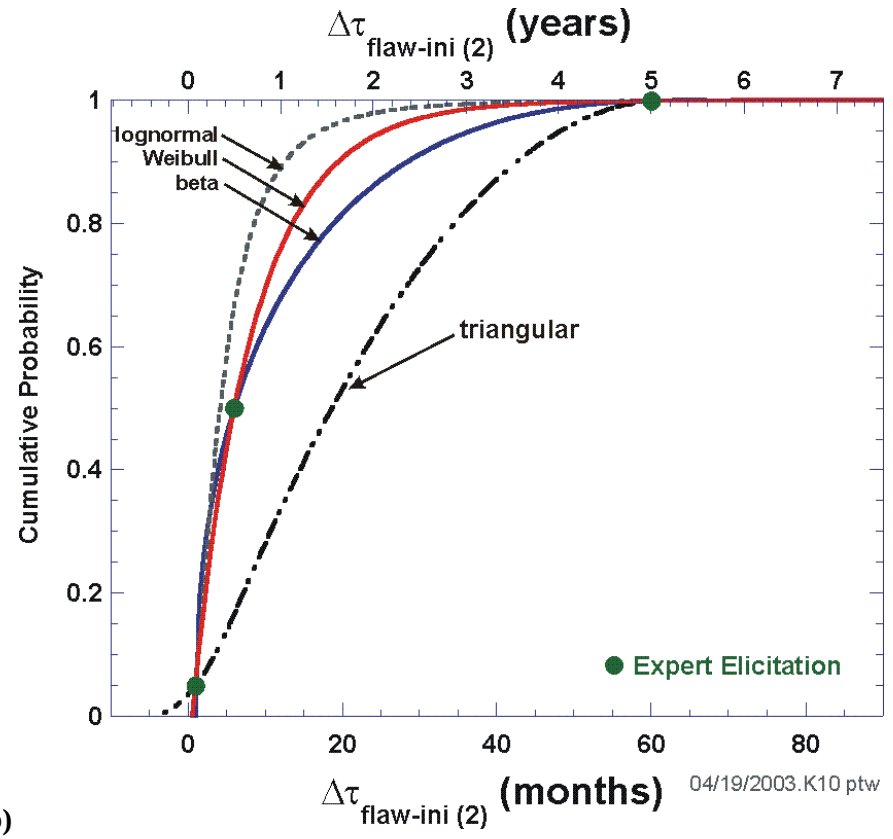

(b)

Fig. 39. Candidate sampling distributions for the Case 2 flaw initiation time, $\Delta\tau_{\text{flaw-ini (1)}}$: (a) probability densities and (b) cumulative probabilities. (ASP analysis only).

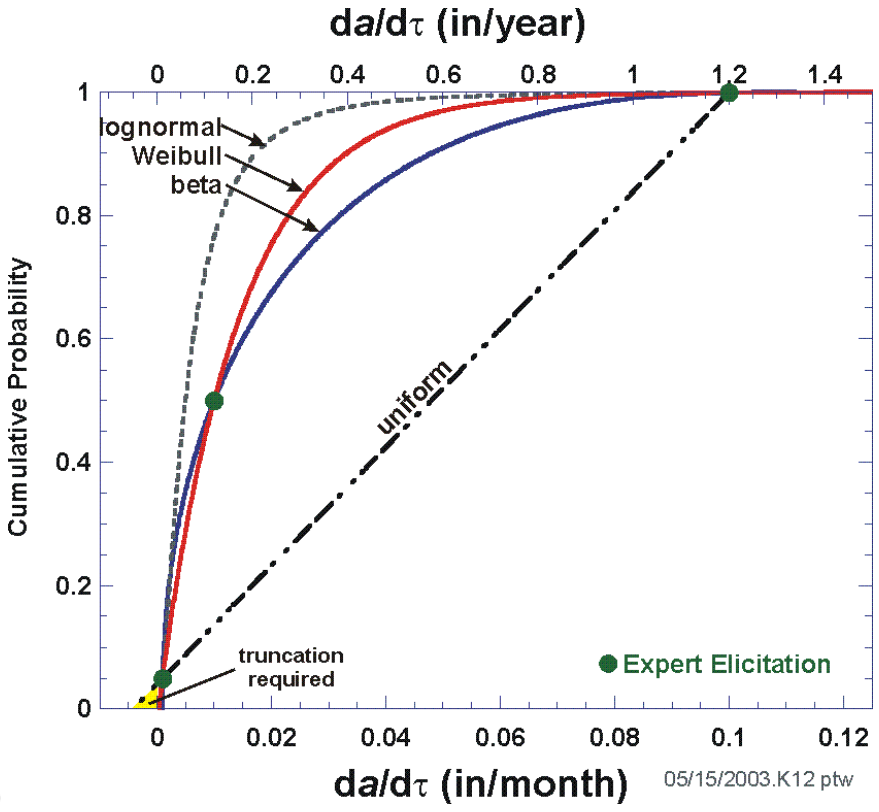

(a)

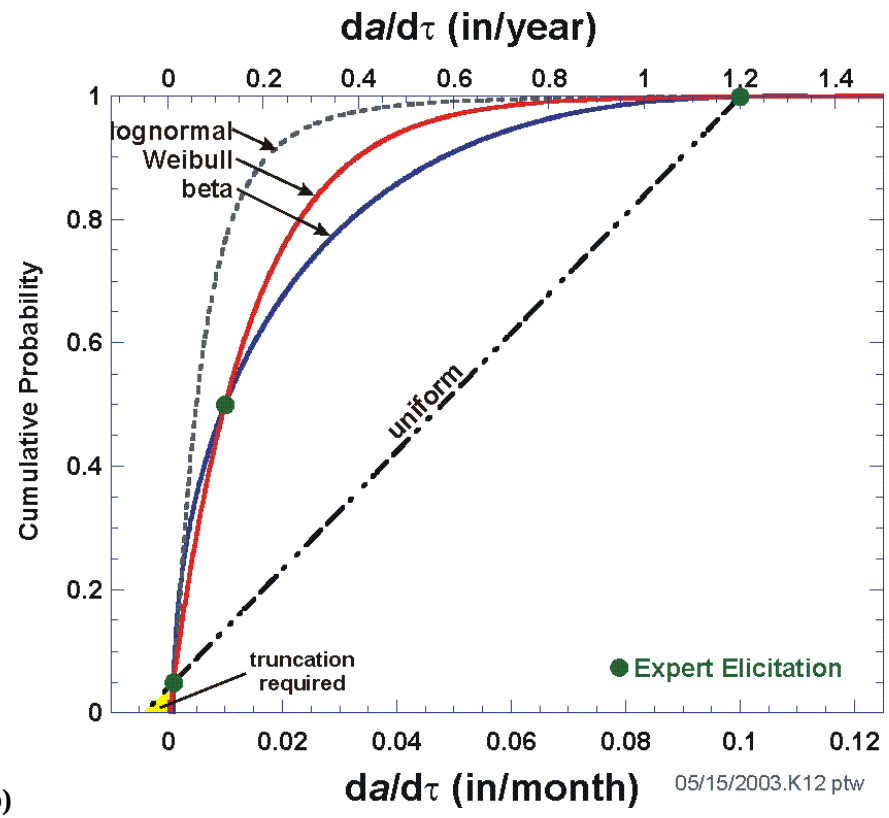

(b)

Fig. 40. Candidate sampling distributions for flaw growth rate, $da/d\tau$: (a) probability densities and (b) cumulative probabilities.

Triangular Distribution – *T(a,b,c)*

A triangular distribution is commonly applied as a rough model of a random variable when there are essentially no data available.

Density:
$$f(x \mid a,b,c) = \begin{cases} \dfrac{2(x-a)}{(b-a)(c-a)} & \text{if } a < x \le c \\ \dfrac{2(b-x)}{(b-a)(b-c)} & \text{if } c < x < b \\ 0 & \text{otherwise} \end{cases}$$

CDF:
$$Pr(x \le X) = \begin{cases} \dfrac{(x-a)^2}{(b-a)(c-a)} & \text{if } x \le a \\ 1 - \dfrac{(b-x)^2}{(b-a)(b-c)} & \text{if } a < x \le c \\ 1 & \text{if } b \le x \end{cases}$$

Moments:

Mean
$$\mu = \frac{a+b+c}{3}$$

Variance
$$\sigma^2 = \frac{a^2+b^2+c^2-ab-ac-bc}{18}$$

Sampling from a 3-parameter triangular distribution: $X_i \leftarrow T(a,b,c)$

A random variate is sampled from a 3-parameter triangular distribution *T*(*a*,*b*,*c*) by

$$P_i \leftarrow U(0,1)$$
$$X_i = \begin{cases} a + \sqrt{P_i(b-a)(c-a)} & \text{if } P_i \le \dfrac{(c-a)}{(b-a)} \\ b - \sqrt{(1-P_i)(b-a)(b-c)} & \text{otherwise} \end{cases} \quad \text{for } a < c < b$$

Beta Distribution – $\beta(\alpha_1, \alpha_2, a, b)$

$$f(x \mid a, b, \alpha_1, \alpha_2) = \begin{cases} \dfrac{y^{(\alpha_1 - 1)}(1-y)^{(\alpha_2 - 1)}}{B(\alpha_1, \alpha_2)} & \text{for } 0 < y < 1;\ y = \left(\dfrac{x-a}{b-a}\right) \\ 0 & \text{otherwise} \end{cases}$$

PDF:

$$B(\alpha_1, \alpha_2) = \int_0^1 t^{(\alpha_1 - 1)}(1-t)^{(\alpha_2 - 1)}\, dt$$

where there is no closed form relation for the cumulative distribution function of a beta distribution.

Moments:

Mean $\mu = a + \left[(b-a)\left(\dfrac{\alpha_1}{\alpha_1 + \alpha_2}\right)\right]$

Variance $\sigma^2 = (b-a)^2\left[\dfrac{\alpha_1 \alpha_2}{(\alpha_1 + \alpha_2)^2(\alpha_1 + \alpha_2 + 1)}\right]$

Estimates for the two shape parameters (α_1, α_2) can be developed from an estimated range (a, b) and mode c [33] by

$$\alpha_1(a,b,c) \approx \frac{(\mu - a)(2c - a - b)}{(c - \mu)(b - a)};\ \alpha_2(a,b,c) \approx \frac{(b - \mu)\alpha_1}{(\mu - a)};\ \mu(a,b,c) \approx \frac{(a + b + c)}{3}$$

If we define $Q_\beta^{-1}(p, \alpha_1, \alpha_2)$ as the percentile function[9] for the standard beta distribution and assign probabilities for estimates for a lower bound, *LB* (e.g., $p_{LB} = 0.05$), a median, *MV* (e.g., $p_{MV} = 0.5$), and an upper bound, *UB* (e.g., $p_{UB} = 0.95$), then the parameter set $(a, b, c, \mu, \alpha_1, \alpha_2)$ can be determined by solving the following nonlinear system of equations:

$$a + \left[(b-a) \times Q_\beta^{-1}(p_{LB}, \alpha_1, \alpha_2)\right] - LB = 0$$
$$a + \left[(b-a) \times Q_\beta^{-1}(p_{MV}, \alpha_1, \alpha_2)\right] - MV = 0$$
$$a + \left[(b-a) \times Q_\beta^{-1}(p_{UB}, \alpha_1, \alpha_2)\right] - UB = 0$$
$$\alpha_1 - \frac{(\mu - a)(2c - a - b)}{(c - \mu)} = 0$$
$$\alpha_2 - \frac{(b - \mu)\alpha_1}{(\mu - a)} = 0$$
$$\mu - \frac{(a + b + c)}{3} = 0$$

[9] The *percentile function* is derived by inverting the cumulative distribution function such that the random variate is expressed as a function of the cumulative probability and the parameters of the distribution.

Sampling from 4–term beta distribution - $X_i \leftarrow \beta(\alpha_1, \alpha_2, a, b)$

The inverse of a standard beta distribution is calculated in this analysis by the *dcdflib* FORTRAN statistical routine, **CDFBET** [41] (designated as $Q_\beta^{-1}(P_i, \alpha_1, \alpha_2)$) and then scaled to the required nonstandard distribution by

$$P_i \leftarrow U(0,1)$$
$$X_i = a + \left[(b-a) \times \mathrm{Q}_\beta^{-1}(P_i, \alpha_1, \alpha_2) \right]$$

<u>Normal Distribution</u> – $N(\mu, \sigma)$

PDF: $$f_N(x \mid \mu, \sigma) = \frac{1}{\sigma\sqrt{2\pi}} \exp\left[-\frac{(x-\mu)^2}{2\sigma^2} \right]; \quad -\infty < x < +\infty$$

CDF: $$\Pr(X \le x) = \Phi(z) = \frac{1}{\sqrt{2\pi}} \int_{-\infty}^{z} \exp\left(-\frac{\xi^2}{2} \right) d\xi \; ; \quad z = \frac{x-\mu}{\sigma}; \quad -\infty < x < +\infty$$

Moments:

Mean μ

Variance σ^2

Sampling from a 2-parameter normal distribution: $X_i \leftarrow N(\mu, \sigma)$

In this analysis, the *dcdflib* FORTRAN subroutine **CDFNOR** is called to sample, Z_p, from a standard unit-normal distribution. The standard normal deviate is then scaled to obtain the required quantile by

$$X_p = Z_p \sigma + \mu \tag{72}$$

<u>Lognormal Distribution</u> – $LN(\mu_{\log}, \sigma_{\log})$

PDF: $$f_\Lambda(x \mid \mu_{\log}, \sigma_{\log}) = \begin{cases} 0 & ; \quad x \le 0 \\ \dfrac{1}{\sigma_{\log} x \sqrt{2\pi}} \exp\left[-\dfrac{\left(\ln x - \mu_{\log} \right)^2}{2\sigma_{\log}^2} \right] & ; \quad 0 < x < \infty \end{cases}$$

CDF: $$\Pr(X \le x) = \Phi(z) = \begin{cases} 0 & ; \quad x \le 0 \\ \dfrac{1}{\sqrt{2\pi}} \displaystyle\int_{-\infty}^{z} \exp\left(-\frac{\xi^2}{2} \right) d\xi \; ; \; z = \frac{\ln x - \mu_{\log}}{\sigma_{\log}} & , \quad 0 < x < \infty \end{cases}$$

Moments:

Mean $$\mu = \exp\left(\mu_{\log} + \frac{\sigma_{\log}^2}{2}\right)$$

Variance $$\sigma^2 = \omega(\omega-1)\exp(2\mu_{\log}); \quad \omega = \exp(\sigma_{\log}^2)$$

Sampling from a 2-parameter Lognormal Distribution: $X_i \leftarrow LN\left(\mu_{\log}, \sigma_{\log}\right)$

The log-transformed deviate is sampled from a standard unit normal distribution using *dcdflib* FORTRAN routine **CDFNOR** [28]. With the mean equal to the lognormal mean, $\mu_{\log}$, and standard deviation equal to the lognormal standard deviation, $\sigma_{\log}$, the log-transformed deviate is then converted into the required random deviate by the exponential function.

$$\begin{aligned} Y_i &\leftarrow N(\mu_{\log}, \sigma_{\log}) \\ X_i &= \exp(Y_i) \end{aligned} \tag{73}$$

<u>Weibull Distribution</u> – $W(a,b,c)$

(a = location parameter, b = scale parameter, c = shape parameter)

PDF: $$f_w(x|a,b,c) = \begin{cases} 0 \quad ; & x \le a \\ \dfrac{c}{b} y^{c-1} \exp\left(-y^c\right); & (y = (x-a)/b, x > a,\ b,c > 0) \end{cases}$$

CDF: $$\Pr(X \le x) = F_w(x \mid a,b,c) = \begin{cases} 0 \quad ; & x \le a \\ 1 - \exp\left[-y^c\right]; & (y = (x-a)/b, x > a,\ b,c > 0) \end{cases}$$

Moments:

Mean $$\mu = a + b\,\Gamma\left(1 + \frac{1}{c}\right)$$

Variance $$\sigma^2 = b^2\left[\Gamma\left(1 + \frac{2}{c}\right) - \Gamma^2\left(1 + \frac{1}{c}\right)\right]$$

where $\Gamma(x)$ is Euler's gamma function.

Sampling from a 3-parameter Weibull Distribution: $X_i \leftarrow W(a,b,c)$

A random number is drawn from a uniform distribution on the open interval (0,1) and then transformed to a Weibull variate with the Weibull percentile function.

$$\begin{aligned} U_i &\leftarrow U(0,1) \\ X_i &= a + b\left[-\ln(1-U_i)\right]^{1/c} \end{aligned} \tag{74}$$

2.2.7 Best-Estimate, More Conservative, and Less Conservative Sampling Distributions

The sampling distributions shown in Table 6 and Figs. 36-40 were grouped into three categories: (1) best-estimate (BE), (2) more conservative (MC), and (3) less conservative (LC) as shown below. The MC and LC sets of distributions were selected such that, when taken together as a set, that they would be expected to produce either higher or lower LOCA probabilities, respectively, than the BE set of distributions.

Sampling Distributions Categories	dR/dτ (in/yr)	da/dτ (in/month)	R_0 (in)	$\Delta\tau_{flaw\text{-}ini}$ (months)
BE	beta-1	Weibull	beta	Weibull
MC	triangluar	lognormal	triangular	lognormal
LC	Weibull	uniform	normal	triangular

In the CCA Case Matrix to be discussed in Sect. 3, additional distributions are included in the study to test the sensitivity of the final CCA results to the applied statistical distributions used to characterize the uncertainties in the analysis. In the ASP study, the BE set of distributions was applied exclusively.

2.2.8 Variance Reduction – The Method of Antithetic Variates

A variance reduction technique (VRT) called the *Method of Antithetic Variates* (AV) [33,42] is applied in the Monte Carlo code developed for this analysis. The objective of this method is to provide a more rapid convergence of the estimated LOCA probabilities to their asymptotic values than the standard Monte Carlo approach, thus producing a more computationally-efficient algorithm. The central idea of the AV method, due originally to Hammersly and Morton [43], is to make *pairs* of trials (2 trials for each Monte Carlo *realization*) such that a "small" observation on one of the trials in a pair tends to be offset by a "large" observation on the other one; i.e., the two observations are negatively correlated. Taking the average of the results of the two trials as the result for the realization should produce an estimate of the mean (or common expectation) that is closer to the true probability due to the induced negative covariance between the paired trials.

For example, at a given point in time, τ_k, let there be a total of *N* realizations with $N_f^{(1)}(\tau_k)$ from the *Trial 1* set and $N_f^{(2)}(\tau_k)$ from the *Trial 2* set of realizations experiencing a LOCA at some time, $\tau \le \tau_k$. The cumulative probability of failure at time τ_k, is therefore

$$p_f^{(1)}(\tau_k, N) = \frac{N_f^{(1)}(\tau_k)}{N}; \quad p_f^{(2)}(\tau_k, N) = \frac{N_f^{(2)}(\tau_k)}{N}$$
$$p_f(\tau_k, N) = \frac{p_f^{(1)}(\tau_k, N) + p_f^{(2)}(\tau_k, N)}{2} \text{ at } \tau_k \text{ for } N \text{ realizations} \tag{75}$$

Equation (75) represents an unbiased point estimator of the statistical expectation, $\mu_{LOCA}(\tau_k) = E\left(p_f(\tau_k)\right)$, of the cumulative probability of a LOCA occurring at or before the time τ_k. An estimate for the variance of $E\left(p_f\right)$ for $\tau \le \tau_k$ as a function of the number of Monte Carlo realizations, *N*, is from [33, 42]

$$\mathrm{var}\left[p_f(\tau_k)\right] \approx \frac{\mathrm{var}\left[p_f(\tau_k, N)\right]}{N} =$$
$$\frac{\mathrm{var}\left[p_f^{(1)}(\tau_k, N)\right] + \mathrm{var}\left[p_f^{(2)}(\tau_k, N)\right] + 2\,\mathrm{cov}\left[p_f^{(1)}(\tau_k, N),\ p_f^{(2)}(\tau_k, N)\right]}{4N} \tag{76}$$

The individual trial streams (1) and (2) satisfy the requirements of a *Bernoulli sequence* of discrete random variables such that the estimates provided by Eq. (75) are distributed by a discrete *binomial distribution* [42]. An unbiased point estimator for the variance of $p_f^{(i)}(\tau_k, N)$ is, therefore,

$$\mathrm{var}\left(p_f^{(i)}(\tau_k, N)\right) \approx \frac{\left(1 - p_f^{(i)}(\tau_k, N)\right) p_f^{(i)}(\tau_k, N)}{N}; \quad \text{for } i = 1, 2 \tag{77}$$

If the two trials within a pair were sampled independently, then the covariance between the two trials would be, $\mathrm{cov}\left(p_f^{(1)}(\tau_k, N), p_f^{(2)}(\tau_k, N)\right) = 0$; however, by inducing a negative covariance between $p_f^{(1)}$ and $p_f^{(2)}$, the overall variance for the estimate of $\mu_{LOCA}(\tau_k)$ should be reduced.

The required negative covariance is applied through the use of *complementary* random numbers in the sampling protocols required to create the input for each Monte Carlo trial/realization. For the first trial (of

the paired trials) for the i^{th} realization $\left(1 \le i \le N\right)$, nine random variates are drawn from a standard uniform distribution using the random number generator, *ranf*(), such that:

$$
\begin{aligned}
U_{1(i)}^{(1)} &\leftarrow U\left(0,1\right) && \text{for sampling } R_0 \text{ (not used in CCA runs)} \\
U_{2(i)}^{(1)} &\leftarrow U\left(0,1\right) && \text{for sampling the cavity wastage rate, } dR/d\tau \\
U_{3(i)}^{(1)} &\leftarrow U\left(0,1\right) \\
U_{4(i)}^{(1)} &\leftarrow U\left(0,1\right) && \text{for lognormal bivariate sampling of ductile tearing model parameters } \left(J_{Ic}, m\right) \\
U_{5(i)}^{(1)} &\leftarrow U\left(0,1\right) && \text{for sampling } \Delta\tau_{\text{flaw-ini}} \text{ (not used in CCA runs)} \\
U_{6(i)}^{(1)} &\leftarrow U\left(0,1\right) && \text{for sampling the flaw growth rate, } da/d\tau \\
U_{7(i)}^{(1)} &\leftarrow U\left(0,1\right) \\
U_{8(i)}^{(1)} &\leftarrow U\left(0,1\right) && \text{for correlated sampling of the plastic-flow properties } \left(\sigma_{yield}, \sigma_{ult}\right); \; U_{9(i)}^{(1)} \text{ used only in the trivariate reduction protocol for the bivariate gamma distribution} \\
U_{9(i)}^{(1)} &\leftarrow U\left(0,1\right)
\end{aligned}
$$

These uniform random variates are then converted into their respective sampling distributions using the *Inverse Transform Method* as discussed in Sect. 2.2.6. For the second trial of the paired trials in the i^{th} realization $\left(1 \le i \le N\right)$, the complements of each uniform random variate are calculated by:

$$
\begin{aligned}
U_{1(i)}^{(2)} &= 1 - U_{1(i)}^{(1)} && \text{for sampling } R_0 \text{ (not used in CCA runs)} \\
U_{2(i)}^{(2)} &= 1 - U_{2(i)}^{(1)} && \text{for sampling the cavity wastage rate, } dR/d\tau \\
U_{3(i)}^{(2)} &= 1 - U_{3(i)}^{(1)} \\
U_{4(i)}^{(2)} &= 1 - U_{4(i)}^{(1)} && \text{for lognormal bivariate sampling of ductile tearing model parameters } \left(J_{Ic}, m\right) \\
U_{5(i)}^{(2)} &= 1 - U_{5(i)}^{(1)} && \text{for sampling } \Delta\tau_{\text{flaw-ini}} \text{ (not used in CCA runs)} \\
U_{6(i)}^{(2)} &= 1 - U_{6(i)}^{(1)} && \text{for sampling the flaw growth rate, } da/d\tau \\
U_{7(i)}^{(2)} &= 1 - U_{7(i)}^{(1)} \\
U_{8(i)}^{(2)} &= 1 - U_{8(i)}^{(1)} && \text{for correlated sampling of the plastic-flow properties } \left(\sigma_{yield}, \sigma_{ult}\right); \; U_{9(i)}^{(2)} \text{ used only in the trivariate reduction protocol for the bivariate gamma distribution} \\
U_{9(i)}^{(2)} &= 1 - U_{9(i)}^{(1)}
\end{aligned}
$$

with subsequent conversion into their respective sampling distributions. As discussed in [33], synchronization of the random number stream is vital to ensure that the necessary negative correlation is correctly induced for each realization.

2.2.9 LOCA Screening Rules

Three sets of LOCA screening rules are presented in Fig. 41 in terms of Event Trees that lead from the initiating event to a failure consequence. These screening rules are designated: (a) best-estimate (BE), (b) more conservative (MC), and (c) less conservative (LC). As was the case with the sampling distributions, the MC and LC LOCA screening rules were developed to produce higher and lower total LOCA probabilities, respectively, than produced by the BE screening rules, thus providing estimated bounding probabilities as a measure of the uncertainties about the predicted best-estimate values.

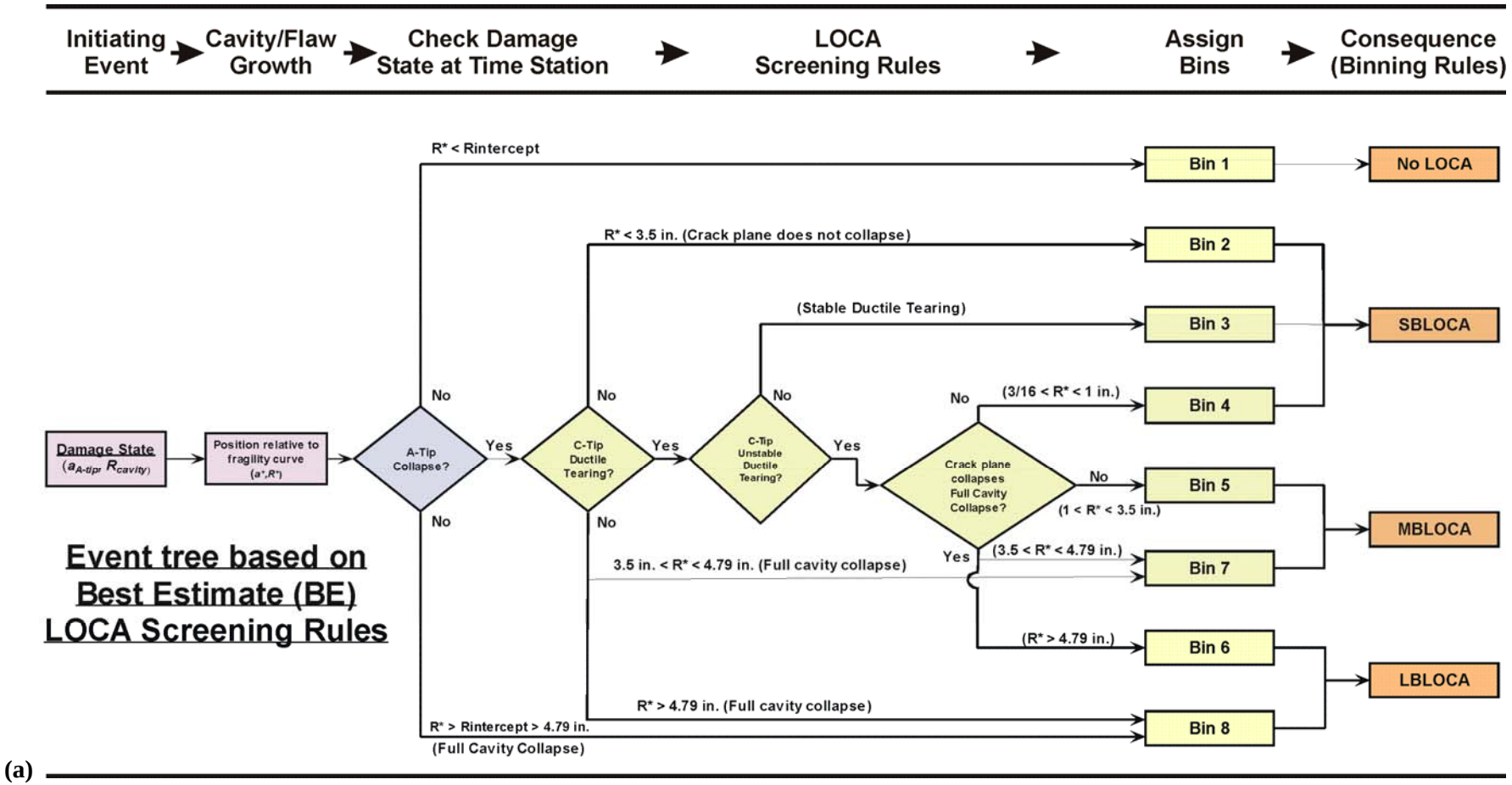

(a)

Fig. 41. Event trees based on LOCA screening rules representing (a) best-estimate (BE),

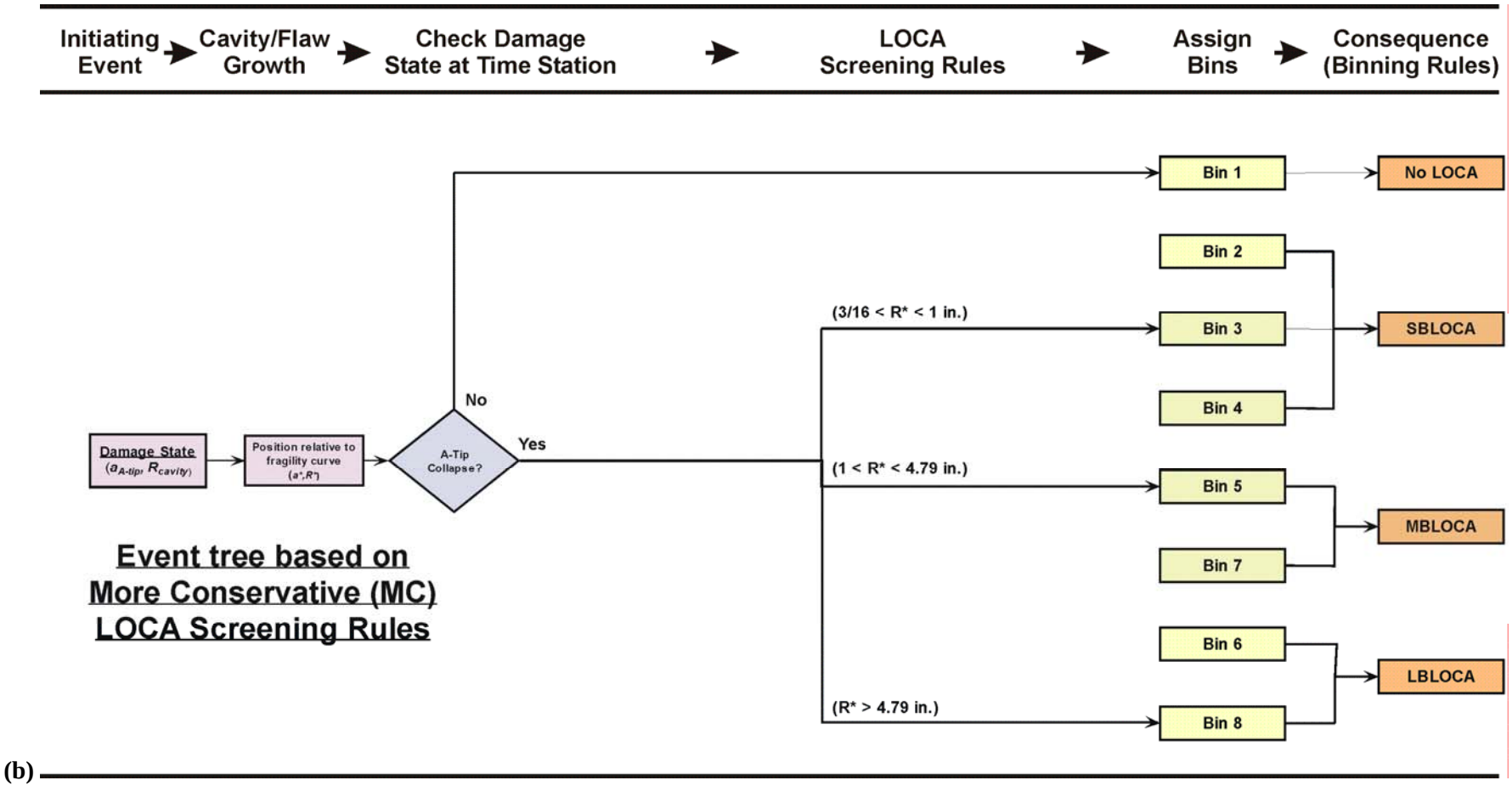

Fig. 41. (continued) Event trees based on LOCA screening rules representing: (b) more conservative (MC),[10]

[10] Bins 2, 4, 6, and 7 are not used in the MC event-tree definition.

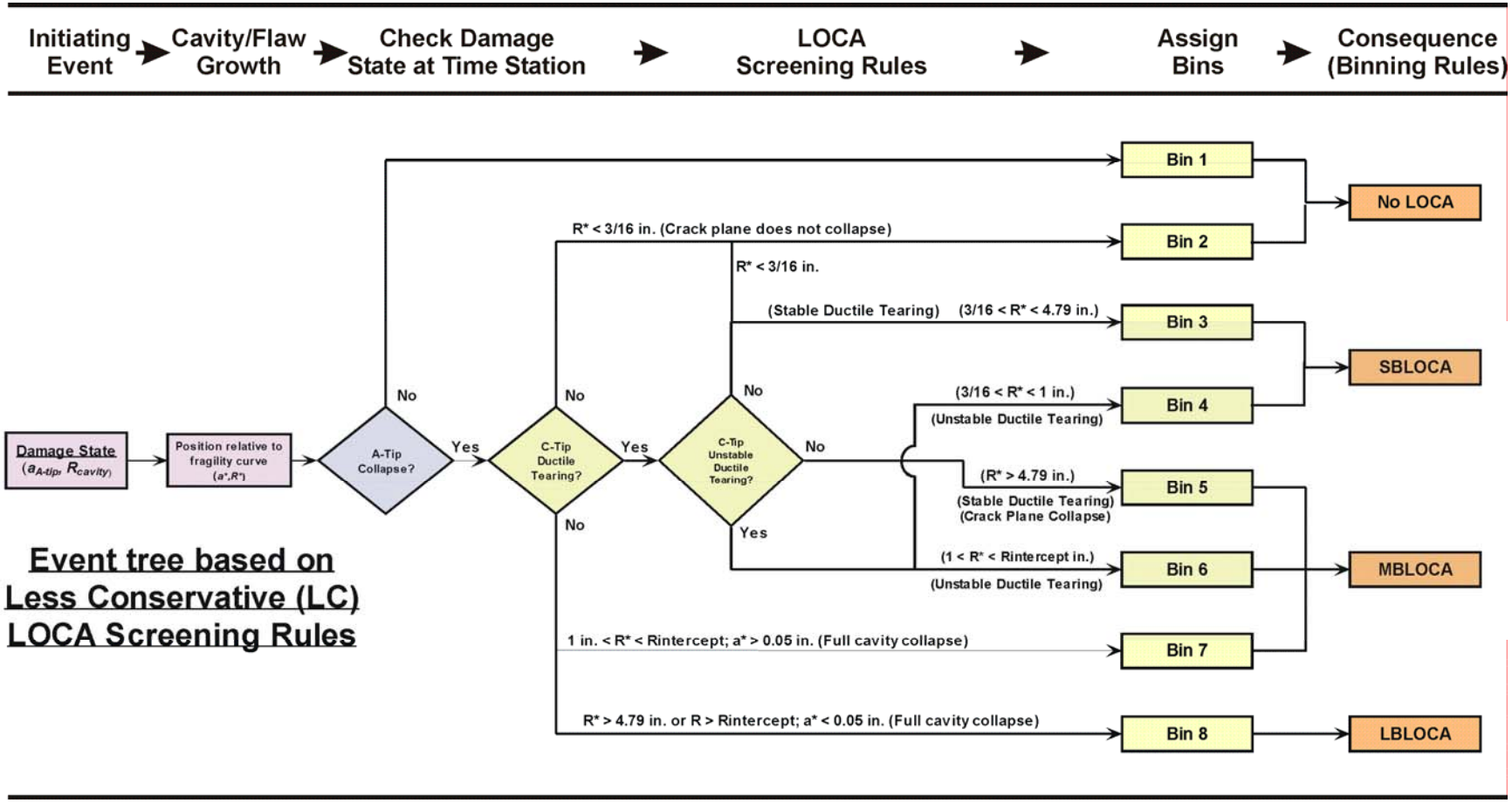

(c)

Fig. 41. (continued) and (c) less conservative (LC) rules.

2.2.10 LOCA Break Size Definitions

Effective break sizes were provided by NRC/RES to define a range of Loss of Coolant Accident (LOCA) characterizations. These effective break sizes are presented in Table 7.

Table 7. LOCA Sizes Defined by Effective Break Sizes

LOCA SIZE	Wastage Area (in^2)	Effective Cavity Footprint Diameter (in)	Effective Cavity Footprint Radius (in)
SBLOCA	0.1104 to 3.14	0.375 to 2	0.1875 to 1
MBLOCA	3.14 to 72	2 to 9.57	1 to 4.79
LBLOCA	> 72	> 9.57	> 4.79

2.2.11 Cavity Growth-Shape Scaling Rules

Scaling factors are applied to the sampled cavity wastage rates, $dR_{cavity}/d\tau$, to approximate different assumptions on how the wastage cavity's unbacked area grows over time. The growth-shape scaling factors are as follows:

(1) $\Phi_{R_{cavity}} = \frac{1}{2}$ (designated as LC) to approximate the cavity growing as a semi-ellipse with the major axis growing twice as fast as the minor axis

(2) $\Phi_{R_{cavity}} = \frac{1}{\sqrt{2}}$ (designated as BE) to approximate the cavity growing as a semi-circle

(3) $\Phi_{R_{cavity}} = 1$ (designated as MC) to approximate the cavity growing as a complete circle

where Eq. (55) is now modified to be

$$\widehat{\frac{dR_{cavity}}{d\tau}} \sim \Phi_{R_{cavity}} \times D_{(dR/d\tau)} \tag{78}$$

3 Results and Discussion

3.1 Results of Deterministic FEM Analysis

The three Davis-Besse Flaw Models, embedded independently as surface flaws on the exposed side of the unbacked cladding, were run with the Davis-Besse wastage-cavity ABAQUS FEM submodel, starting from a zero pressure load up to the point of numerical stability. The resulting driving-force load paths ($J_{applied}$ vs Pressure) are presented in Fig. 42, where J_{Ic} percentiles from the Davis-Besse lognormal model (see Fig. 19) have been overlaid on the plot. At an operating pressure of 2165 psi, the cumulative probabilities that the Model-Flaw driving forces will exceed the ductile-tearing initiation toughness of the Davis-Besse cladding are 9.6×10^{-13} %, 3.1×10^{-11} %, and 5.0×10^{-6} % for Model Flaws #1, #2, and #3, respectively. At the relief-valve setpoint pressure of 2500 psi, the probabilities of nonexceedance are 2.6×10^{-7} %, 7.9×10^{-6} %, and 1.1×10^{-1} % for Model Flaws #1, #2, and #3, respectively. Table 8 presents the pressures, predicted by the Davis-Besse FEM submodel, that were required to initiate stable ductile tearing in the three Model Flaws at the 5th, 50th, and 95th J_{Ic} percentiles. The margins against ductile-tearing initiation of the Model Flaws at the normal operating pressure of 2165 psi are presented in Table 8a, and the margins at the relief-valve setpoint pressure of 2500 psi are given in Table 8b. For Model Flaw #3 the margin against ductile initiation ranges from 1.2 to 1.5 (with a median of 1.4) at the operating pressure and from 1.08 to 1.3 (with a median of 1.2) at the relief-valve setpoint pressure.

In Fig. 43, the load paths under increasing pressure are presented for Model Flaws 1 (Fig. 43a) and 3 (Fig 43b) in terms of flaw driving forces ($J_{submodel}$) vs applied pressure. These FEM driving forces are also compared to those predicted by Eq. (44) which was developed from 2 in. long flaws centered in a circular burst disk. It is apparent that flaws in the Davis-Besse wastage-cavity are under significantly different constraint conditions than similar flaws in a circular burst disk. To establish an approximate driving-force similitude between the detailed Davis-Besse submodel ($J_{submodel}$) and the Monte Carlo model (J_{MC}), a driving-force scaling rule was developed as shown in Fig. 43c. Equation (44) now becomes

$$J_{applied}\left(a_{A-tip}, R_{cavity}\right) = \Phi_{flaw} \exp\left\{C_0 + \frac{C_1}{\sqrt{a_{A-tip}}} + \frac{C_2}{a_{A-tip}} + C_3 R_{cavity} + C_4 R_{cavity} \ln\left(R_{cavity}\right) + C_5\left[\ln\left(R_{cavity}\right)\sqrt{R_{cavity}}\right] + C_6\left[\ln\left(R_{cavity}\right)\right]^2\right\} \quad (79)$$

where

$$\Phi_{flaw} = 0.64335 - 0.71197\left(\frac{a_{A-tip}}{t_{clad}}\right)$$

Table 8a. DB Submodel Pressures to Initiate Ductile Tearing for the 5th, 50th , and 95th Percentiles with Margins Against Ductile Initiation at the Operating Pressure of 2165 psi

Model Flaw	Flaw Depth $a_{A\text{-}tip}$ (in)	Flaw Length L (in)	Pressures Required for J_{Ic} Probabilities and Margins at Operating Pressure					
			5% (psi)	Margin for Initiation	50% (psi)	Margin for Initiation	95% (psi)	Margin for Initiation
1	0.0650	0.660	3963	1.83	5186	2.40	6503	3.00
2	0.0995	0.606	3109	1.44	3553	1.64	4375	2.02
3	0.0995	2.000	2709	1.25	2985	1.38	3306	1.53

Table 8b. DB Submodel Pressures to Initiate Ductile Tearing for the 5th, 50th , and 95th Percentiles with Margins Against Ductile Initiation at the Relief-Valve Setpoint Pressure of 2500 psi

Model Flaw	Flaw Depth $a_{A\text{-}tip}$ (in)	Flaw Length L (in)	Pressures Required for J_{Ic} Probabilities and Margins at Safety Valve Setpoint					
			5% (psi)	Margin for Initiation	50% (psi)	Margin for Initiation	95% (psi)	Margin for Initiation
1	0.0650	0.660	3963	1.59	5186	2.07	6503	2.60
2	0.0995	0.606	3109	1.24	3553	1.42	4375	1.75
3	0.0995	2.000	2709	1.08	2985	1.19	3306	1.32

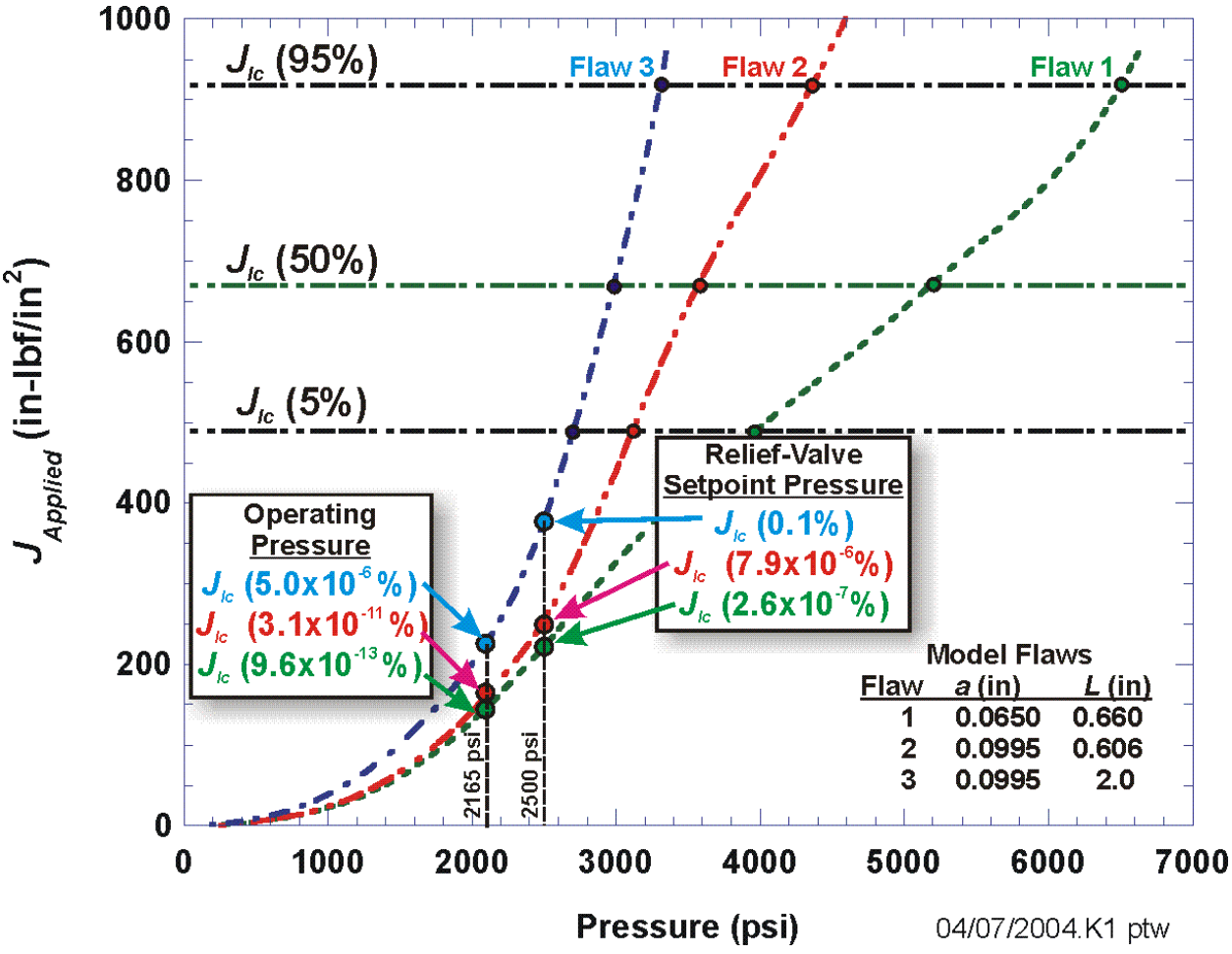

Fig. 42. Load paths ($J_{applied}$ vs Applied Pressure) for three model surface flaws placed in the Davis-Besse finite-element submodel compared to the cladding material's ductile-tearing initiation fracture toughness with cumulative probabilities from the lognormal model shown in Fig. 19.

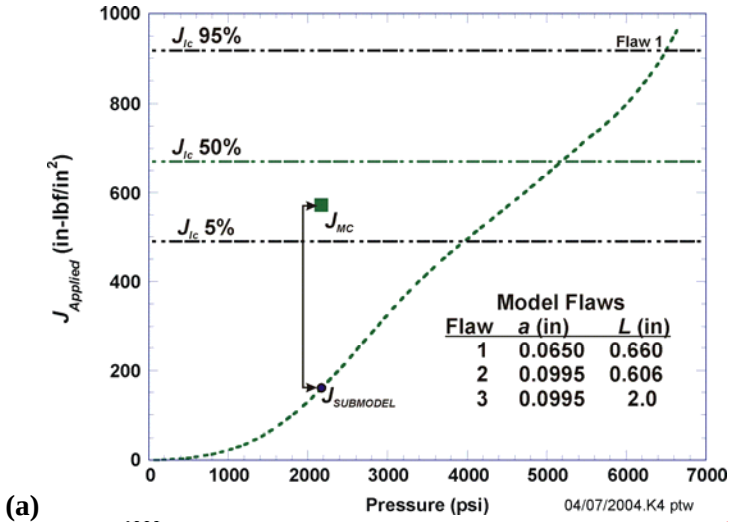

(a)

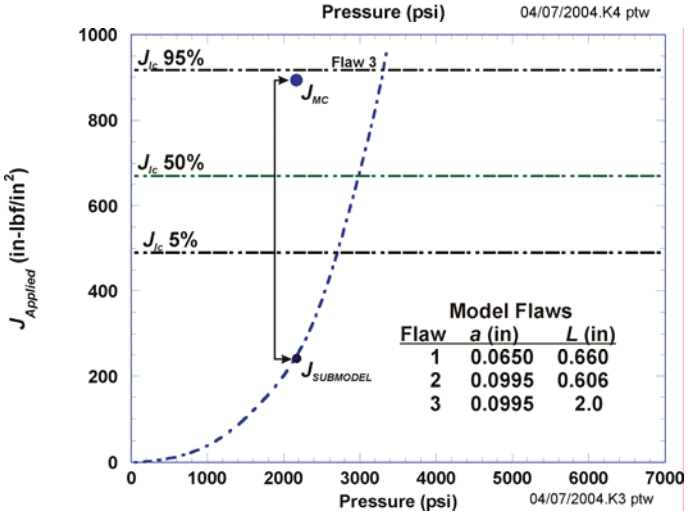

(b)

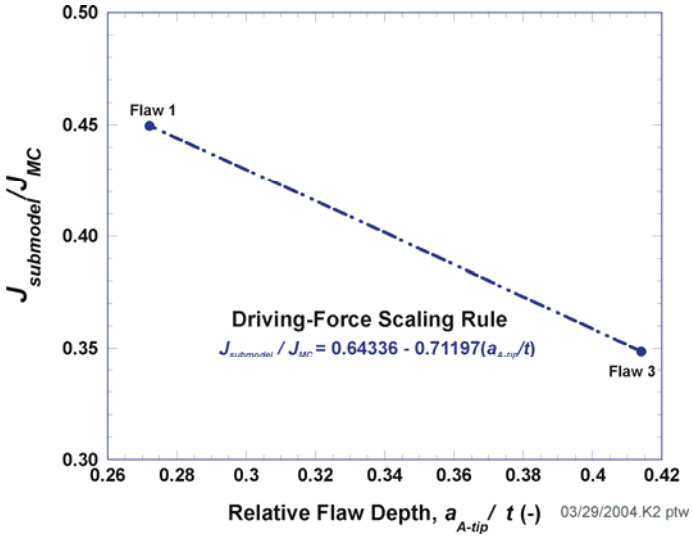

(c)

Fig. 43. A scaling rule is applied to the Driving-Force Model (Eq. (44) to bring the Monte Carlo model driving forces into agreement with the results of the detailed FEM wastage cavity submodel (a) scaling required for Model Flaw 1, (b) scaling required for Model Flaw 3, and (c) linear fit developed between Model Flaws 1 and 3.

3.2 Cladding Capacity Analysis (CCA) – Sensitivity Study Results

For the *Cladding Capacity Analysis* (CCA) study, which treats the damage state discovered in Davis Besse on February 16, 2002 as both known and certain, a matrix of 21 cases (see Table 9) was constructed to investigate the sensitivity of the *best-estimate* case (CCA-001) to many of the assumptions that were applied in the construction of the Davis-Besse Monte Carlo damage-state model. The conditions for each of the CCA cases are presented in Table 9 in which the perturbed conditions (relative to Case CCA-001) are highlighted in **red** for Cases CCA-002 to CCA-021. The results of all 21 cases are presented in Table 10 for three time stations: (1) the *time of discovery* (TOD), 16 February 2002, τ_1, (2) 6 weeks after the time of discovery, τ_2, and (3) 1 year after the time of discovery, τ_3. The cumulative probabilities of a LOCA occurring are further partitioned into small-break, medium-break, and large-break LOCAS as defined in Table 7. For the best-estimate Case CCA-001, the calculated probability of a LOCA occurring at τ_1 is 0%, as required by the fact that at the time of discovery the Davis-Besse wastage cavity had not failed in terms of breaching the integrity of the pressure boundary.

3.2.1 Convergence of Monte Carlo Simulations

Figure 44 plots the coefficient of variation, *COV*, for the total cumulative probability of a LOCA (irrespective of break size) occurring at τ_3, one year after the time of discovery. The *COV* of p_f is defined as the ratio of its estimated standard deviation to its estimated mean, where the *COV* is a function of the number of Monte Carlo trials, *N*.

$$\mathrm{COV}\left[\, p_f\left(\tau_k\right)\right] = \frac{\sqrt{\mathrm{var}\left[\, p_f\left(\tau_k, N\right)\right]}}{p_f\left(\tau_k, N\right)} = \frac{\sqrt{\dfrac{\left(1 - p_f\left(\tau_k, N\right)\right) p_f\left(\tau_k, N\right)}{N}}}{p_f\left(\tau_k, N\right)} \tag{80}$$

where the cumulative probability of failure is estimated by Eq. (75). The convergence history shown in Fig. 44 indicates that the cumulative LOCA probabilities estimated by the Monte Carlo code are approaching an asymptotic solution after 50,000 realizations (or 100,000 antithetic-paired trials).

Table 9. Case Matrix for Cladding Capacity Analysis (CCA)

Case Number	A-Tip Ductile Tearing	A-Tip Instability Tested?	As-Found Atip Depth (in)	Sampling of Plastic Flow Props.	Scale Driving Forces	Sampling Distributions $dR/d\tau$ (in/yr)	Sampling Distributions $da/d\tau$ (in/month)	Sampling Distribution Group	Cavity Growth Rules	LOCA Binning Rules
CCA-001	Yes	Yes	0.0650	bivariate lognormal	Yes	beta-1	Weibull	BE	BE	BE
CCA-002	Yes	Yes	0.0650	bivariate lognormal	Yes	beta-1	Weibull	BE	MC	BE
CCA-003	Yes	Yes	0.0650	bivariate lognormal	Yes	beta-1	Weibull	BE	LC	BE
CCA-004	Yes	Yes	0.0650	bivariate lognormal	Yes	triangluar	lognormal	MC	MC	MC
CCA-005	Yes	Yes	0.0650	bivariate lognormal	Yes	Weibull	uniform	LC	LC	LC
CCA-006	Yes	Yes	0.0650	bivariate lognormal	Yes	triangluar	Weibull	mixed	BE	BE
CCA-007	Yes	Yes	0.0650	bivariate lognormal	Yes	Weibull	Weibull	mixed	BE	BE
CCA-008	Yes	Yes	0.0650	bivariate lognormal	Yes	beta-1	lognormal	mixed	BE	BE
CCA-009	Yes	Yes	0.0650	bivariate lognormal	Yes	beta-1	uniform	mixed	BE	BE
CCA-010	Yes	Yes	0.0650	bivariate lognormal	Yes	beta-2	Weibull	mixed	BE	BE
CCA-011	Yes	No	0.0650	bivariate lognormal	Yes	beta-1	Weibull	BE	BE	BE
CCA-012	Yes	No	0.0650	bivariate lognormal	No	beta-1	Weibull	BE	BE	BE
CCA-013	No	No	0.0650	bivariate lognormal	No	beta-1	Weibull	BE	BE	BE
CCA-014	Yes	Yes	0.0650	bivariate lognormal	No	beta-1	Weibull	BE	BE	BE
CCA-015	Yes	Yes	0.0650	bivariate lognormal	Yes	beta-1	Weibull	BE	BE	LC
CCA-016	Yes	Yes	0.0650	bivariate lognormal	Yes	beta-1	Weibull	BE	BE	MC
CCA-017	Yes	Yes	0.0350	bivariate lognormal	Yes	beta-1	Weibull	BE	BE	BE
CCA-018	Yes	Yes	0.0995	bivariate lognormal	Yes	beta-1	Weibull	BE	BE	BE
CCA-019	Yes	Yes	0.0650	inverse Weibull; r = 1	Yes	beta-1	Weibull	BE	BE	BE
CCA-020	Yes	Yes	0.0650	bivariate gamma	Yes	beta-1	Weibull	BE	BE	BE
CCA-021	Yes	Yes	0.0650	inverse Weibull; r = 0	Yes	beta-1	Weibull	BE	BE	BE

Table. 10. Monte Carlo Results – Summary of LOCA Probabilities (N = 50,000)

Case Number	LOCA Probabilities (%) Time of Discovery				LOCA Probabilities (%) 6 weeks after Time of Discovery				LOCA Probabilities (%) 1 year after Time of Discovery			
	No LOCA	SBLOCA	MBLOCA	LBLOCA	No LOCA	SBLOCA	MBLOCA	LBLOCA	No LOCA	SBLOCA	MBLOCA	LBLOCA
CCA-001	100.000%	0.000%	0.000%	0.000%	99.757%	0.243%	0.000%	0.000%	29.218%	64.906%	5.188%	0.688%
CCA-002	100.000%	0.000%	0.000%	0.000%	99.562%	0.438%	0.000%	0.000%	24.732%	65.879%	8.220%	1.169%
CCA-003	100.000%	0.000%	0.000%	0.000%	99.809%	0.191%	0.000%	0.000%	33.895%	62.950%	2.832%	0.323%
CCA-004	100.000%	0.000%	0.000%	0.000%	99.288%	0.000%	0.712%	0.000%	16.919%	0.000%	79.181%	3.900%
CCA-005	100.000%	0.000%	0.000%	0.000%	87.919%	12.057%	0.024%	0.000%	5.535%	93.852%	0.613%	0.000%
CCA-006	100.000%	0.000%	0.000%	0.000%	99.693%	0.307%	0.000%	0.000%	20.304%	70.594%	8.054%	1.048%
CCA-007	100.000%	0.000%	0.000%	0.000%	99.732%	0.268%	0.000%	0.000%	29.043%	65.682%	4.700%	0.575%
CCA-008	100.000%	0.000%	0.000%	0.000%	99.679%	0.321%	0.000%	0.000%	46.402%	44.567%	7.803%	1.228%
CCA-009	100.000%	0.000%	0.000%	0.000%	86.892%	13.108%	0.000%	0.000%	4.288%	94.664%	0.944%	0.104%
CCA-010	100.000%	0.000%	0.000%	0.000%	99.835%	0.165%	0.000%	0.000%	39.798%	59.518%	0.659%	0.025%
CCA-011	99.999%	0.001%	0.000%	0.000%	99.685%	0.315%	0.000%	0.000%	28.623%	65.634%	5.100%	0.643%
CCA-012	79.667%	20.333%	0.000%	0.000%	20.309%	79.691%	0.000%	0.000%	0.207%	99.793%	0.000%	0.000%
CCA-013	100.000%	0.000%	0.000%	0.000%	99.763%	0.237%	0.000%	0.000%	29.265%	64.750%	5.172%	0.813%
CCA-014	99.826%	0.174%	0.000%	0.000%	84.032%	15.968%	0.000%	0.000%	6.526%	93.474%	0.000%	0.000%
CCA-015	100.000%	0.000%	0.000%	0.000%	99.757%	0.243%	0.000%	0.000%	29.218%	64.649%	6.133%	0.000%
CCA-016	100.000%	0.000%	0.000%	0.000%	99.757%	0.000%	0.243%	0.000%	29.218%	0.000%	69.830%	0.952%
CCA-017	100.000%	0.000%	0.000%	0.000%	99.964%	0.036%	0.000%	0.000%	40.558%	46.940%	3.533%	8.969%
CCA-018	100.000%	0.000%	0.000%	0.000%	97.923%	2.077%	0.000%	0.000%	17.059%	82.867%	0.074%	0.000%
CCA-019	100.000%	0.000%	0.000%	0.000%	99.753%	0.247%	0.000%	0.000%	29.416%	64.615%	5.165%	0.804%
CCA-020	100.000%	0.000%	0.000%	0.000%	99.759%	0.241%	0.000%	0.000%	29.507%	64.455%	5.172%	0.866%
CCA-021	100.000%	0.000%	0.000%	0.000%	99.760%	0.240%	0.000%	0.000%	29.403%	64.624%	5.189%	0.784%

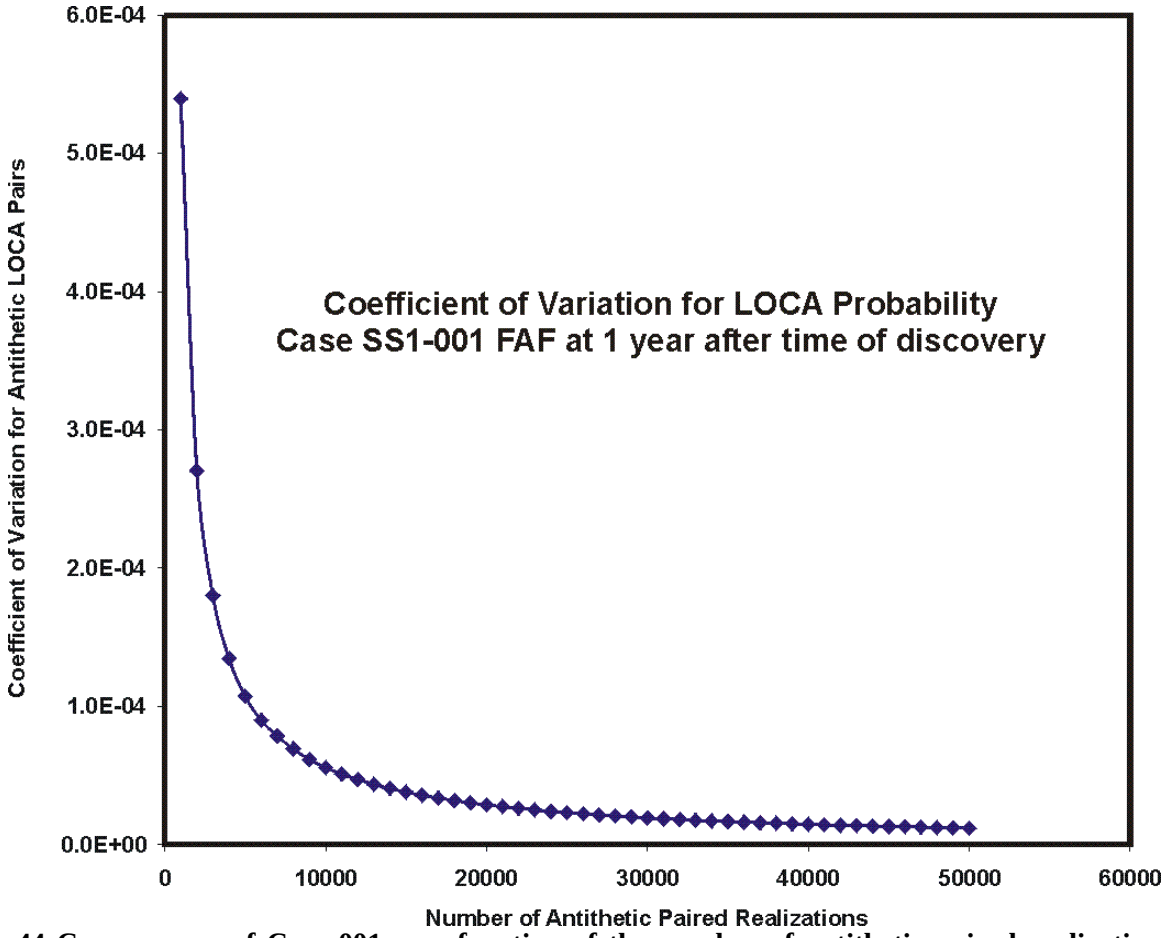

Fig. 44. Convergence of Case 001 as a function of the number of antithetic paired realizations at 1 year after time of discovery.

3.2.2 Best-Estimate CCA Results

The results of Case CCA-001 present *best-estimate* cumulative probabilities of a LOCA (see Fig. 45a) occurring over a time period from 1 year before the time of discovery (TOD) up to an elapsed time of 500 days after TOD. These probabilities are intended to answer the question of how long could the Davis-Besse RPV have continued in service if the wastage cavity *had not been discovered* on 16 February 2002. From Table 10, the best-estimate case indicates that 6 weeks after 16 February 2002 the estimated cumulative probability of an SBLOCA occurring was approximately 0.24 %. The probabilities of an MBLOCA or LBLOCA occurring for this elapsed time are 0%. After 1 year (on 16 February 2003), the cumulative probability of a failure of the pressure boundary was approximately 70.8 %. These LOCA probabilities have been further binned into 64.9 % for an SBLOCA, 5.2 % for an MBLOCA, and 0.7 % for an LBLOCA. The SBLOCA probabilities at this time are exclusively Bin 3 (see Fig. 41a) type failures in which, after the A-tip has failed, both the flaw's C-tip and the full cavity itself remains stable.

The results from Cases CCA-017 and CCA-018 can be used to provide an approximate 90 % confidence interval covering the best estimate for the median failure of the cladding, as predicted by the results of Case CCA-001. The times to failure after TOD for these cases are presented in Table 11 for 5 %, 50 %, and 95 % cumulative probabilities, and the failure histories are plotted in Fig. 45b. These results predict that, at a confidence level of 90%, Davis-Besse could have continued operating from 2 to 22 months before cladding failure would be expected.

3.2.3 Results of the CCA Sensitivity Study

The sensitivity of the *best-estimate* Monte Carlo results to variations in the input conditions and statistical distributions are presented in Figs. 46-48.

Figure 46a examines the sensitivity of the overall LOCA probability to the assumed flaw depth at the time of discovery. The sensitivity of the LOCA probability to the assumed cavity growth/shape rule is presented in Fig. 46b. The more conservative cavity growth/shape rule (the cavity grows equally in all directions, i.e., an expanding circular footprint) produces the highest cumulative probabilities of failure.

Table 11. Times to Failure after TOD

Model Flaw Depth at TOD (in)	Time to Failure After TOD at Cumulative Probability 5% (days)/(months)	50% (days)/(months)	95% (days)/(months)
0.035	103/3.4	304/10	1318/43.3
0.065	79/2.6	232/7.6	982/32.3
0.1	52/1.7	150/4.9	678/22.3

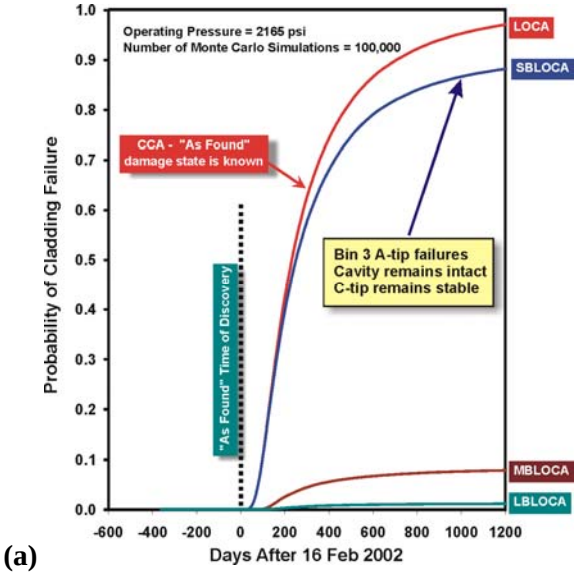

(a)

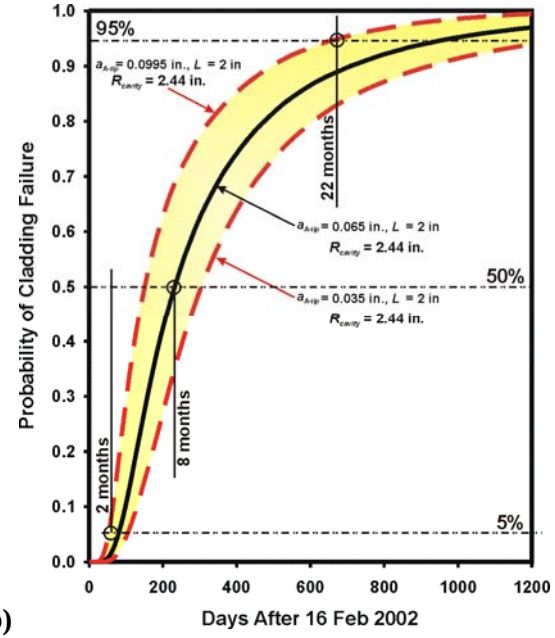

(b)

Fig. 45. LOCA probability history for: (a) the best-estimate Cladding Capacity Analysis (CCA) case (Case CCA-001) with a further categorization into small-break LOCA (SBLOCA), medium-break LOCA (MBLOCA), and large-break LOCAs (LBLOCA) and (b) varying model flaw depth at TOD, 0.035 in., 0.065 in., and 0.0995 in.

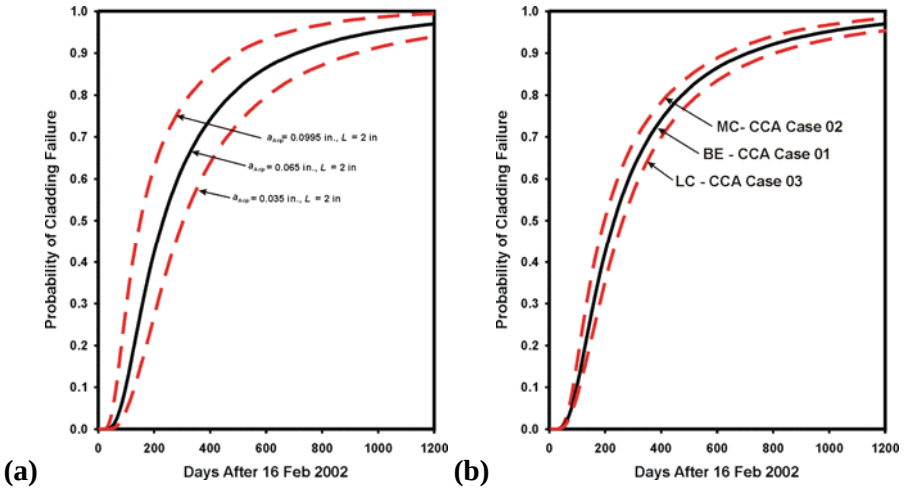

Fig. 46. Sensitivity of CCA LOCA probabilities to: (a) model flaw depth at TOD (b) cavity growth/shape rules.

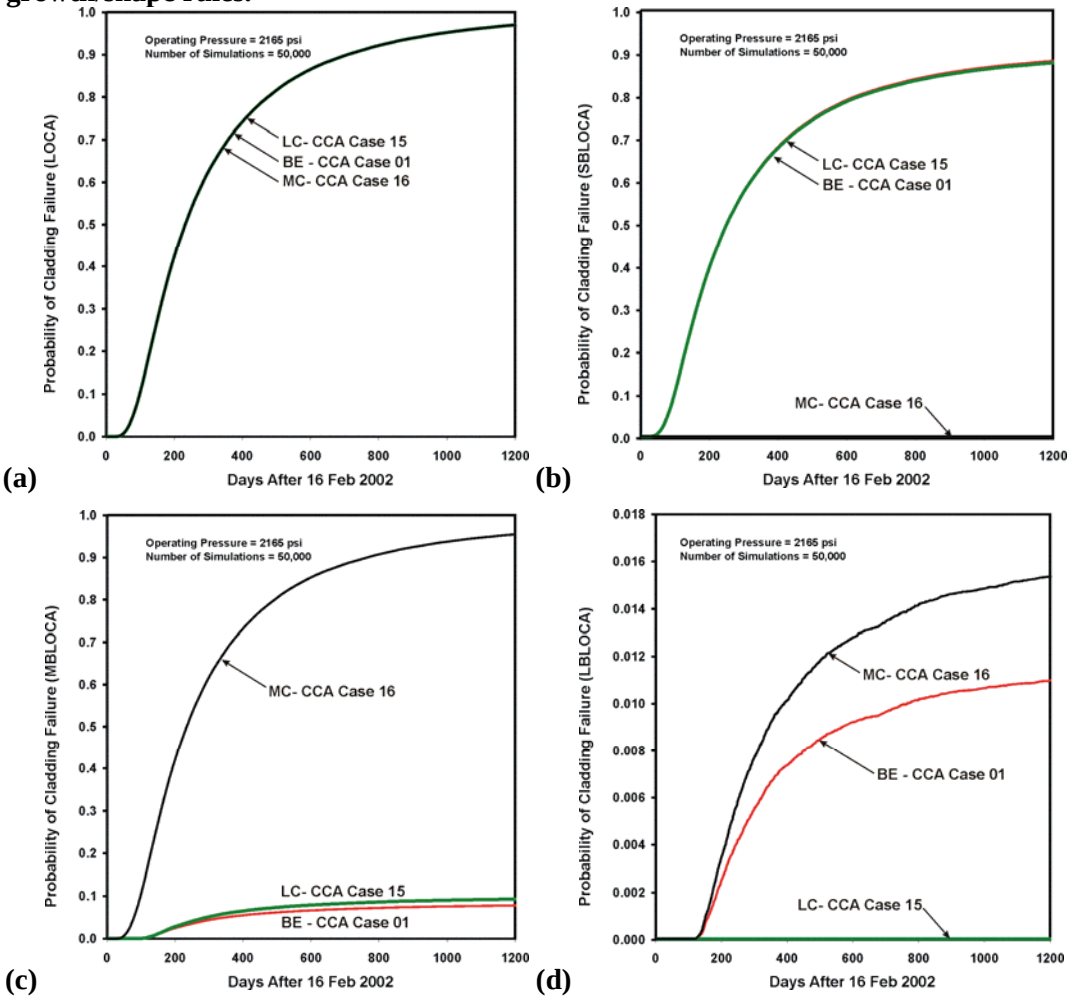

Fig. 47. Sensitivity of CCA LOCA probabilities to LOCA binning rules (a) total LOCA probability, (b) SBLOCA probability, (c) MBLOCA probability and (d) LBLOCA probability.

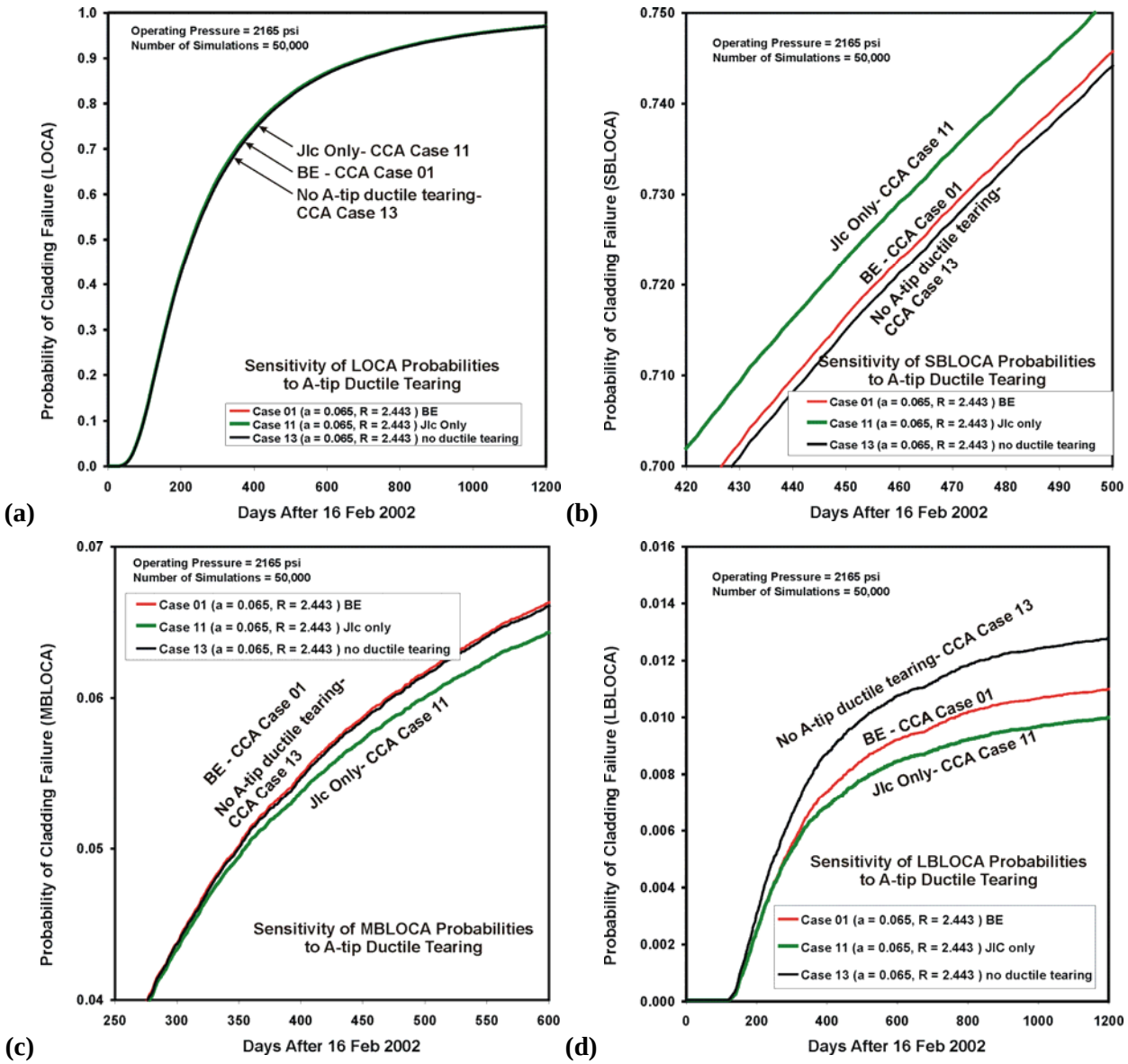

Fig. 48. Sensitivity of CCA LOCA probabilities to modeling of A-tip ductile tearing (a) total LOCA probability, (b) SBLOCA probability, (c) MBLOCA probability and (d) LBLOCA probability.

Figure 47a demonstrates, as required, that the LOCA Binning Rules (see Figs. 41a, 41b, and 41c) influence only the partitioning or binning of the LOCA cumulative probabilities into their size categories and not the overall LOCA probability. The sensitivity of the resulting SBLOCAs, MBLOCAs, and LBLOCAs to the binning rules are shown in Figs. 47b, 47c, and 47d, respectively comparing Case CCA-001 to Cases CCA-015 and CCA-016.

The influence of the treatment of A-tip ductile tearing is presented in Figs. 48 comparing case CCA-001 to cases CCA-011 and CCA-013. In Fig. 48b, the inclusion of A-tip ductile tearing in the analysis produces slightly higher probabilities of SBLOCA relative to applying plastic collapse of the remaining ligament. It is important to note that the flaw continues to grow over time, irrespective of any ductile fracture, because of the flaw's exposure to the corrosive environment of the wastage cavity; therefore, the increased probabilities of failure over time are due the combined effects of both cavity growth and flaw growth. Ductile tearing of the A-tip tends to cause the cavity to fail slightly earlier in time relative to no ductile tearing, thus increasing the probability of SBLOCAs and reducing the probabilities of MBLOCAs and LBLOCAs.

Additional sensitivities are investigated in the Case Matrix, such as the influence of the statistical distributions assumed for the cavity and flaw growth rates (see Cases CCA-006 to CCA-010) and the influence of the combined Sampling Distribution groups, the cavity growth/shape rules, and the LOCA Binning Rules (see Cases CCA-004 and CCA-005). Cases CCA-001 and CCA-011 indicate that using A-tip ductile-tearing initiation compared to A-tip ductile-tearing instability as the A-tip failure criterion produces only slightly different LOCA probabilities. The much more significant influence of correctly scaling the Monte Carlo model driving forces to establish similitude with the detailed Davis-Besse submodel is demonstrated by comparing Case CCA-001 to Case CCA-012.

3.3 Accident Sequence Precursor Analysis – Best Estimate and Sensitivity Study Results

As discussed in Sect. 2.2.5.3, for ASP analyses the damage state at TOD is treated as uncertain, and two additional distributions are sampled in order to provide an estimate for the effective cavity radius, R_1, and model flaw depth, a_1, at TOD. These two distributions are the effective cavity radius at 1 year before TOD, R_0, and the elapsed time since flaw initiation, $\Delta\tau_{flaw-ini}$. Distributions were originally developed based on the results of the Expert Elicitation discussed in Sect. 2.2.6. These distributions were then modified slightly to produce median values for the damage state at TOD that match the assumed fixed values applied in the CCA study. Figures 49 and 50 compare the original derived distributions for R_0 and $\Delta\tau_{flaw-ini}$, respectively, to the modified distributions. These distributions are then combined (see Eq. (70))

with the sampled values of the cavity wastage rate, $dR/d\tau$ (see Fig. 51), and flaw growth rate, $da/d\tau$ (see Fig. 52), to produce distributions for R_1 (Fig. 53) and a_1 (see Fig. 54).

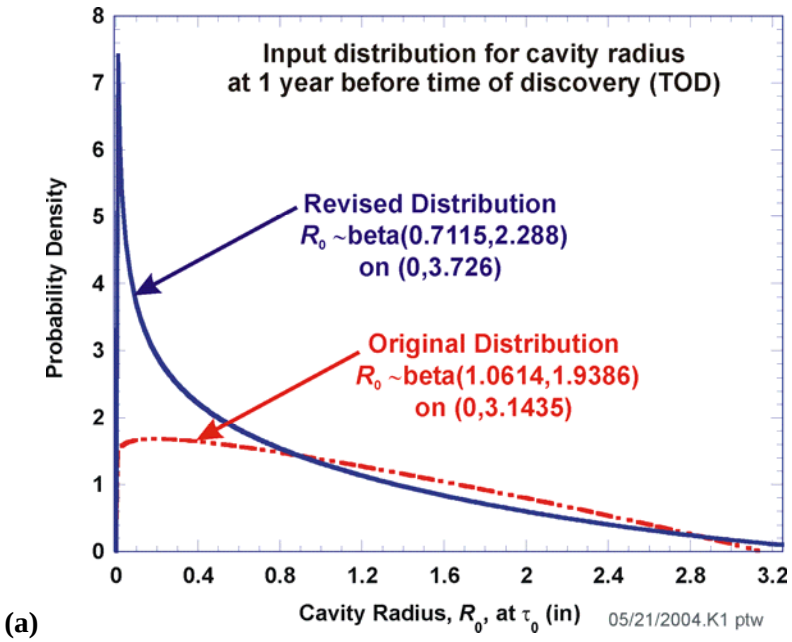

(a)

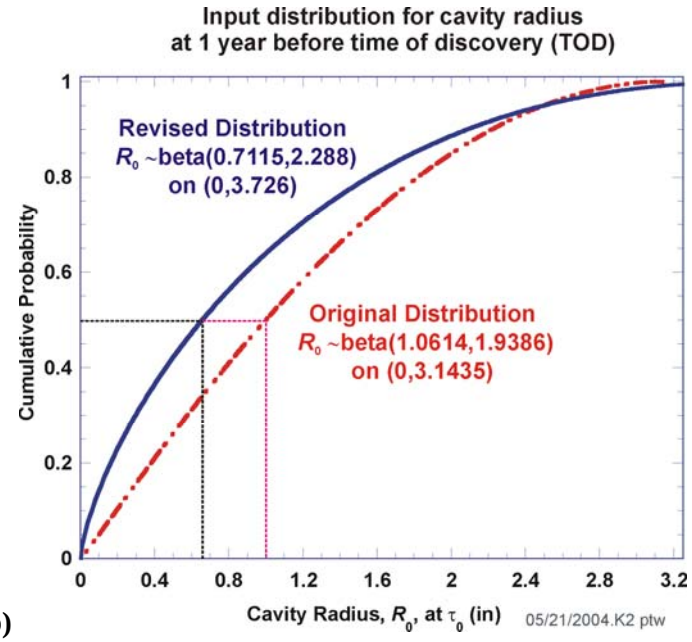

(b)

Fig. 49. Comparison of beta distributions for effective cavity radius at TOD-1 year, τ_0, where the original distribution (based on the results of an *Expert Elicitation*) has been revised to produce a sampled $R_{1(\text{median})}$ closer to the observed valued used in the CCA: (a) probability densities and (b) cumulative probabilities.

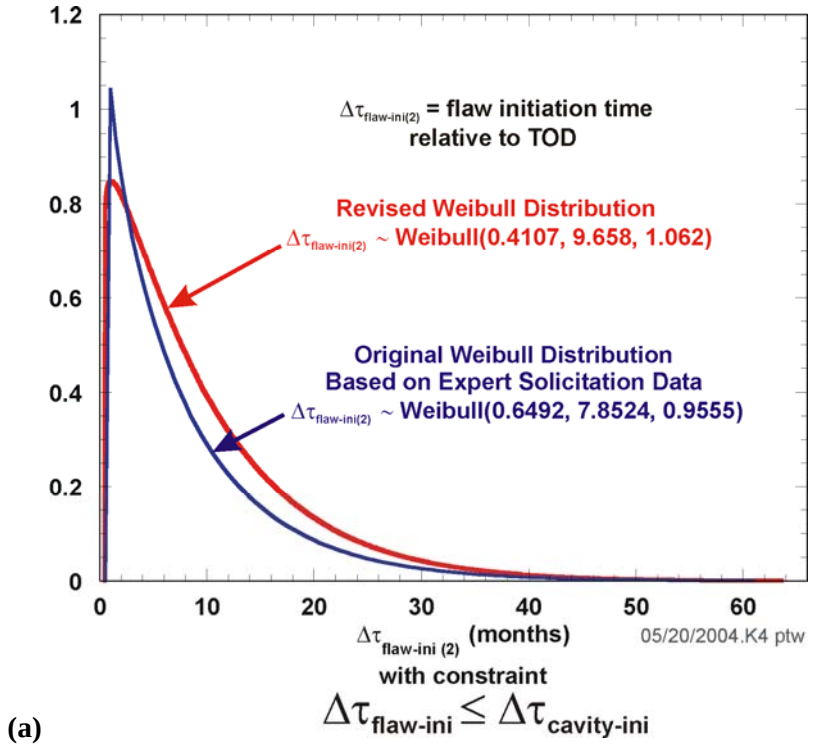

(a)

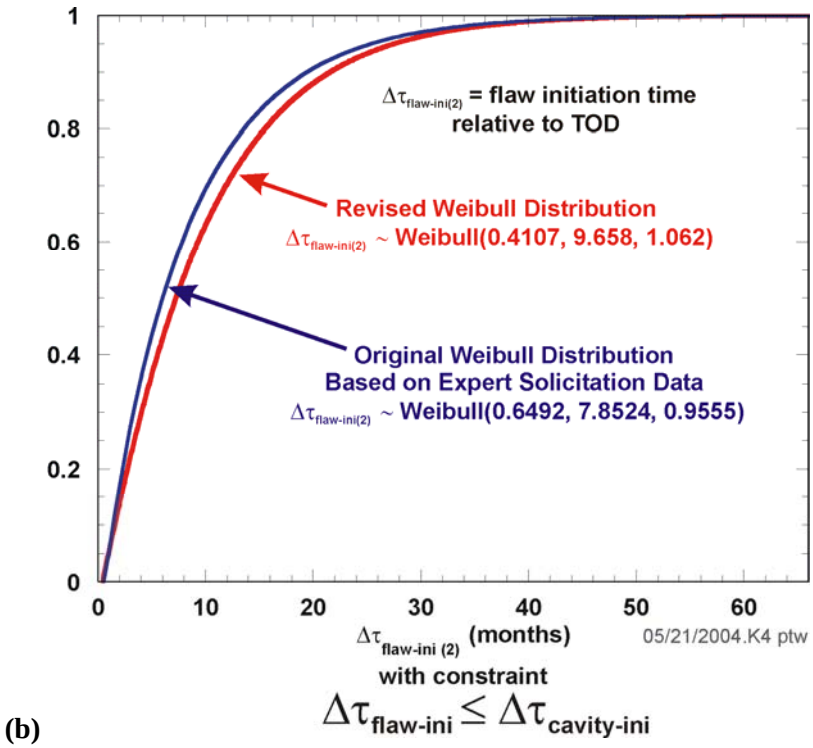

(b)

Fig. 50. Comparison of Weibull distributions for the time of flaw initiation (relative to TOD), $\Delta\tau_{\text{flaw-ini}(2)}$ (see the time line in Fig. 1), where the original distribution (based on the results of an *Expert Elicitation*) has been revised to produce a sampled $R_{1(\text{median})}$ closer to the observed valued used in the CCA: (a) probability densities and (b) cumulative probabilities.

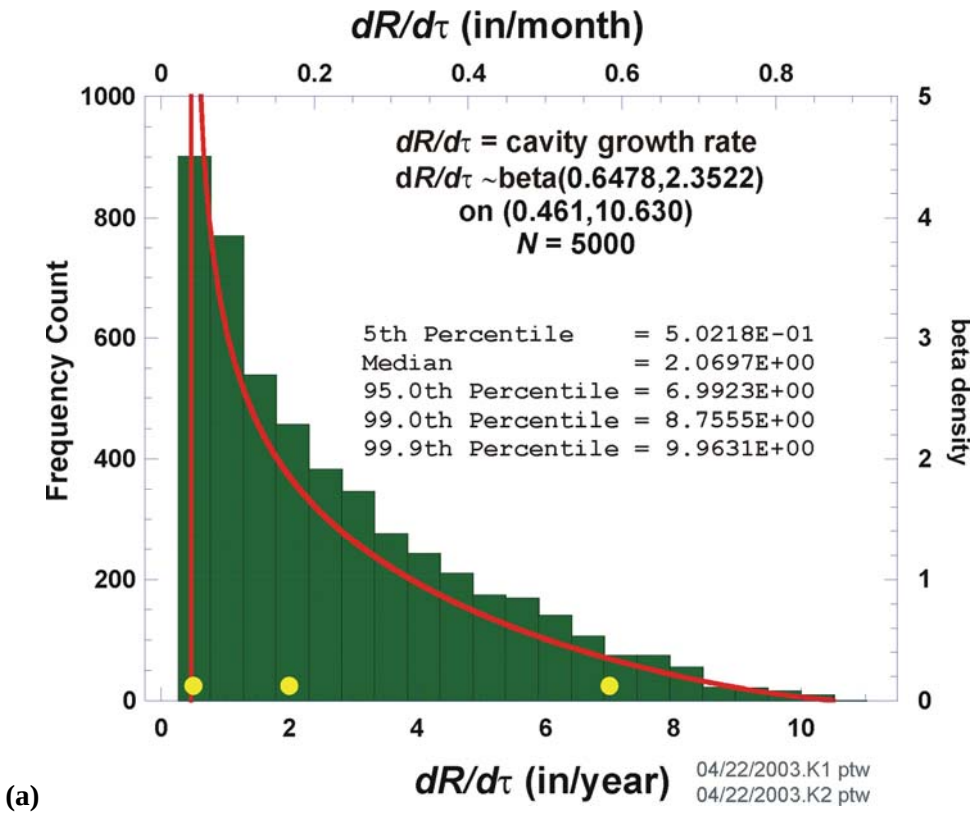

(a)

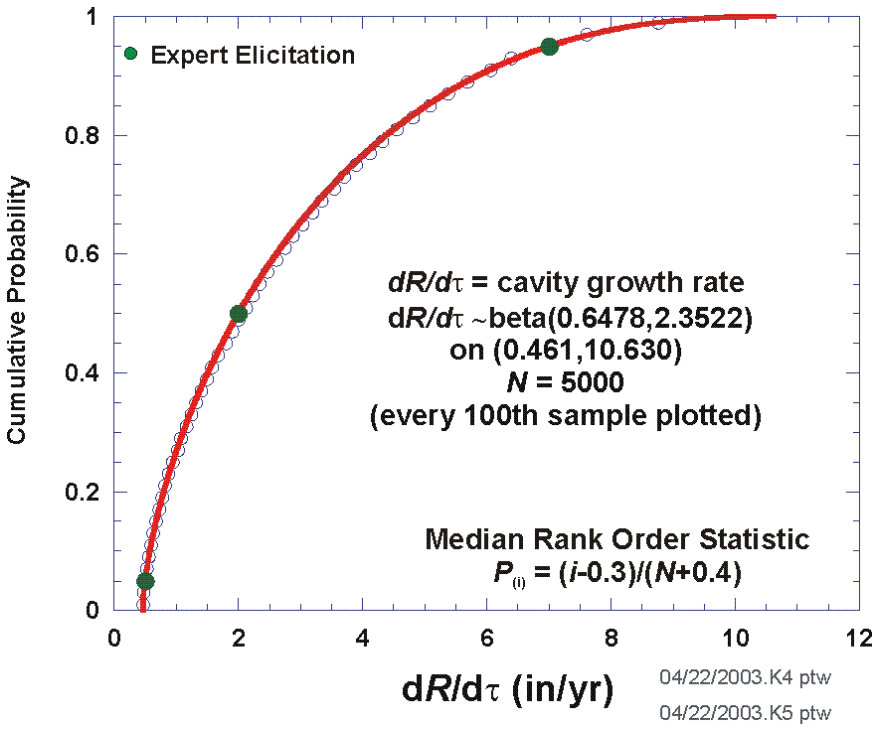

(b)

Fig. 51. Best-estimate sampling distribution for cavity wastage rate compared to sampled values: (a) probability density and (b) cumulative probabilities.

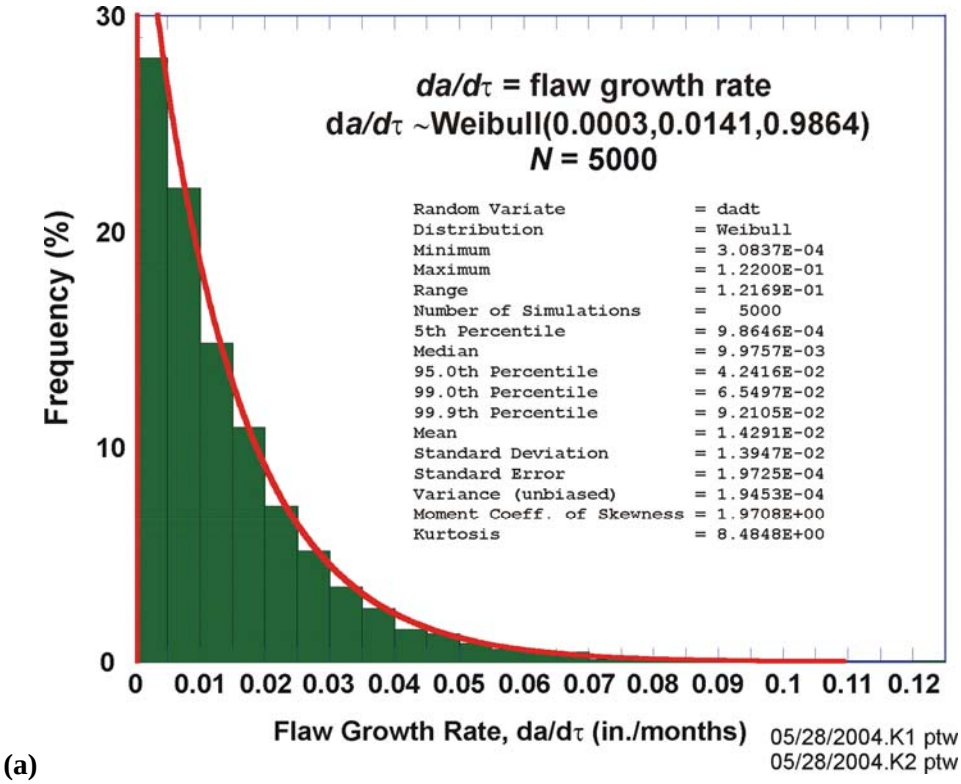

(a)

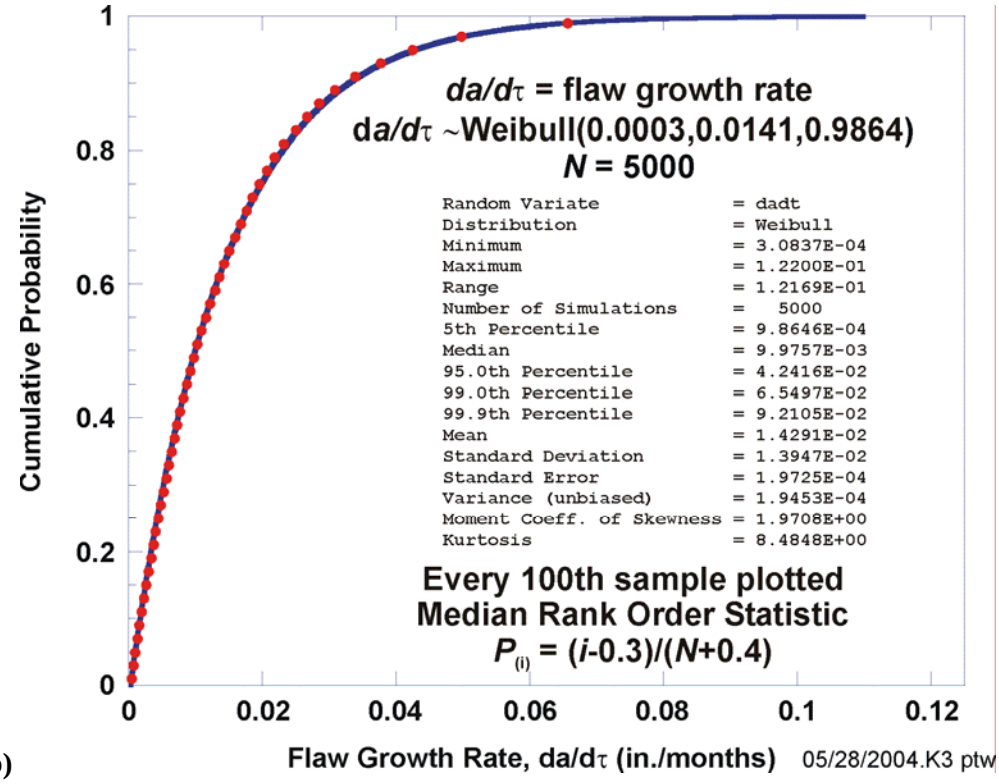

(b)

Fig. 52. Best-estimate sampling distribution for flaw growth rate compared to sampled values: (a) probability density and (b) cumulative probabilities.

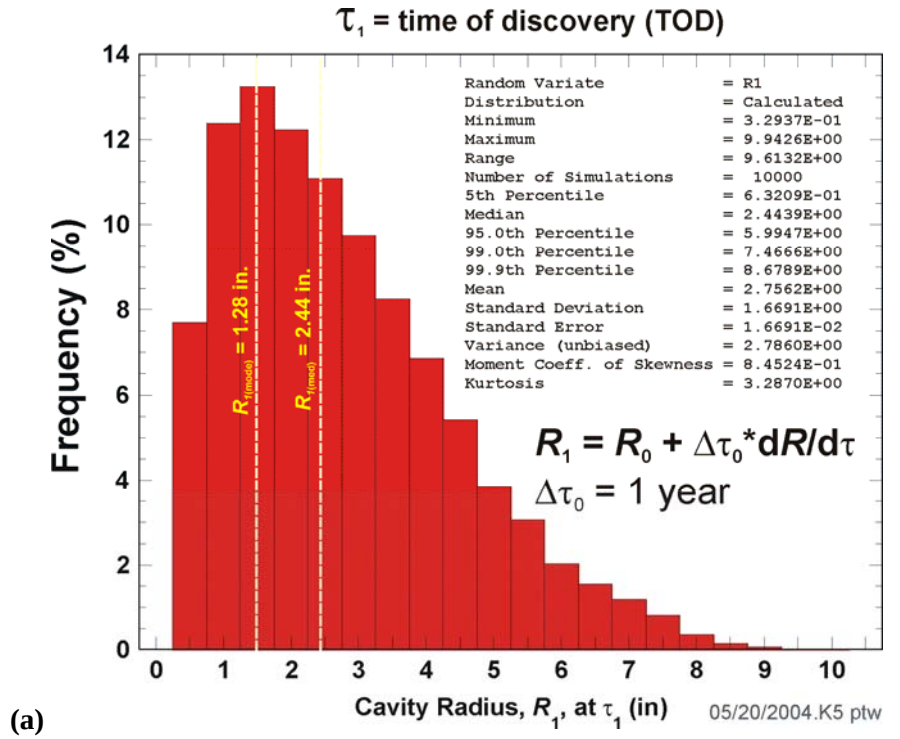

(a)

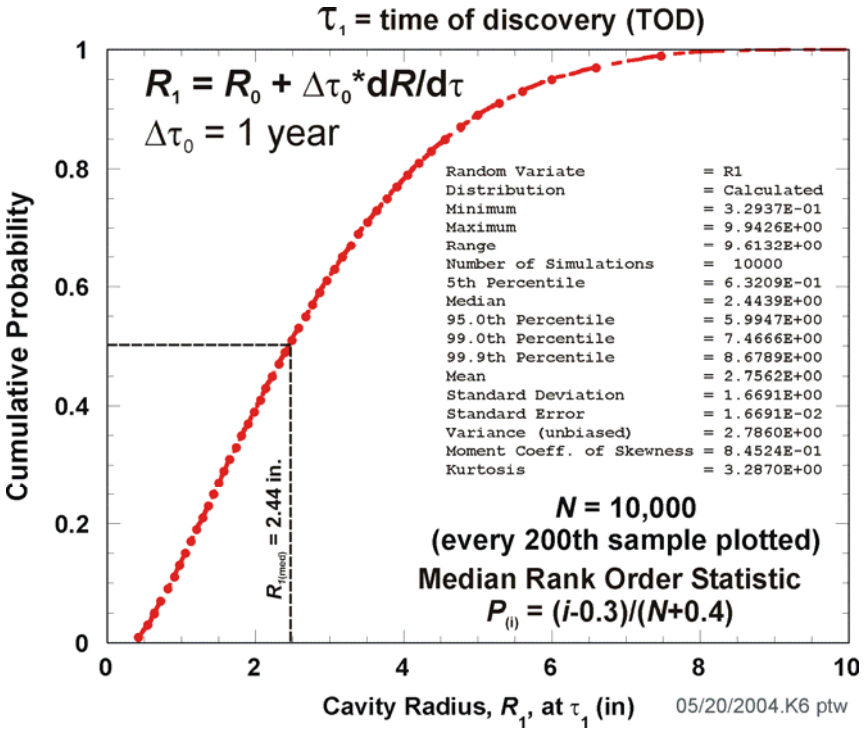

(b)

Fig. 53. Distribution of uncertain effective cavity radius calculated for the time of discovery (TOD): (a) frequency distribution and (b) cumulative probabilities.

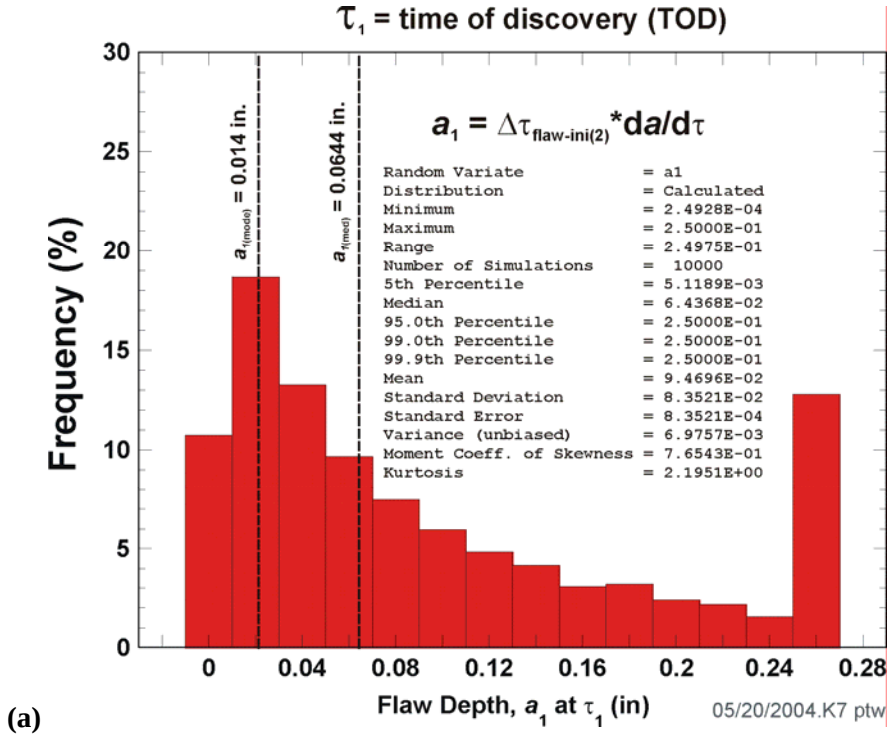

(a)

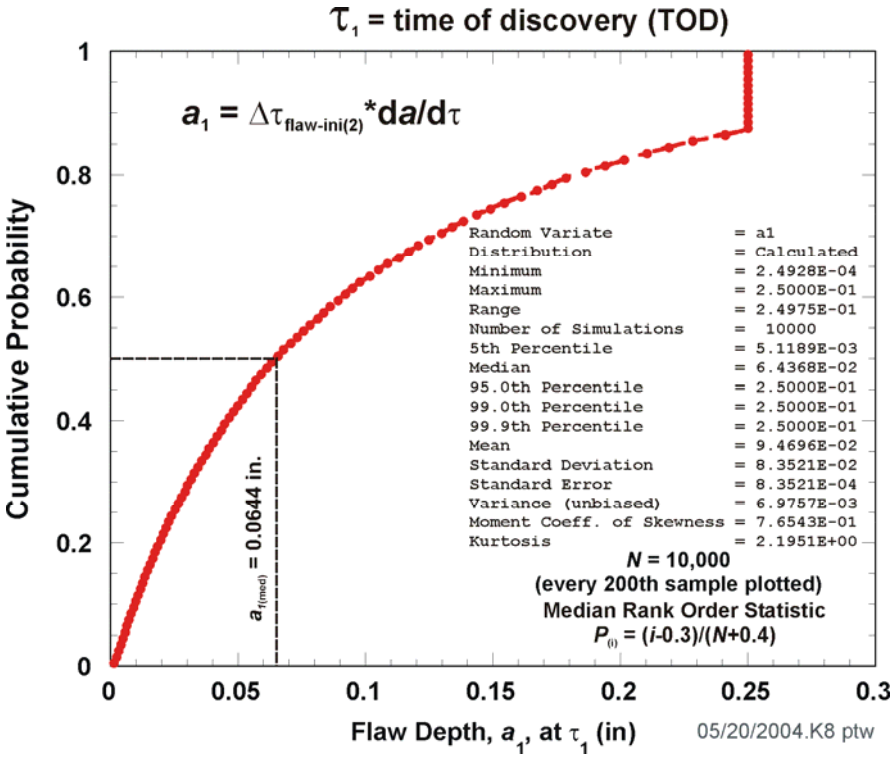

(b)

Fig. 54. Distribution of uncertain effective flaw depth calculated for the time of discovery (TOD): (a) probability density and (b) cumulative probabilities

3.3.1 Case Matrix for ASP Study

Table 12 presents the 9 cases developed for the ASP study, where Case ASP-001 represents the "best-estimate" case. Table 13 gives a layout key that indicates the combination of LOCA screening rules and cavity grow/shape rules used to develop the matrix. Sensitivities to sampling distributions were not addressed in the ASP study; however, they were investigated in the CCA study.

3.3.2 Best-Estimate ASP Results

The time histories for the probability of cladding failure (i.e., the probability of a LOCA) are compared in Fig. 55 for the best-estimate cases of the CCA (CCA-001) and the ASP (ASP-001) studies. At TOD, the probability of a LOCA is 0 % for the CCA conditions and 20.1 % for the ASP condition. This difference is due to the combined uncertainties in the cavity wastage rate, the cavity size at TOD-1 (R_0), the flaw growth rate, and the time of flaw initiation which affect the ASP results but do not enter into the CCA results. Recall that the damage state at TOD is assumed known (i.e., with no uncertainty) for the CCA study. A breakdown of the LOCA categories in the best-estimate ASP case is shown in Fig. 56, where the dominant SBLOCA probability is due to a combination of Bin 2 and Bin 3 failures using the BE LOCA screening rules.

3.3.3 Results of the ASP Sensitivity Study

Figures 57 and Table 14 present the results of the ASP sensitivity study. As demonstrated by the time histories shown in Fig. 57a, the LC and MC LOCA screening rules and the cavity growth/shape rules were developed to provide estimated bounding curves for the BE total LOCA history. When the individual LOCA categories are compared (as in Figs. 57b for SBLOCA and 57c for MBLOCA), different cases may be required to set the bounding conditions.

Table 12. Case Matrix for ASP Sensitivity Study

Case Number	A-Tip Ductile Tearing	A-Tip Instability Tested?	Sampling of Plastic Flow Props.	Scale Driving Forces	$dR/d\tau$ (in/yr)	$da/d\tau$ (in/month)	R_0 (in)	$\Delta\tau_{flaw\text{-}ini}$ (months)	Sampling Distributions	Cavity Growth Rules	LOCA Binning Rules
ASP-001	Yes	Yes	bivariate lognormal	Yes	beta-1	Weibull	beta	Weibull	BE	BE	BE
ASP-002	Yes	Yes	bivariate lognormal	Yes	beta-1	Weibull	beta	Weibull	BE	BE	LC
ASP-003	Yes	Yes	bivariate lognormal	Yes	beta-1	Weibull	beta	Weibull	BE	BE	MC
ASP-004	Yes	Yes	bivariate lognormal	Yes	beta-1	Weibull	beta	Weibull	BE	LC	BE
ASP-005	Yes	Yes	bivariate lognormal	Yes	beta-1	Weibull	beta	Weibull	BE	LC	LC
ASP-006	Yes	Yes	bivariate lognormal	Yes	beta-1	Weibull	beta	Weibull	BE	LC	MC
ASP-007	Yes	Yes	bivariate lognormal	Yes	beta-1	Weibull	beta	Weibull	BE	MC	BE
ASP-008	Yes	Yes	bivariate lognormal	Yes	beta-1	Weibull	beta	Weibull	BE	MC	LC
ASP-009	Yes	Yes	bivariate lognormal	Yes	beta-1	Weibull	beta	Weibull	BE	MC	MC

Table 13. Case Matrix Layout Key

Cavity Growth Rule	LOCA Screening Rules		
	LC	BE	MC
LC	ASP-005	ASP-004	ASP-006
BE	ASP-002	ASP-001	ASP-003
MC	ASP-008	ASP-007	ASP-009
LC - less conservative than best estimate			
BE - best estimate			
MC - more conservative than best estimate			

Table 14. Summary of LOCA Probabilities for ASP Sensitivity Study

Case Number	1 year before TOD LOCA Probabilities					Time of Discovery (TOD) LOCA Probabilities					1 year after TOD LOCA Probabilities				
	No LOCA	LOCA	SBLOCA	MBLOCA	LBLOCA	No LOCA	LOCA	SBLOCA	MBLOCA	LBLOCA	No LOCA	LOCA	SBLOCA	MBLOCA	LBLOCA
ASP-001	98.6%	1.4%	1.39%	0%	0%	79.9%	20.1%	16.92%	0.50%	2.65%	35.8%	64.2%	44.05%	2.08%	18.06%
ASP-002	99.1%	0.9%	0.21%	0.73%	0%	82.9%	17.1%	7.45%	9.62%	0.05%	41.2%	58.8%	22.49%	32.88%	3.40%
ASP-003	98.6%	1.4%	0.44%	0.94%	0%	80.0%	20.0%	2.93%	14.23%	2.89%	35.8%	64.2%	5.40%	39.44%	19.32%
ASP-004	98.2%	1.8%	1.79%	0.00%	0%	82.2%	17.8%	16.95%	0.24%	0.63%	42.1%	57.9%	47.48%	1.69%	8.78%
ASP-005	98.9%	1.1%	0.25%	0.90%	0%	86.1%	13.9%	6.19%	7.73%	0.00%	50.0%	50.0%	21.69%	27.30%	0.99%
ASP-006	98.2%	1.8%	0.63%	1.14%	0%	82.2%	17.8%	3.84%	13.20%	0.73%	42.1%	57.9%	7.91%	40.41%	9.57%
ASP-007	99.0%	1.0%	1.03%	0%	0%	75.2%	24.8%	15.87%	0.75%	8.13%	29.2%	70.8%	38.94%	2.28%	29.57%
ASP-008	99.3%	0.7%	0.15%	0.58%	0%	77.3%	22.7%	7.96%	13.55%	1.24%	32.3%	67.7%	21.77%	37.83%	8.06%
ASP-009	99.0%	1.0%	0.29%	0.73%	0%	75.2%	24.8%	2.01%	14.18%	8.57%	29.2%	70.8%	3.14%	36.55%	31.11%

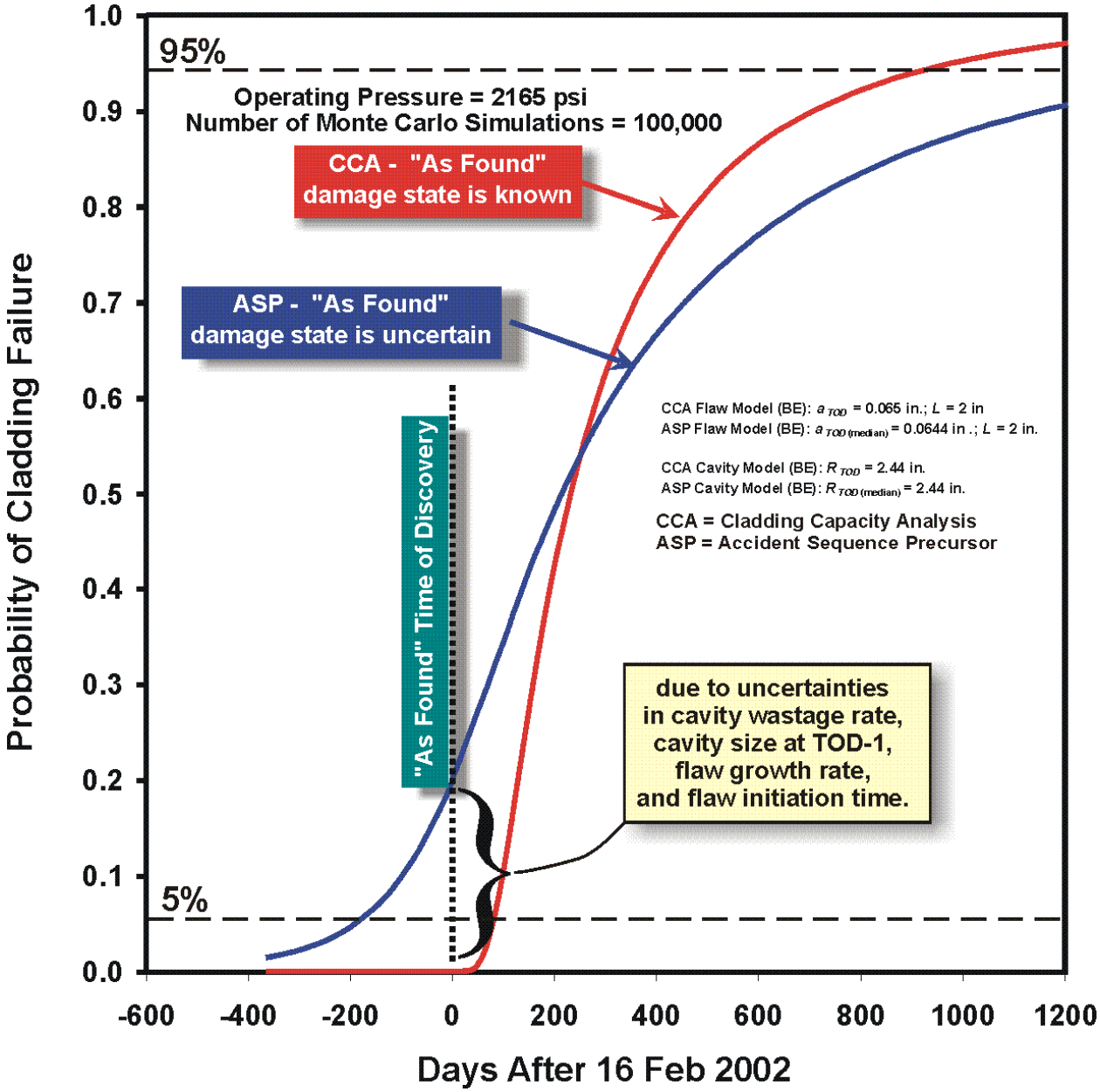

Fig. 55. Comparison of LOCA probability histories between the CCA study and the ASP study conditions where the deviation is due to uncertainties in cavity wastage rate, cavity size at TOD-1, flaw growth rate, and flaw initiation time. For the CCA study, the damage state at TOD was treated as known with no uncertainty.

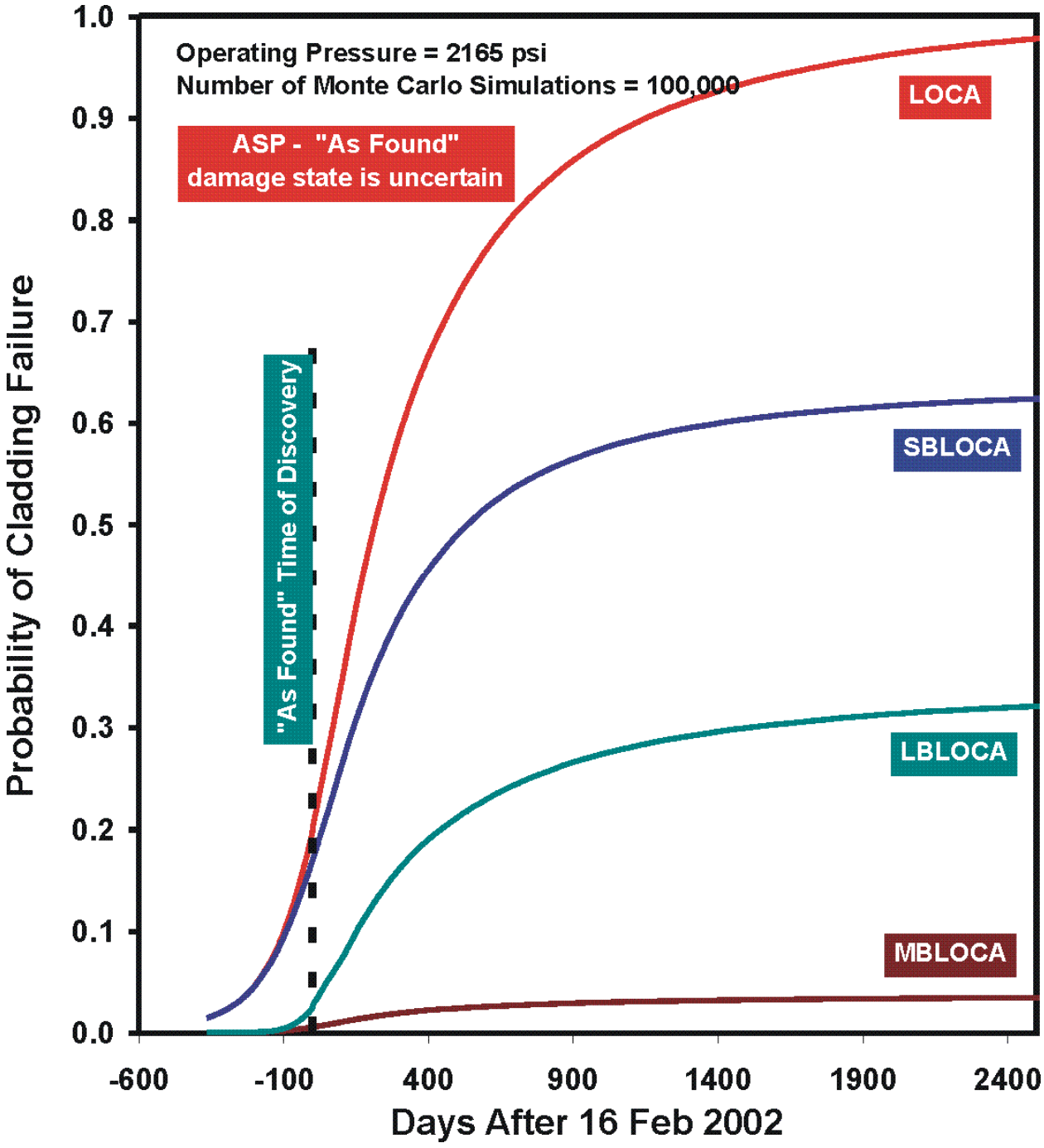

Fig. 56. LOCA probability history for the best-estimate ASP case (Case ASP-001) with a further categorization into small-break LOCA (SBLOCA), medium-break LOCA (MBLOCA), and large-break LOCAs (LBLOCA).

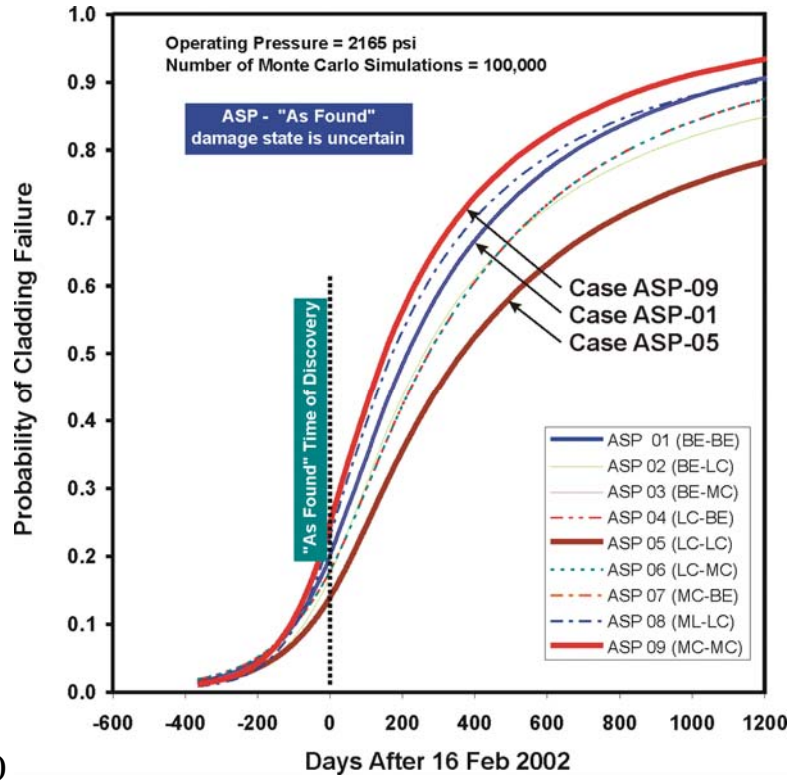

(a)

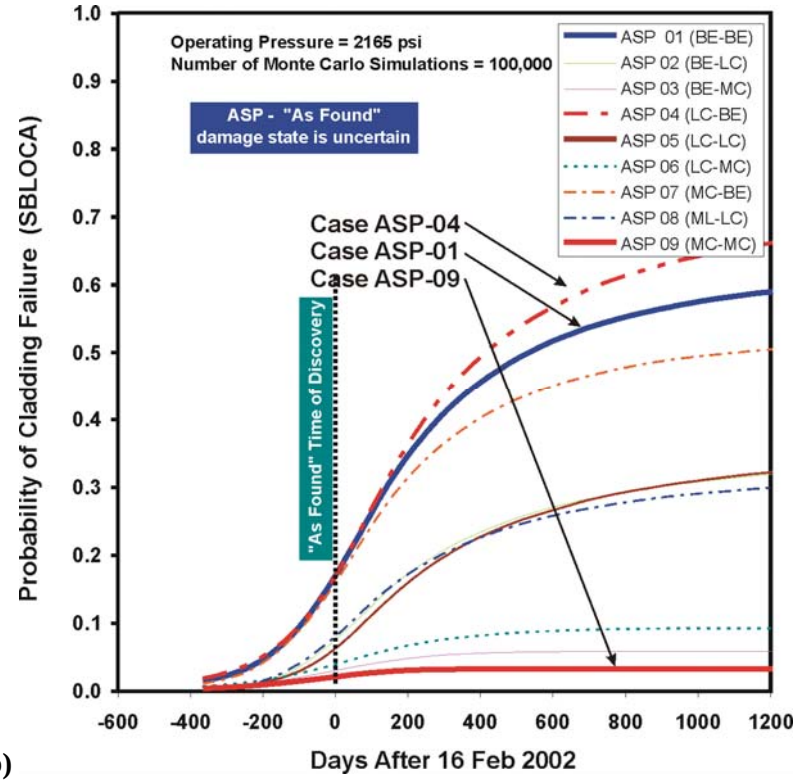

(b)

Fig. 57. LOCA probability histories for full case matrix: (a) total LOCA probabilities, (b) SBLOCA probabilities,

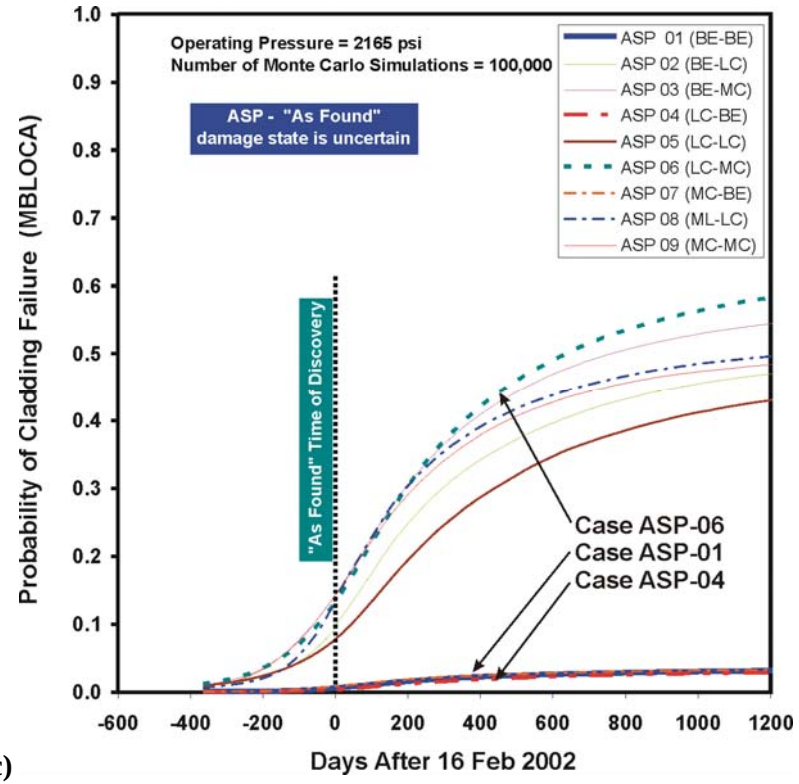

(c)

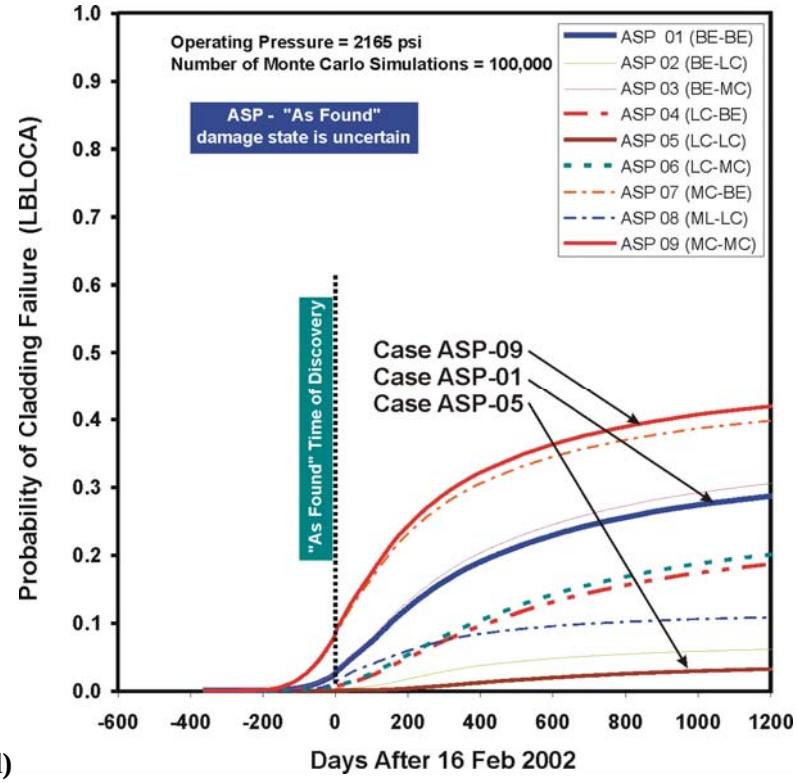

(d)

Fig. 57. (continued) LOCA probability histories for full case matrix: (c) MBLOCA probabilities, and (d) LBLOCA probabilities.

4 Summary and Conclusions

This report has presented the results of a PSM analysis of the degraded Davis-Besse RPV head, including a description of the Davis-Besse wastage-area damage model, the technical basis for the model, and the results of a *cladding capacity analysis* (CCA) and an *accident sequence precursor* (ASP) analysis of the wastage cavity.

The objectives of CCA and ASP studies were to provide approximate answers to three questions regarding the Davis-Besse event:

(1) What applied pressure would have failed the wastage-cavity cladding at the time of discovery (TOD), 16 February 2002 (CCA)?

(2) How much longer could the Davis-Besse RPV have continued in service without failure of the pressure boundary if the wastage cavity had not been discovered on 16 February 2002 (CCA)?

(3) Including uncertainties in the "As-Found" damage state of the wastage cavity, what was the probability of failure one year before TOD, and how do these uncertainties affect the estimated probability of failure at TOD (ASP)?

The answer to question No. #1 required the construction of a detailed FEM model of the Davis-Besse wastage cavity which incorporated the results of extensive laboratory measurements and metallographic examinations of the damaged site after it had been removed from the RPV head. The Davis-Besse cladding material was carefully characterized in terms of both strength (plastic-flow properties) and fracture toughness (ductile-tearing initiation and flaw growth). The fracture-toughness characterization (at a service temperature of 600 °F) was carried out by the HSST Program using pre-cracked Charpy V-Notch specimens taken from the Davis-Besse wastage cavity. All of the characterization studies included investigations of the uncertainties in the property measurements. Experimental studies with clad burst disk tests were also carried out by the HSST program at ORNL in parallel with the analytical effort to aid in validating the failure models applied in this analysis.

The results of the deterministic FEM analysis indicate that, for the most conservative assumptions regarding flaw size and depth, the estimated failure pressures all exceed the relief-valve set-point pressure of 2500 psi. This result is in agreement with the forensic finding that exposure of the wastage cavity to the nominal operating pressure of 2165 psi did not produce any evidence of crack initiation. Median pressures needed to fail the wastage cavity (by ductile-tearing initiation of the Model Flaw) were estimated to range between 3000 and 5200 psi, representing a 1.4 to 2.4 margin against the operating pressure. A 90 percent

confidence interval covering the median estimates was 2710 psi to 6500 psi (or 1.25 to 3.0 margin against the operating pressure).

Question No. #2 was addressed with a PSM analysis that reflected the very limited *state-of-knowledge* of how the wastage cavity might be expected to evolve over time, beyond the known damage state at the time of discovery. An *Expert Elicitation* was carried out by the NRC staff to provide estimates for the wastage-cavity growth rate and the rate of stress-corrosion crack development due to exposure of the unbacked cladding to the concentrated boric acid solution inside the wastage cavity. The resulting best-estimate (Case CCA-001) predicts that the cumulative probability of survival decreases to 50% after approximately 230 days of additional operation. When applying the most conservative flaw model, this median time decreased to approximately 150 days of additional operation (Case CCA-018).

Additionally, the results from Cases CCA-017 and CCA-018 can be used to provide an approximate 90 % confidence interval covering the best estimate for the median failure of the cladding, as predicted by the results of Case CCA-001. The times to failure after TOD for these cases are presented in Table 11 for 5 %, 50 %, and 95 % cumulative probabilities, and the failure histories are plotted in Fig. 45b. These results predict that, at a confidence level of 90%, Davis-Besse could have continued operating from 2 to 22 months before cladding failure would be expected.

Question No. #3 was addressed in the ASP study wherein additional uncertainty in the damage state at TOD was applied in the analysis. For the TOD, the best-estimate probability of cladding failure increased from 0% for the CCA to approximately 20% for the ASP analysis. At 1 year before TOD, the ASP analysis estimated a low probability of failure of approximately 1%.

References

1. S. A. Loehlein, *Root Cause Analysis Report, Significant Degradation of Reactor Pressure Vessel Head*, CR 2002-0891, Davis-Besse Power Station, April 15, 2002.
2. B. R. Bass, W. J. McAfee, P. T. Williams, S. Yin, R. K. Nanstad, and M. Sokolov, *Experimental Program for Investigating the Influence of Cladding Defects on Burst Pressure*, ORNL/NRC/LTR-04/13, Oak Ridge National Laboratory, Oak Ridge, TN, May 2004.
3. *Risked-Based Inspection – Development of Guidelines*, NUREG/GR – 005/CRTD – Vol. 20 – 1, prepared by the *Research Task Force on Risk-Based Inspection Guidelines*, American Society of Mechanical Engineers, prepared for the U.S. Nuclear Regulatory Commission, 1992.
4. M. G. Morgan and M. Henrion, *Uncertainty – A Guide to Dealing with Uncertainty in Quantitative Risk and Policy Analysis*, Cambridge University Press, Cambridge, UK, 1990.
5. NRC Bulletin 2001-01, "Circumferential Cracking of Reactor Pressure Vessel Head Penetration Nozzles", August 3, 2001.
6. *Recent Experience with Degradation of Reactor Pressure Vessel Head*, NRC Information Notice 2002-11, United States Nuclear Regulatory Commission, Office of Nuclear Reactor Regulation, Washington, DC, March 12, 2002.
7. W. H. Cullen, Jr., *Overview of Reactor Vessel Head Degradation*, U. S. Nuclear Regulatory Commission internet web site, http://www.nrc.gov/reactors/operating/ops-experience/vessel-head-degradation.html , 2004.
8. William D. Travers, *Status Report on Accident Sequence Precursor Program and Related Initiatives*, NRC Report SECY-99-289, U.S. Nuclear Regulatory Commission, December 20, 1999.
9. U. S. Nuclear Regulatory Commission, *Risk Assessment Review Group Report*, NUREG/CR-0400, Washington, D. C., September 1978.
10. R. J. Belles, J. W. Cletcher, D. A. Copinger, B. W. Dolan, J. W. Minarick, and P. D. O'Reilly, "1994 Accident Sequence Precursor Program Results, " *Nuclear Safety*, **37**(1)**,** (1996) 73-83.
11. P. T. Williams and B. R. Bass, *Stochastic Failure Model for the Davis-Besse RPV Head*, ORNL/NRC/LTR-02/10, Oak Ridge National Laboratory, Oak Ridge, TN, September 2004.
12. P. T. Williams and B. R. Bass, *Structural Assessment of a Corrosion-Degraded Reactor Pressure Vessel Head, Transactions of the 17th International Conference on Structural Mechanics in Reactor Technology (SMiRT 17)*, Paper No. D03-5, held in Prague, Czech Republic, on August 17-22, 2003.
13. P. T. Williams and B. R. Bass, *Analysis of the Davis-Besse RPV Head Wastage Area and Cavity*, ORNL/NRC/LTR-02/09, Oak Ridge National Laboratory, Oak Ridge, TN, September 2004.
14. *ABAQUS/Standard User's Guide, Volume I*, v6.2-4, Hibbitt, Karlsson, and Sorensen, Inc., Pawtucket, RI, 2001.
15. J. Chakrabarty and J. M. Alexander, "Hydrostatic Bulging of Circular Diaphragms," *J. Strain Anal.* **5**(3), (1970) 155-161.
16. J. W. Hyres, *Final Report: Examination of the Reactor Vessel (RV) Head Degradation at Davis-Besse*, Report No. 1140-025-02-24, Lynchburg Technology Center for Metallurgical Examinations, BWXT Technologies, Inc., BWXT Services, Inc., Nuclear and Environmental Operations, Lynchburg, VA, June 2003.
17. Solidworks® 2001 Plus, Solidworks Corporation, Concord, Massachusetts, 2002.

18. Personal communication with Dr. M. T. Kirk, Office of Nuclear Regulatory Research, United States Nuclear Regulatory Commission, Rockville, MD, February, 2004.

19. *American Society of Mechanical Engineers Boiler and Pressure Vessel Code*, Section XI, Rules for Inservice Inspection of Nuclear Power Plant Components, Division 1, Subsection IWA-3300 – *Flaw Characterization*, American Society of Mechanical Engineers, New York, 1998.

20. *American Society of Mechanical Engineers Boiler and Pressure Vessel Code*, Section XI, Rules for Inservice Inspection of Nuclear Power Plant Components, Division 2, Subsection IWB-3600 – *Analytical Evaluation of Flaws*, American Society of Mechanical Engineers, New York, 1998.

21. *American Society of Mechanical Engineers Boiler and Pressure Vessel Code*, Section XI, Rules for Inservice Inspection of Nuclear Power Plant Components, Appendix A, *Analysis of Flaws*, American Society of Mechanical Engineers, New York, 1998.

22. S. Rahman, N. Ghadiali, D. Paul, and G. Wilkowski, *Probabilistic Pipe Fracture Evaluation for Leak-Rate-Detection Applications*, NUREG/CR-6004, U. S. Nuclear Regulatory Commission, Washington, D.C, 1995.

23. S. Rahman, "Probabilistic Elastic-Plastic Fracture Analysis of Circumferentially Cracked Pipes with Finite-Length Surface Flaws," *Nuclear Engineering Design* **195**, (2000) 239-260.

24. T. W. Anderson and D. A. Darling, "A Test of Goodness of Fit," *J. Am. Statist. Assoc.* **49**, (1954) 765-769.

25. M. A. Stephens, "EDF Statistics for Goodness of Fit and Some Comparisons," *J. Am. Statist. Assoc.* **69**, (1974) 730-737.

26. K. Pearson, "On a Criterion that a Given System of Deviations from the Probable in the Case of a Correlated System of Variables is Such That it can be Reasonably Supposed to Have Arisen in Random Sampling," *Phil. Mag.* **50**(5), (1900) 157-175.

27. A. M. Law, *ExpertFit© User's Guide*, Averill M. Law & Associates, Tucson, Arizona, May 2002.

28. Kennedy and Gentle, *Statistical Computing*, Marcel Dekker, NY, (1980) 95.

29. A. R. DiDinato and A. H. Morris, "Computation of the Incomplete Gamma Function Ratios and Their Inverse," *ACM Trans. Math. Softw.* **12,** (1986) 377-393.

30. R. M. Jones and K. S. Miller, "On the Multivariate Lognormal Distribution," *J. Indust. Math.* **16**, (1966) 63-76.

31. M. E. Johnson and J. S. Ramberg, *Transformations of the Multivariate Normal Distribution with Applications to Simulation*, Technical Report LA-UR-77-2595, Los Alamos Scientific Laboratories, Los Alamos, New Mexico, 1978.

32. B. C. Arnold, "A Note on Multivariate Distributions with Specified Marginals," *J. Am. Statist. Assoc.* **62**, (1967) 1460-1461.

33. A. M. Law and W. D. Kelton, *Simulation and Modeling Analysis*, 3rd ed., McGraw-Hill Book Co., New York, N.Y., 2000.

34. N. E. Dowling, *Mechanical Behavior of Materials: Engineering Methods for Deformation, Fracture, and Fatigue*, 2nd ed., Prentice Hall, Upper Saddle River, N.J., (1999).

35. F. M. Haggag, W. R. Corwin, and R. K. Nanstad, *Irradiation Effects on Strength and Toughness of Three-Wire Series-Arc Stainless Steel Weld Overlay Cladding*, NUREG/CR-5511 (ORNL/TM-11439), Oak Ridge National Laboratory, February 1990.

36. F. M. Haggag and R. K. Nanstad, *Effects of Thermal Aging and Neutron Irradiation on the Mechanical Properties of Three-Wire Stainless Steel Weld Overlay Cladding*, NUREG/CR-6363 (ORNL/TM-13047), Oak Ridge National Laboratory, May 1997.

37. A. Saxena, *Nonlinear Fracture Mechanics for Engineers*, CRC Press LLC, Boca Raton, FL, 1998, pp. 175-179.

38. *Standard Test Method for Measurement of Fracture Toughness*, ASTM E 1820-1, Annual Book of ASTM Standards 2002, Section Three, Metals Test Methods and Analytical Procedures, Volume 03.01, American Society for Testing and Materials, West Conshohocken, PA (2002).

39. *TableCurve® 3D User's Manual*, SPSS Inc., Chicago, IL, 1997.

40. P. L'Ecuyer and S. Cote, "Implementing a Random Number Package with Splitting Facilities." *ACM Transactions on Mathematical Software* **17**, (1991) 98-111.

41. A. R. DiDinato and A. H. Morris, "Algorithm 708: Significant Digit Computation of the Incomplete Beta Function Ratios," *ACM Trans. Math. Softw.* **18**, (1993) 360-373.

42. A. Haldar and S. Mahadevan, *Probability, Reliability, and Statistical Methods in Engineering Design*, John Wiley & Sons, New York, 2000.

43. J. M. Hammersley and K. W. Morton, "A New Monte Carlo Technique: Antithetic Variates," *Proc. Camb. Phil. Soc.* **52**, (1956) 449-475.